From test-tube to the gut: Uncovering phage evolution and ecology within the gut-on-a-chip mucus layer

Wai Hoe Chin

BSc (Hons), The University of Edinburgh

A thesis submitted for the degree of Doctor of Philosophy at

Monash University in 2021

School of Biological Sciences

Copyright notice

Table of contents

This page is intentionally left blank

Abstract

Background

Bacteriophages (or phages in short) are the most abundant viruses in the human gut. Crucially, phages are viruses that infect bacteria. Their overwhelming presence in the gut imposes significant influence on the gut microbiome which impacts our health and well-being. Therefore, gut microbiome research in the past decades has increasingly involved the gut phages, revealing complex interplays between phages, bacteria and the human gut. Despite these efforts, the nature of gut phages remain stubbornly elusive particularly in areas of fundamental evolution and ecology. This was also contributed in part, by highly reductionistic or overly holistic approaches in studying microorganisms in the gut. Both of which, resulted in findings with limited relevance and intangible outcomes, respectively.

Aims

With that, this doctoral thesis aims to address the technical hurdles and fundamental knowledge gaps on gut phages through:

- A literature review on current knowledge of phage evolution and ecology in the gut.
- A proposal to adopt microfluidic “organ-on-a-chip” technology in microbiome and virome research.
- Manufacturing a gut-on-a-chip to recapitulate key features of the mammalian gut mucosal environment.
- Experimental evolution of a model phage within the gut-on-a-chip mucosal environment.
- Competing virulent and temperate phage populations within the gut-on-a-chip mucosal environment.

Methods

The gut-on-a-chip was fabricated following 3D-printing and soft-lithography principles. Mucus-secreting epithelial cell lines were grown within the device and maintained under constant perfusion to establish a dynamic gut mucus layer. Devices were then inoculated with phages and bacteria for experimental evolution (T4 phage and *Escherichia coli* bacteria) and competition assays between virulent and temperate phage populations (isogenic λ phage isolates and *E. coli* bacteria). Experimentally evolved phages were DNA-extracted and sequenced to investigate phage adaptation to the mucosal environment. Meanwhile, phage-bacteria populations from the competition assay were sampled at high temporal resolution and quantified using quantitative PCR to track population dynamics overtime.

Results

Soft-lithography fabrication yielded a single-channel microfluidic device that is optically clear, biocompatible, and capable of supporting a co-culture of mucus-secreting gut epithelial cells with bacteria and phages. Experimental evolution of T4 phages in these devices revealed the capacity of phages to directly adapt to the gut mucosa via capsid domains that were previously known for binding to mucus. Competition between virulent and temperate λ phages in the mucosa also revealed the ecological role of superinfection exclusion in driving complex interplays between lytic and lysogenic phage regimes. These regimes subsequently led to stochastic phage-bacteria establishment within the mucosa.

Conclusions

The gut-on-a-chip offers major advantages as an experimentally amenable platform whilst recapitulating key features of the mammalian gut mucosa. Phage experiments via the gut-on-a-chip have uncovered fundamental insights on phage evolutionary relationships and ecological mechanisms within the mucosal environment, which ultimately shed light on the unique composition and dynamics of phages in our gut.

Significance

Phage research *in vivo* is confounded by complexities of the *in vivo* environment. Pioneering work in this thesis will hopefully encourage prospective researchers to embrace the organ-on-a-chip platform in designing integrated experiments that could further drive explorations into fundamental and applied *in vivo* phage research.

Authorship declaration

This thesis is an original work of my research and contains no material which has been accepted for the award of any other degree or diploma at any university or equivalent institution and that, to the best of my knowledge and belief, this thesis contains no material previously published or written by another person, except where due reference is made in the text of the thesis.

Signature:

Print Name: Wai Hoe Chin

Date: 10th November 2021

Publications during enrolment

1. W. H. Chin, J. J. Barr, Phage research in “organ-on-chip” devices. *Microbiol. Aust.* **40**, 28–32 (2019). DOI: 10.1071/MA19006

2. W. H. Chin, C. Kett, O. Cooper, D. Müseler, Y. Zhang, R. S. Bamert, R. Patwa, L. C. Woods, C. Devendran, D. Korneev, J. Tiralongo, T. J. Lithgow, M. J. McDonald, A. Neild, J. J. Barr, Bacteriophage evolves enhanced persistence to a mucosal surface; *submitted for review.*
    - Preprint available at: *bioRxiv*, DOI: https://doi.org/10.1101/2021.05.11.443681 with the version titled “Bacteriophage adaptation to a mammalian mucosa reveals a trans-domain evolutionary axis”, dated 11th May 2021.
    - Manuscript version included in this thesis has undergone a single-round of peer review with the journal *Cell Host & Microbe* where feedback and comments from reviewers have been incorporated. Current version is resubmitted to the journal *Proceedings of the National Academy of Sciences of the United States of America* (*PNAS*) for subsequent review and consideration for publication as of 6th September 2021.

Thesis including published works declaration

I hereby declare that this thesis contains no material which has been accepted for the award of any other degree or diploma at any university or equivalent institution and that, to the best of my knowledge and belief, this thesis contains no material previously published or written by another person, except where due reference is made in the text of the thesis.

This thesis includes one (1) original paper published in peer reviewed journals and one (1) submitted publication for peer-review. The core theme of the thesis is “Phage evolution and ecology”. The ideas, development and writing up of all the papers in the thesis were the principal responsibility of myself, the student, working within the School of Biological Sciences under the supervision of Dr Jeremy J. Barr.

The inclusion of co-authors reflects the fact that the work came from active collaboration between researchers and acknowledges input into team-based research.

Thesis Chapter	Publication Title	Status	Nature and % of student contribution	Co-author name(s) Nature and % of Co-author’s contribution*	Co-author(s), Monash student Y/N*
1	Phage research in ‘organ-on-chip’ devices	Published	85%. Conceived article main structure. Undertaken relevant literature search and information extraction., Wrote the manuscript. Edited abstract. Conceptualised and realised figures. Involvement in article peer review	1) Jeremy Barr. Conceived article main structure. Written article abstract. Reviewed and edited article text and figures. (15%)	No

			and publication process.		
3	Bacteriophage evolves enhanced persistence to a mucosal surface	Submitted	70%. Conceived the study. Designed experiments. Designed, fabricated and maintained gut-on-a-chip devices. Performed high-resolution phage-bacteria temporal dynamics, phage experimental evolution, recombination assay, competition assay, phage-glycan washout assay and assisted in molecular cloning for recombinant protein expression. Performed formal analysis of results. Written the manuscript. Submitted the manuscript and involvement in article peer review process.	1) Ciaren Kett Assisted in gut-on-a-chip fabrication and maintenance. Assisted in and performed qPCR for high resolution phage-bacteria temporal dynamics experiment (4.25%) 2) Oren Cooper. Glycan array and SPR experiments with full data processing and analysis (3.25%) 3) Deike Müseler Designed and manufactured automated dispensing platform used in high resolution phage-bacteria temporal dynamics experiment (2.5%) 4) Yaqi Zhang Designed and manufactured automated dispensing platform used in high resolution phage-bacteria temporal dynamics experiment (2.5%)	1, 3, 4, 7: Yes 2, 5, 6, 8 – 14: No

				5) Rebecca S. Bamert. Recombinant Hoc protein expression, purification and modelling (1%). 6) Ruzeen Patwa. Molecular cloning for recombinant protein expression (1%). 7) Laura C. Woods. Assisted with formal analysis of mutational dataset (0.5%). 8) Citsabehsan Devendran. Assisted with gut-on-a-chip fabrication techniques and microfabrication expertise (0.5%). 9) Denis Korneev. Electron microscopy sample processing and imaging (1%) 10) Joe Tiralongo. Provided resources and expertise on glycan array and SPR experiments (0.5%). 11) Trevor J. Lithgow. Provided resources and expertise on recombinant Hoc	

				protein expression, purification and modelling (0.5%) 12) Michael J. McDonald. Conceived and supervised the study. Advised on formal analysis of mutational dataset. Reviewed first manuscript (2.5%). 13) Adrian Neild. Conceived and supervised the study. Provided paid access to core engineering facilities for gut-on-a-chip fabrication (2.5%). 14) Jeremy J. Barr. Conceived, funded and supervised the study. Wrote and reviewed the manuscript. Involvement in article peer review process (7.5%).	

I have not renumbered sections of submitted or published papers in order to generate a consistent presentation within the thesis.

Student name: Wai Hoe Chin

Student signature: **Date:**

I hereby certify that the above declaration correctly reflects the nature and extent of the student's and co-authors' contributions to this work. In instances where I am not the

responsible author, I have consulted with the responsible author to agree on the respective contributions of the authors.

Main Supervisor name: Jeremy J. Barr

Main Supervisor signature: **Date:**

Acknowledgements

Borrowing from the butterfly effect, small lessons and inspirations instilled at a young age can immensely define the trajectories of one's life; where in mine, a life as a budding scientist. To that, I owe this to everyone from past to present that has contributed to my growth, notwithstanding some honourable "shoutouts" that follows.

First and foremost, a massive thanks to my supervisor Jeremy Barr for taking a chance on a young and naïve individual four years ago. Not only have you taught me how to be a scientist but also, in overcoming one of my biggest enemies: my inner critic. Words cannot adequately convey my gratitude for your guidance, tutelage, and your unfaltering support. The occasional wit was definitely an added bonus to the privilege of working with you! Thank you for helping me in achieving one of my life's dreams.

Equally, my heartfelt thanks to Monash University and the Australian Government for their generous support through their scholarship and stipend programs. Without which, this entire doctoral experience would not have been possible. This research was supported by an Australian Government Research Training Program (RTP) Scholarship.

Secondly, to my lab mates and colleagues, I could not have asked for a more motivating, accepting and supporting lot to work with; you are as close as family gets for me while being abroad. Thank you for being there through all the ups and arguably some of the toughest downs we all have faced in the new decade. Special mentions to Marion, Sofia and Ruzeen for regularly entertaining my eccentric shenanigans in and out of the lab.

Thirdly, to my co-supervisors and mentors, my deepest thanks for supporting my love for learning by enriching my academic experience beyond microbiology, in addition to your guidance and encouragements throughout. Special mentions to Tim Connallon and Douglas Brumley for reviving my passion in mathematical biology. As for my co-authors, my work would not have been possible without your expertise and contributions. It has been an honour to have collaborated with all of you.

Finally, to my family and friends back home (and some in the Northern Hemisphere), I miss you all dearly. I would not be the person that I am today without each and every one of you. Iman, I am waiting for your turn to join the ranks!

Mum and dad, this is for you. Thank you for everything.

Introduction and literature review

Phage evolution and ecology in the mammalian gut

This chapter written as a traditional thesis chapter which includes an introduction and an extensive literature review on our current stance regarding phage evolution and ecology in the gut. This chapter is then finalised with a prospectus which foreshadows on experimental approaches adopted in subsequent chapters to address some of the knowledge gaps highlighted within this literature review.

Phage evolution and ecology in the mammalian gut

1. Introduction

Bacteriophages (phages in short) are viruses that infect bacteria to propagate. To-date, there are four known lifecycles in which phages may propagate: lytic, lysogenic, pseudolysogenic and chronic (1). The majority of phages adopt the lytic and lysogenic lifecycles, resulting in two major phage types: virulent phages and temperate phages. Virulent phages – as the name suggests – propagates exclusively via the lytic cycle, resulting in the formation of viral progeny which are then released from the bacterium via cell lysis to further infect susceptible hosts. Meanwhile, temperate phages adopt both lytic and lysogenic cycles where in the latter, the phage genome is integrated into the bacterial host genome, lending a “dormant” state in which the phage co-exists within the bacterium’s chromosome. Here, the integrated phage genome known as a prophage, propagates vertically when the bacterial host, known as the lysogen, divides. This dormant state is maintained until certain environmental cues trigger prophage induction where the prophage exits the lysogenic cycle and enters into the lytic cycle (2).

Through their lifecycles, phages are able to shape the overall bacterial community within an ecosystem. In doing so, phages can significantly impact on higher order processes built upon the underlying phage-bacterial community. A prime example is the mass predation of pelagic bacteria by virulent phages, contributing significantly to the dissolved organic matter pool within the marine food web (3). In addition, phages

also foster marine microbial diversity by imposing evolutionary and ecological pressures, which are key to a functioning “healthy” ecosystem (4–6). Given the global ubiquity of phages and bacteria, it is becoming ever more pertinent to improve our understanding on phage evolution and ecology in nature.

The human gut is an exemplary natural environment that is densely populated with microbes and viruses. Gut bacteria remain the centre of gut microbiome research to-date and have been unequivocally demonstrated to impact human health and well-being (7, 8). The collection of gut viruses known as the gut virome, is also increasingly recognised as a key element to the gut ecosystem, especially since phages are the majority member of the gut virome (9–11). Consequently, explorations into the gut virome – specifically gut phages – have chiefly focused on their role in modulating the gut microbiome through evolutionary and ecological mechanisms. Adding to the growing body of knowledge on gut phages, there is emerging evidence that phages are capable of directly interacting with the mammalian gut (12). These evidences for phage-mammalian interactions are profound since phages have only been known to interact with prokaryotes for the purpose of propagation. Hence, the discovery of phage-mammalian interactions also presents the possibility of direct co-evolution between phages and their mammalian “host”, in addition to their conventional co-evolution with the commensal microbiome. However, most studies on gut phage evolution and ecology were limited to sequencing-based approaches or controlled experiments via *in vitro* and *in vivo* models. All of which have their respective assumptions, extrapolations and challenges in arriving to precise conclusions on the nature of gut phages. Despite these challenges, many valuable insights have been

uncovered (13, 14); progressively exposing the silver linings behind the viral “dark matter” of our gut.

This review dives into key literature to provide an overview of our knowledge of phage evolution and ecology in the human gut. Evolution and ecology in any given environment are inextricably intertwined. However, for the purpose of structuring this review, I will attempt to explore both concepts in two independent sections. In the first, I will explain the common theories used to describe phage-bacteria co-evolution in the gut. To which, I then present and discuss the scientific evidences for phage-bacteria co-evolution in the gut or lack thereof. I will also elaborate on the relatively recent discovery of phage-mammalian interactions in the gut, and how this may be key in shifting our perspective of gut phages from viruses that co-evolve exclusively with the gut microbiome, to a three-way engagement between phages, bacteria and the mammalian gut (referred to as the *in vivo* tripartite theory of gut phages). In similar fashion to the first section on gut phage evolution, the second section begins with the ecological hypotheses that are currently proposed to govern phage-bacteria population ecology in the gut. These ecological hypotheses revolve around the lifecycles adopted by phages within the gut. To that, I will explore the evidences on the predominant lifecycles of gut phages while shedding light on the current debate arising from approaches undertaken to verify these hypotheses. Finally, I will conclude the review with a forward-looking perspective on achieving a unified eco-evolutionary theory of gut phages and the prospects of disentangling the intricate relationship between phages, microbiome and the mammalian gut.

2. Phage evolutionary theories

As obligate bacterial viruses, phage evolution was chiefly studied between phages and their bacterial hosts. Given the parasitic nature of phages on bacteria, their co-evolutionary relationship is often antagonistic. Bacteria evolve defences in efforts to mitigate phage infection i.e. phage resistance mechanisms. Generally, phage resistance mechanisms include surface mutations to abrogate phage adsorption. Other forms of resistance include components that interfere and cleave invading phage genomes such as restriction-modification (RM) systems, and the renown clustered regularly interspaced short palindromic repeats (CRISPR)-CRISPR associated protein (Cas) system. An in-depth review on the molecular bases of phage resistance is available here for further reading (15). As a result, phages respond by evolving counter-defences to overcome these phage resistance mechanisms; for example, by mutating receptor-binding domains to regain host adsorption, host-range expansion and escaping cleavage by RM and CRISPR-Cas systems (16). The back-and-forth evolution of defence and counter-defence traits between bacteria and phages forms the very basis of antagonistic co-evolution between phages and bacteria. Phage-bacteria antagonistic co-evolution can be described along a spectrum beginning with arms-race to fluctuating selection dynamics, the latter also commonly referred to as “Red-Queen dynamics” (17).

2.1 Arms-race dynamics

In an arms-race, selection for antagonistic traits is directional, meaning that there is a strong reciprocal selection between defence and counter-defence genotypes (18). This results in both bacteria and phages accumulating defence and counter-defence traits respectively, which leads to an overall community with highly phage-resistant bacterial populations and increasingly infective and/or generalist phages. To this end,

robust arms-race dynamics are often thought to limit overall genetic diversity within a phage-bacteria community since the population is constantly replaced by the most resistant bacterial population and infective phage via selective sweeps (18). However, accumulation of these traits is often costly, which reduces the overall fitness of the phage-bacteria community overtime. Consequently, a phage-bacteria community engaging in a robust arms-race is vulnerable and sensitive to external perturbations notably, nutrient abundance (19, 20) and population homogeneity (21, 22). This renders arms-race dynamics unsustainable for indefinite progression under most physiological conditions beyond nutrient-rich and homogeneous laboratory cultures; eventually giving way to fluctuating selection dynamics (23).

2.2 Fluctuating selection dynamics

In contrast to arms-race, fluctuating selection dynamics (also known as “Red-Queen” dynamics) between phages and bacteria is non-directional (18). Here, phages that target the commonest bacterial genotype within the community, result in selection favouring the expansion of rarer host genotypes that were not subjected to significant predation pressure. Consequently, as the rare host genotype flourishes, cognate phages will also expand and the cycle of selection repeats for the following rare host genotype. The result is a phage-bacteria genotypes that fluctuates in a negative-frequency dependent manner. Since phage predation is not directed to the rare host genotype – and hence, non-directional selection – neither bacteria nor phages accumulate resistance and infectivity traits. As a result, the phage-bacteria population is polymorphic, typically consisting of diverse specialist phages accompanied by a bacterial population adopting a diverse set of phage resistance traits; unlike arms-race where mutation accumulation favours phage generalists and a universally resistant

bacterial population. Moreover, without the accumulation of costly mutations, the mean fitness of the phage-bacteria population remains constant overtime and is more robust to external perturbations compared to arms-race evolution (23). In principle, a population undergoing pure fluctuating selection is stable and may progress indefinitely.

3. Phage-bacteria co-evolution in the gut

3.1 Brief lessons and challenges from the wider environment

Determining where a phage-bacteria population lies within the arms-race or fluctuating dynamics spectrum typically requires time-shift assays (17, 24). Here, clonal phages and bacteria are co-evolved under highly controlled experimental settings. The population is sampled periodically where the phages and bacteria are separated by purification, followed by cryo-preservation as historical time-stamps of the population. Phages from selected timestamps are then subjected to bacteria across a broader range of timestamps and vice versa, in order to assess temporal changes in phage infectivity and bacterial resistance. As previously discussed, both infectivity and resistance are expected to increase in an arm race overtime, while these traits remain constant or decrease under a fluctuating selection regime. However, natural phage-bacteria communities are highly diverse with complex phage-bacteria networks (25, 26). This complex network coupled with the manifold of environmental factors present significant obstacles in explicitly demonstrating phage-bacteria co-evolutionary dynamics beyond controlled laboratory settings.

Despite the challenges, antagonistic co-evolution is ubiquitous and has been documented from marine environments (27) to terrestrial soil (28, 29) and arboreal

settings (30, 31). The majority of these studies adopts a combination of environmental sampling which are followed up with controlled experiments to implicate the underlying co-evolutionary dynamics of the community. Phage evolution in the marine environment are amongst the most well-studied. In one attempt to describe the marine phage-bacteria network and the evolutionary patterns of bacterial resistance to phages, 21 strains of *Cellulophaga baltica* along with 45 phages were isolated from Danish waters and all phage-bacteria permutations were tested (26). Not only did the authors discover an intricate infection network between phages and bacteria, but there was also significant variability in phage infectivity and bacterial resistance across the phage-bacteria permutations. The majority of phages exhibited broad host ranges with only six phages demonstrating highly specific infections (26). This suggests that the marine phage-bacteria communities tended towards an arms race, although no time-shift assays were performed in this study to ascertain this.

To this, Marston et al. initiated an experimental co-evolution between a clonal population of a pelagic, virulent cyanophage and a cyanobacterium *Synechococcus* spp. within a chemostat environment (32). During the six months of experimental co-evolution, both phage and cyanobacterium diversified across four independent replicate chemostats, yielding 4 to 13 distinct phage phenotypes and 4 to 11 bacterial phenotypes with varying levels of bacterial infectivity and phage resistance, respectively. Crucially, time-shift assays revealed that the mean infectivity and resistance of phages and bacteria in the replicate chemostats increased over the six-month experiment, indicative of an arms-race evolution. Marine phage diversification was later recapitulated in a follow up sequencing and cluster analysis of 108 marine cyanophages isolated from coastal waters across 15 years (33). Here, the

cyanophages diversified to distinct ecotypes with phage clusters persisting stably for over a decade. This suggests the local adaptation of phages to bacterial populations along the coastal regions, implying a fluctuating selection regime (33). However, the study lacked a defined phage-host network and vital environmental contexts, which precludes the revealing of evolutionary mechanisms underlying the collective diversity and stability of these phage clusters. Overall, these particular example studies highlight the conundrum in elucidating phage-bacteria antagonistic coevolution in nature i.e. the trade-offs between reductionistic laboratory approaches capable of identifying evolutionary regimes and environmental sample snapshots in preserving and capturing natural community complexity.

3.2 Evidences from metagenomic sequencing of human cohorts

As a natural habitat for phages and bacteria, the mammalian gut is no exception in harbouring a complex and active phage-bacteria community. The gut mucosa is more densely populated with phages and bacteria in comparison to marine environments ((34); discussed in further depth in the gut phage ecology section). One would be convinced that with high abundance and density in the gut, co-evolution between phages and bacteria is inevitable. However, providing clear-cut evidence towards a generalised consensus on gut phage-bacteria co-evolution is much harder than anticipated; as alluded from brief lessons and challenges on co-evolution in the wider environment.

Studies adopting sequencing-based approaches to track phages and bacterial metagenomes overtime largely supported the presence of co-evolution between gut phages and bacteria. Minot et al. tracked the gut virome of a single adult individual for 2.5 years (35) and demonstrated that the gut virome was generally stable with 80% of

478 well-defined viral contigs persisting throughout the study period. However, finer scale analysis at the nucleotide level showed high rates of base substitutions, especially in virulent phages relative to their temperate counterparts. In particular, four contigs of the virulent *Microviridae* phages experienced up to 4% base substitution over 2.5 years, which exceeds the 3.1% threshold for *Microviridae* phage speciation. In addition to rapid diversification of phages, contigs from gut bacteria also indicated evidence for antagonistic evolution via CRISPR-associated adaptations. One CRISPR array underwent a complete turnover of CRISPR spacers over 2.5 years, suggesting the progressive loss and acquisition of spacers by gut bacteria as the gut virome rapidly evolves; although no assignment between phage and host taxa was performed (35). In support of CRISPR-based resistance evolution in the gut, a separate study catalogued over 50,000 CRISPR spacers from a 124-individual cohort within a publicly available faecal metagenome repository (36). The majority demonstrated that the presence of CRISPR spacers correlated with the absence of the targeted phage at the time of isolation. In the minority cases where both spacer-harbouring bacteria and phages co-existed, targeted phages were often found at low levels. This not only supports antagonistic co-evolution through CRISPR spacers but also the effectiveness of CRISPR mechanisms in protecting against infection by gut phages.

While the identical nature of nucleotide sequences between CRISPR spacers and the targeted phage is more amenable to detection via metagenomics, other forms of phage-bacteria antagonistic co-evolution were also observed. In one study, 252 faecal metagenomes from public datasets were filtered to identify 11 highly abundant bacterial species (37). Analysis of genome variation across the 11 species found that 33% of variation were on genes encoding for glycosyltransferases. Moreover, large

gene deletions were found in capsular polysaccharide synthetic (CPS) gene clusters commonly associated with glycosyltransferases, in 41 independent *Bacteroides thetaiotamicron* detected from the faecal metagenomes. Glycosyltransferases are responsible for modifying bacterial surface epitopes. Non-sense mutations or phase variation in glycosyltransferase-encoding genes have been demonstrated as counter-evolutionary strategies in conferring bacterial resistance against phages (38, 39). Hence, selection pressure from gut phages could be driving the independent emergence of these glycosyltransferase gene variations and CPS deletion mutants. This is especially resounding when considering that the most abundant gut phage – the crAssphage – infects bacteria of the *Bacteroides* genus (40, 41).

Most early public repository metagenomes used in these key studies (36, 37), lack temporal contexts that are necessary to infer the underlying phage-bacteria co-evolutionary dynamics. Moreover, these datasets depend heavily on available annotated protein and genomes references to predict and identify co-evolving phage and bacterial members in the gut; although this is rapidly changing in more contemporary gut virome metagenomic studies (refer to Section 5.1 on taxonomic classification approaches between older and recent gut metagenomic studies). This limitation is highlighted by the gargantuan effort required to identify the crAssphage despite its highly abundant and globally distributed nature in the gut (40, 41); let alone rarer phage-host pairs which will inevitably be precluded from analysis until an improved annotated reference databases are available. Finally, even if temporal information is available, inferring co-evolutionary dynamics from metagenomic read abundances overtime is highly sensitive to the taxonomic level observed. By that, the phage community may appear relatively stable at “coarser” taxonomic levels.

However, at “finer” taxonomic scales, rapid population fluctuations were observed to predominate the underlying population dynamics (42). In this case, the circular problem remains where taxonomic identification at finer taxa e.g. genus- and species-level, is only as precise as the most contemporary reference genomes available.

3.3 Evidences from experimentation with *in vivo* models

To address the limitations of sequencing-based approaches, certain studies have attempted to utilise *in vivo* models for controlled study of phage-bacteria co-evolution directly within the gut environment. Even then, evidence of gut phage-bacteria co-evolution is mixed and varies depending on the experimental design adopted. In a pioneering study of phage-bacteria dynamics and co-evolution in the gut, germ-free mice were colonised with *E. coli*, followed by inoculation with T4 or T7 phages in two independent experiments (43). Here, the T4 phage experienced an initial population spike after 8 hours post-inoculation but subsequently decreases over the experimental course. No T4-resistant *E. coli* colonies were recovered indicating the absence of co-evolution between T4 phages and *E. coli* hosts in the gut. Meanwhile, the T7 phage persisted stably with their bacterial hosts throughout the experiment. 20% of bacteria recovered exhibited resistance to T7 phage, indicating the presence of co-evolution. The authors also noted that 20% phage resistance is much less compared to chemostat experiments where T7 phage resistance arises to 99% of the bacterial population (43). The collective outcome was primarily explained by two factors: i) fundamental differences between T4 and T7 phage biology where the T4 is not efficient at infecting late-stage stationary hosts in the gut but the T7 could, and ii) spatial refuge of bacterial microcolonies in the gut which limits co-evolution (later supported by (44)). Already, this simple study suggests that phage-bacteria co-

evolution in the gut is highly context-dependent and that a purely reductionistic approach to studying gut phages one phage-host pair at a time, may not be the best in achieving accurate representation on phage-bacteria co-evolution in the gut.

To this, several studies have established animal models harbouring complex phage-microbial communities to recapitulate natural phage-bacteria population settings in the gut. The earliest study involved inoculating germ-free mice with a 15-member artificial microbiome, followed by viral-like particles (VLPs) purified from faecal samples of five healthy human subjects (45). Key findings were centred on five previously unknown phages identified from the VLP pool that predominated and influenced the microbial community structure in the murine gut. One of the earliest phages to expand in the gut infected *Bacteroides caccae* where population initially collapsed followed by recovery. The population recovery was not linked to any genetic factors that may lend phage resistance indicating the absence of antagonistic co-evolution between the phage-host pair. Instead, epigenetic and/or ecological mechanisms such as epistasis or bacterial spatial refuge was implicated in bacterial population recovery. In contrast, there is partial evidence for co-evolution in the fifth predominant phage identified amongst the VLP pool. This phage exhibited genomic variation overtime that is most likely driven by co-evolution with its bacterial host; although none of the genomic variations were described nor the bacterial host was identified (45).

In a separate and later study, a relatively similar murine model was adopted by inoculating germ-free mice with 10 bacterial species representing the major phyla found in the human gut microbiome, along with four virulent phages targeting four of the representative bacterial species, respectively (46). Here, the authors revealed the

cascading effects caused by phage predation on the four representative species across the entire 10-species consortium, leading to compositional changes to the gut microbiome. Importantly, none of the phage-targeted bacterial species were eradicated. One of the phage-targeted bacterial species, *Enterococcus faecalis* had 68% resistant colonies after 10 days post-phage challenge, providing evidence for phage resistance evolution in the gut. Despite this, all four virulent phages persisted alongside the 10-species microbiome; contrasting with previous mono-colonised murine models that could not sustain lytic T4 persistence (43).

Notwithstanding the mixed evidences thus far, these *in vivo* models suggest that phage-bacteria antagonistic co-evolution could occur in the gut, but its extent is likely influenced by ecological factors such as gut bacterial diversity and spatial distribution of phage and bacterial populations. Following on more recent examples, the conventional murine gut microbiome was crucial in providing an intermediate susceptible bacterial host that enabled a virulent phage to switch from its original host to infect a non-susceptible host strain (47). In this case, the multispecies context of the gut microbiome promotes phage-bacteria co-evolution in the murine gut by facilitating phage-host jump events. In contrast, a further study demonstrated that the heterogeneous distribution of phages and bacteria in the murine gut resulted in bacterial populations that were protected from phage eradication by spatial refuge (44). This enabled stable phage-bacteria coexistence in the gut without evolving phage resistance traits, and that the spatial context of the gut mucosa tempers phage-bacteria co-evolution by segregating phage-bacteria populations (44). In summary, both metagenomic sequencing and experimentation with animal models support the possibility of phage-bacteria co-evolution in the gut. However, neither has yet provided

a clear consensus nor described the extent of co-evolution between gut phages and their bacterial hosts. Consequently, evolutionary dynamics between gut phages and bacteria (i.e. arms-race and fluctuating selection dynamics) remains elusive and will warrant robust and elegant experimentation to uncover in the future.

3.4 Exploring the interactions between phages, the mammalian gut and the potential for co-evolution

Phages and bacteria do not co-evolve in isolation within the gut. The mammalian gut is also an active contributor by imposing selection in the form of spatial and temporal heterogeneity. Spatially, the gut mucus layer is comprised of an inner and outer layer. The inner layer is a densely-packed and impermeable layer, which gradually expands to form a permeable outer mucus layer (48). This mucosal gradient along with the highly structured mucosal epithelial layer defines the spatial heterogeneity of the gut mucosa (49). Temporally, the mucus layer also experiences turnover dynamics from the constant production of mucus by the underlying epithelium and sloughing from luminal flow (50). Furthermore, mucosal profile and chemistry may also fluctuate depending on the physiological and immunological state of the mammalian gut e.g. homeostasis, infection, inflammation, etc. (51).

Bacteria – as living organisms – are able to effectuate mechanisms and strategies to persist under the dynamic conditions of the gut (52, 53). However, phages exist as inanimate viral particles that rely hitherto exclusively on their bacterial hosts to propagate and therefore, persist within the gut. In this linear interpretation of symbiosis between phages, bacteria and the mammalian gut (54), phages interact with bacteria and vice versa, resulting in compositional changes to the gut virome and microbiome.

Changes to the gut microbiome lends physiological responses from the gut mucosa which feeds back to the gut microbiome and subsequently, the gut virome. Through this linear perspective, phages in the gut virome only engage with the mammalian gut indirectly. However, there is an mounting evidence that phages are able to interact directly with the mammalian gut and its secreted factors, particularly mucus.

Phages have been shown to adhere to mucus as described by the bacteriophage adherence to mucus (BAM) model (55). In this model, immunoglobulin (Ig)-like domains of the highly immunogenic outer capsid (Hoc) protein were demonstrated to interact with mucin glycoproteins, resulting in phage-adherence to mucus. This promoted the enrichment of phages within the mucus layer to form a protective barrier against invading bacterial pathogens (55, 56). A study later demonstrated the BAM model in action where phages adhering to the primary mucus of rainbow trout fostered phage persistence within the mucosal surface, thereby conferring protection against the pathogenic bacterium *Flavobacterium columnare* (57). Interestingly, approximately a quarter of double-stranded DNA (dsDNA) *Caudovirales* phages are predicted to encode these Ig-like folds (58). This implies that these Ig-like domains are highly prevalent in the gut virome since dsDNA *Caudovirales* phages are relatively abundant in the gut (59). Furthermore, these Ig-like domains are exceptionally variable with the potential to accommodate over 10^{13} functional configurations (60), suggesting that gut phages possess an unprecedented adaptive potential to respond directly to changes in the gut mucosa through these Ig-like domains.

In addition to Hoc Ig-like domains, other phage structural domains such as proteoglycan-binding domains (61), C-type lectin folds (62, 63) and the Ig-folds of

Bacteroides-associated carbohydrate-binding often N-terminal (BACON) domains (64), have been implicated with the capacity to engage with the mammalian mucosal environment. For example, through a combination of *in vitro* and murine gut models of pathogenic *E. coli* infection, the phage ES17 was isolated and demonstrated enhanced lytic activity under mucin-rich environments (61). Further experimentation revealed that phage ES17 possess tail fibres that bind to mammalian-derived heparan sulfated glycoproteins. These glycoproteins served as a co-receptor to enhance adsorption to bacterial cells in mucin-rich environments. More importantly, phage ES17 was the only phage that did not experience lytic activity inhibition by mucin, while 12 other phages that were screened in the study could not propagate in mucin (61). This implies that the gut can be highly selective to phages by directly affecting their ability to propagate within the mucosal environment. An earlier study also reported the direct influence of the gut mucosa on phage activity by demonstrating that phages are more virulent towards *Clostridium difficile* when co-cultured on a gut mucosal epithelium compared to test-tube cultures (65). Further investigation revealed that the increased virulence is attributed to phage adsorption to the mucosal epithelium, although the phage receptor responsible was not identified. When three different *C. difficile* phages were applied to bacteria-free mucosal epithelia, one of the phages showed no adsorption while two other phages exhibited 40% and 70% adsorption, respectively. However, when the three phages were added to non-mucus producing HeLa cell layers, none of the phages were adsorbed (65). This again suggests that the gut mucosa can be highly selective in retaining phages and that mucus is a key component in determining phage-selectivity.

In summary, these studies underscore the direct selection imposed by the gut mucosa on phages. In doing so, they also uncovered the ability of phages to engage directly with the gut mucosa; to which, selection can act upon to facilitate co-evolution between the phage and the mammalian gut. Given this knowledge, phage research *in vivo* should adopt a more holistic perspective where phages, bacteria and the mammalian entity are all engaged in a three-way i.e. “tripartite”, symbiosis (Fig.1); in place of the aforementioned linear interpretation. In other words, we would gain a better understanding of phage evolution within the gut by accounting for interactions along the phage-mammalian axis within future evolutionary frameworks.

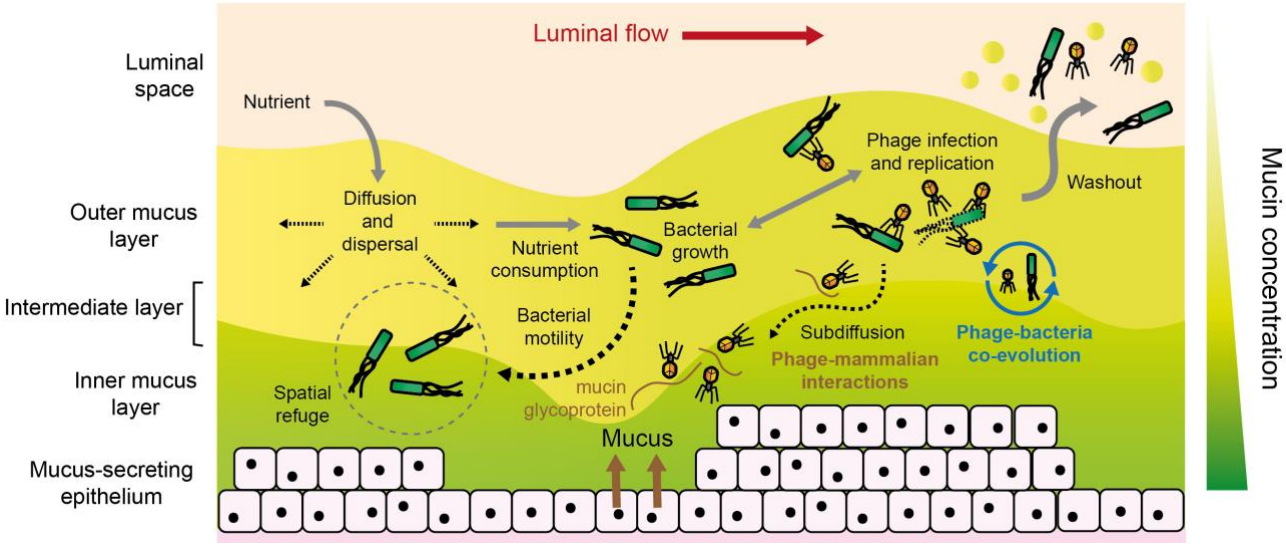

Fig.1: Phage-bacteria-mammalian three-way symbiosis in the gut mucosal environment. Bacterial growth is supported by nutrients dissolved into the mucosa from gut lumen contents and mucus secreted by the gut epithelium. Growing bacterial populations are either predated by resident phages for replication, or protected from phage predation through spatial refuge within the mucosal layer. In the former, antagonistic co-evolution between phages and bacteria likely occur as both entities attempt to persist and co-habit within the mucosal environment, while the latter tempers phage predation pressure on bacterial populations to constrain antagonistic co-evolution. This suggests that co-evolution within the gut mucosal environment is highly context-dependent.

In addition to selection between phages and bacteria, the mucosal environment also imposes selection pressures more globally through upward pressure from mucus secretion and washout from sloughing. In this case, phages and bacteria also require strategies to overcome mucosal turnover dynamics in order to persist such as bacterial motility and phage binding to mucin (i.e. BAM model) (55, 66). The latter also results in the subdiffusion of phages to lend phage enrichment within the mucosal environment (56). At a broader context, this phage-mucus interaction also highlights the potential for phages to interact with the mammalian environment, potentially evolving traits to leverage the mucosal environment for persistence.

4. Some theories on phage-bacteria population ecology

Infection by a virulent phage on a susceptible bacterial host leads to lytic cell death. Through this, virulent phages exert significant top-down control on the prokaryotic community which plays an important role in maintaining microbial population equilibrium and diversity. However, the effects of temperate phage behaviour on the overall phage-bacteria population is less explicit since temperate phages are able to alternate between the lytic and lysogenic lifecycles, with the latter not lending bacterial host mortality. In fact, the acquisition of prophage via lysogeny could instead, provide fitness benefits to the bacterial host through lysogenic conversion and superinfection exclusion (67). Given the ubiquity and abundance of phages and bacteria in nature, deciphering the underlying phage replication regime of a phage-bacterial community is critical in understanding the functional ecology of phages within the grander perspective of an ecosystem. To-date, there are two primary ecological theories that were founded on the virulent and temperate phage lifestyles, respectively: Kill-the-Winner and Piggyback-the-Winner. Each describes their respective phage-bacteria population ecology and its implications on the overall viral and microbial community.

4.1 Kill-the-Winner

The theories describing the virulent and temperate regimes of phages on microbial ecology were largely derived from studies in marine ecosystems. It is well-accepted that phages in marine environments outnumber their prokaryotic counterparts by a whole order of magnitude, although this could even be as high as two orders (68). The outnumbering of bacteria by phages is partly explained by the Kill-the-Winner (KtW) theory, which was originally conceptualised as an ecological mechanism underlying pelagic phage and bacterial diversity (69, 70). The Kill-the-Winner theory is defined

when a phage population suppresses the fittest (and most abundant) bacterial population within a phage-bacteria community through classical prey-predator dynamics (Fig.2A). By suppressing high-fitness populations, phages level the competitive field, allowing for other bacterial subpopulations to dominate the niche in succession. The successive domination by bacterial subpopulations, reciprocated by virulent phage suppression, is often described through rapid fluctuations of individual phage-host pair population abundances (71, 72) or genotypes at finer taxonomic levels within the community (42). This, on average, or at coarser taxonomic levels, promotes the co-existence of diverse subpopulations within a given niche (42). Since KtW is founded upon density-dependent predation by phages, the overall community is expected to sustain a high ratio of phages-to-bacteria; hence, explaining the 10:1 phage-to-bacteria ratio (PBR) often cited in global marine estimates (69). However, the primary caveat of KtW is that it describes phage-bacteria population ecology solely within the lytic context of virulent phages whilst discounting lysogenic features of temperate phages.

4.2 Piggyback-the-Winner

Theoretical limitations of KtW arise when considering that temperate phages are ubiquitous, and in certain environments such as the gut, comprise a significant viral fraction (discussed in Section 5). Unlike virulent phages where infection typically leads to only one outcome i.e. bacterial cell death, infection by a temperate phage may lead to either lytic cell death or lysogeny. The choice between lysis and lysogeny is inherently stochastic – albeit studies are increasingly demonstrating that this choice is largely dependent on the multiplicity-of-infection (MOI; the number of phage particles infecting a single bacterial cell) where higher MOIs lends higher lysogeny rates (73–

75). In this case, a phage-bacteria community exhibiting high lysogenic activity will result in a community with decreasing phage density (from prophage integration within bacterial host genome) and increasing bacterial density (from non-lethal lysogenic infection). Collectively, this implies that temperate phage-bacteria communities with high lysogeny rates will have PBRs that contract from the global 10:1 estimate.

A seminal study attempted to assess the extent of lysogeny by quantifying phages and bacteria in aquatic samples whilst accounting for temperate phage signatures (76). Rather than obtaining a steady linear 10:1 PBR trend expected under a KtW lytic regime, the authors observed that phage densities increased sublinearly with increasing bacterial densities i.e. contracting from the expected 10:1 trend. Moreover, metagenomic sequencing reads associated with temperate phage features such as integrases, excisionases and prophages were positively correlated with increasing bacterial density. Overall, this suggests that pelagic phage dynamics – within the sample space of this study – were predominantly lysogenic (76). Evidently, findings here do not fit within the KtW framework which led the authors to propose the Piggyback-the-Winner (PtW) hypothesis as an extension from the canonical KtW theory (Fig.2B). Simply, the “piggyback”-ing arose from the temperate phages choosing to lysogenise and integrate with the most abundant bacterial host in the community. Since its conceptualisation, PtW has been implicated in a follow-up study by Coutinho et al. (77), by leveraging metagenomic sequences from 78 published marine viromes and host abundance data to infer negative correlation between virus-to-host ratio; and another study by Paterson et al. (78), revealing virus-to-host ratios much lower than 10:1 in a hydrocarbon-polluted aquifier system.

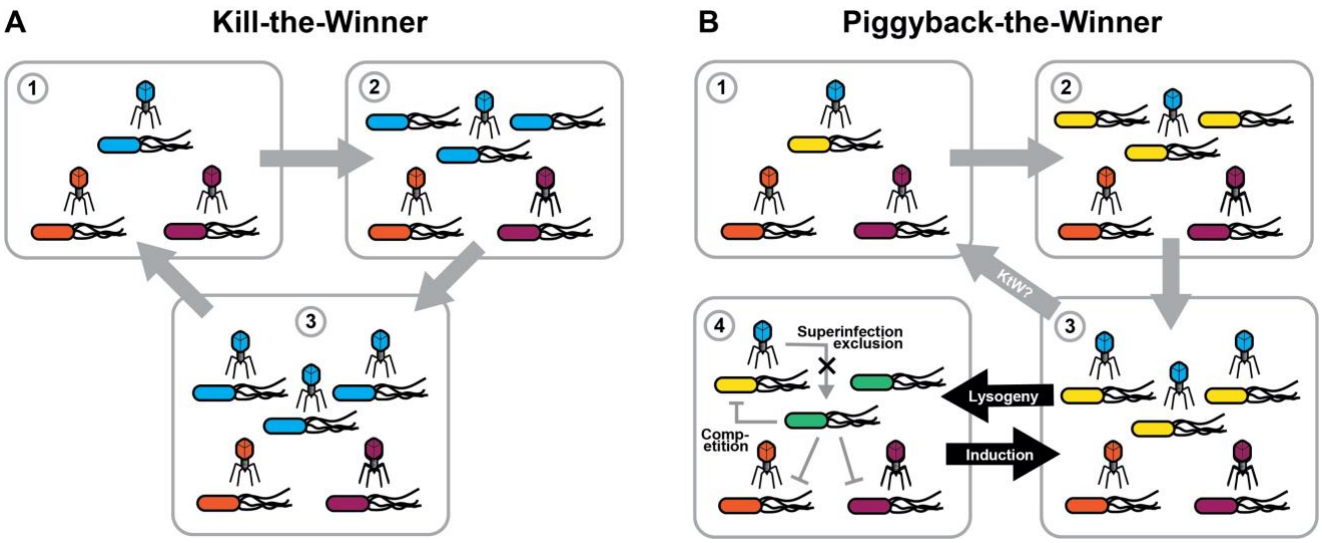

Fig.2 Simplified schematic of Kill-the-Winner and Piggyback-the-Winner theories. A) KtW begins when a bacterial species is selectively favoured in the environment for population growth to lend population dominance (blue bacteria). The expansion of the bacterial species also favours the lytic expansion of its phage counterpart (blue phage). This results in increasing phage predation pressure thereby suppressing the dominant bacterial population. The expansion-suppression cycle repeats depending on the bacterial species (and thus, phages) that are next favoured for expansion in the niche. B) PtW also begins with the selected growth of a bacterial species in a niche (yellow bacteria), leading to the expansion to its cognate phage population (blue phage). If a lytic regime is favoured, the phage-bacteria population recapitulates the KtW cycle. However, if lysogeny is favoured, PtW results in phage integration with the bacterial chromosome to lend the emergence of lysogens (green bacteria). Prophages may confer fitness advantages to lysogens through superinfection exclusion and lysogenic conversion, enabling lysogens to compete with other bacterial species within the niche. Under conditions where lysogeny is no longer favoured, the lysogens may undergo induction to produce viral progeny.

4.3 KtW-PtW continuity and the virus-to-microbe ratio debate

Both KtW and PtW theories offer parsimonious descriptions on phage-bacteria population ecology depending on the lytic or lysogenic contexts of the community.

However, phage communities in natural environments are neither purely virulent nor temperate and realistically, would comprise a mixture of both. This creates a discontinuity between the lytic-dominant KtW and the lysogenic-dominant PtW theories. To that, the original authors whom proposed the PtW theory, conjectured that both theories exist along a spectrum that is dependent on virus-to-microbe ratio (VMR) and the balance between energetic costs and fitness benefits in maintaining a prophage (76).

VMR – which I also define analogously with PBR on the basis that phages and bacteria are the predominant entities in natural viral and microbial communities, respectively – is a widely used metric to infer phage-bacteria encounter and microbial lysis rates within a niche. These rates are subsequently leveraged to predict the underlying phage-bacteria community dynamics and its knockdown effects on the overall ecosystem such as the marine biogeochemical cycle (3, 68, 76, 79). However, the concern arises when VMR (or PBR) becomes the sole or overemphasised metric adopted to describe phage-bacteria community dynamics. This undermines other equally essential metrics such as phage-bacterial infection networks, community diversity and even, fundamental phage infection biology (e.g. adsorption rates, infection latency, and burst sizes). This was highlighted in a substantial reanalysis of 5,508 oceanic VMR datasets demonstrating that oceanic VMR varies significantly from the commonly cited 10:1 ratio (from 3.9:1 to 74:1) and that viral density does not scale linearly with microbial density along the 10:1 VMR; rendering microbial abundance “a poor predictor of viral abundance” (68).

Adding to this concern, metagenomic datasets are increasingly used to correlate the abundance of sequencing reads of interest (e.g. temperate phage genes) with viral and microbial abundances (derived either from direct counts or read abundances) to infer viral regimes. This has sparked contentious debates on the validity of PtW as an ecological mechanism behind the lytic-to-lysogenic switch that lend sublinear virus-to-microbe relationships. In one exchange targeting the original PtW publication [reference (76)], Weitz et al. underscored the need for appropriate correlational tests and statistical thresholds to minimise type I errors (i.e. false positive correlations) when associating read abundances of temperate phage sequences with microbial counts to estimate the extent of lysogeny in relation to microbial density (80). This was counter-argued in a reply from the original authors that the statistics employed by Weitz et al. in (80) had not accounted for data non-normality and had falsely advocated for normality-sensitive statistical analyses which were excessively stringent, leading to type II errors instead (false negatives) (81). Weitz et al. also criticised the study for drawing conclusions based on sequences derived from extracellular viral particles (which was deduced from the viral purification methods adopted by the PtW study). They argued that the prevalence of temperate phage sequences based on extracellular viral particles instead, implies that temperate phages are adopting a lytic regime over a lysogenic one (80); no specific address was made in the original author's reply to this critique (81). A similar communication was also directed to Coutinho et al. (77) arguing the need for mathematical rigour to robustly define a sublinear VMR relationship from metagenomic read abundance datasets (refer to Alrasheed et al. in (82) on comparing viral abundance directly with microbial abundance i.e. "*y against x*", and comparing VMR with microbial abundance i.e. "*y/x against x*"). Alrasheed et al. argued that the "*y/x against x*" analysis adopted in

Coutinho et al. without supplementation and statistical significance from "*y against x*" plots may lead to spurious sublinear conclusions drawn from self-correlation with the *x* parameter (i.e. "*y/x against x*" tested against a "*1/x against x*" slope).

In summary, the heavy reliance on VMR remains as a sticking point in verifying PtW as an ecological theory alongside the more rigorously tested KtW theory. To my knowledge, there is no clear empirical evidence to support PtW apart from conclusions based on VMR estimate and correlations. Indeed, what constitute as "evidences" for PtW apart from VMRs have only been recently proposed in a minireview (83) which will be dissected in a later section. However, it is important to heed the advices from Wigington et al. (68) and Weitz et al. (80) on the need for an integrated approach comprising of comprehensive metagenomics, mechanistic models, empirical measurements and statistical rigour, in order to establish robust foundations for PtW in describing lytic-to-lysogenic switching, and vice versa.

5. Phage regimes in the gut

Both KtW and PtW theories have not been directly tested in the gut, largely due to the inherent noisiness of ecological data and the complex integrated approach required to disentangle lytic and lysogenic extents in a phage-bacteria community. Nonetheless, numerous studies have attempted to broadly describe the phage lifestyles in the gut chiefly through metagenomic sequencing of human gut-derived communities. Based on these studies, certain educated inferences on KtW lytic and/or PtW lysogenic regimes in the gut can be gathered.

5.1 Is the healthy gut virome lytic or temperate? It depends on time

Detection of microbes and virus-like particles in meconium (neonate's first stool) revealed that the neonatal gut is largely devoid of microorganisms (84). However, within 24 hours to 1 week postpartum, the neonatal gut is rapidly colonised by microbes mostly originating from the mother's microbiome from multiple sites (85, 86). The initial or "pioneering" virome is highly diverse and consists of temperate phages of the *Caudovirales* order alongside a much smaller proportion of principally virulent *Microviridae* family phages (86, 87). During the first month, the neonatal gut virome undergoes rapid fluctuations where an early study demonstrated a 56% turnover of the gut virome between the first and second week postpartum (88). Crucially, a more recent study discovered that virulent phages commonly associated with *Microviridae* and crAssphages, are relatively rare in the one-month old neonate gut despite the high viral load at ~10^9 viral particles per gram of stool (which would otherwise imply a lytic-dominant regime) (84). Instead, the authors found that the majority of these viral particles were temperate phages that were induced from the establishing microbiome, indicating a lysogenic-to-lytic switch in the early neonatal virome. However, the triggers underlying this mass induction remains elusive to-date (84).

Following from the first month to two-years of age, the infant gut virome contracts with the increasing dominance of *Microviridae* phages (87, 89), demonstrating the maturation of the infant gut virome to match the maternal virome (86). The contracting phage diversity was correlated with increasing gut microbiome diversity, suggesting that the initial high phage diversity could not be maintained by low gut bacterial diversity (perhaps as a result of extensive prophage induction events in the early microbiome? (84)). The contracting phage diversity reduces overall phage

suppression pressure to enable microbial diversification which subsequently favoured the lytic propagation of *Microviridae* phages (87). Collectively, evidence hints that the infant gut virome is predominantly lytic from the expansion of *Microviridae* phages. It is also worth noting that crAssphages are still uncommon within this infantile period of the gut virome (87).

Direct studies of children's gut virome between 3 to 18 years of age are surprisingly scarce or at least, nested as healthy controls in the investigations of diseased children cohorts such as Fernandes et al. (90) and Coffey et al. (91). In these cohorts, the healthy gut virome maintains a significant lytic-associated *Microviridae* phage population, particularly *Gokushovirinae* (a subfamily of *Microviridae*) (91). However, there is a re-emergence of *Caudovirales* phages in both reported healthy children cohorts, although neither the proportion of temperate *Caudovirales* phages nor the extent of lysogeny were reported. The re-emergence of *Caudovirales* phages was later recapitulated when the same gut virome dataset from Fernandes et al. (90) was subjected to an age-dependent analysis using an extensively curated phage metagenomic database (92). Although the age-dependent analysis relied solely on Fernandes et al.'s dataset to represent the gut virome of developing children, the study reported the largest gut virome shift between this period and adulthood (92). Despite this, the exact mechanism governing this significant gut virome shift remains unknown, which precludes formulating inferences on phage regimes in children gut viromes.

The transition to the adult gut virome follows an increase in both virulent *Microviridae* phage and crAssphages alongside *Caudovirales* phages, particularly *Siphoviridae* and *Podoviridae* (92). This transition eventually results in a virulent *Microviridae* and

crAssphage majority that forms the persistent virome fraction within an adult individual gut virome (93). This persistent virome is in-line with an earlier study demonstrating 80% of gut viral contigs persisting within an individual for up to 2.5 years (35). Furthermore, the persistent virome is highly individualistic in terms of viral abundance and composition, with only two viral contigs (of the 833 contigs) shared across five or more individuals in a ten-person study cohort (93). In other words, the adult gut virome is predominantly lytic, compositionally stable and highly individualistic. The presence of a stable and persistent virome may initially imply the absence of KtW-driven fluctuations. However, closer inspection on the viral contigs of the virulent *Microviridae* and crAssphages majority at single nucleotide polymorphism (SNP) level revealed high substitution rates and rapid replacements of phage variants within a one-year period (93). Furthermore, each phage species was represented by several but closely-related genotypes at any given timepoint; to which the authors termed as viral "microheterogeneity" (93). Collectively, while gut viral composition appears stable at coarser levels, analysis at nucleotide level supports an ongoing succession and diversification of individual phage genotypes (42, 93). This hints at the KtW mechanisms that underlie the virulent phage majority within the adult gut virome.

Despite the numerically dominating lytic phages, peak diversity is achieved in the adult gut virome. The remaining non-persistent viral fraction consisted of a diverse group of *Caudovirales* phage families especially *Siphoviridae* phages; most of which were predicted as temperate phages (92, 93). Interestingly, viral richness (i.e. the number of viral species irrespective of abundance) strongly correlated with the abundance of temperate *Siphoviridae* phages, indicating temperate phages as key contributors to gut virome diversity despite their numerical minority (92). This was further exemplified

in an individual outlier within the previously discussed ten-persons cohort study, whose gut virome was predominated by temperate *Caudovirales* phages instead of virulent *Microviridae* and crAssphages; demonstrating high viral diversity and low viral loads in the gut (93). This suggests that the gut virome of this particular adult individual was exhibiting PtW-like signatures with lysogeny and spontaneous induction from multiple lysogen species, contributing to low viral loads and high viral diversity, respectively. Intriguingly, robust temperate phage presence and lysogeny in the gut have been also reported in earlier studies, which contrasts with more recent studies [i.e. (92, 93)] that support a chiefly virulent and lytic gut virome, as previously discussed. A 2010 study of adult monozygotic twins with their mothers reported that the majority of phages retrieved over the one-year period were temperate phages, although the extent of lysogenic activity was not probed (94). Another empirical study leveraging murine commensal gut models also revealed an abundant, diverse and widespread prophage distribution across the murine gut with extensive lysogenic activity (95). However, it is worth noting that the different outcomes between these older studies and more recent investigations may be attributed to the approaches adopted in classifying taxonomy of viral contigs. Older studies (94, 95) were heavily reliant on taxonomic information from limited public reference databases, while more recent studies (92, 93, 96) adopted curated databases from large metagenomic datasets with arguably more comprehensive viral taxonomy coverage. Hence, contemporary studies are also able to identify and classify previously unknown and disregarded high-abundance virulent reads such as the virulent crAssphages. In summary, more recent evidences depict a generally stable and virulent adult gut virome accompanied by a temperate phage minority which drives gut virome diversity.

This implies – and realistically so – that the mature gut virome operates on a mixed lytic and lysogenic propensity, and that KtW and PtW are likely not mutually exclusive.

5.2 What exactly should we be looking for? On KtW and PtW in the gut moving forward

In an attempt to reconcile the possible co-existence of KtW and PtW in the human gut, an ecological model was proposed where the mucosal spatial layout and bacterial growth rates along the mucin gradient dictate the transition of the phage-bacteria communities between KtW lytic and PtW lysogenic regimes (97). The model describes that high nutrient abundance in the outer mucus layer lends high bacterial growth rates which in turn, promotes lysogeny and the low PBRs often described by PtW. The prophages at the outer mucus layer are maintained by conferring competitive advantages to commensals through lysogenic conversion and superinfection immunity (Fig.2B). This also renders the outer mucus layer a highly competitive microbial environment that is robust against invasion from non-commensal microbes. However, previous empirical studies have shown that phages are enriched in mucosal environments, which could result in a PBR as high as 39:1 (55), contrasting with PtW's low PBR predictions. To explain this, the ecological model transitions deeper into the intermediary mucosal layer where mucin concentration increases and hypoxia becomes a limiting factor to bacterial growth. This environmental change triggers prophage induction and a significant release of phage particles within the intermediary mucus layer. Here, phages are thought to subdiffuse and propagate lytically on incoming bacteria from the outer mucus layer (56). Altogether, this lysogenic-to-lytic switch contributes to the high PBR reported in the mucus layer while also providing a mechanistic framework for the co-existence of PtW and KtW in the gut (97). However,

this co-existence model was published on the backdrop of a newly conceptualised PtW theory (76). As a result, there were mechanistic gaps in the model that warranted further elaboration on the specific determinants underlying the lysogenic-to-lytic switch and vice versa within the mucus layer.

The mechanistic gaps were later addressed in a follow-up minireview detailing three key determinants that future studies should consider when examining for PtW and KtW in the gut; all of which may have significant roles on affecting lysogeny rates in the mucus layer (83). The first determinant relates to bacterial growth; more specifically, cellular metabolism and energetics. Here, bacterial metabolism is described as efficient or inefficient depending on the cumulative level of ATP and oxidative co-enzymes NADPH. Efficient metabolism is characterised by cell growth in optimal nutrient environment resulting in high ATP yields. This supports the cleavage of phage repressors by ATP-dependent enzymes and hence, trigger prophage induction and favouring lytic propagation in metabolically efficient cells. Meanwhile, inefficient metabolism occurs when excessive nutrient conditions trigger ATP “spilling” and favours metabolic pathways with lower ATP yields and high NADPH output such as the Entner-Duodoroff and the Pentose-phosphate pathways (98, 99). The reduced intracellular ATP level facilitates the accumulation of lytic repressors, favouring phage lysogeny (83). Within the context of the gut, the mucus layer is incredibly nutrient abundant from by-products of digestion and particularly, eukaryotic-secreted mucin glycans; the latter forming a key source of polysaccharides for some of the most abundant bacterial members of the gut microbiome (100, 101). Unfortunately, no studies to-date have examined the nutrient gradient along the mucus depth thereby, precluding further investigations on microbial energetics of bacterial populations along

this gradient. However, there is evidence that bacteria in the gut recovered from faecal samples (as a proxy of the outer mucus layer) grow significantly slower compared to laboratory conditions which may imply inefficient bacterial metabolism (102). Assuming that nutrient diffusion is limited drastically by mucus layer depth (from increasing mucin gradient), then inefficient metabolism would prevail in the outer mucus layer to favour a lysogenic phage regime. As nutrients eventually reach optimal abundance at the intermediary mucus layer, efficient bacterial metabolism is restored which triggers a lysogenic-to-lytic switch in phage regimes at intermediate mucus depth.

The second determinant is the frequency of phage co-infections i.e. when two or more phages infect a single bacterial cell (83). Empirical evidence of phage infections at single virus resolution and *in silico* models with varied multiplicity-of-infections (MOI) have demonstrated that higher MOIs led to increased lysogenic propensity (73–75). However, MOI is often defined as the ratio of phages-to-bacteria at the initial experimental state and does not provide further context on co-infection frequencies beyond the initial timepoint. To that, a biophysical model was recently developed to track the frequency of co-infections as a function of MOI alongside two other fundamental phage parameters: phage adsorption rate and length of the lytic-lysogenic decision period (referred to as commitment time) (34). Using parameter values derived from a meta-analysis of gut phage-bacteria communities, the model was able to accurately recapitulate lysogeny rates in the gut that match empirical data from a previously described murine gut commensal model (34, 95). Of the three parameters, longer commitment times had the most significant contribution in increasing co-infections and thus, lysogeny. This is because bacteria with longer

commitment times are more likely to encounter multiple phages to increase lysogeny likelihoods before committing to either lytic or lysogenic lifecycles (34). Future validation within physiological gut models – particularly optically clear and highly amenable microfluidic organ-on-a-chips (103, 104) – could employ live imaging, tracking and quantification of co-infection events by inoculating gut models with temperate phages and bacterial hosts that are tagged with fluorescent markers and lysogeny reporters (75).

Since phage infection is highly specific to their bacterial host species, community diversity is also a key determinant to impacting lysogeny rates (83). Phage-bacteria communities with low diversity is typically dominated by a few phage-host species pairs; referred to as high rank-abundance phages and bacteria (3). This facilitates productive phage-bacteria encounters that drives co-infections to promote lysogeny within the community (34). While not directly demonstrated, the inverse is presumed to hold true where co-infections decrease when phage-bacteria communities are highly diverse. As discussed, the typical adult gut virome is dominated by lytic phage with *Microviridae* and crAssphages likely occupying the high rank-abundance hierarchy in the gut (40, 41, 93). This leaves the remaining *Caudovirales* order phages with predominantly temperate *Siphoviridae* phages (recall from (92)) to occupy lower rank-abundances. By extrapolation, community diversity is thus unlikely to contribute as a main driver to lysogeny in the gut. Perhaps, this is compensated by the high overall microbial abundance in the gut (~10^9 per ml (10)) where even a small percentage induction from existing lysogens could result in significant release of temperate phages. These phages will likely encounter and co-infect another host to contribute to lysogeny within the gut, as predicted by the biophysical model (34).

Future work could adopt inducible prophage mutants (e.g. heat-inducible λ phages) to stimulate controlled waves of induction in parallel with real-time quantification of co-infections to assess the extent of lysogeny in the gut under varying phage-host rank-abundances.

Conclusion and prospectus

The advent of metagenomics has granted researchers with unparallel insights into the wonderous complexity of our gut microbiomes and viromes, particularly in areas of microbial evolution and population ecology. Despite the gargantuan advances on our current understanding of gut phage evolution and ecology, we are only at the cusp of painting an overview on our viral dark matter and its dynamic features. The ecology and evolution of phages in the gut are inextricably intertwined. Hence, precise description on evolutionary and ecological theories that apply to gut phage-bacteria communities, will be the first milestone in establishing a foundational understanding of our gut virome and microbiome dynamics. Following this, our second milestone should seek to understand how these evolutionary and ecological descriptions function in unison and the outcomes of this eco-evolutionary *tête-à-tête* within the human gut niche. However, achieving these scientific milestones in the current epoch warrants further fundamental exploration on the three-way symbiosis of phages, bacteria and the mammalian gut. To this end, the following chapters in my thesis aims to:

1. Establish a microfluidic gut-on-a-chip device to recapitulate a dynamic gut mucosal environment.
2. Experimentally evolve phages in the gut-on-a-chip to assess the capacity for phages to adapt to the mucosal environment.
3. Elucidate the population dynamics and ecology of a model virulent and temperate phage-bacteria community in the gut-on-a-chip mucosal environment.

Evidently, establishing the gut-on-a-chip device (i.e. Aim 1) was highly contingent in providing an experimental platform to empirically address Aims 2 and 3. The device

serves as a model gut system that is experimentally amenable yet faithfully recapitulating key micro- and macrolevel features of the mammalian gut; in essence, a middle ground between traditional *in vitro* cell cultures and *in vivo* models of the gut. Thus, the gut-on-a-chip – or more generally, the organ-on-a-chip – offers an attractive route for further studies of gut phage dynamics and evolution under highly controlled and refined conditions (104–107). By recapitulating a polarised gut mucosal epithelium with active mucosal turnover dynamics, phage and microbial populations tested are subjected to global selective pressures to persist within the mucosal environment.

To this, my first thesis chapter presented an extended literature review on the organ-on-a-chip technology to underscore its utility and potential in advancing the field of phage and microbial sciences. This was then followed by the second chapter which was written in a methods format, detailing the fabrication of the gut-on-a-chip that would later form the experimental basis for the following chapters. The third chapter addressed Aim 2 which builds upon the BAM model (55) to assess the capacity for phages to evolve to the mucosal environment by experimentally evolving phages within the gut-on-a-chip. I hypothesised that phages could adapt to persist within the mucosal environment by evolving their mucus-binding capsid domains. Determining this will have significant ramifications on our evolutionary perspective of phages *in vivo,* from being regarded as purely bacteriotropic entities, to viruses that could potentially engage in evolution with the mammalian “host” environment. Following this, the fourth chapter addressed Aim 3 by tracking the population densities of a model virulent and temperate phage community in high temporal resolution. I hypothesised that the model phage community will exhibit complex population dynamics that are dictated by the extent of phage-mediated lysis and lysogeny. The temporal data

obtained here will provide some of the first empirical evidence on the hitherto untested *in silico* findings and predictions of phage population dynamics *in vivo*. This is also particularly resounding given that phages in the gut comprised of both virulent and temperate phages, to which the ecological mechanisms governing their interactions and co-existence remain elusive. Finally, I closed the thesis by concluding my findings within the broader context of phages *in vivo* and how we might be able to leverage their fundamental evolutionary and ecological nature to redefine what it means to co-exist with one of the most abundant viruses globally.

References

1. M. K. Mirzaei, C. F. Maurice, Ménage à trois in the human gut: Interactions between host, bacteria and phages. *Nat. Rev. Microbiol.* **15**, 397–408 (2017).
2. A. M. Nanda, K. Thormann, J. Frunzke, Impact of spontaneous prophage induction on the fitness of bacterial populations and host-microbe interactions. *J. Bacteriol.* **197**, 410–419 (2015).
3. M. Breitbart, C. Bonnain, K. Malki, N. A. Sawaya, Phage puppet masters of the marine microbial realm. *Nat. Microbiol. 2018 37* **3**, 754–766 (2018).
4. B. J. Finlay, S. C. Maberly, J. I. Cooper, Microbial Diversity and Ecosystem Function. *Oikos* **80**, 209 (1997).
5. M. Delgado-Baquerizo, *et al.*, Microbial diversity drives multifunctionality in terrestrial ecosystems. *Nat. Commun. 2015 71* **7**, 1–8 (2016).
6. S. Louca, L. W. Parfrey, M. Doebeli, Decoupling function and taxonomy in the global ocean microbiome. *Science (80-.).* **353**, 1272–1277 (2016).
7. E. Holmes, J. V. Li, T. Athanasiou, H. Ashrafian, J. K. Nicholson, Understanding the role of gut microbiome–host metabolic signal disruption in health and disease. *Trends Microbiol.* **19**, 349–359 (2011).
8. S. Ghaisas, J. Maher, A. Kanthasamy, Gut microbiome in health and disease: Linking the microbiome–gut–brain axis and environmental factors in the pathogenesis of systemic and neurodegenerative diseases. *Pharmacol. Ther.* **158**, 52–62 (2016).
9. M. Breitbart, *et al.*, Metagenomic analyses of an uncultured viral community from human feces. *J. Bacteriol.* **185**, 6220–6223 (2003).
10. M. S. Kim, E. J. Park, S. W. Roh, J. W. Bae, Diversity and abundance of single-stranded DNA viruses in human feces. *Appl. Environ. Microbiol.* **77**,

8062–8070 (2011).

11. A. S. Waller, *et al.*, Classification and quantification of bacteriophage taxa in human gut metagenomes. *ISME J. 2014 87* **8**, 1391–1402 (2014).
12. A. Wahida, F. Tang, J. J. Barr, Rethinking phage-bacteria-eukaryotic relationships and their influence on human health. *Cell Host Microbe* **29**, 681–688 (2021).
13. A. N. Shkoporov, C. Hill, Bacteriophages of the Human Gut: The “Known Unknown” of the Microbiome. *Cell Host Microbe* **25**, 195–209 (2019).
14. J. M. Kirsch, *et al.*, Bacteriophage-Bacteria Interactions in the Gut: From Invertebrates to Mammals. *Annu. Rev. Virol.* **8**, 1–19 (2021).
15. H. G. Hampton, B. N. J. Watson, P. C. Fineran, The arms race between bacteria and their phage foes. *Nat. 2020 5777790* **577**, 327–336 (2020).
16. J. E. Samson, A. H. Magadán, M. Sabri, S. Moineau, Revenge of the phages: defeating bacterial defences. *Nat. Rev. Microbiol. 2013 1110* **11**, 675–687 (2013).
17. A. Betts, O. Kaltz, M. E. Hochberg, Contrasted coevolutionary dynamics between a bacterial pathogen and its bacteriophages. *Proc. Natl. Acad. Sci. U. S. A.* **111**, 11109–11114 (2014).
18. M. E. J. Woolhouse, J. P. Webster, E. Domingo, B. Charlesworth, B. R. Levin, Biological and biomedical implications of the co-evolution of pathogens and their hosts. *Nat. Genet. 2002 324* **32**, 569–577 (2002).
19. E. Harrison, A.-L. Laine, M. Hietala, M. A. Brockhurst, Rapidly fluctuating environments constrain coevolutionary arms races by impeding selective sweeps. *Proc. R. Soc. B Biol. Sci.* **280** (2013).
20. L. L. Pascua, *et al.*, Higher resources decrease fluctuating selection during

host–parasite coevolution. *Ecol. Lett.* **17**, 1380–1388 (2014).

21. M. A. Brockhurst, A. D. Morgan, P. B. Rainey, A. Buckling, Population mixing accelerates coevolution. *Ecol. Lett.* **6**, 975–979 (2003).
22. B. Ashby, S. Gupta, A. Buckling, Spatial Structure Mitigates Fitness Costs in Host-Parasite Coevolution. *https://doi.org/10.1086/674826* **183** (2015).
23. A. R. Hall, P. D. Scanlan, A. D. Morgan, A. Buckling, Host–parasite coevolutionary arms races give way to fluctuating selection. *Ecol. Lett.* **14**, 635–642 (2011).
24. B. Koskella, Bacteria-phage interactions across time and space: Merging local adaptation and time-shift experiments to understand phage evolution. *Am. Nat.* **184** (2014).
25. C. O. Flores, J. R. Meyer, S. Valverde, L. Farr, J. S. Weitz, Statistical structure of host–phage interactions. *Proc. Natl. Acad. Sci.* **108**, E288–E297 (2011).
26. K. Holmfeldt, M. Middelboe, O. Nybroe, L. Riemann, Large variabilities in host strain susceptibility and phage host range govern interactions between lytic marine phages and their Flavobacterium hosts. *Appl. Environ. Microbiol.* **73**, 6730–6739 (2007).
27. J. B. H. Martiny, L. Riemann, M. F. Marston, M. Middelboe, Antagonistic Coevolution of Marine Planktonic Viruses and Their Hosts (2013) https:/doi.org/10.1146/annurev-marine-010213-135108 (September 2, 2021).
28. M. Vos, P. J. Birkett, E. Birch, R. I. Griffiths, A. Buckling, Local adaptation of bacteriophages to their bacterial hosts in soil. *Science (80-.).* **325**, 833 (2009).
29. P. Gómez, A. Buckling, Bacteria-phage antagonistic coevolution in soil. *Science (80-.).* **332**, 106–109 (2011).
30. K. B, T. JN, P. GM, B. A, Local biotic environment shapes the spatial scale of

bacteriophage adaptation to bacteria. *Am. Nat.* **177**, 440–451 (2011).

31. B. Koskella, J. N. Thompson, G. M. Preston, A. Buckling, Local Biotic Environment Shapes the Spatial Scale of Bacteriophage Adaptation to Bacteria. *https://doi.org/10.1086/658991* **177**, 440–451 (2015).
32. M. F. Marston, *et al.*, Rapid diversification of coevolving marine Synechococcus and a virus. *Proc. Natl. Acad. Sci.* **109**, 4544–4549 (2012).
33. M. F. Marston, J. B. H. Martiny, Genomic diversification of marine cyanophages into stable ecotypes. *Environ. Microbiol.* **18**, 4240–4253 (2016).
34. A. Luque, C. B. Silveira, Quantification of Lysogeny Caused by Phage Coinfections in Microbial Communities from Biophysical Principles. *mSystems* **5** (2020).
35. S. Minot, *et al.*, Rapid evolution of the human gut virome. *Proc. Natl. Acad. Sci. U. S. A.* **110**, 12450–12455 (2013).
36. A. Stern, E. Mick, I. Tirosh, O. Sagy, R. Sorek, CRISPR targeting reveals a reservoir of common phages associated with the human gut microbiome. *Genome Res.* **22**, 1985 (2012).
37. A. Zhu, S. Sunagawa, D. R. Mende, P. Bork, Inter-individual differences in the gene content of human gut bacterial species. *Genome Biol. 2015 161* **16**, 1–13 (2015).
38. N. T. Porter, *et al.*, Phase-variable capsular polysaccharides and lipoproteins modify bacteriophage susceptibility in Bacteroides thetaiotaomicron. *Nat. Microbiol. 2020 59* **5**, 1170–1181 (2020).
39. F. Gordillo Altamirano, *et al.*, Bacteriophage-resistant Acinetobacter baumannii are resensitized to antimicrobials. *Nat. Microbiol. 2021 62* **6**, 157–161 (2021).
40. B. E. Dutilh, *et al.*, A highly abundant bacteriophage discovered in the

unknown sequences of human faecal metagenomes. *Nat. Commun.* **5**, 1–11 (2014).

41. A. N. Shkoporov, *et al.*, ΦCrAss001 represents the most abundant bacteriophage family in the human gut and infects Bacteroides intestinalis. *Nat. Commun. 2018 91* **9**, 1–8 (2018).
42. B. Rodriguez-Brito, *et al.*, Viral and microbial community dynamics in four aquatic environments. *ISME J.* **4**, 739–751 (2010).
43. W. M, *et al.*, In vivo replication of T4 and T7 bacteriophages in germ-free mice colonized with Escherichia coli. *Virology* **393**, 16–23 (2009).
44. M. Lourenço, *et al.*, The Spatial Heterogeneity of the Gut Limits Predation and Fosters Coexistence of Bacteria and Bacteriophages. *Cell Host Microbe* **28**, 390-401.e5 (2020).
45. A. Reyes, M. Wu, N. P. McNulty, F. L. Rohwer, J. I. Gordon, Gnotobiotic mouse model of phage-bacterial host dynamics in the human gut. *Proc. Natl. Acad. Sci. U. S. A.* **110**, 20236–20241 (2013).
46. B. B. Hsu, *et al.*, Dynamic Modulation of the Gut Microbiota and Metabolome by Bacteriophages in a Mouse Model. *Cell Host Microbe* **25**, 803-814.e5 (2019).
47. L. De Sordi, V. Khanna, L. Debarbieux, The Gut Microbiota Facilitates Drifts in the Genetic Diversity and Infectivity of Bacterial Viruses. *Cell Host Microbe* **22**, 801-808.e3 (2017).
48. P. T, *et al.*, The mucus and mucins of the goblet cells and enterocytes provide the first defense line of the gastrointestinal tract and interact with the immune system. *Immunol. Rev.* **260**, 8–20 (2014).
49. C. Tropini, K. A. Earle, K. C. Huang, J. L. Sonnenburg, The Gut Microbiome:

Connecting Spatial Organization to Function. *Cell Host Microbe* **21**, 433–442 (2017).

50. H. Schneider, T. Pelaseyed, F. Svensson, M. E. V. Johansson, Study of mucin turnover in the small intestine by in vivo labeling. *Sci. Reports 2018 81* **8**, 1–11 (2018).

51. L. R. Muniz, C. Knosp, G. Yeretssian, Intestinal antimicrobial peptides during homeostasis, infection, and disease. *Front. Immunol.* **3** (2012).

52. G. P. Donaldson, S. M. Lee, S. K. Mazmanian, Gut biogeography of the bacterial microbiota. *Nat. Rev. Microbiol. 2015 141* **14**, 20–32 (2015).

53. F. Hildebrand, *et al.*, Dispersal strategies shape persistence and evolution of human gut bacteria. *Cell Host Microbe* **29**, 1167-1176.e9 (2021).

54. J. J. Barr, Missing a Phage: Unraveling Tripartite Symbioses within the Human Gut. *mSystems* **4** (2019).

55. J. J. Barr, *et al.*, Bacteriophage adhering to mucus provide a non-host-derived immunity. *Proc. Natl. Acad. Sci.* **110**, 10771–10776 (2013).

56. J. J. Barr, *et al.*, Subdiffusive motion of bacteriophage in mucosal surfaces increases the frequency of bacterial encounters. *Proc. Natl. Acad. Sci. U. S. A.* **112**, 13675–13680 (2015).

57. G. M. F. Almeida, E. Laanto, R. Ashrafi, L. R. Sundberg, Bacteriophage adherence to mucus mediates preventive protection against pathogenic bacteria. *MBio* **10**, 1–12 (2019).

58. J. S. Fraser, Z. Yu, K. L. Maxwell, A. R. Davidson, Ig-Like Domains on Bacteriophages: A Tale of Promiscuity and Deceit. *J. Mol. Biol.* **359**, 496–507 (2006).

59. R. Sausset, M. A. Petit, V. Gaboriau-Routhiau, M. De Paepe, New insights into

intestinal phages. *Mucosal Immunol.* **13**, 205–215 (2020).

60. D. M. Halaby, J. P. E. Mornon, The immunoglobulin superfamily: An insight on its tissular, species, and functional diversity. *J. Mol. Evol. 1998 464* **46**, 389–400 (1998).

61. S. I. Green, *et al.*, Targeting of Mammalian Glycans Enhances Phage Predation in the Gastrointestinal Tract. *MBio* **12** (2021).

62. S. Minot, S. Grunberg, G. D. Wu, J. D. Lewis, F. D. Bushman, Hypervariable loci in the human gut virome. **109** (2012).

63. S. A. McMahon, *et al.*, The C-type lectin fold as an evolutionary solution for massive sequence variation. *Nat. Struct. Mol. Biol.* **12**, 886–892 (2005).

64. P. A. de Jonge, F. A. B. von Meijenfeldt, L. E. van Rooijen, S. J. J. Brouns, B. E. Dutilh, Evolution of BACON Domain Tandem Repeats in crAssphage and Novel Gut Bacteriophage Lineages. *Viruses* **11**, 1085 (2019).

65. J. Shan, *et al.*, Bacteriophages are more virulent to bacteria with human cells than they are in bacterial culture; Insights from HT-29 cells. *Sci. Rep.* **8**, 5091 (2018).

66. K. L. Joiner, A. Baljon, J. Barr, F. Rohwer, A. Luque, Impact of bacteria motility in the encounter rates with bacteriophage in mucus. *Sci. Reports 2019 91* **9**, 1–12 (2019).

67. N. Obeng, A. A. Pratama, J. D. van Elsas, The Significance of Mutualistic Phages for Bacterial Ecology and Evolution. *Trends Microbiol.* **24**, 440–449 (2016).

68. C. H. Wigington, *et al.*, Re-examination of the relationship between marine virus and microbial cell abundances. *Nat. Microbiol. 2016 13* **1**, 1–9 (2016).

69. T. F. Thingstad, Elements of a theory for the mechanisms controlling

abundance, diversity, and biogeochemical role of lytic bacterial viruses in aquatic systems. *Limnol. Oceanogr.* **45**, 1320–1328 (2000).

70. T. F. Thingstad, S. Vage, J. E. Storesund, R. A. Sandaa, J. Giske, A theoretical analysis of how strain-specific viruses can control microbial species diversity. *Proc. Natl. Acad. Sci. U. S. A.* **111**, 7813–7818 (2014).
71. S. Maslov, K. Sneppen, Population cycles and species diversity in dynamic Kill-the-Winner model of microbial ecosystems. *Sci. Rep.* **7**, 1–8 (2017).
72. C. Xue, N. Goldenfeld, Coevolution Maintains Diversity in the Stochastic “kill the Winner” Model. *Phys. Rev. Lett.* **119** (2017).
73. L. Zeng, *et al.*, Decision Making at a Subcellular Level Determines the Outcome of Bacteriophage Infection. *Cell* **141**, 682–691 (2010).
74. V. Sinha, A. Goyal, S. L. Svenningsen, S. Semsey, S. Krishna, In silico Evolution of Lysis-Lysogeny Strategies Reproduces Observed Lysogeny Propensities in Temperate Bacteriophages. *Front. Microbiol.* **8**, 1386 (2017).
75. J. T. Trinh, T. Székely, Q. Shao, G. Balázsi, L. Zeng, Cell fate decisions emerge as phages cooperate or compete inside their host. *Nat. Commun.* **8**, 14341 (2017).
76. B. Knowles, *et al.*, Lytic to temperate switching of viral communities. *Nature* **531**, 466–470 (2016).
77. F. H. Coutinho, *et al.*, Marine viruses discovered via metagenomics shed light on viral strategies throughout the oceans. *Nat. Commun. 2017 81* **8**, 1–12 (2017).
78. J. S. Paterson, *et al.*, A hydrocarbon-contaminated aquifer reveals a Piggyback-the-Persistent viral strategy. *FEMS Microbiol. Ecol.* **95** (2019).
79. L. He, K. Yin, X. Yuan, Double Maximum Ratios of Viruses to Bacteria in the

Water Column: Implications for Different Regulating Mechanisms. *Front. Microbiol.* **0**, 1593 (2019).

80. J. S. Weitz, S. J. Beckett, J. R. Brum, B. B. Cael, J. Dushoff, Lysis, lysogeny and virus–microbe ratios. *Nat. 2017 5497672* **549**, E1–E3 (2017).

81. B. Knowles, F. Rohwer, Knowles & Rohwer reply. *Nat. 2017 5497672* **549**, E3–E4 (2017).

82. H. Alrasheed, R. Jin, J. S. Weitz, Caution in inferring viral strategies from abundance correlations in marine metagenomes. *Nat. Commun. 2019 101* **10**, 1–4 (2019).

83. C. B. Silveira, A. Luque, F. Rohwer, The landscape of lysogeny across microbial community density, diversity and energetics. *Environ. Microbiol.* **23**, 4098–4111 (2021).

84. G. Liang, *et al.*, The stepwise assembly of the neonatal virome is modulated by breastfeeding. *Nat. 2020 5817809* **581**, 470–474 (2020).

85. P. Ferretti, *et al.*, Mother-to-Infant Microbial Transmission from Different Body Sites Shapes the Developing Infant Gut Microbiome. *Cell Host Microbe* **24**, 133-145.e5 (2018).

86. R. Maqsood, *et al.*, Discordant transmission of bacteria and viruses from mothers to babies at birth. *Microbiome 2019 71* **7**, 1–13 (2019).

87. E. S. Lim, *et al.*, Early life dynamics of the human gut virome and bacterial microbiome in infants. *Nat. Med.* **21**, 1228–1234 (2015).

88. M. Breitbart, *et al.*, Viral diversity and dynamics in an infant gut. *Res. Microbiol.* **159**, 367–373 (2008).

89. A. Reyes, *et al.*, Gut DNA viromes of Malawian twins discordant for severe acute malnutrition. *Proc. Natl. Acad. Sci.* **112**, 11941–11946 (2015).

90. M. A. Fernandes, *et al.*, Enteric Virome and Bacterial Microbiota in Children with Ulcerative Colitis and Crohn's Disease. *J. Pediatr. Gastroenterol. Nutr.* **68**, 30 (2019).

91. M. J. Coffey, *et al.*, The intestinal virome in children with cystic fibrosis differs from healthy controls. *PLoS One* **15**, e0233557 (2020).

92. A. C. Gregory, *et al.*, The Gut Virome Database Reveals Age-Dependent Patterns of Virome Diversity in the Human Gut. *Cell Host Microbe* **28**, 724-740.e8 (2020).

93. A. N. Shkoporov, *et al.*, The Human Gut Virome Is Highly Diverse, Stable, and Individual Specific. *Cell Host Microbe* **26**, 527-541.e5 (2019).

94. A. Reyes, *et al.*, Viruses in the faecal microbiota of monozygotic twins and their mothers. *Nature* **466**, 334–338 (2010).

95. M.-S. Kim, J.-W. Bae, Lysogeny is prevalent and widely distributed in the murine gut microbiota. *ISME J. 2018 124* **12**, 1127–1141 (2018).

96. L. F. Camarillo-Guerrero, A. Almeida, G. Rangel-Pineros, R. D. Finn, T. D. Lawley, Massive expansion of human gut bacteriophage diversity. *Cell* **184**, 1098-1109.e9 (2021).

97. C. B. Silveira, F. L. Rohwer, Piggyback-the-Winner in host-associated microbial communities. *npj Biofilms Microbiomes 2016 21* **2**, 1–5 (2016).

98. J. B. Russell, G. M. Cook, Energetics of Bacterial Growth: Balance of Anabolic and Catabolic Reactions. *Microbiol. Rev.* **59**, 48–62 (1995).

99. C. B. Silveira, *et al.*, Biophysical and physiological processes causing oxygen loss from coral reefs. *Elife* **8** (2019).

100. J. L. Sonnenburg, *et al.*, Glycan foraging in vivo by an intestine-adapted bacterial symbiont. *Science (80-.).* **307**, 1955–1959 (2005).

101. R. W. P. Glowacki, E. C. Martens, If you eat it or secrete it, they will grow: The expanding list of nutrients utilized by human gut bacteria. *J. Bacteriol.* **203** (2020).

102. C. Myhrvold, J. W. Kotula, W. M. Hicks, N. J. Conway, P. A. Silver, A distributed cell division counter reveals growth dynamics in the gut microbiota. *Nat. Commun. 2015 61* **6**, 1–10 (2015).

103. S. Jalili-Firoozinezhad, *et al.*, Complex human gut microbiome cultured in anaerobic human intestine chips. *bioRxiv*, 421404 (2018).

104. A. Sontheimer-Phelps, *et al.*, Human Colon-on-a-Chip Enables Continuous In Vitro Analysis of Colon Mucus Layer Accumulation and Physiology. *Cmgh* **9**, 507–526 (2020).

105. S. Jalili-Firoozinezhad, *et al.*, A complex human gut microbiome cultured in an anaerobic intestine-on-a-chip. *Nat. Biomed. Eng.* **3**, 520–531 (2019).

106. W. H. Chin, J. J. Barr, Phage research in “organ-on-chip” devices. *Microbiol. Aust.* **40**, 28–32 (2019).

107. H. Tang, *et al.*, Human Organs-on-Chips for Virology. *Trends Microbiol.* **28**, 934–946 (2020).

Chapter I

Phage biology in ‘organ-on-chip’ devices

RESEARCH ARTICLE

Phage research in ‘organ-on-chip’ devices

Wai Hoe Chin [A B] and Jeremy J Barr [A C]

+ Author Affiliations

Microbiology Australia 40(1) 28-32 https://doi.org/10.1071/MA19006

Published: 21 February 2019

This chapter is published as a perspective article on *Microbiology Australia* and aims to provides a summary approach on organ-on-a-chip fabrication and its prospect in furthering phage and microbiology research.

Abstract

The use of ‘Organ-on-chip’ devices in microbiology research presents enormous opportunities for fundamental and translational research (1–4). Yet these approaches have not been widely embraced by the microbiology field. This is particularly evident with bacteriophage (phage) research applications. Traditionally phage research has been an early adopter of experimental techniques and approaches (5), having catalysed research in biotechnology, environmental biology, sequencing, and synthetic biology. Here, we discuss some of the opportunities that organ-on-chip devices present to both phage and microbiology research, and provide a ‘how to’ guide for researchers interested in utilising this approach.

1. Introduction

‘Organ-on-chips’ are micro-engineered biomimetic devices that replicate key functions, activities and physiological responses of entire living organs (6). The approach has been used to develop beating hearts (7), simulate breathing lungs (8), sustain a gut microbiome (3, 9) and even develop interconnected neurons of the brain (10). Devices are typically micro-fabricated to contain channels that are lined with cultured human cells, which mimic organ-specific architecture and functions *in vitro* (6). The device structure varies depending on the organ of interest. For instance, the gut-on-chip can comprise of a single (11) or double channel structure (9), with channel dimensions varying between 500–1000 µm wide and 150–250 µm high. The single-channel gut-on-chip forms the simplest structure, being enclosed by a glass slide upon which, a layer of gut epithelial cells is grown. In comparison, the double-channel gut-on-chip is constructed by joining two single-channel devices together with a thin porous membrane separating the two channels. The membrane supports the gut cell

layer within the top channel while the bottom channel represents the vascular system of the gut.

The fabrication, operation and experimentation of organ-on-chip devices typically require the convergence of numerous fields including engineering, cell biology and microbiology; presenting a high technical barrier for research applications. Yet overcoming these challenges allows us to probe the interactions between phages, their bacterial hosts and 'life-like' organs to answer therapeutic, ecological, and fundamental questions. For example, a mucus-producing lung-on-chip model was used to describe phage adherence to mucus layer, thereby forming a non-host-derived barrier against bacterial infection (4). Other studies have demonstrated the maintenance of a gut microbiome and Coxsackie virus infection using a gut-on-chip model (3, 9); approaches which can be modified to investigate gut phage-bacteria interactions. In essence, the organ-on-chip provides researchers the benefit of *in vitro* amenability while experimenting with phages under biologically relevant conditions.

2. The organ-on-chip in four steps

Step 1: Designing the organ-on-chip mould

The first step to creating an organ-on-chip is to fabricate a mould. Two commonly used options are photolithography and 3D-printing. Photolithography (Fig.1) is commonly used in engineering fields, but is technically challenging; requiring specialist equipment and reagents. However, this technique is virtually limitless in creating complex designs at the nanoscale (12). The technique starts with depositing a photosensitive polymer on a substrate. By controlling ultraviolet (UV) light exposure

on the substrate, the polymer will polymerise to the desired feature pattern, which is subsequently developed by washing away soluble unpolymerised regions.

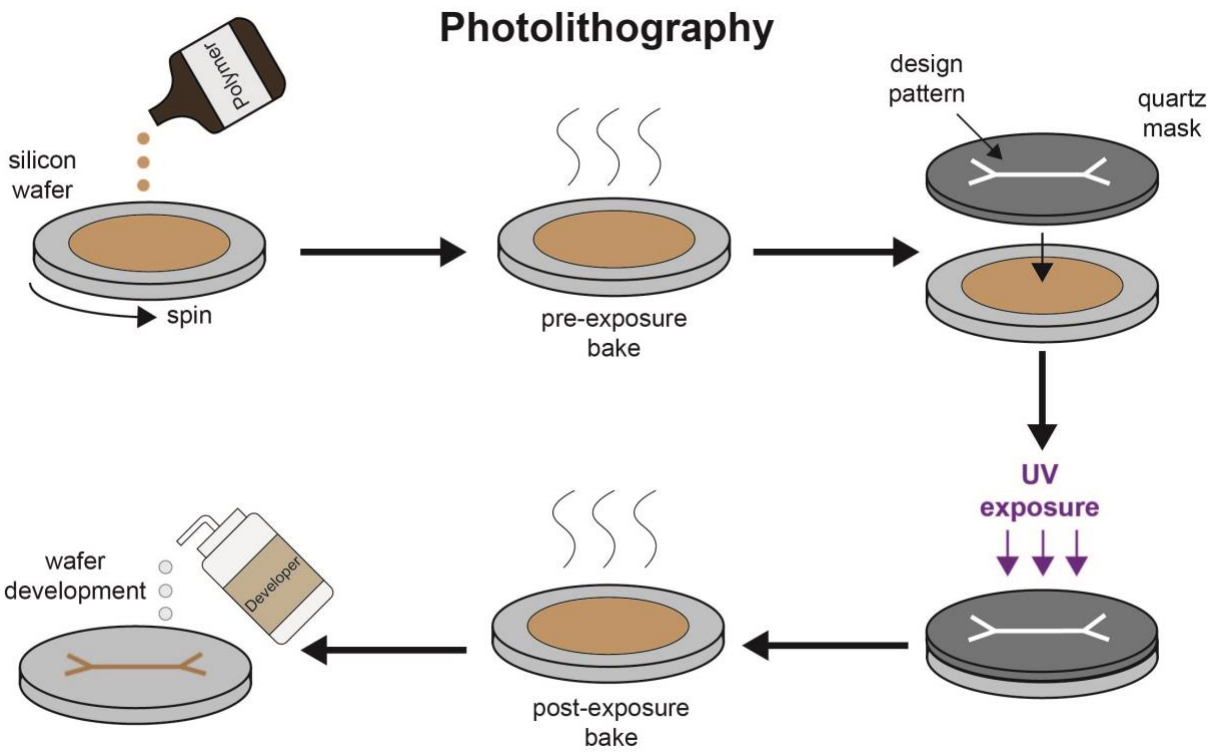

Fig.1. Organ-on-chip mould fabrication using photolithography. In this process, a photosensitive polymer (SU-8 is commonly used) is deposited onto a silicon wafer, baked, and overlayed with a quartz mask containing the desired features of the device. Exposure to UV light polymerises and solidifies the polymer to create the mould for subsequent use.

Alternatively, 3D-printing (Fig.2) offers a much quicker, easier, and cheaper route to fabricate organ-on-chip moulds. Unlike photolithography however, 3D printing has a much lower printing resolution, typically in the micrometre scale (13). Nonetheless, the accessibility and speed that 3D-printing offers enable researchers to quickly create simple organ-on-chip moulds for subsequent manufacturing, set-up, and experimentation (12).

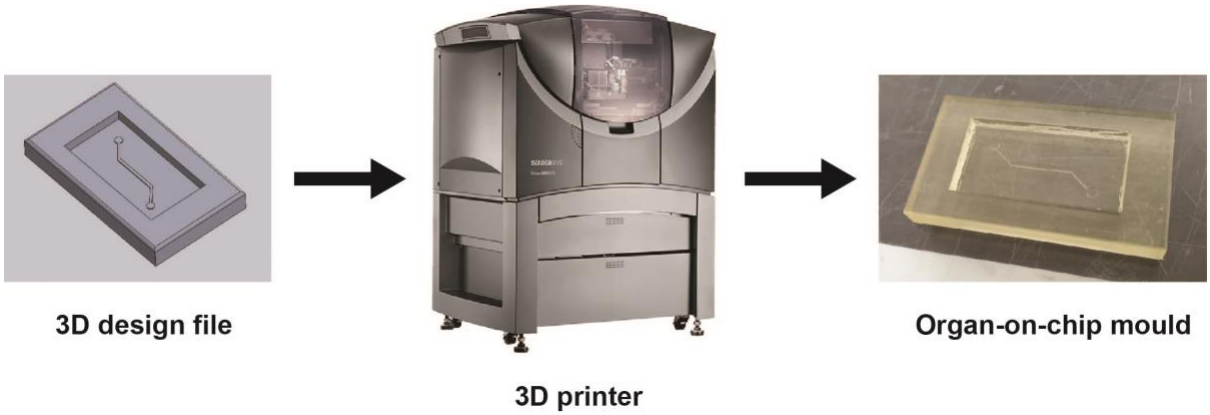

Fig.2. 3D printing the organ-on-chip mould. The mould is drawn using a modelling software, such as SolidWorks®, then converted to a 3D printer-readable file (.STL format) and sent to a 3D printer for device printing.

Step 2: Making the organ-on-chip

Once a mould is obtained, a variety of materials can be used to manufacture organ-on-chip devices. However, none has matched polydimethylsiloxane (PDMS) for its advantages in biocompatibility, permeability to gases, optical transparency and material flexibility (14). In addition to its advantages in biological applications, fabricating with PDMS is fairly straightforward (Fig.3) and does not require special expertise. The only specialist equipment required is a plasma cleaner to bond the PDMS device onto a substrate (typically a glass slide or another PDMS base). However, labs without access to this equipment can utilise a portable plasma “torch” for bonding organ-on-chips (Corona SB, Elveflow Microfluidics). Alternatively, researchers can purchase ready-made devices that are immediately amenable to cell culture, such as the LiverChip® (CN Bio Innovations, United Kingdom) or Intestine Bio-Kit (Emulate Bio, USA). For further details on organ-on-chip fabrication methods, consult references (6, 12, 15).

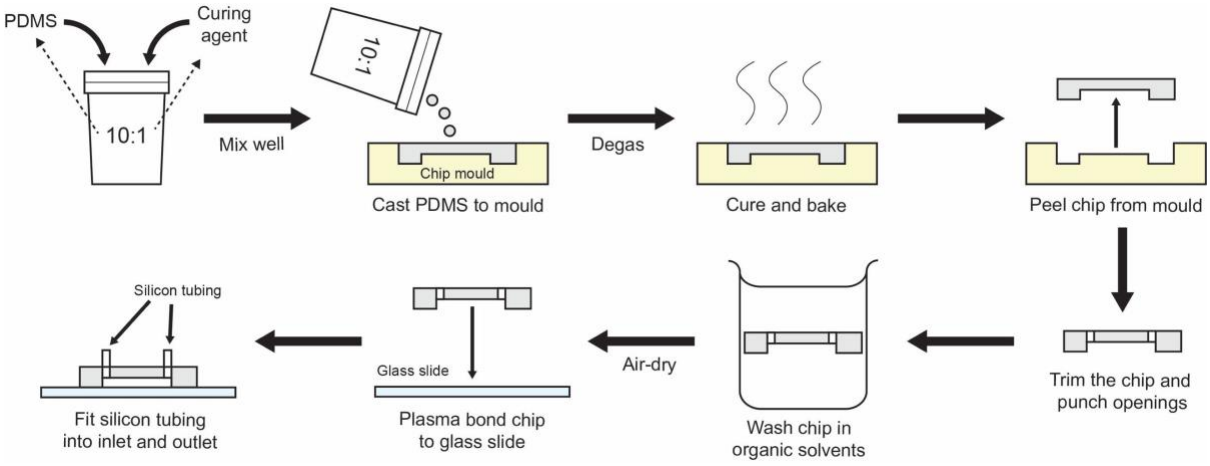

Fig.3. Workflow for organ-on-chip manufacture using PDMS. PDMS is a viscous fluid that solidifies when mixed at a recommended ratio of 10:1 with its curing agent. The mixture is then casted into the mould and baked at 95°C for curing. The PDMS chip is then peeled from the mould, trimmed and washed with organic solvent to remove residual uncured PDMS. The PDMS is then plasma bonded onto a glass slide – although other substrates can be used. Plasma activates the PDMS surface chemistry so that it forms irreversible chemical bonds when in contact with glass. Openings are punched into the PDMS and flexible silicon tubing fitted to create the device.

Step 3: Recreating the "organ" in the organ-on-chip

Any given organ is functionally and architecturally complex. Therefore, we must be mindful that organ-on-chips serve to approximate these complexities by "building the organ" using tissues or cells in culture. Nonetheless, with a fair amount of creativity and innovation, these approximations can recapitulate key functions and fundamental architecture of an organ unit. Recreating the functioning organ-on-chip relies on tissue culture work that is no different to traditional cell culture in flasks (Fig.4). Researchers

need only to scale their techniques to efficiently handle tissue culture at the microfluid-level – a simple act of replacing serological pipettes with micropipettes.

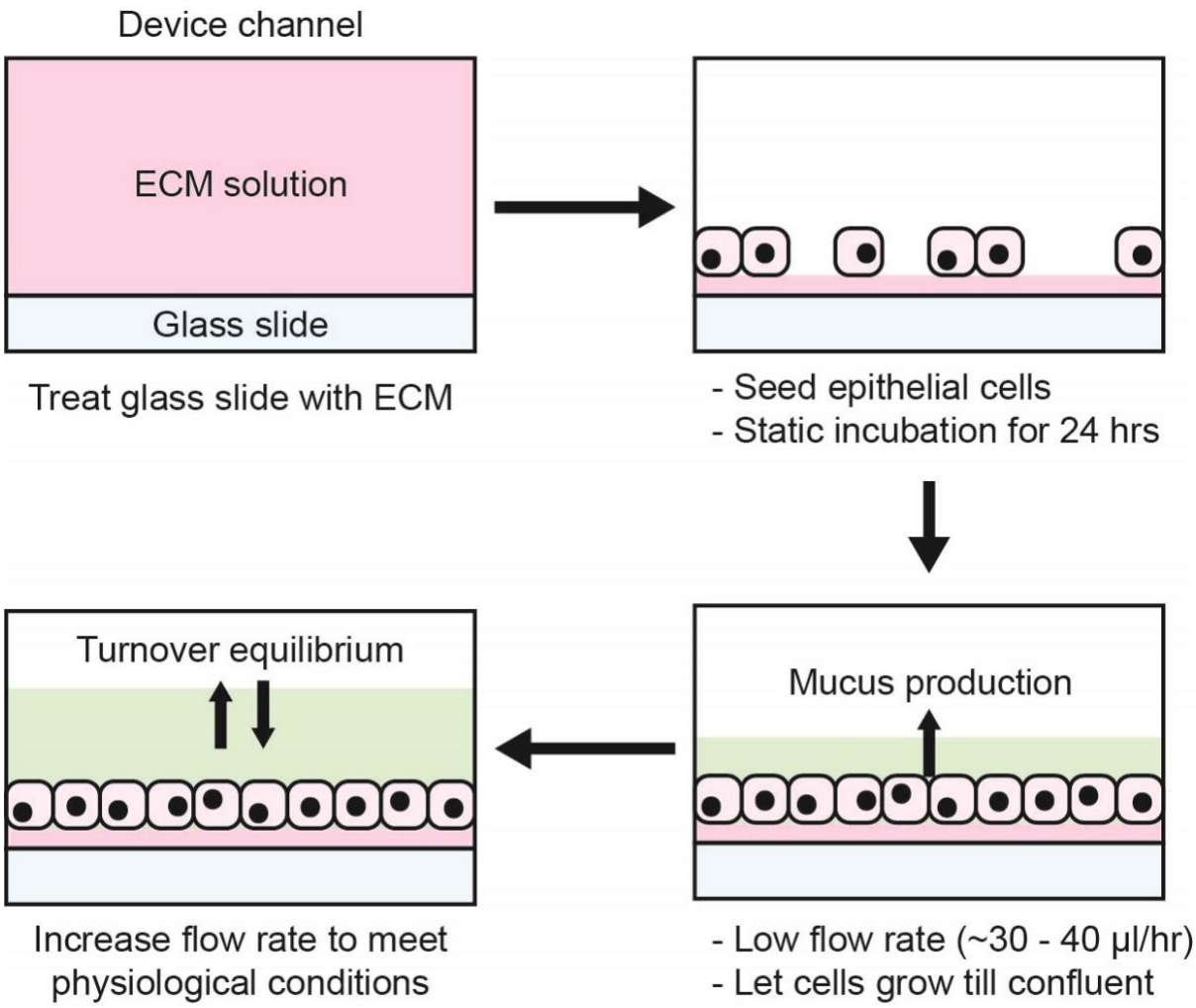

Fig.4. Workflow for reconstructing a mucus-secreting organ-on-chip. First, the device is treated with biopolymers to provide cells with an extracellular matrix (ECM) to attach and grow within the channel (15). The desired cell lines are propagated, harvested using standard trypsinisation and carefully seeded into the device using a micropipette. Cells are then incubated under static cell culture conditions to allow cell attachment to the ECM-treated substrate. Subsequently, the attached cells are perfused with tissue culture media to drive cell growth and differentiation within the organ-on-chip. In this example, a mucus-secreting gut epithelial cell line is used to recreate a gut-on-chip device.

Difficulties in transitioning cell cultures from flasks into the organ-on-chip are often encountered, but can be overcome with a few simple solutions. Toxicity from uncured PDMS in the devices can potentially cause cell death, but is easily eliminated through organic solvent washes (16). Determining the optimal cell seeding density will vary depending on the device and cell line used and often requires troubleshooting. Cell layer maintenance within the device requires a continual flow rate that does not impose excessive shear stress to the cells. Again, this will depend on the cell line used as some cell lines, such as endothelial lines, are more robust in withstanding high shear stress (17). Consulting publications that have used similar cell lines and devices will provide a ballpark figure to start troubleshooting.

Step 4: Operating the organ-on-chip

As outlined in step 3, cell growth and maintenance within the organ-on-chip is dependent on constant perfusion with culture media. Syringe pumps and pressure-driven systems are two widely-adopted approaches to perfuse organ-on-chip devices; each with their advantages and limitations. Setting up syringe pumps is simpler and requires less tubing, but has limited flow control and sample inoculation options. Conversely, pressure-driven systems are computerised setups made up of multiple components to regulate air pressure that will drive fluid flow from a media reservoir into the device. Connecting these components requires various adaptors and considerable tubing length, but offer increased flexibility for device control and inoculation. Furthermore, the computer interface in these systems offers fast response

times and can incorporate flow sensor feedback loops that provide superior fluid flow stability compared to syringe pumps (18).

3. Moving forward: Phage research in organ-on-chips

Traditionally, investigations of phage-bacteria interactions have been confined to *in vitro* broth culture. While these studies have proven instrumental for our understanding of phage biology, they neglect the complex environment and interactions seen *in vivo*. Recently, animal models have demonstrated the surprising diversity and stability of the phageome (19), and tissue culture-based *in vitro* studies have shown surprising interactions between phage and eukaryotic cells and tissues (4, 20–22). Organ-on-chip systems offer a unique way to study phage interactions within life-like systems that are cheap, accessible, and experimentally amenable.

3.1. Phage therapy approaches utilising organ-on-chips

Phages are known for their antimicrobial properties and are currently being pursued as an alternative to antibiotics in treating bacterial infections. Today, animal models are still the “bread-and-butter” for preclinical testing of therapeutics, including the therapeutic validation of phages. However, animal models are costly, labour-intensive, and ethically questionable (9). There are further concerns regarding the suitability of animal infection models to recapitulate human pathological conditions. Organ-on-chip models provide a middle-ground between traditional static cell cultures and animal models for preclinical testing. A recent example was the use of a gut-on-chip to reproduce Coxsackie virus infection of a highly differentiated human villus intestinal epithelium, which reproduced cytopathic effects (3). The use of organ-on-chip devices for phage therapy approaches offers large potentials, including the validation of

antimicrobial capacity within an organ of interest, pharmacokinetic and pharmacodynamics studies, and tracking the emergence of phage resistance.

3.2. Gut-on-chip: Moving gut phageome and microbiome studies from faeces to mucus

The human gut is home to a diverse repertoire of microbial species. This gut microbiome is comprised of trillions of microbial cells that influence our health, well-being and even psychological behaviour (23). Numerically, the gut viruses, of which phages account for ~90%, are as abundant, if not more, than their microbial counterparts (24). However, very little is known regarding the nature of phage-bacteria interactions within the gut. This is primarily due to the difficulty in studying and sampling the gut environment directly. Faecal samples are often used as a proxy to direct sampling, yet the faecal microbial communities differ significantly from intestinal mucosa (25). Gut-on-chip devices address these limitations by providing a life-like environment for phage-bacteria experimental studies (Fig.4). This relatively simple set-up mimics essential aspects of the *in vivo* gut, namely the mucus layer, luminal flow, and spatial elements of the cell layer. Using gut-on-chip devices, it was demonstrated that phages were able to adhere to gut-produced mucus layer and as a result, exhibit enhanced antimicrobial activity within the mucus layer, providing a layer of non-host-derived immunity (4, 20). A microbiome gut-on-chip approach demonstrated the recapitulation of pathogenic microbially-induced inflammation and the correction of these effects through probiotic and antibiotic therapies (26). Finally, recent cell culture studies demonstrated that phages targeting the gut pathogen *Clostridium difficile* had increased antimicrobial affects when in co-culture with human

gut cell lines (22). These studies illustrate the potential of phage and microbiology studies within organ-on-chip devices.

3.3. Phage-bacteria ecology and evolution using organ-on-chip

To-date, most evolutionary and ecological hypotheses attempting to explain phage-bacteria diversity in nature are confined to test-tube experiments and mathematical models. However, these are limited by the complexity of the experimental environment and assumptions of the models tested. Comparatively, the organ-on-chip approach allows for experimental investigations of these hypotheses under life-like conditions, adding increased complexity and biological relevance. Building off recent organ-on-chip microbiome devices (11, 26), researchers are now able to study emergent microbial properties, such as co-evolutionary phage-host dynamics, experimental evolution of microbial communities, and investigations of gut phage-bacteria ecology. These devices are further amenable to the introduction of genetically modified phages and bacteria, including the insertion of fluorescence markers for real-time visualisation (27) or antibiotic or CRISPR locus for quantification of target populations (28, 29). The collective evolutionary and ecological results obtained may validate models and further explain gut microbiome diversity.

4. Conclusion

Phages have been at the forefront of many biological advances. Today, not only are they impacting the medical field through therapeutic applications, but also continually fuel fundamental research, such as evolutionary biology and ecology. However, experimental phage research has been mostly confined *in vitro* and *in silico*. To that, we propose organ-on-chips as an experimental approach to further propel phage and

microbiology research. The amenability of organ-on-chips allows researchers to conduct various phage and microbiological studies within life-like conditions; without the cost associated with animal models. Despite requiring high interdisciplinary knowledge, the organ-on-chip remains accessible to non-engineers through collaborations or simpler alternatives in setting up the platform.

References

1. S. Jalili-Firoozinezhad, *et al.*, Complex human gut microbiome cultured in anaerobic human intestine chips. *bioRxiv*, 421404 (2018).
2. A. Bein, *et al.*, Microfluidic Organ-on-a-Chip Models of Human Intestine. *Cell. Mol. Gastroenterol. Hepatol.* **5**, 659–668 (2018).
3. R. Villenave, *et al.*, Human gut-on-a-chip supports polarized infection of coxsackie B1 virus in vitro. *PLoS One* **12**, 1–17 (2017).
4. J. J. Barr, *et al.*, Subdiffusive motion of bacteriophage in mucosal surfaces increases the frequency of bacterial encounters. *Proc. Natl. Acad. Sci. U. S. A.* **112**, 13675–13680 (2015).
5. F. Rohwer, A. M. Segall, In retrospect: A century of phage lessons. *Nature* **528**, 46–8 (2015).
6. D. Huh, *et al.*, Microfabrication of human organs-on-chips. *Nat. Protoc.* **8**, 2135–57 (2013).
7. A. Grosberg, P. W. Alford, M. L. McCain, K. K. Parker, Ensembles of engineered cardiac tissues for physiological and pharmacological study: Heart on a chip. *Lab Chip* **11**, 4165 (2011).
8. D. Huh, *et al.*, Reconstituting organ-level lung functions on a chip. *Science* **328**, 1662–8 (2010).
9. H. J. Kim, D. Huh, G. Hamilton, D. E. Ingber, Human Gut-on-a-Chip inhabited by microbial flora that experiences intestinal peristalsis-like motions and flow. *Lab Chip* **12**, 2165–74 (2012).
10. J. Park, *et al.*, Three-dimensional brain-on-a-chip with an interstitial level of flow and its application as an in vitro model of Alzheimer's disease. *Lab Chip* **15**, 141–150 (2015).

11. J. J. Barr, *et al.*, Subdiffusive motion of bacteriophage in mucosal surfaces increases the frequency of bacterial encounters. *Proc. Natl. Acad. Sci.* **112**, 13675–13680 (2015).
12. M. Leester-Schädel, T. Lorenz, F. Jürgens, C. Richter, “Fabrication of Microfluidic Devices” in *Microsystems for Pharmatechnology*, (Springer International Publishing, 2016), pp. 23–57.
13. B. C. Gross, J. L. Erkal, S. Y. Lockwood, C. Chen, D. M. Spence, Evaluation of 3D Printing and Its Potential Impact on Biotechnology and the Chemical Sciences. *Anal. Chem.* **86**, 3240–3253 (2014).
14. N. Beißner, T. Lorenz, S. Reichl, “Organ on Chip” in *Microsystems for Pharmatechnology*, (Springer International Publishing, 2016), pp. 299–339.
15. V. Faustino, S. O. Catarino, R. Lima, G. Minas, Biomedical microfluidic devices by using low-cost fabrication techniques: A review. *J. Biomech.* **49**, 2280–2292 (2016).
16. K. J. Regehr, *et al.*, Biological implications of polydimethylsiloxane-based microfluidic cell culture. *Lab Chip* **9**, 2132 (2009).
17. L. Kim, Y.-C. Toh, J. Voldman, H. Yu, A practical guide to microfluidic perfusion culture of adherent mammalian cells. *Lab Chip* **7**, 681 (2007).
18. W. Zeng, I. Jacobi, D. J. Beck, S. Li, H. A. Stone, Characterization of syringe-pump-driven induced pressure fluctuations in elastic microchannels. *Lab Chip* **15**, 1110–1115 (2015).
19. A. Reyes, *et al.*, Gut DNA viromes of Malawian twins discordant for severe acute malnutrition. *Proc. Natl. Acad. Sci.* **112**, 11941–11946 (2015).
20. J. J. Barr, *et al.*, Bacteriophage adhering to mucus provide a non-host-derived immunity. *Proc. Natl. Acad. Sci.* **110**, 10771–10776 (2013).

21. S. Nguyen, *et al.*, Bacteriophage transcytosis provides a mechanism to cross epithelial cell layers. *MBio* **8** (2017).

22. J. Shan, *et al.*, Bacteriophages are more virulent to bacteria with human cells than they are in bacterial culture; Insights from HT-29 cells. *Sci. Rep.* **8**, 5091 (2018).

23. C. A. Lozupone, J. I. Stombaugh, J. I. Gordon, J. K. Jansson, R. Knight, Diversity, stability and resilience of the human gut microbiota. *Nature* **489**, 220–30 (2012).

24. E. Scarpellini, *et al.*, The human gut microbiota and virome: Potential therapeutic implications. *Dig. Liver Dis.* **47**, 1007–1012 (2015).

25. M. R. Ingala, *et al.*, Comparing Microbiome Sampling Methods in a Wild Mammal: Fecal and Intestinal Samples Record Different Signals of Host Ecology, Evolution. *Front. Microbiol.* **9**, 803 (2018).

26. H. J. Kim, H. Li, J. J. Collins, D. E. Ingber, Contributions of microbiome and mechanical deformation to intestinal bacterial overgrowth and inflammation in a human gut-on-a-chip. *Proc. Natl. Acad. Sci. U. S. A.* **113**, E7–E15 (2016).

27. J. T. Trinh, T. Székely, Q. Shao, G. Balázsi, L. Zeng, Cell fate decisions emerge as phages cooperate or compete inside their host. *Nat. Commun.* **8**, 14341 (2017).

28. A. L. Borges, *et al.*, Bacteriophage Cooperation Suppresses CRISPR-Cas3 and Cas9 Immunity. *Cell* **174**, 917-925.e10 (2018).

29. W. N. Chaudhry, *et al.*, Leaky resistance and the conditions for the existence of lytic bacteriophage. *PLoS Biol.* **16**, 1–23 (2018).

Chapter II

Gut-on-a-chip fabrication and microfluidic set-up

This chapter is written as a methods chapter detailing the fabrication process for the gut-on-a-chip that forms the experimental basis for subsequent research chapters.

Abstract

One of the many advantages of the organ-on-a-chip technology is its ability to support cultures of various cell types depending on the organ and biological question of interest. To-date, various organ-on-a-chips have been manufactured to recapitulate the pulmonary environment (lung-on-a-chip) (1, 2), epidermis (skin-on-a-chip) (3), hepatic tissue architecture and circulation (liver-on-a-chip) (4, 5), intestinal mucosal epithelium (gut-on-a-chip) (6, 7) and even the blood-brain-barrier (blood brain barrier-on-a-chip) (8). Essentially, these devices serve as middle-grounds between traditional *in vitro* approaches and *in vivo* subjects using microfluidic technologies. Here, I describe in detail, the fabrication and cell culturing processes for a gut-on-a-chip microfluidic device and demonstrate the capacity for this device to simulate a simplified yet dynamic mucosal environment. This device forms the empirical basis for my subsequent research chapters in probing phage and bacteria evolution and ecology within a mammalian-derived mucosal setting.

Introduction

There are various gut-on-a-chip models to-date. Each achieving different forms of technological innovation through different fabrication approaches; for a detailed review of different gut-on-a-chip models, refer to (9). The most well-regarded gut-on-a-chip model is the dual-channel system that was initially conceptualised and established by Kim et al. (6, 10), The dual channel system comprised of two polydimethylsiloxane (PDMS) devices that were casted from silicon wafer moulds, where the design and dimensions of the device channels were etched using SU-8 photoresist polymer. In between the two PDMS devices, a 10 µm-thick PDMS porous membrane was sandwiched to divide the channels into two compartments i.e. a “top” and a “bottom”

compartment. Vacuum chambers were also etched adjacent to these compartments where peristalsis can be mimicked through a cyclic vacuum and positive pressure source. Gut epithelial cells were then seeded to the top compartment and allowed to adhere and grow, while the bottom compartment mimics the vascular system to deliver nutrient-rich oxygenated media basolaterally to maintain the gut cells. In some examples, the dual channel device could also facilitate immune cell residency for immunological studies or inverted to enable endothelial cell culture underlying the porous membrane (11, 12). Overall, the dual channel gut-on-a-chip system was able to recapitulate various key physiological aspects of the gut. However, the protocol described often requires specialist knowledge on microengineering and microfabrication (10), which is not conducive to the majority of biologists. Here, we introduced a simplified version of the gut-on-a-chip consisting of a single-channel device that was able to support the growth of a mucosal epithelium under physiological flow conditions. While this design is not as representative of the dual channel system, the fabrication protocol leveraged 3D-printing technology to manufacture chip moulds at high resolution within a rapid timeframe; unlike silicon with photoresist etching. The single-channel design also circumvents the challenges of manufacturing and manoeuvring thin membranes. Collectively, the single-channel design and the protocol described, not only provide a more accessible route for non-specialists to adopt the gut-on-a-chip, but also an efficient method to rapidly design, manufacture and test iterations of device moulds depending on the scientific question of interest.

1. Designing and fabricating the gut-on-a-chip mould

The channel design and dimensions for the gut-on-a-chip are similar to the lung-on-a-chip device adopted in Barr et al. (13). The design comprised of a 13 mm straight channel where the ends were extended by 8 mm channels at a 45°-angled bend leading to a 2 mm diameter inlet and outlet port, respectively (Fig.1A). Along the entire length of the channel up to the ports, the cross-sectional dimensions were 350 µm (0.35 mm) in height and 500 µm (0.5 mm) in width. The channel sits within a hollowed region of the mould that was 40 mm in length, 25 mm in width and 3.5 mm in depth. The overall external dimensions of the mould were, 70 mm in width, 35 mm in length and 5 mm in height. These channel and mould specifications were drawn using a solid modelling computer-aided program SOLIDWORKS (Dassault Systèmes, France) which renders the completed design file in .STL format, compatible with three-dimensional (3D) printing. The mould was printed using a clear photopolymer resin, Stratasys® Clear PolyJet^{TM} FC720 with the Stratasys® Objet Eden 260V 3D printer, provided by Melbourne Centre for Nanofabrication (Fig.1B). The surface of printed moulds were silanized overnight with Trichloro(1H, 1H, 2H, 2H-perfluorooctyl)silane (Sigma-Aldrich, USA) in a vacuum chamber to enhance surface hydrophobicity which will facilitate device detachment during soft lithography fabrication in Section 2.

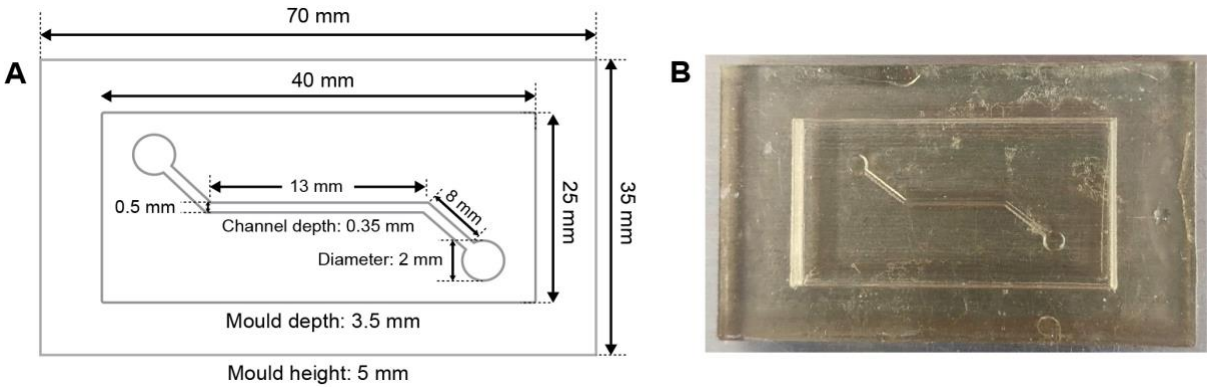

Fig.1 Mould design and dimensions. A) Schematic design of device mould with specified dimensions of the channel, hollowed region of the mould and mould exterior (not drawn to

scale). B) Actual image of the 3D-printed device mould printed with FC720 clear photopolymer resin.

2. PDMS soft lithography of gut-on-a-chip devices

Polydimethylsiloxane (PDMS) is a clear viscous polymer commonly used in soft lithography procedures. Combining PDMS with its curing agent followed by curing between 70 - 90°C, results in a solidified polymer that is biocompatible, gas permeable and optically clear, rendering PDMS highly suitable for biological studies and applications. Depending on ratio of PDMS-to-curing agent mixed, a range of product elasticity can be achieved. However, a 10:1 ratio of PDMS-to-curing agent is standard for the majority of downstream biological applications. The following sections were written in a step-by-step format to facilitate readers through the gut-on-a-chip fabrication protocol.

Materials

Reagents	Equipment
• Polydimethysiloxane [PDMS] – Sylgard 184 (Sigma-Aldrich) • PDMS curing agent (Sigma-Aldrich) • n-Pentane (Merck) • Acetone • Glacial ethanol for cleaning	• Silanized 3D-printed moulds • Electronic weighing scale • Vacuum desiccator • Hot plate • Stir plate with stir bars (can be combined with heating element). • Chemical fume hood
Miscellaneous • Styrofoam cups • Glass rod • Forceps • Scalpels and/or blades • 2 mm biopsy punches	• 1 L glass beaker • Aluminium foil • Scotch tapes • Kimwipes™ (KimTech® Science™) • 60 mm × 15 mm tissue-culture dishes

2.1 Casting PDMS onto 3D-printed moulds

Important: Ensure that all 3D-printed moulds are properly silanized before casting PDMS. Cured PDMS will not detach cleanly (if at all) from unsilanized surfaces and will therefore, compromise microchannel structures and the overall structural integrity of the casted device.

1. In a beaker or disposable Styrofoam cup, add 10:1 ratio of PDMS to curing agent by weight (e.g. 100 g of PDMS to 10 g of curing agent).
2. Mix thoroughly using a clean glass rod (Fig.2).

Important: The mixture should turn from clear to white and frothy once thoroughly mixed (Fig.2). Insufficient mixing will result in uneven curing of the polymer.

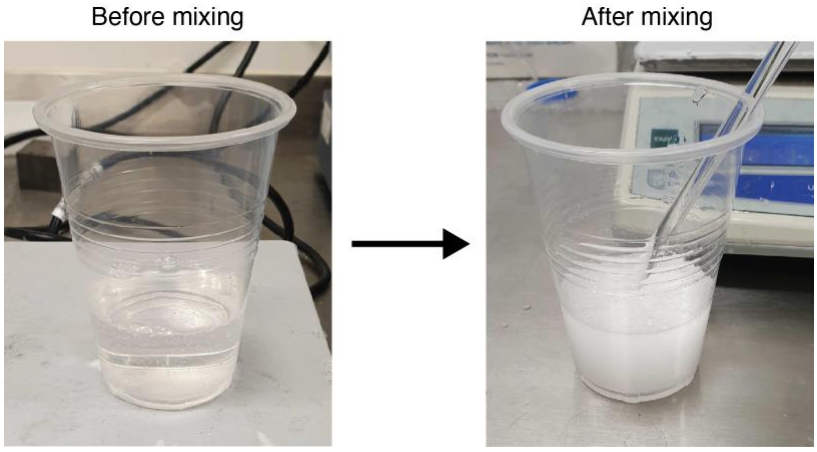

Fig.2 Before and after mixing a 10:1 PDMS-to-curing agent mixture. Mixing will incorporate air into the PDMS-curing agent mixture causing it to turn from clear to white and frothy.

3. Degas the PDMS-curing agent mixture by placing it into a vacuum desiccator for at least 1 hour.
4. Carefully cast the degassed PDMS-curing agent mixture into silanized moulds from Section 1.

5. Store leftover PDMS-curing agent mixture in -20°C to inhibit polymerisation of PDMS (You will need this in Section 3, step 23; or to cast additional devices at a later time).
6. Since casting will re-introduce air into the mixture, degas the casted moulds for another 15 minutes in a vacuum desiccator.
7. Place the degassed casted moulds onto a hot plate and cure at 70°C overnight (or 90°C for 3 hours).
8. Once cured, carefully peel the cured and solidified PDMS from the moulds using a sharp scalpel and a pair of forceps.

Important: Release the cured PDMS from the corners of the moulds using the scalpel and carefully peel away with the forceps. Be careful to avoid damaging the mould features when handling with the scalpel.

Note: If you experience difficulties with releasing and peeling the cured PDMS from the device, the mould is likely not adequately silanized. PDMS often cures irreversibly to the unsilanized moulds and unless the cured PDMS can be removed cleanly without damaging the mould features, you will have to manufacture new moulds as per Section 1 and repeat the silanization procedure.

9. *Optional*: Trim the device by using a sharp scalpel if necessary, to ensure that the device fits within the surface area of the glass slide for plasma bonding.
10. Carefully punch the device inlet and outlet ports using a 2.0 mm biopsy punch and discard the punched PDMS core (Fig.3)

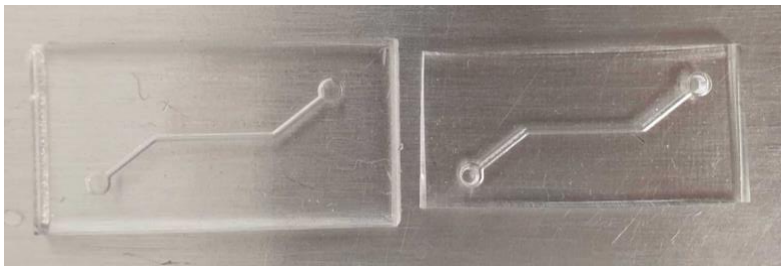

Fig.3 Trimming and punching PDMS device. PDMS devices before (left) and after (right) trimming with scalpel and punching with 2.0 mm biopsy punch.

11. Clean the device feature side using a Scotch tape to remove dust particles.

12. After cleaning, apply a layer of Scotch tape on the feature side to avoid contamination from dust or other fine particulates from the environment.
13. Depending on the number of devices required, repeat Steps 1 – 12 until sufficient number of devices have been casted for Section 2.2.

2.2 Washing devices to remove residual uncured PDMS

1. Place a magnetic stirrer plate within a chemical fume hood.

> **Safety check:** If the stirrer plate also contains a heating element, ensure that the heating is turned off. Washing steps comprise of highly volatile and combustible organic solvents!

2. Prepare a clean 1 L glass beaker and place a stirring rod within the beaker.
3. Remove the Scotch tape from devices casted in Section 2.1 and place the devices into the beaker.
4. Once all the devices are placed into the beaker, transfer the beaker to the stirrer plate within the chemical fume hood.
5. Submerge the devices in 400 ml of n-Pentane (Merck, Germany) **OR** twice the volume occupied by the devices in the beaker i.e. if the devices are at ~300 mL gradation on the beaker, pour 600 ml of n-Pentane.

> **Note:** PDMS devices will expand in n-Pentane. By submerging in twice the volume of the devices in the beaker, you will ensure that the devices remain submerged in the beaker despite expansion.

6. Cover the beaker with an aluminium foil and set on a gentle stir.
7. Allow the devices to wash in n-Pentane for at least 2 hours; an overnight wash is recommended for best results.

8. Carefully discard the n-Pentane into an appropriate waste container. Use the aluminium foil as a barrier to prevent devices from falling out of the beaker when discarding the waste n-Pentane.
9. Submerge the devices in 400 ml of acetone **OR** equal volume occupied by the devices in the beaker i.e. if the devices are at ~300 mL gradation on the beaker, pour 300 ml of acetone.
10. Cover the beaker with an aluminium foil and set on a gentle stir.
11. Allow the devices to wash in acetone for at least 2 hours; an overnight wash is recommended for best results.
12. Carefully discard the acetone into an appropriate waste container as per Step 8.
13. Repeat the acetone wash Steps 9 – 12 two more times, for a total of three acetone washes.
14. Line a clean tissue culture dish or acetone-resistant container with two layers of Kimwipes™ (KimTech® Science™, USA).
15. Place washed devices onto the lined tissue culture dish or container and allow the devices to dry under the chemical fume hood.

Note: Ensure that the device is completely dried of acetone before proceeding to Section 3 for plasma bonding. Residual acetone will interfere with plasma surface treatment and will result in poor bonding outcomes.

16. Cover the dried devices and store in a clean dust-free environment before proceeding to Section 3 for plasma bonding.

3. Device plasma bonding

Plasma-activated bonding is a common technique adopted in the fabrication of PDMS-based devices. Bonding typically occurs between the PDMS and another silicon-based material such as another PDMS surface, or in our case, a typical 25 mm × 76 mm × 1 mm microscopy glass slide. The plasma generated functionalises the PDMS surface by silicon oxidation to generate Si-OH groups. The contact between the Si-OH groups from the PDMS and its mating surface lead to a condensation reaction and the formation of covalent siloxane Si-O-Si bonds between the PDMS and the mated surface (14). This results in an irreversible covalent attachment between the PDMS and its mated counterpart. The protocol described here uses low pressure (or vacuum) plasma bonding via a tabletop plasma cleaner (Harrick Plasma, USA). For inverted confocal microscopy applications, the protocol can be adapted to bond devices onto a microscopy glass cover slip.

Materials

Reagents	Equipment
• Solvent-washed PDMS devices • 10:1 PDMS/curing agent mix (leftover from Section 2.1) • Glacial ethanol for cleaning	• Plasma cleaner with barometer (Harrick Plasma) • Vacuum source • Hot plate
Miscellaneous • 25 mm × 76 mm × 1 mm • Silicon tube (inner diameter: 1 mm, outer diameter: 1.8 mm) • Scotch tapes	• Kimwipes™ (KimTech® Science™) • Timer • Forceps • Scalpels and/or blades

1. Turn on the plasma cleaner and barometer (Fig.4)

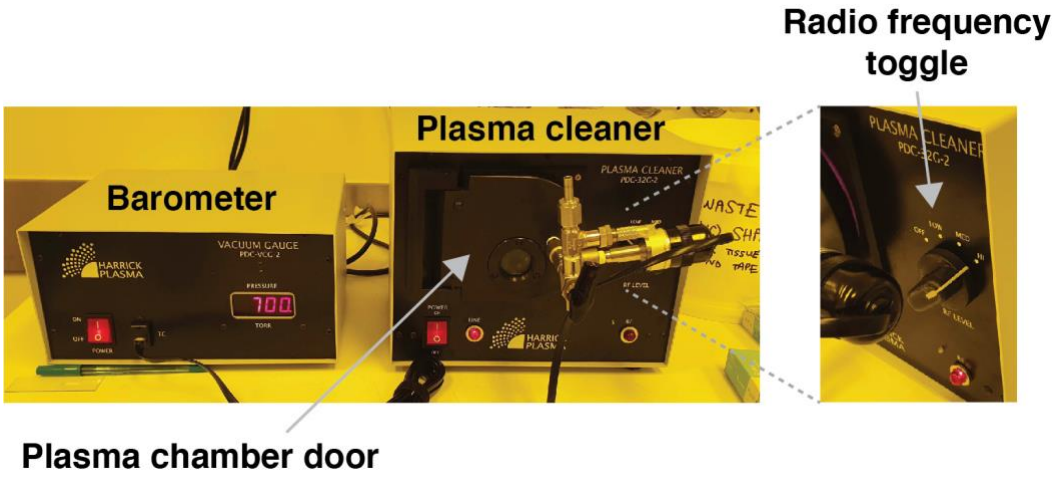

Fig.4 Plasma cleaner set-up. The plasma cleaner is connected to an electronic barometer that monitors the plasma chamber pressure with pressure readings displayed in units Torr. The plasma chamber door seals the chamber to allow the chamber pressure to drop upon activation of the vacuum source. When the desired pressure is achieved, the plasma cleaner is activated via a radio frequency toggle with four settings: “off, low, medium and high”; toggle setting shown in the right image is set on “high"

2. While the plasma cleaner powers up, clean glass slides with glacial ethanol and dry using Kimwipes.
3. Place the cleaned glass slides into the plasma cleaner chamber.
4. Close the chamber and the pressure valve (Fig.5A)

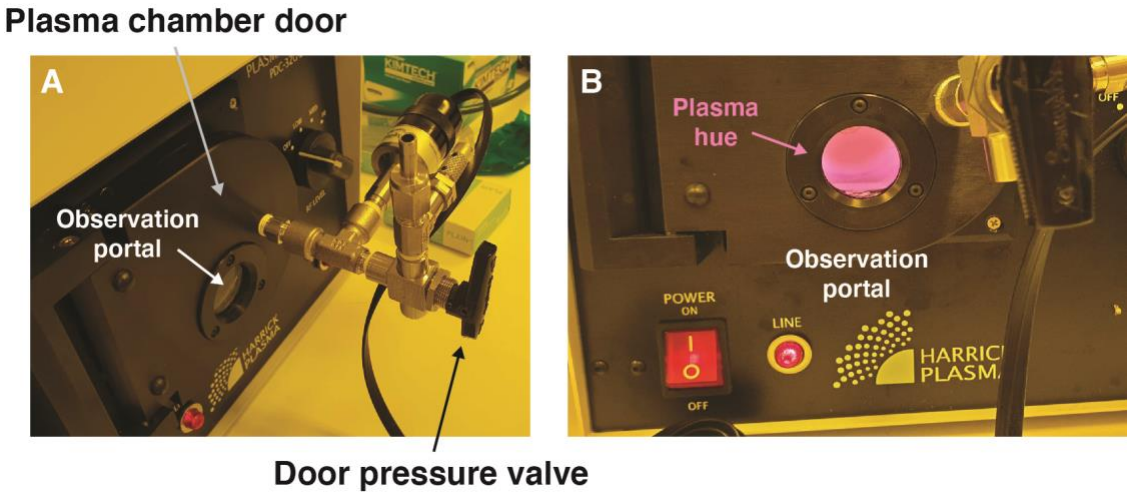

Fig.5 Plasma chamber door and plasma hue. A) Once the vacuum source is activated, the chamber is depressurised by rotating the door pressure valve 180° clockwise. The radio

frequency toggle is then switched to high when the chamber pressure reaches 0.65 – 0.75 Torr to generate a purple/violet plasma hue, which can be verified through the observation portal embedded in the plasma chamber door.

5. Turn on the vacuum source and allow the chamber to depressurize to 0.65 – 0.75 Torr (85 – 100 Pascals).
6. Activate the plasma chamber by switching the radio frequency toggle to “High”.
7. Check the plasma hue and ensure that the hue is purple or violet for an optimal plasma environment (Fig.5B).
8. Allow the glass slide at least 20 seconds of exposure to plasma to further clean the glass surface. This step is not time-sensitive and the glass slides can be plasma-treated for >20 seconds without affecting downstream fabrication.
9. Meanwhile, retrieve a washed PDMS device from Section 2.2 using a clean pair of forceps.
10. Clean the feature surface of the device using Scotch tape to remove any dust or fine debris.
11. Tape the cleaned PDMS surface with a new Scotch tape to keep the surface as clean and dust-free as possible in the next steps.
12. Turn off the radio frequency.
13. Turn off the vacuum source and reset the pressure valve to allow the chamber to re-pressurize to atmospheric pressure.
14. As quickly as possible and using a pair of forceps to minimise dust contamination, peel off the Scotch tape from the PDMS device and place the device within the plasma cleaner chamber feature-side up adjacent to the glass slide.
15. Close the chamber and the pressure valve and repeat Steps 5 – 7.

Important: Plasma at 0.65 – 0.75 Torr should result in a violet hue. If the hue is blue, this may indicate residual acetone within PDMS devices. In this case, remove the device from the plasma chamber and ensure that the device is properly dried and acetone-free before proceeding with bonding.

16. Treat the PDMS and the glass slide with plasma for a maximum of 20 seconds (Fig.6A).

Important: Over-activating the PDMS surface for >20 seconds may compromise bonding success rates.

17. Turn off the radio frequency.
18. Turn off the vacuum source and reset the pressure valve to allow the chamber to re-pressurize to atmospheric pressure.
19. As quickly as possible and using a pair of forceps, mate the device feature side onto the glass surface (Fig.6B – D)

Important: The plasma-activated surface is time-sensitive and the surface adhesiveness rapidly diminishes with time. Work quickly but ensure that the device is properly aligned to the glass slide before mating the surfaces. The condensation reaction and formation of covalent bonds during the mating process is very rapid upon contact between plasma-activated surfaces.

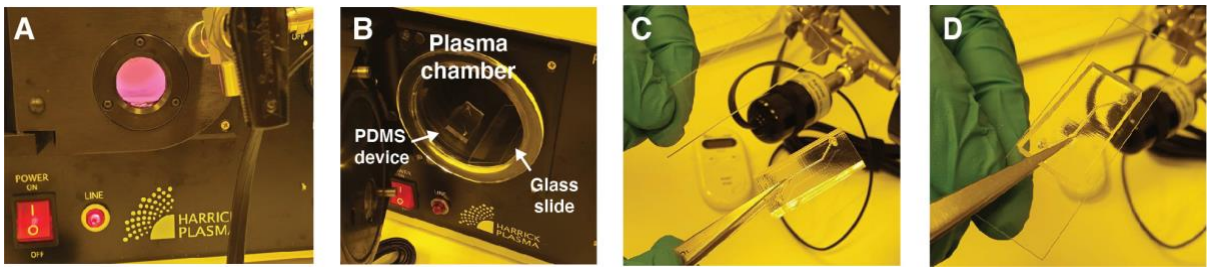

Fig.6 Plasma activation of PDMS and glass for bonding. A) PDMS and glass slide are treated in plasma for 20 seconds. B) The plasma is switched off and the chamber depressurised to retrieve the surface-activated PDMS device and glass slide. C) A pair of clean forceps is used handle the activated PDMS device while the glass slide is held securely

with the remaining hand. D) The feature-side of the PDMS device is mated onto the glass slide to enclose the device channel. The condensation reaction occurs immediately upon contact.

20. Place the mated device on a hot plate at 70°C for 5 minutes finalise the bonding (condensation) process.
21. While the device is on the hot plate, cut and prepare 1 cm segments of silicone tubing (inner diameter: 1 mm, outer diameter: 1.8 mm).
22. Using a pair of forceps, insert the 1 cm segments into the inlet and outlet ports of bonded device.

Important: Be careful to not insert the silicon tube down the entire depth of the device as this may block the device channel. Alternatively, you may cut the silicon tube at an angle to ensure that the channel is not obstructed in the event if the tube is inserted down the entire length.

Note: Silicon tubes are flexible and elastic. Short segments of silicon tubes inserted in the inlet and outlet ports of the bonded device ensures that the Teflon tube fitted to the device ports during experimental application is compliant and leak-free.

23. Using a toothpick or a blunt-end needle, apply 10:1 PDMS-to-curing agent mixture (leftover from Section 2.1) around the silicon tube and the PDMS device surface to form a meniscus.
24. Cure the device at 70 - 90°C for at least 2 hours to seal the silicon tube to the device.
25. Repeat steps 3 – 24 until the desired number of devices is manufactured.
26. Devices are ready to use for downstream applications (Fig.7).
27. Store in a sterile and dust-free container for up to 3 weeks until ready to use (refer to Section 4.4 on device shelf-life under troubleshooting).

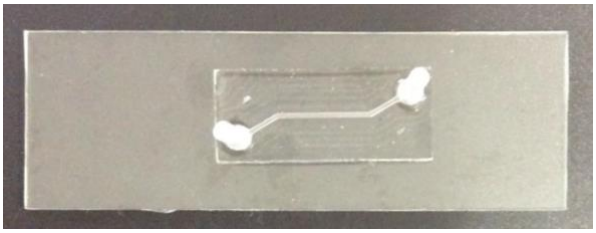

Fig.7 Assembled gut-on-a-chip device. The PDMS device was bonded onto a standard 25 mm × 76 mm × 1 mm glass slide. Protrusions from the inlet and outlet of the device are 1 cm segments of silicon tubing that are fitted into the 2 mm diameter opening and sealed with 10:1 PDMS-to-curing agent mix, cured at 70 - 90°C for 2 hours.

4. Culturing cells in the gut-on-a-chip

This section describes the steps to culture the gut cell-line HT29-MTX-E12 within the gut-on-a-chip device, with the aim of recapitulating a simple and dynamic gut mucosal epithelium. The HT29-MTX-E12 is a mucus-secreting gastrointestinal carcinoma cell line, originating from a parent culture of HT29 cells that was treated with methotrexate to induce goblet cell differentiation. Besides their mucus producing capabilities, HT29-MTX-E12 cells are also known to form confluent polarised cell layers with tight junctions and shallow crypts when grown and maintained under the presence of chemical inducers and gut-like physiological conditions (15, 16). Within the channel environment, the cell layer will experience a peak shear stress of 0.025 dyne cm^{-2} based on calculations of the channel height and width dimensions reported in Fig.1A at a 120 µl/hr flow rate (Fig.8A)(17). This shear stress is within physiological range typically reported in the intestine (6), and is a key mechanical force that promotes cellular differentiation via mechanotransduction, in addition to chemical induction. The terminal differentiation results in goblet cell structures lending to the production of a mucosal layer that also experiences turnover dynamics as a result of shear stress within the channel (Fig.8B).

A

$$T\ (shear\ stress) = \frac{6\mu Q}{WH^2}\ where,$$

$$\begin{bmatrix} \mu\ (viscosity\ of\ media\ at\ 37℃) = 0.78\ mPa \cdot s \\ Q\ (media\ flow\ rate) = 120\ \mu l/hr \\ W(channel\ width) = 500\ \mu m \\ H\ (channel\ height) = 350\ \mu m \end{bmatrix}$$

B

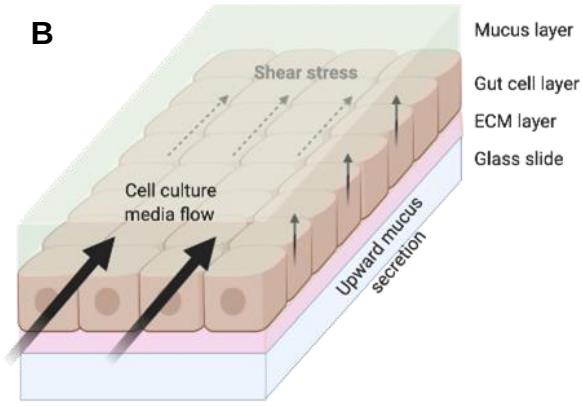

Fig.8 The mucosal microenvironment in the gut-on-a-chip. A) Shear stress calculations from reference (17), following channel parameters reported in Fig.1A. B) The balance between shear force introduced by cell culture media flow and the upward pressure of mucus secretion by mucosal epithelium recapitulates mucosal turnover dynamics.

Materials

Reagents	Equipment

• Bonded gut-on-a-chip device
• Dulbecco Modified Eagle Medium (DMEM) base
• 100× MEM non-essential amino acids
• 100× Penicillin-Streptomycin antibiotics (Pen-Strep)
• Foetal bovine serum (FBS)
• Extracellular matrix (MaxGel™, Sigma Aldrich).
• 0.25% trypsin
• 1× Dulbecco's phosphate buffer saline (DPBS)
• 80% (v/v) ethanol for disinfecting
• Inducers:
  ○ N-[N-(3,5-Difluorophenacetyl)-L-alanyl]-S-phenylglycine t-butyl ester (**DAPT**, Sigma-Aldrich)
  ○ Phorbol 12-myristate 13-acetate (**PMA**, Sigma-Aldrich)
	• Biosafety level 2 cabinet
	• Tissue culture incubator (37°C and 5% CO_2).
	• Multi-channel syringe pump
	• Inverted light microscope
	• Centrifuge
	
	Miscellaneous
	• Cell culture pipettes and disposables
	• Foldback clips
	• 1 ml syringes
	• 10 ml syringes
	• 21 G needles
	• Teflon tube (inner diameter: 0.8 mm, outer diameter: 1.6 mm)

Important: Perform all steps within a **biosafety level 2 cabinet** that is strictly assigned for tissue culture work. All surfaces and items e.g. pipettes, reagent tubes, racks, foldback clips, etc. should be ethanol-disinfected and ultraviolet (UV)-treated to minimise contamination risks.

4.1 Media preparation and cells

1. Two types of supplemented base media are required. All formulations were written for 40 ml media aliquots and stored in the dark at 4°C when not in use. Adjust reagent volumes as necessary if larger or smaller aliquots are required.

Complete media

Reagent	Volume	Final concentration
DMEM base	36 ml	N/A
FBS	4 ml	10%
MEM non-essential amino acids	0.4 ml	1×
Pen-Strep antibiotics	0.4 ml	1×

Differentiation media (antibiotic-free)

Reagent	Volume	Final concentration
DMEM base	36 ml	N/A
FBS	4 ml	10%
MEM non-essential amino acids	0.4 ml	1×
DAPT	Adjust according to final concentration	10 µM
PMA	Adjust according to final concentration	20 nM

2. Prepare a T25 flask of confluent HT29-MTX-E12 cells in complete media.

Notes:

- If recovering cells from cryogenic stock, add the thawed cells to 5 ml of pre-warmed complete media and incubate at 37°C and 5% CO_2.
- The HT29-MTX-E12 cell-line is slow to recover from cryogenic preservation and requires ~1 week to achieve 70 – 90% confluency.
- Subsequent passages after recovery should be straightforward with little to no complications. A 1 in 5 passage from a fully confluent T25 flask will achieve confluency in ~3 days.
- Harvest cells by washing thrice with 1× DPBS and 2 ml of 0.25% trypsin.
- A confluent HT29-MTX-E12 flask is relatively resistant to trypsinisation and may require >5 minutes of incubation.
- If incubation with trypsin exceeds 7 minutes, use a cell scraper.

3. Ensure that the tissue culture media is exchanged with fresh complete media on the day of seeding devices with cells.

4.2 Disinfecting and preparing devices for cell seeding

Recommended: Pre-warm all reagents (except the MaxGel™ extracellular matrix solution and an aliquot of complete media) to 37°C to minimise cold-shock on tissue culture cells.

1. Sterilise devices by wiping the devices with 80% (v/v) ethanol and pipetting 20 µl of ethanol through the device channel.
2. Rinse away excess ethanol by pipetting 1× DPBS through the channel twice and remove any residual 1× DPBS.
3. UV-treat the devices for at least 10 minutes.
4. Thaw out MaxGel™ extracellular matrix (ECM) solution from -80°C storage.
5. Prepare a 1:50 dilution of MaxGel™ ECM with **cold** complete media.
6. Pipette 10 µl of diluted MaxGel™ ECM into the device channel.
7. Clip the silicon tubes of the inlet and outlet of chips with foldback clips to prevent solution evaporation from the device in the incubator (Fig.8).

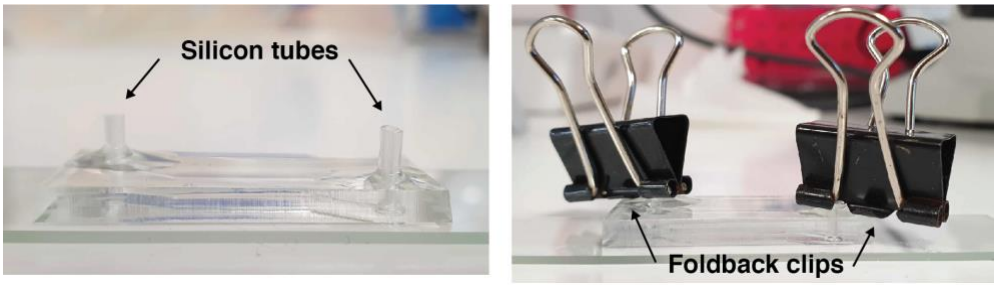

Fig.9 Preventing liquid evaporation from the device. The silicon protrusions are closed using stationery foldback clips to prevent liquid evaporation from the device channel.

8. Incubate the devices with the MaxGel™ ECM in 37°C, 5% CO_2 for at least 3 hours to allow the ECM to coat the channel surface.
9. Proceed to Section 4.3 at least 45 minutes before the end of the 3-hour incubation.

4.3 Harvesting cells and seeding into devices

1. Harvest the HT29-MTX-E12 cells removing the tissue culture media from the flask.
2. Wash the cells thrice with 1× DPBS and add 2 ml of 0.25% trypsin.
3. Allow the cells to trypsinise; use cell scraper if trypsinisation exceeds 7 minutes.
4. Add 3 ml of complete media to inactivate the trypsin (resulting in 5 ml total volume).
5. Quantify the cell density using a cytometer slide (expect ~4 × 10^6 cells/ml for a confluent T25 flask).
6. Split the 5 ml cell suspension to two separate tubes containing 2.5 ml each.

> **Note:** One tube will be used for device seeding and the other tube will be used to maintain cell passage for subsequent chip seedings.

7. Centrifuge the cells at 1,500 rpm for 3 minutes.
8. Remove the inactivated trypsin medium from **a single tube** and resuspend the cell pellet gently in **2.5 ml of fresh complete media**.

9. Perform a 1 in 5 passage (adjust as necessary depending on device seeding frequency) in a T25 flask to maintain the cell culture for future seedings.
10. Remove the inactivated trypsin medium from **the remaining tube** and resuspend the cells accordingly to achieve 3.5×10^7 cells/ml.

Example: For a concentration of 4×10^6 cells/ml in 2.5 ml, use dilution calculation $C_1 \times V_1 = C_2 \times V_2$.

4×10^6 cells/ml $\times$ 2.5 ml = 3.5×10^7 cells/ml $\times V_2$

V_2 = 0.285 ml or 285 µl

$\therefore$, resuspend the cell pellet in 285 µl of complete media

11. Remove devices from the incubator after 3 hours and discard the excess MaxGel™ ECM by gently pipetting the solution out from the channel.
12. Pipette 10 µl of the cell resuspension at 3.5×10^7 cells/ml into the device channel (Fig.9A and 9B).

Important: Ensure that no air bubbles or pockets are present. If air is present, discard the cell suspension by pipetting and repeat step 12.

13. Clip the silicon tubes of the inlet and outlet of chips with foldback clips to prevent volume evaporation from the device in the incubator.

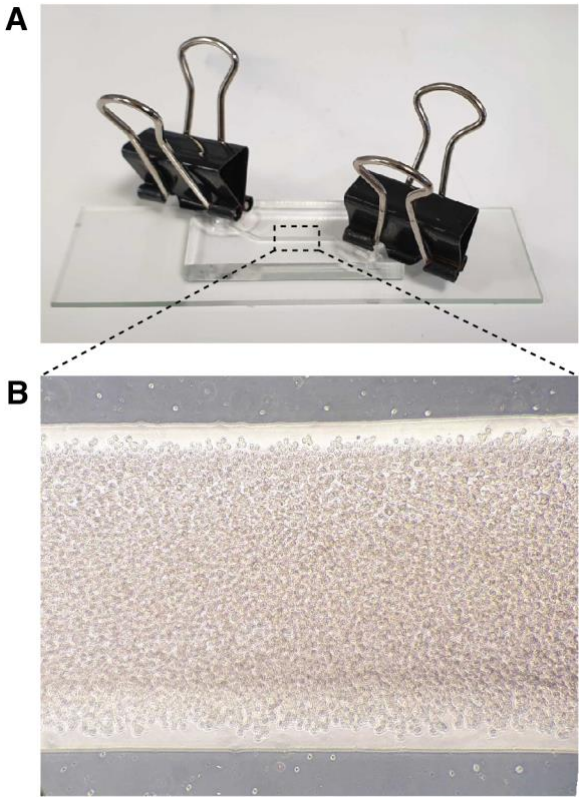

Fig.10 Density of cells seeded into the device channel. A) Image of a clipped device seeded with HT29-MTX-E12 cells. Dotted square region represents the field of vision visualised using an inverted light microscope. B) Image of cell density seeded into the device channel at 3.5×10^7 cells/ml.

14. Incubate the cells in the device at 37°C and 5% CO_2 for at least 16 hours under static conditions i.e. without flow, to allow cells to attach to the glass slide in the device channel.

Important: Do not exceed 24 hours of static incubation as cells will be nutrient deprived.

4.4 Cell layer perfusion, growth and induction

Important: Check the seeded devices to assess cell attachment profile before proceeding to perfusion. If cells did not attach appropriately, discard the device and repeat from Section 4.3 with freshly sterilised devices.

Troubleshooting: When cells do not attach!

- Devices are more than 3 weeks old since plasma bonding. The glass surface adhesive property is enhanced upon plasma treatment and bonding. This adhesive property diminishes with storage time.
  Solution: Only fabricate devices in 3-week batches. Devices can be casted and washed in advance, and stored in a dust-free environment until ready for plasma bonding.

- Devices were not wash appropriately in Section 2.2 resulting in leaching of uncured PDMS which is toxic to cells and increases channel surface hydrophobicity; the latter diminishes the adhesive environment of the device channel.
  Solution: Increase solvent volume and extend wash time, preferably overnight for all washes.

- Insufficient surface functionalisation with extracellular matrix solution.
  Solution: Increase extracellular matrix concentration in cold media and extend incubation time to ensure sufficient surface coating of the device channel with extracellular matrix.

1. Cut out two 40 cm segments of Teflon tube (inner diameter: 0.8 mm, outer diameter: 1.6 mm) with a clean blade or scissors.
2. Disinfect the exterior by running the tube through an 80% (v/v) ethanol-wetted paper towel.
3. Using a 1 ml syringe loaded with a 21 G needle and draw up 1 ml of 80% (v/v) ethanol.
4. Carefully fit the needle into the Teflon tube and disinfect the lumen by hand-infusing the ethanol through the entire length of the tube.
5. Using a 1 ml syringe loaded with a 21 G needle, draw up 1 ml of 1× DPBS.

6. Carefully fit the needle into the Teflon tube and purge out the ethanol from the lumen.
7. Draw air into the syringe and purge out the 1× DPBS.
8. Using a 10 ml syringe loaded with a 21 G needle, draw up 2 ml of complete media.

Note: The volume of media required depends on the perfusion flow rate and duration. In this protocol, the first perfusion with complete media will be carried out at a flow rate of 40 µl/hr for 48 hours.

∴, Total media volume required: 40 µl/hr × 48 hrs = 1,980 µl (~2 ml)

9. Carefully fit the media-filled syringe into a 40 cm Teflon tube segment and prefill the entire length of the tube with complete media and set aside.
10. Remove the foldback clips from the devices with the attached cells.
11. **Very carefully and gently** insert the prefilled Teflon tube segment to the device inlet through the silicon tube inner diameter.

Important: Avoid sudden motions when inserting the tube as this may introduce sudden fluid surges into the channel that will dislodge attached cells.

12. Repeat step 11 for the remaining empty 40 cm Teflon tube segment into the device outlet.
13. Connect the outlet Teflon tube into a waste container (e.g. running the tube through a parafilmed 15 ml Falcon tube).
14. Carefully transport the connected set-up to an inverted light microscope and check for cell attachment integrity.
15. If cells remained attached, place the syringe on a syringe pump and program to infuse at 40 µl/hr in an incubator at 37°C and 5% CO_2 (Fig.10A and 10B).

Safety check: Some syringe pumps are sensitive to elevated temperatures and humidity in the incubator. If possible, place the syringe pump outside of the incubator

and run the Teflon tube through incubator door and to the device in the incubator. The small 1.6 mm outer diameter Teflon tube should not cause significant gas leakage and temperature loss from the incubator. Adjust tube length if necessary, to accommodate syringe pump placement.

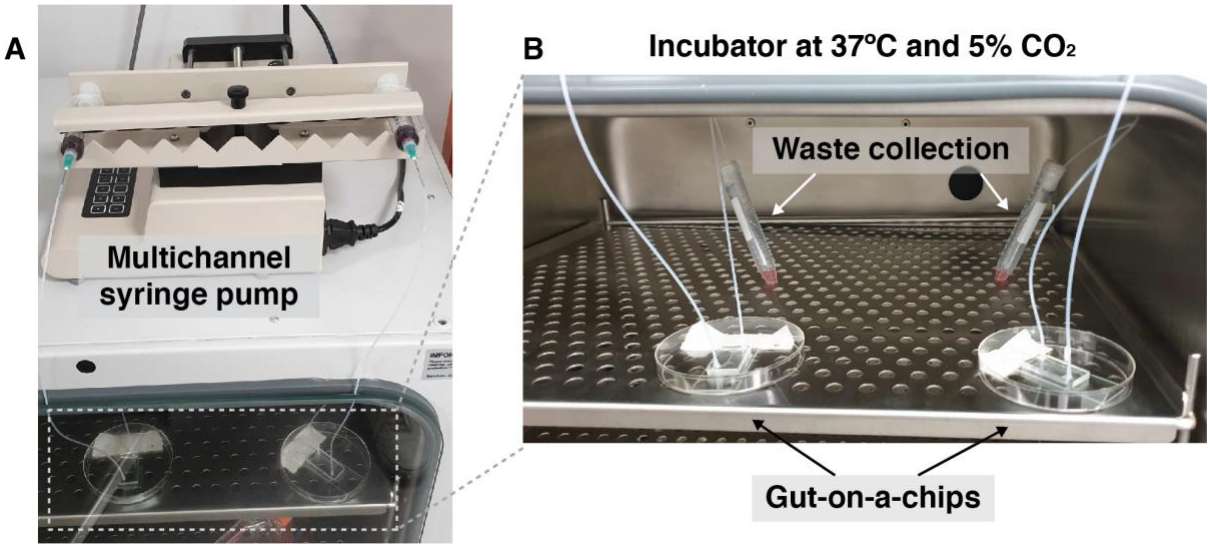

Fig.11. Gut-on-a-chip flow set-up. A) Syringe filled with media is loaded onto a multichannel syringe pump which is set to perfuse the gut-on-a-chip at a fixed flow rate. The syringe pump is placed outside of the incubator to ensure optimal equipment performance and safety from the elevated temperature and humidity within the incubator. B) A close-up of the gut-on-a-chips within the incubator at 37°C and 5% CO_2. The outlet Teflon tube is fed into two parafilmed 15 ml Falcons to collect waste media egressing from the gut-on-a-chip.

16. Perfuse the device for 48 hours with complete media until a highly adherent and confluent cell layer is established.
17. Using a 10 ml syringe loaded with a 21 G needle, draw up 5 ml of antibiotic-free differentiation media.
18. At the end of the 48-hour perfusion with complete media, carefully switch the syringe with the antibiotic-free differentiation media.
19. Increase the flow rate between 120 – 200 µl/hr and perfuse for an additional 24 hours to purge out antibiotics from the device and to allow the cell layer to induce, differentiate and acclimatise to physiological shear stress from increased flow rate.

Note: Media perfusion flow rate and time can be adjusted depending on requirements for downstream applications.

20. Visualise the cell layer via an inverted light microscope and assess for desired cell layer characteristics (Fig.11).

21. The 'gut-on-a-chip' device is now ready for downstream applications.

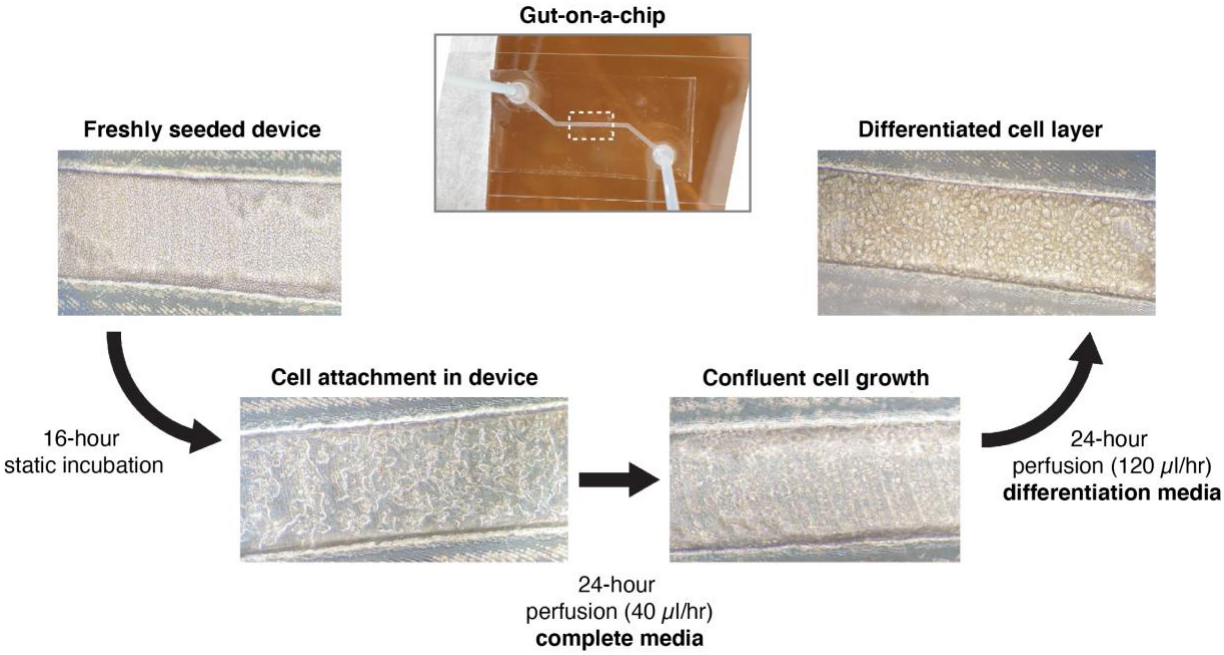

Fig.12 Cell layer visualisation throughout the seeding protocol. The white dotted box on the gut-on-a-chip aerial view indicates the microscopy field of vision in the follow panels. The left-most panel shows a device that was freshly seeded with HT29-MTX-E12 cell line at 3.5×10^7 cells/ml. After static incubation for 16 hours, the cells have attached to the glass surface of the device channel and is perfused for 24 hours under a low flow rate (40 µl/hr) for 24 hours with complete media. The nourished cells then grow to form a confluent cell layer which is subsequently perfused with antibiotic-free differentiation media at a physiologically relevant flow rate (120 µl/hr), resulting in a differentiated cell layer with extensive goblet cell morphology.

References

1. D. Huh, *et al.*, Reconstituting organ-level lung functions on a chip. *Science* **328**, 1662–8 (2010).
2. A. O. Stucki, *et al.*, A lung-on-a-chip array with an integrated bio-inspired respiration mechanism. *Lab Chip* **15**, 1302–1310 (2015).
3. M. Wufuer, *et al.*, Skin-on-a-chip model simulating inflammation, edema and drug-based treatment. *Sci. Reports 2016 61* **6**, 1–12 (2016).
4. N. S. Bhise, *et al.*, A liver-on-a-chip platform with bioprinted hepatic spheroids. *Biofabrication* **8**, 014101 (2016).
5. Yu Du, *et al.*, Mimicking liver sinusoidal structures and functions using a 3D-configured microfluidic chip. *Lab Chip* **17**, 782–794 (2017).
6. H. J. Kim, D. Huh, G. Hamilton, D. E. Ingber, Human Gut-on-a-Chip inhabited by microbial flora that experiences intestinal peristalsis-like motions and flow. *Lab Chip* **12**, 2165–74 (2012).
7. S. Jalili-Firoozinezhad, *et al.*, Complex human gut microbiome cultured in anaerobic human intestine chips. *bioRxiv*, 421404 (2018).
8. T.-E. Park, *et al.*, Hypoxia-enhanced Blood-Brain Barrier Chip recapitulates human barrier function and shuttling of drugs and antibodies. *Nat. Commun. 2019 101* **10**, 1–12 (2019).
9. N. Ashammakhi, *et al.*, Gut-on-a-chip: Current progress and future opportunities. *Biomaterials* **255**, 120196 (2020).
10. D. Huh, *et al.*, Microfabrication of human organs-on-chips. *Nat. Protoc.* **8**, 2135–57 (2013).
11. S. Jalili-Firoozinezhad, *et al.*, A complex human gut microbiome cultured in an anaerobic intestine-on-a-chip. *Nat. Biomed. Eng.* **3**, 520–531 (2019).

12. H. J. Kim, H. Li, J. J. Collins, D. E. Ingber, Contributions of microbiome and mechanical deformation to intestinal bacterial overgrowth and inflammation in a human gut-on-a-chip. *Proc. Natl. Acad. Sci. U. S. A.* **113**, E7–E15 (2016).
13. J. J. Barr, *et al.*, Subdiffusive motion of bacteriophage in mucosal surfaces increases the frequency of bacterial encounters. *Proc. Natl. Acad. Sci. U. S. A.* **112**, 13675–13680 (2015).
14. T. Suni, K. Henttinen, I. Suni, J. Mäkinen, Effects of Plasma Activation on Hydrophilic Bonding of Si and SiO[sub 2]. *J. Electrochem. Soc.* **149**, G348 (2002).
15. N. Navabi, M. A. McGuckin, S. K. Lindén, Gastrointestinal Cell Lines Form Polarized Epithelia with an Adherent Mucus Layer when Cultured in Semi-Wet Interfaces with Mechanical Stimulation. *PLoS One* **8**, e68761 (2013).
16. M. Lindner, A. Laporte, S. Block, L. Elomaa, M. Weinhart, Physiological shear stress enhances differentiation and mucus-formation of intestinal epithelial cells in vitro . 1–19 (2020).
17. Y. Son, Determination of shear viscosity and shear rate from pressure drop and flow rate relationship in a rectangular channel. *Polymer (Guildf).* **48**, 632–637 (2007).

Chapter III

Bacteriophage evolve enhanced persistence to a mucosal surface

On May 11th, 2021, this chapter was published as a preprint available on *bioXriv*. As of writing, the manuscript is currently under peer-review in *Proceedings of the National Academy of Sciences of the United States of America* (*PNAS*). The version embedded in this chapter is an extended version of the *PNAS* manuscript version, adapted to match the format of this thesis. All supplementary data and figures are included as main text figures, with the exception of three mutational tabular datasets and a graphical compilation for surface plasmon resonance (SPR) curves included as four separate annexes to this thesis.

Preprint link: https://www.biorxiv.org/content/10.1101/2021.05.11.443681v1.full

Bacteriophages evolve enhanced persistence to a mucosal surface

Wai Hoe Chin[1]**, Ciaren Kett[1], Oren Cooper[2], Deike Müseler[3], Yaqi Zhang[3], Rebecca S. Bamert[4], Ruzeen Patwa[1], Laura C. Woods[1], Citsabehsan Devendran[3], Denis Korneev[5], Joe Tiralongo[2], Trevor Lithgow[4], Michael J. McDonald[1], Adrian Neild[3] and Jeremy J. Barr[1]*

[1] School of Biological Sciences, Monash University, VIC, 3800, Australia

[2] Institute for Glycomics, Griffith University, Gold Coast Campus, QLD, 4222, Australia

[3] Department of Mechanical and Aerospace Engineering, Monash University, VIC, 3800, Australia

[4] Infection and Immunity Program and Department of Microbiology, Monash Biomedicine Discovery Institute, Monash University, VIC, 3800, Australia

[5] Department of Biochemistry and Molecular Biology, Monash University, VIC, 3800, Australia

* Corresponding author. Email: jeremy.barr@monash.edu

** Co-corresponding author. Email: wai.chin@monash.edu

Abstract

The majority of viruses within the gut are obligate bacterial viruses known as bacteriophages (phages). Their bacteriotropism underscores the study of phage ecology in the gut, where they modulate and co-evolve with gut bacterial communities. Traditionally, these ecological and evolutionary questions were investigated empirically via *in vitro* experimental evolution and more recently, *in vivo* models were adopted to account for physiologically relevant conditions of the gut. Here, we probed beyond conventional phage-bacteria co-evolution to investigate potential tripartite evolutionary interactions between phages, their bacterial hosts and the mammalian gut mucosa. To capture the role of the mammalian gut, we recapitulated a life-like gut mucosal layer using *in vitro* lab-on-a-chip devices (to wit, the gut-on-a-chip) and showed that the mucosal environment supports stable phage-bacteria co-existence. Next, we experimentally co-evolved lytic phage populations within the gut-on-a-chip devices alongside their bacterial hosts. We found that while phages adapt to the mucosal environment via *de novo* mutations, genetic recombination was the key evolutionary force in driving mutational fitness. A single mutation in the phage capsid protein Hoc – known to facilitate phage adherence to mucus – caused altered phage binding to fucosylated mucin glycans. We demonstrated that the altered glycan-binding phenotype provided the evolved mutant phage a competitive fitness advantage over their ancestral wildtype phage in the gut-on-a-chip mucosal environment. Collectively, our findings revealed that phages – in addition to their evolutionary relationship with bacteria – engage in evolution with the mammalian host.

Significance statement

Bacteriophages (phages in short) are viruses that infect bacteria. Phages are abundant in the gut and are compositionally unique across the human population. While phages are in constant evolutionary battle with bacteria, their potential evolution with the mammalian gut remains overlooked. Here, we test – for the first time – whether phages are capable of adapting directly to the mammalian “host”. Using a co-culture of phages, bacteria and a gut-like mucosa, we found that phage evolution was driven by *de novo* mutations and recombination. This contributed to a unique phage capsid mutation, lending enhanced phage persistence in the mucus layer. Our findings propose a potential co-evolutionary mechanism between phages and the gut mucosa, which could contribute to the individuality of gut viromes.

1. Introduction

Bacteriophages (phages) are viruses that predate upon bacteria in order to replicate and are thus, as ubiquitous as their bacterial counterparts. Their significance on shaping the underlying bacterial community in an ecosystem is reflected by the manifold of studies on phage-bacteria antagonistic co-evolution (1–4). The human gut is an exemplary ecosystem where phages are abundantly found alongside a rich bacterial community, known collectively as the gut microbiome. Here, antagonistic co-evolutionary dynamics between gut phages and their bacterial hosts are key in maintaining long-term microbiome homeostasis and diversity (5–8). While the focus on phages and bacteria within traditional gut microbiome studies has been extremely insightful (9), there is a rapidly expanding interest into the role that the mammalian host provides for these microbial communities. In particular, the interaction between the bacteria and the mammalian host remains a popular research paradigm where the complexity of bacterial-mammalian gut interactions is increasingly unfolding and disentangling (10). However, phage-mammalian interactions were often overlooked and consequently, much less is known regarding these interactions and their co-evolutionary potential.

Bacteriophages were previously demonstrated to adhere directly to mucus to form a non-host derived immunity against bacterial invasion (11). Phage-mucosal adherence was shown to promote increased encounter rates with bacterial hosts resulting in phage enrichment within the mucosal layer (12). Subsequent studies have expanded on this phage-mucus interaction. A study by Almeida et al. (13), found that phages bind to primary mucus on rainbow trout and persisted for up to seven days, protecting against the pathogenic bacterium *Flavobacterium columnare.* In addition, the mucosal

environment altered the bacterial phenotype lending increased bacterial virulence but at the cost of augmented susceptibility to phage infection, resulting in an ecological trade-off that maintains phages in metazoan mucosal surfaces. Other studies have further demonstrated the direct effect of the mammalian epithelial cell layer (14) and mammalian mucin glycans (15) on enhancing phage virulence towards their bacterial hosts within mucosal surfaces. At an ecological level, the gut mucosa segregates phage and bacterial populations, establishing spatial refuges, which further promote phage-bacteria co-existence (16). Collectively, these studies underscore the importance of the mammalian component – in this case, the mucosal epithelium – on phage persistence, ecology, and evolution within the gut.

Mucosal surfaces are critical layers that interface the mammalian host with their environment. They are both principal sites of defence and habitats for large and diverse microbial communities. The mucus layer itself is primarily formed by large, mammalian-derived mucin glycoproteins that are extensively glycosylated with diverse glycans (17). The adherence and enrichment of phages in mucus occurs via binding interactions between these diverse glycan residues covering mucin glycoproteins and immunoglobulin (Ig)-like protein domains exposed on the phage capsids (11). Importantly, these Ig-like proteins can accommodate large sequence variations of $>10^{13}$ potential alternatives, whilst still maintaining their structural fold integrity and function (18). As such, there is potential for phage Ig-like proteins to adapt increased or altered adherence to the mammalian host's mucin glycosylation patterns. However, to our knowledge, there is no evidence demonstrating the evolutionary potential between phages and the mammalian "host". To this, we questioned whether phages

have the capacity to co-evolve to the mammalian mucosal environment within a tripartite setting.

Using an *in vitro* lab-on-chip device to simulate a mammalian mucosal layer colonised with a bacterial host population (19), we tested if phage co-evolution would result in phenotypes that persist within the mammalian mucosal environment. We showed that both phage-bacteria populations and phage evolutionary dynamics were unique across replicate populations in the gut-on-a-chip, and that genetic recombination was a key evolutionary force in driving mutational fitness. Despite the inter-replicate disparity, we were able to derive an evolved phage with a mutation affecting the phage Ig-like domain within the Hoc capsid protein, that was previously shown to mediate phage adherence to mucus (11). This mutation conferred a fitness advantage by altering phage binding affinity to fucosylated mucin glycans. In summary, we present empirical evidence on the capacity of phages to co-evolve within a mammalian mucosal environment to adapt increased persistence and adherence to the mucosa.

2. Results

2.1. The gut-on-a-chip supports phage-bacteria co-existence within a mucosal layer.

To investigate the capacity of phages to adapt to the mammalian mucosal environment, we fabricated a simple gut-on-a-chip microfluidic device that recapitulates key features of the mammalian gut mucosa (Fig.1A). These devices are experimentally amenable, provide an accessible platform for biological replication, and recapitulate essential organ-level functions of the gut (19, 20) (Fig.1B). Our gut-on-a-chip consisted of a single channel containing a confluent HT29-MTX-E12 colonic cell layer, which was grown and maintained under constant media perfusion (Figs.1C and 1D). We verified that the colonic cell layer was also capable of mucus production by visualising the mucosal layer via scanning electron microscopy (Figs.1E and 1F).

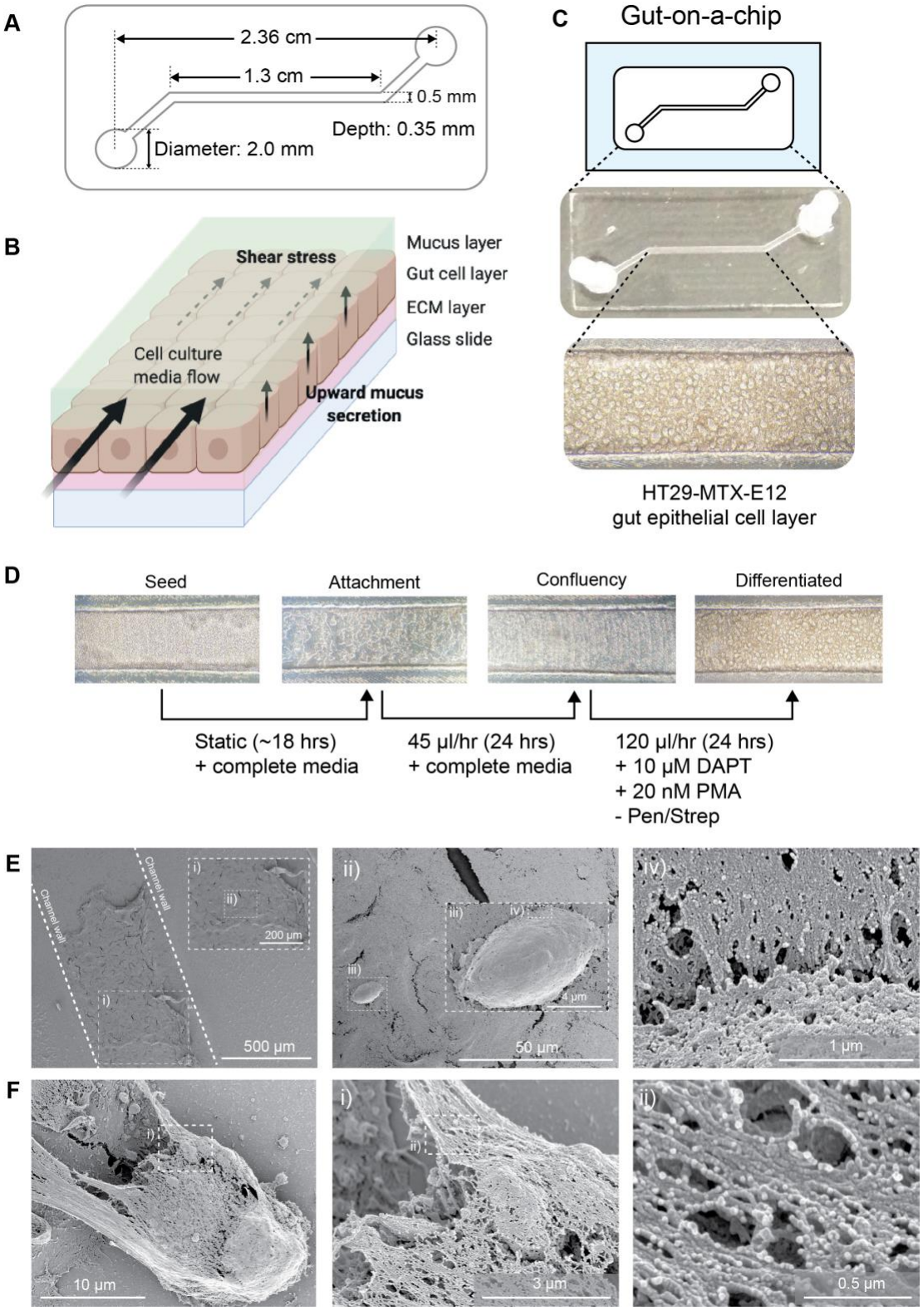

Fig.1 The gut-on-a-chip recapitulates a mammalian gut mucosal layer. A) Schematic and channel dimension of the gut-on-a-chip. B) Mucus turnover dynamics from the device is driven by shear stress from fluid flow and upward mucus secretion from the epithelial layer. C) HT29-

MTX-E12 cell line grows and differentiates within the device channel environment to produce a mucus layer at ~72 hours post-seeding. D) HT29-MTX-E12 cell culture timeline in the gut-on-a-chip. Cells were seeded to a density of 3.0×10^7 cells/ml in the device channel and allowed to incubate under static conditions for ~18 hours for attachment. Attached cells were subsequently fed with tissue culture media at low perfusion rate of 45 µl/hr until the cell layer has established confluency (~24 hours). Following that, antibiotic-free (-Pen/Strep) media, supplemented with inducers – 10 µM N-[N-(3,5-Difluorophenacetyl)-L-alanyl]-S-phenylglycine t-butyl ester (DAPT) and 20 nM 12-myristate 13-acetate (PMA) – to promote terminal cellular differentiation and mucus production, respectively – were perfused at a 120 µl/hr to mimic physiological shear stresses of the *in vivo* gut. The resulting acclimatised cell layer possessed extensive goblet cell morphologies and exhibited mucus production visible from alterations in cell layer shade and opacity under light microscopy. E) Scanning electron microscopy (SEM) of the HT29-MTX-E12 mucosal epithelium in a gut-on-a-chip from the anterior perspective i.e. top-view. The parallel lines indicate the position of the channel walls before removal of the gut-on-a-chip PDMS encasing for ethanol graded dehydration and imaging of the mucosal layer. Numbered dotted boxes represents the focused and magnified fields of vision of the mucosal blanket of the epithelium (i and ii) leading up to a high magnification image (iii and iv) of the net-like structure of the mucus glycoprotein layer. F) Up-close SEM of a single HT29-MTX-E12 cell within the gut-on-a-chip. Numbered dotted boxes represents the focused and magnified fields of vision on the mucosal network enveloping a single cell (i) and the net-like structure of the mucosal network (ii).

First, we assessed the microbial population dynamics in our simplified gut mucosa. 10^4 colony forming units (CFU) of *Escherichia coli* bacteria and 10^4 plaque forming units (PFU) of T4 phages – resulting in an inoculation with multiplicity-of-infection (MOI) 1 – were seeded into three replicate devices. The co-culture was maintained for

24 hours under constant perfusion with sterile media at 120 µl/hr, equating to 12 turnover cycles of the channel environment per hour. An automated sample collection system was developed (Figs.2A and 2B) where egressing samples from the device were heat-inactivated, followed by collection at 30-minute intervals, with phages and bacteria subsequently quantified via quantitative PCR (qPCR) (Fig.2C). Despite inoculating each replicate device with similar phage-bacterial densities, we observed immediate differences within the first hour across the replicates. Hereafter, both phages and bacteria remained under the limit of detection (LOD; refer to Tables 2 and 3 in Material and Methods for standard curves) until an initial growth phase between 2 – 4 hours where phages in particular achieved high densities accompanied by a small bacterial population recovery above LOD. Subsequently, we saw a second phage growth phase between 5 – 6 hours in tandem with bacterial population decrease below LOD, suggesting lytic phage suppression during this window. Thereafter, we saw divergent ecological dynamics occurring between replicate gut-on-a-chip devices. In replicate 1, bacteria remained under the LOD while phage populations were consistently high. Given the turnover rate of the channel environment of 12 times per hour, the stable phage persistence suggests that the phages are maintained by a non-extinct but undetectable bacterial population. In replicate 2, the bacterial population overtook the phage population potentially through the emergence of phage resistance, but both phages and bacteria nonetheless, remained in co-existence. Finally, in replicate 3 phage-bacteria populations fluctuated above and below LOD, exhibiting classical prey-predator dynamics. In summary, we demonstrated that the gut-on-a-chip was able to support phage-bacteria co-existence for up to 24 hours, albeit with considerable variation between replicate devices in terms of population abundances and dynamics. This suggests that microbial ecology in each device was unique and

delineated by inherent fluctuations and ecological stochasticity. Overall, the gut-on-a-chip provided a tripartite model system that supported mammalian, bacterial and phage co-culture.

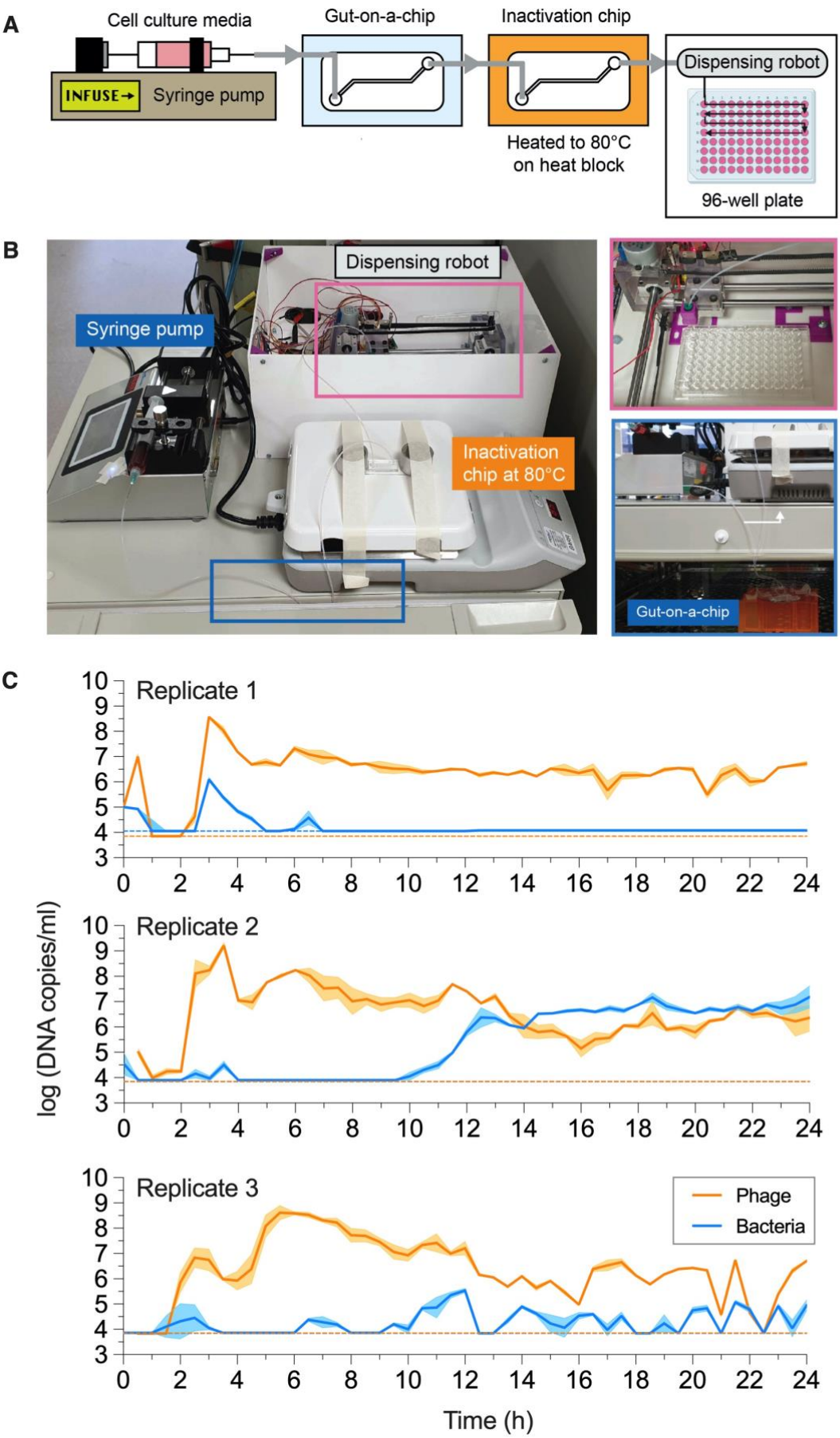
A
Cell culture media
Gut-on-a-chip
Inactivation chip
INFUSE
Syringe pump
Heated to 80°C
on heat block
Dispensing robot
96-well plate
B
Dispensing robot
Syringe pump
Inactivation
chip at 80°C
Gut-on-a-chip
C
Replicate 1
Replicate 2
Replicate 3
log (DNA copies/ml)
Time (h)
Phage
Bacteria

Fig.2 The gut-on-a-chip supports phage-bacteria co-culture within a mucus environment. A) Schematic for overall gut-on-a-chip set-up for chip perfusion, continuous sample inactivation via heat and automated sample collection for qPCR quantification. B) Actual image for the overall gut-on-a-chip set-up with an automated sampling platform for high temporal resolution sampling from the gut-on-a-chip. The gut-on-a-chip was perfused by a syringe pump where egressing fluid from the device was channelled to an "inactivation chip" – an empty device placed on a heat-block at 80°C – to inactivate phages and bacteria within the egressing fluid sample. The inactivated sample was subsequently channelled to a dispensing robot which dispenses the inactivated sample across a sterile 96-well plate over 24 hours, which were then quantified for phage and bacteria abundances via qPCR. The robot was manufactured in-house, consisting of Arduino-driven stepper motors and conveyer belts that moves along the horizontal X-Y plane following written code with relevant time-steps. C) qPCR-quantified phage-bacteria population in three separate devices at 30-minute intervals over 24 hours. Plotted line and shaded region represents mean ± SEM of three qPCR technical replicates (n = 3) per experimental replicate; with three replicate gut-on-a-chip devices in total (N = 3). Orange and blue dotted lines represent the qPCR limit of detection (LOD) threshold for phage and bacteria respectively (refer to Tables 2 and 3 in Material and Methods for T4 phage and *E. coli* B standard curves and LOD thresholds, respectively).

2.2. The mammalian mucus layer influences phage evolution.

Based on experimental evidence that our gut-on-a-chip supports a tripartite co-culture (Figs.1 and 2C), we next experimentally evolved independent phage populations in either the tripartite gut-on-a-chip system, or a test-tube control, which lacked a mammalian mucus layer (Fig.3A). Here, both systems were inoculated with populations of T4 phages and *E. coli* bacteria (the founding phage population herein referred to as the "ancestral" phage), which were maintained for 24 hours; an incubation length commonly adopted in classical *in vitro* experimental evolution studies. At the end of 24-hour period, we collected the entire population from both the gut-on-a-chip and test-tube environments, followed by phage and bacterial quantification via traditional plating. We then conducted successive transfers of the "evolved" phage populations into either fresh gut-on-a-chip devices grown from naïve gut cells and seeded with naïve bacterial populations ("naïve" referring to entities that had no prior exposure to phages), or new test-tube controls with naïve bacterial populations. Both gut cells and bacterial populations were kept naïve in order to capture phage evolution within the two differing environmental contexts (i.e. the gut-on-a-chip and test-tube). In total, we performed five successive transfers of evolved phages across three biological replicates in gut-on-a-chip devices and in test-tubes, respectively (Fig.3B).

Both phages and bacteria were consistently recovered from the gut-on-a-chip (Fig.3B). In-line with our previous findings, phage-bacteria population densities varied across all replicates between experimental transfers which again, reflects on the stochasticity inherent to the gut-on-a-chip system (Fig.2C). This contrasted with test-tube control where bacterial populations frequently went extinct (Fig.3B, test-tube).

We posit that the absence of spatial heterogeneity within a test-tube setting lends a high likelihood for productive phage-bacteria encounters. In contrast, the mucosal layer is spatially heterogeneous, largely dictated by the mucin gradient along the polarised mucosal epithelial layer (21, 22). This heterogeneity provides spatial refuge for bacterial micropopulations which consequently tempers phage predation pressures within the mucosal environment, resulting in stable tripartite co-culture of phages, bacteria and the mammalian mucosa (16).

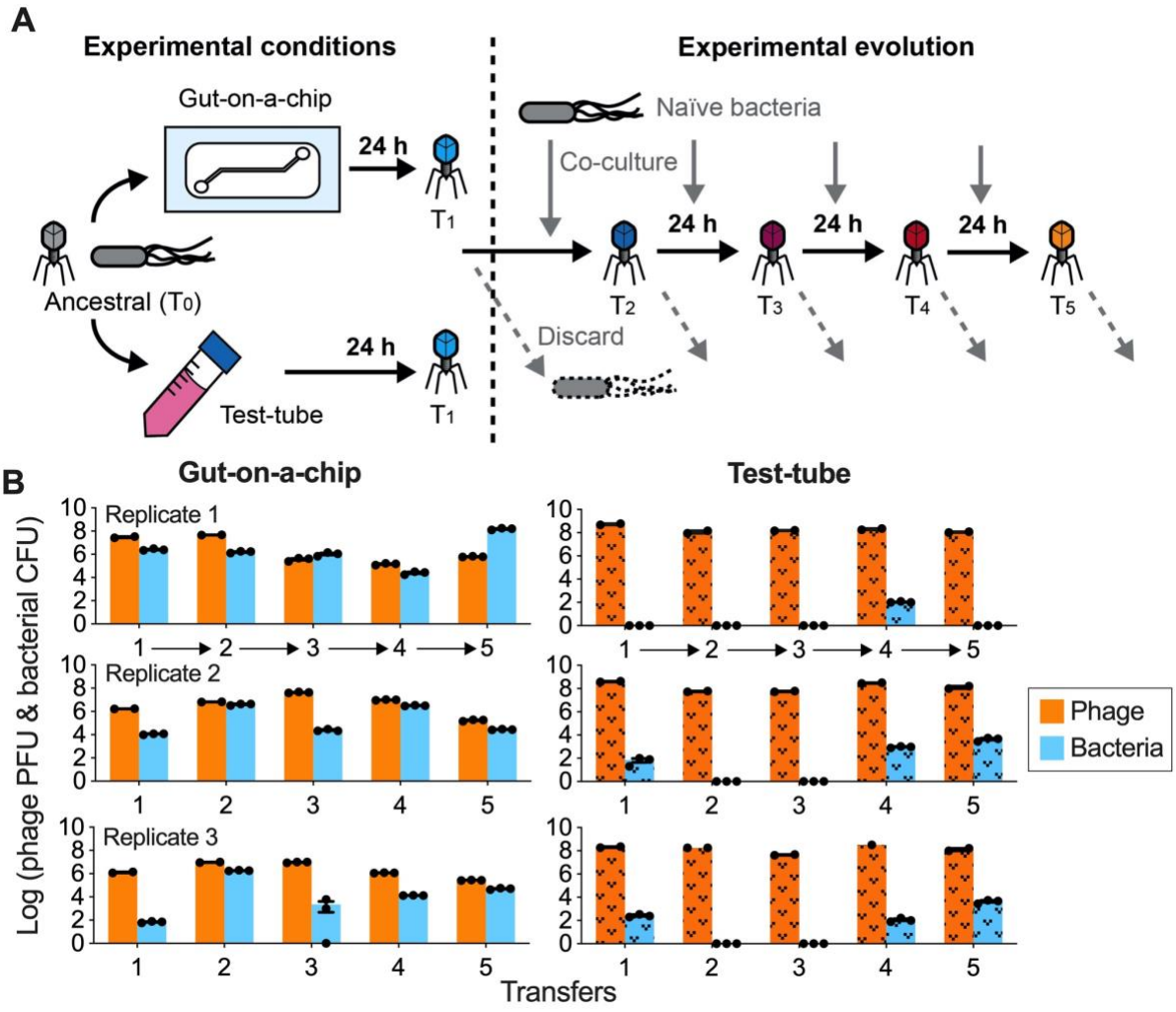

Fig.3 Phages experimental evolution passage and recovered population densities. A) Ancestral (zeroth transfer; T_0) T4 phage and *E. coli* bacterial hosts were inoculated into three gut-on-a-chip and test-tube set-ups, respectively. The co-cultures were incubated for 24 hours

with phages subsequently harvested for the first transfer (T_1). Phages from T_1 were transferred into either fresh chips or test-tubes seeded with naïve *E. coli* B hosts and the process was repeated till the fifth transfer (T_5). B) Density of phages and bacteria from the mucus layer collected from the gut-on-a-chip (plain coloured bars) and test-tube (textured coloured bars) replicates at the end of each 24-hour passage. The arrows along the x-axis represent the experimental evolution phage transfer in-line with panel A. Data points in panels B were plotted as a bar chart with error bars representing mean ± SEM of technical replicates (n = 2 to 3, except test-tube replicate 3, transfer 4 for phage, where n = 1).

Next, we sought to determine the evolutionary changes that occurred in the phage populations between gut-on-a-chip and test-tubes using whole-genome sequencing, followed by read alignment and mutational calling. First, we screened our ancestral T4 phage population and discovered a number of background mutations comprising of single nucleotide polymorphisms (SNPs) and single-nucleotide insertions, reflective of their long-term laboratory storage and genetic drift (23) (Annex 1). We subtracted these background SNPs and insertions from our mutational readouts in order to highlight *de novo* mutations arising in our gut-on-a-chip and test-tube evolved phage populations.

In the case of our gut-on-a-chip populations, *de novo* mutations were found in genes encoding nucleotide binding and metabolism proteins, structural proteins and hypothetical proteins, most of which were transient and low abundance (Annex 2). Moreover, we did not observe parallel evolution across our chip-evolved populations. This further highlights the generalisable stochasticity of the mucosal environment beyond affecting phage-bacterial population ecology to also constrain parallel evolution in phage populations. Nonetheless, two mutations attained high-abundance

within the first gut-on-a-chip replicate. The first was a non-synonymous SNP within the *hoc* (highly immunogenic outer capsid) gene, which encodes for an accessory outer capsid protein containing three Ig-like domains that has been demonstrated to facilitate phage adherence to mucus (11). This SNP resulted in an amino acid change at position 246 from aspartic acid to asparagine (henceforth referred to as D246N Hoc). The second mutation was an in-frame 21bp-deletion (Δ21bp) of the *goF* gene which encodes for a transcription antitermination factor that antagonises the bacterial ρ (Rho) termination factor from prematurely degrading phage mRNA transcripts (Figs.4A and 4B) (24).

A. *goF* nucleotide sequence:

```
Mutant   1   ATGGCTATTAAATTTGAAGTTAATAAATGGTATCAATTTAAAAATAAACAAGCTCAAGAA  60
             ||||||||||||||||||||||||||||||||||||||||||||||||||||||||||||
Ancest   1   ATGGCTATTAAATTTGAAGTTAATAAATGGTATCAATTTAAAAATAAACAAGCTCAAGAA  60

                    1)Sub:T
Mutant  61   AATTTTATTAAAGACCATACTGATAACGGAATCTATGCACGACGTTTAGGTATGGAGCCT  120
             ||||||||||||||||||||||||||||||||||||||||||||||||||||||||||||
Ancest  61   AATTTTATTAAAGACCATACTGATAACGGAATCTATGCACGACGTTTAGGTATGGAGCCT  120

                         2)5aa-del
Mutant 121   TTTAAAATTTTAGATGCTGATTATCTTGGGCGTCCTACTAAAATTATGACATCCATAGGT  180
             ||||||||||||||||||||||||||||||||||||||||||||||||||||||||||||
Ancest 121   TTTAAAATTTTAGATGCTGATTATCTTGGGCGTCCTACTAAAATTATGACATCCATAGGT  180

Mutant 181   GTACTCAAACGTTGTGCCGGCGGTGATATCCTTGACGAAAACTTTATCTGGCTCTCTACT  240
             ||||||||||||||||||||||||||||||||||||||||||||||||||||||||||||
Ancest 181   GTACTCAAACGTTGTGCCGGCGGTGATATCCTTGACGAAAACTTTATCTGGCTCTCTACT  240

                   3)Sub:A                                          7aa-del
Mutant 241   AACGAAGCTGGGTTCTTTGATGAAGTGGAAAATCCATATCAGGCGGTTG----------  289
             ||||||||||||||||||||||||||||||||||||||||||||||||||
Ancest 241   AACGAAGCTGGGTTCTTTGATGAAGTGGAAAATCCATATCAGGCGGTTGAAGAGCAAGAG  300

Mutant 290   ----------AAGAGCAAGAACAAATAGAAGATTTCACAGAATTCCCAGTCATGAAAGTT  339
                       ||||||||||||||||||||||||||||||||||||||||||||||||||||
Ancest 301   CAGGAAGAGAAAGAGCAAGAACAAATAGAAGATTTCACAGAATTCCCAGTCATGAAAGTT  360
      4)Sub:T (early STOP codon: UAG)

Mutant 340   ACTATTGAAAATAATGATCAGGCGTGGTCTTTATATCAGATGTTGAAAGCTTACTTTAAG  399
             ||||||||||||||||||||||||||||||||||||||||||||||||||||||||||||
Ancest 361   ACTATTGAAAATAATGATCAGGCGTGGTCTTTATATCAGATGTTGAAAGCTTACTTTAAG  420

Mutant 400   GAATAA  405
             ||||||
Ancest 421   GAATAA  426
```

B. GoF protein sequence:

```
Mutant 1    MAIKFEVNKWYQFKNKQAQENFIKDHTDNGIYARRLGMEPFKILDADYLGRPTKIMTSIG  60
            ||||||||||||||||||||||||||||||||||||||||||||||||||||||||||||
Ancest 1    MAIKFEVNKWYQFKNKQAQENFIKDHTDNGIYARRLGMEPFKILDADYLGRPTKIMTSIG  60

Mutant 61   VLKRCAGGDILDENFIWLSTNEAGFFDEVENPYQAVE-------EQEQIEDFTEFPVMKV  113
            ||||||||||||||||||||||||||||||||||||       ||||||||||||||||
Ancest 61   VLKRCAGGDILDENFIWLSTNEAGFFDEVENPYQAVEEQEQEEKEQEQIEDFTEFPVMKV  120

Mutant 114  TIENNDQAWSLYQMLKAYFKE  134
            |||||||||||||||||||||
Ancest 121  TIENNDQAWSLYQMLKAYFKE  141
```

Fig.4 Deletion mutation in *goF* nucleotide and protein sequence. A) Nucleotide sequence of complete (ancestral; Ancest) *goF* gene from the National Centre for Biotechnology Information (NCBI) aligned with Sanger-sequenced *goF* mutant (Mutant). The alignment shows the position of the in-frame 21bp-deletion (Δ21bp) in yellow. Other previously characterised mutations are shown in blue, numbered and labelled in bold (24). B) The corresponding translated protein sequence of the ancestral *goF* gene aligned with the mutant *goF* protein sequence, demonstrating the seven amino acids eliminated by the in-frame Δ21bp in yellow. The green zones represent the acidic region with predicted homology to RNA-binding proteins and RNA helicases (25).

At their peak frequencies in the fourth transfer, both D246N Hoc and Δ21bp *goF* Hoc mutations achieved 83.3% and 72% of the population, which was subsequently followed by a decrease to 18.3% and 16.9%, respectively. Despite this, their rise to high frequencies during the initial four transfers implies a strong selective advantage for these mutations within the gut-on-a-chip (Fig.5A, gut-on-a-chip replicate 1). Unlike replicate 1, we did not observe significant evolutionary events in gut-on-a-chip replicates 2 and 3. Here, mutations were transient and chiefly involved hypothetical genes and intergenic regions except *gp37* long tail fibre subunit in replicate 2 and *t*

holin lysis mediator in replicate 3. Collectively, the varied mutational profiles between the replicate gut-on-a-chip phage populations further reflects on the stochastic nature of phage-bacterial populations within the tripartite system.

By contrast, phages evolving in test-tubes largely possessed mutations in coding regions that were directly involved with bacterial infection. This was anticipated since bacteria were the only other biological entity alongside phages in test-tube settings. In particular, mutations in *gp37* – encoding the phage long-tail fibre distal subunit responsible for phage adsorption onto bacterial hosts – were found across all test-tube replicate populations. However, these *gp37* mutations were observed transiently and at low-frequency in all test-tube replicate populations (Fig.5A, test-tube replicates; Annex 2). We also observed other mutations affecting phage baseplate-associated genes (*gp6* and *gp9*), whose gene products facilitate phage genome injection into the bacterial host during infection. We note that these baseplate mutations were only present in test-tube replicate 3, and only one mutation affecting *gp9* which resulted in a synonymous SNP at residue 141, persisted throughout transfers 1 to 5 (Fig.5A, test-tube replicate 3). Despite the disparate *de novo* mutation profiles between gut-on-a-chip and test-tube populations, we did not observe significant differences in total number of *de novo* mutations across the five transfers between the gut-on-a-chip (6.3 $\pm$ 0.9 mutations) and test-tube phage populations (7.0 $\pm$ 2.1 mutations) (Fig.5B; Annex 2; unpaired two-tailed t-test: t = 0.2561, d.f. = 4, N = 3 [three experimental replicates], P = 0.8105).

Given the relatively low level of mutational events observed across the five transfers, we investigated if our phage transfer size at 10^4 PFU could impose a potential

bottleneck which may limit phage evolution in the gut-on-a-chip. To that, we extended our gut-on-a-chip experimental evolution to a total of 10 phage transfers, where 50% of the phage population, irrespective of the population size recovered from the mucus layer, was transferred from transfers 6 (inclusive) – 10 (Fig.5C). Intriguingly, the ∆21bp *goF* mutation in gut-on-a-chip replicate 1 was not detected after the seventh transfer but the D246N mutation persisted albeit at a low frequency of 5.3%. Meanwhile, two of the three mutations arising from evolved phages in replicate 2 after transfer 6, occurred within intergenic regions while the remaining mutation was a non-synonymous SNP detected in the *rnh* gene encoding for phage ribonuclease H, responsible for degrading RNA primers during DNA replication (26). Lastly, evolved phages from replicate 3 exhibited mutations within a short AT-rich region of the *gp7* gene at transfer 10, corresponding to the C-terminus region of the baseplate wedge initiator protein. However, given the AT-rich repeats in this region, these mutations could be re-classified as unresolvable alignment artefacts upon closer inspection of sequencing reads. Overall, there is no significant difference in the total number of *de novo* mutations before and after increasing the transfer size (Fig.5D; Annex 2).

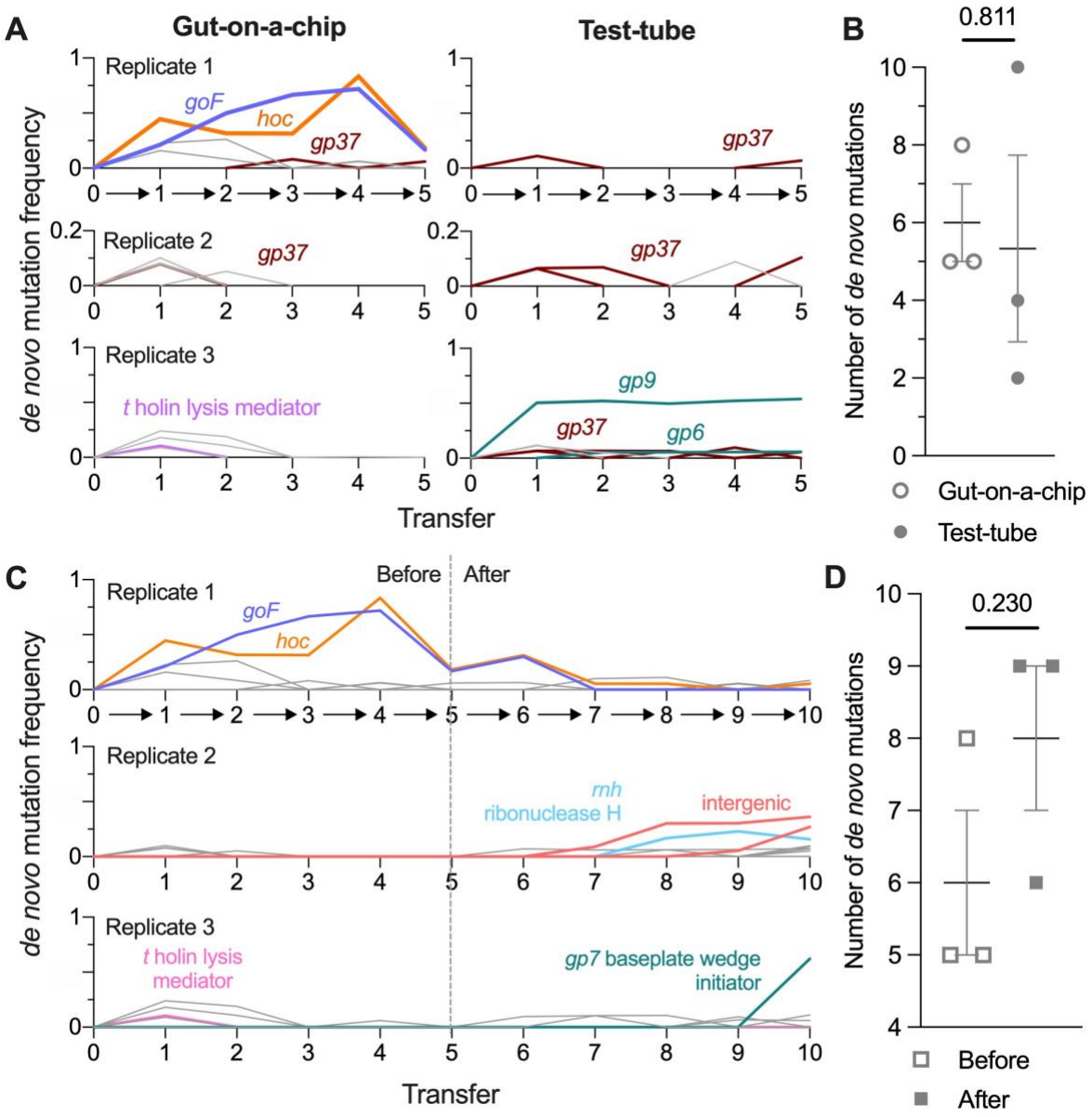

Fig.5 Phages evolve in response to the mammalian mucus layer in the gut-on-a-chip. A) Frequency of *de novo* mutations emerging from the phage population over five transfers from the gut-on-a-chip and test-tube set-ups. Coloured line represents the mutations: D246N *hoc* mutation in orange, Δ21bp *goF* mutation in purple, *gp37* (distal subunit phage long tail fibre) in brown, *t* holin lysis mediator in pink, and *gp6* and *gp9* (phage baseplate subunits) in teal. Grey lines represent other transient and low-frequency *de novo* mutations (see Annex 2). The arrows along the x-axis represent the experimental evolution phage transfer in-line with panel A. B) Average number of *de novo* mutations from phage populations evolved in

gut-on-a-chip and test-tube conditions. C) Frequency of *de novo* mutations from phage populations in the gut-on-a-chip before (transfers 1 – 5) and after (transfers 6 – 10) increasing phage transfer size. Vertical dotted line at transfer 5 indicate the point at which phage transfer regime was altered from 10^4 phages to 50% of the total population recovered from previous transfer. Coloured line represents the mutations: D246N *hoc* mutation in orange, ∆21bp *goF* mutation in purple, intergenic mutations in red, *rnh* mutation in blue, *t* holin lysis mediator in pink and *gp7* mutations in teal. D) Average number of *de novo* mutations before and after increasing phage transfer size. Data points in panels B and D were mutational counts from independent experimental replicates as specified in Annex 2, with lines and error bars plotted as mean ± SEM across three experimental replicates (N = 3). P-value was derived from an unpaired two-tailed t-test from three experimental replicates (N = 3).

2.3. High multiplicity-of-infection is a driver for phage recombination.

In asexual populations, such as phages, genetic recombination is key to enhancing fitness by alleviating clonal interference and genetic hitch-hiking (27, 28). For lytic phages like T4, recombination occurs when multiple phage genotypes co-infect the same bacterial host, allowing for allelic exchange between the phage genomes (29). Since co-infections drive recombination, higher multiplicity-of-infections (MOIs) typically render higher recombination rates (29). Crucially, high MOIs were sustained in our gut-on-a-chip devices, where elevated phage-to-bacteria ratios were observed (Figs.2C and 3B). In our first gut-on-a-chip replicate, we saw the D246N Hoc and Δ21bp *goF* mutations emerged from the first transfer and progressed with independent frequencies until the third transfer. Hereafter, both mutations followed an intertwined frequency trajectory, increasing beyond 50% of the population in the fourth transfer (Fig.5A, gut-on-a-chip replicate 1). Their intertwined trajectories surpassing 50% frequencies indicate that the mutations had recombined onto a shared genetic background to overcome clonal interference. We sought to verify whether high phage-to-bacteria ratios – and thus, high MOI – were drivers for recombination in lytic phage populations. To this end, we first isolated and amplified the D246N Hoc::Δ21bp *goF* double mutant phage (herein shorthandedly referred to as the D246N::Δ*goF* phage) from a plaque derived from transfer 4 of our experimental evolution. Next, we initiated one-step phage growth experiments at high and low MOIs (i.e. 10 and 0.1 respectively) with a 1:1 mix of two phage mutants: i) experimentally-derived D246N::Δ*goF* phage and ii) lab-stock *hoc* deletion mutant (Δ*hoc*) with a wildtype *goF* gene (Fig.6A). We also performed one-step growth curves of the two phage mutants in isolation to confirm that there were no significant differences in latent phase and burst size between the phages (Fig.6B). Using these two independent gene-deletion phage

mutants i.e. the ∆21bp *goF* (gene position: 5842 – 6267) and the ∆*hoc* (gene position: 110187 – 111317), allowed for PCR screening of recombinant phages. By limiting the phages to a single growth step, we limit phage recombination within a single replicative cycle. Following PCR screening of individual plaques, we found that 44% of phage progeny were recombinants at high MOI conditions, with a bias towards wildtype recombinants (43/98 phages screened were recombinants; 31/43 of wildtype recombinants; Figs.6C and 6D; unpaired two-tailed t-test, t = 19.59. d.f. = 194, n = 98 [plaques screened], P < 0.0001). Meanwhile, only 1 wildtype recombinant phage was detected from 98 isolates screened from low MOI conditions, i.e. ~1% recombinant frequency (Figs.6C and 6D). Collectively, this demonstrates that a high phage-to-bacteria ratio facilitates genetic recombination in lytic phages. Furthermore, the rapid emergence of recombinants within a single phage replication cycle suggests that recombination is a key driving force for phage evolution; particularly within the context of sustained high phage-to-bacteria ratios as seen in the gut-on-a-chip devices. This in turn alleviates clonal interference and potentially promotes the selection of beneficial mutations.

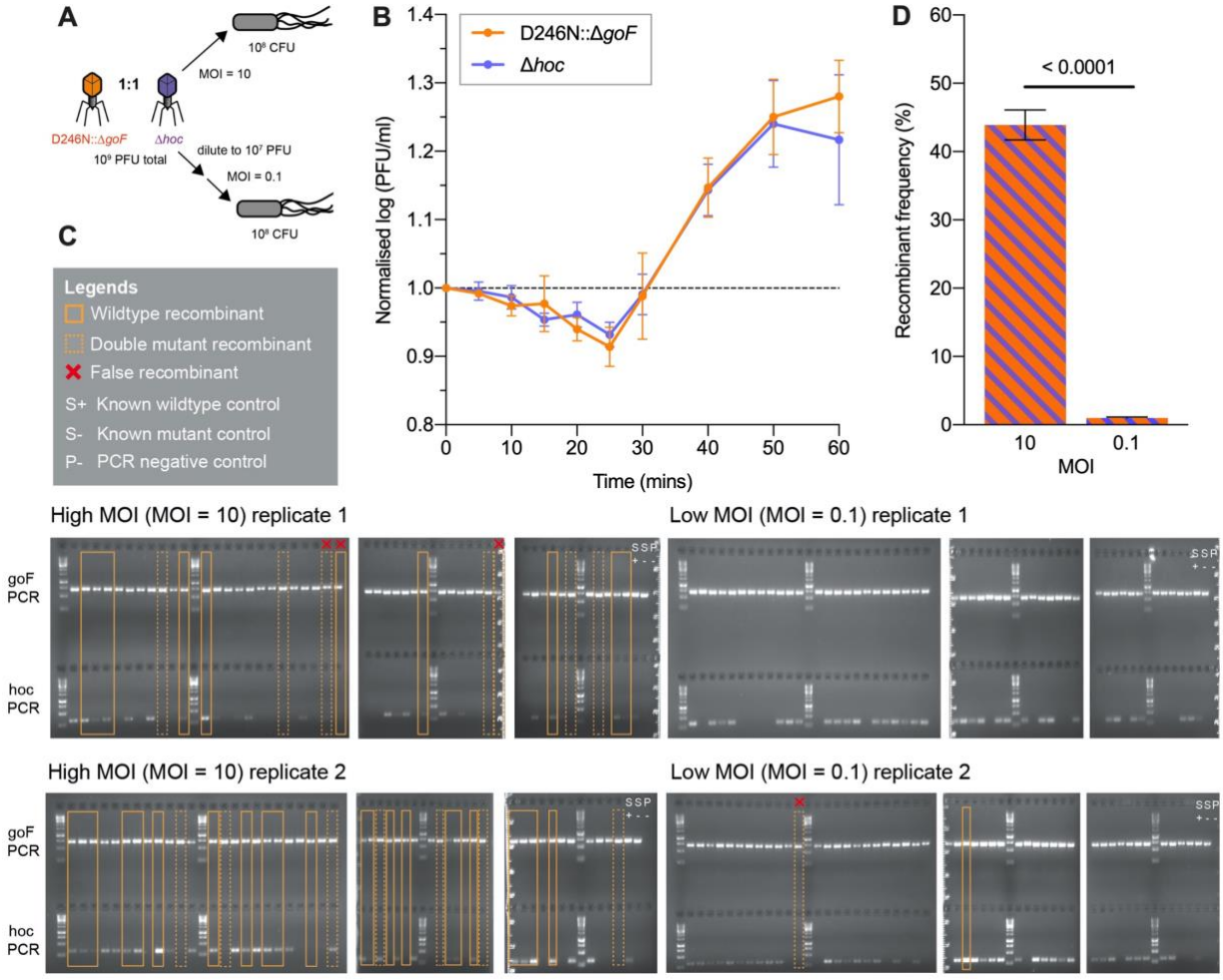

Fig.6 Mucus layer supports phage recombination. A) Gut-on-a-chip-evolved D246N::Δ*goF* phage mutant was mixed at a 1:1 ratio with lab-derived Δ*hoc* mutant. Naïve *E. coli* were infected with the 1:1 phage mixture at MOIs 10 and 0.1 following a one-step growth protocol to ensure that only a single round of viral replication could occur. B) Independent one-step growth curves of D246N::Δ*goF* and Δ*hoc* phages. PFU/ml values were log-transformed and normalised to the initial timepoint (t = 0) i.e. plotted values represent the log-change relative to phage density at t = 0. The dashed line at 1.0 represents the expected value in the absence of change from the initial phage density. Datapoints and error bars were plotted as mean ± SEM of three independent biological replicates (N = 3) for each phage genotype tested. C) PCR gels of phage recombinant screenings from recombination experiment at high and low multiplicities-of-infections (MOIs 10 and 0.1), with two independent replicates per MOI

condition. A total of 49 phage isolates were screened per condition per replicate alongside three controls: i) known wildtype sample control (S+), known mutant control (S-), and sample negative PCR control (P-) to assess for contamination. PCR for *goF* on the top row of the gels discriminates between wildtype (ancestral) and the mutant phage genotypes by observing for band shifts corresponding to the ∆21bp *goF* mutation. PCR for *hoc* on the bottom row of the gels discriminates between wildtype and ∆*hoc* phage genotypes for the presence or absence of PCR product, respectively. Solid rectangles indicate wildtype recombinants, possessing both wildtype alleles of the *goF* and *hoc* gene, while dashed rectangles indicate double mutant recombinants, possessing both ∆21bp *goF* and ∆*hoc* mutations. All recombinants were verified via a separate PCR and false recombinants were labelled accordingly (i.e. red crosses) and were discounted from the total recombinant count. We note that the false recombinants were largely arising from ambiguous amplified products in the initial PCR screen. D) Percentage frequency of phage recombinants from PCR screening for ∆21bp *goF*-∆*hoc* or wildtype-reconstituted recombinants plotted as a bar chart. As per panel C, 49 phage isolates (n = 49) were screened per experimental replicate. There were two experimental replicates (N = 2) leading to a total of 98 phage isolates (n = 98) screened per experimental condition (MOI 10 or 0.1). P-values in panel D were derived from unpaired two-tailed t-test between treatment conditions (MOI 10 and 0.1).

2.4. Phage mutant outcompetes ancestor phage in the gut-on-a-chip.

To assess the fitness of the evolved D246N::Δ*goF* phage, we competed the evolved phage against its ancestral counterpart in the gut-on-a-chip mucus environment. Competition between the D246N::Δ*goF* phage and ancestral phage was initiated by inoculating both phages at a 1:1 ratio into ten gut-on-a-chip replicate devices seeded with naïve bacterial host. The device was maintained at 120 µl/hr flow rate under same conditions as previously described, with the effluent collected for 1 hour after 24 hours of competition. The sampled effluent was subsequently whole-genome sequenced to track the D246N Hoc and Δ21bp-*goF* mutation frequencies over 24 hours of competition (Fig.7A). We verified that our devices were accurately seeded with roughly equal proportions of mutant and wildtype phages as reflected by ~44% frequency of both the D246N Hoc and Δ21bp *goF* mutations at the initial experimental timepoint (t = 0) (Fig.7B). We observed the D246N::Δ*goF* phage out-competed the wildtype phage in three out of ten replicate devices, eventually fixing in one of the replicate populations. Meanwhile, six replicates showed no change from the initial frequency whereas the one remaining replicate showed a decline of the mutant phage to 35% (Fig.7B). To ascertain the strength of selection, we quantified the selection coefficients (*s*) across the replicate populations with coefficients being either positive ($s > 0$), neutral ($s = 0$) or negative ($s < 0$) (Fig.7A, Table 1). On average, we found a positive selection coefficient with $s = 0.6$ for both D246N Hoc and Δ21bp *goF*, although significance from null selection i.e. $s = 0$, was not attained due to significant variability between experimental replicates (Fig.7C; unpaired two tailed t-test of each mutation against $s = 0$, $t_{D246N\ Hoc} = 1.216$, $t_{\Delta 21bp\ goF} = 1.149$, d.f. $_{D246N\ Hoc} = 18$, d.f. $_{\Delta 21bp\ goF} = 18$, $P_{D246N\ Hoc} = 0.2398$, $P_{\Delta 21bp\ goF} = 0.2657$; Table 1). In summary, the D246N and Δ*goF* mutations confer a mild fitness benefit to the phage within the mucosal environment.

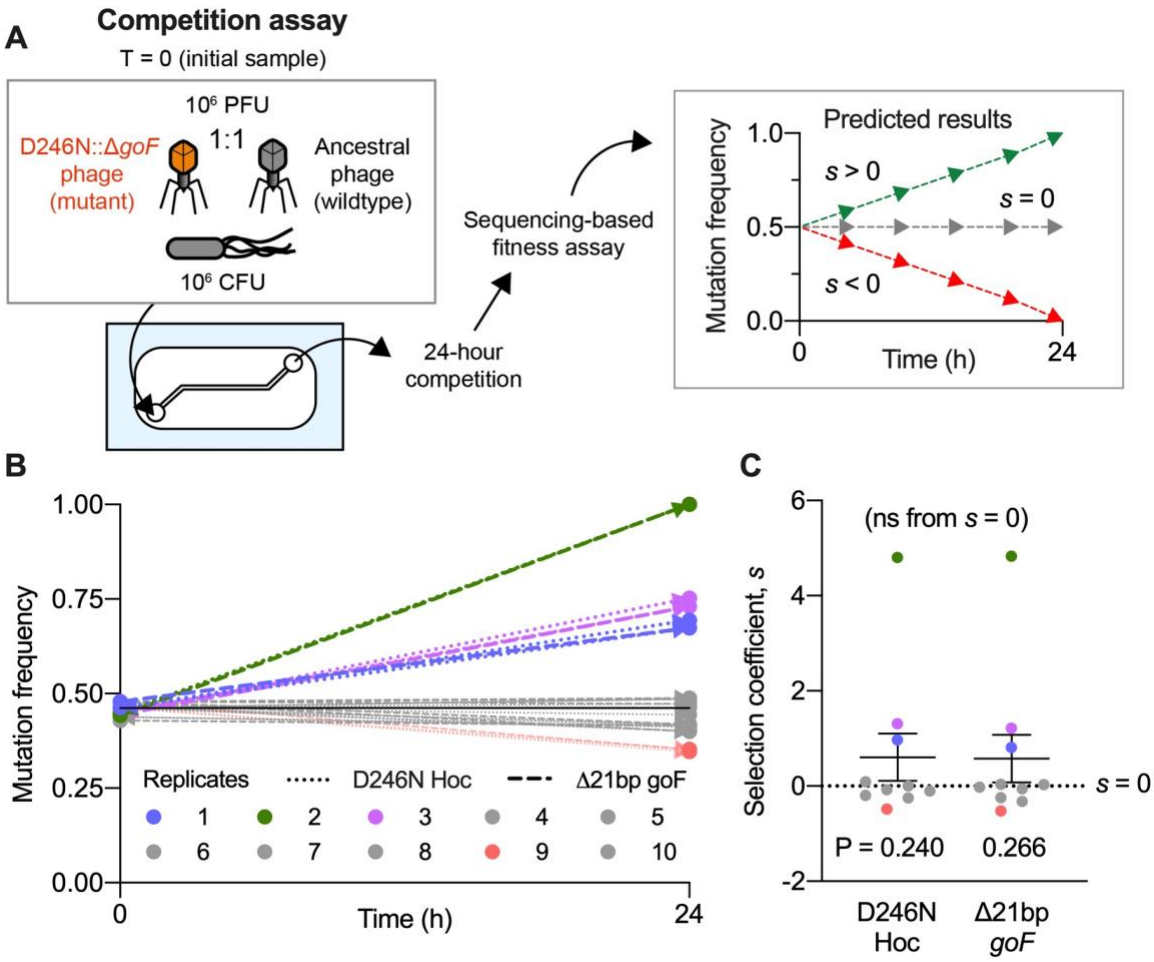

Fig.7 Mucus layer selects for beneficial D246N::Δ*goF* mutant. A) Competition experiment between D246N::Δ*goF* phage mutant with ancestral phage T4 in the gut-on-a-chip. Gut-on-a-chip seeded with naïve *E. coli* was inoculated with equal proportions of the respective phage genotypes. Chip effluents collected for 1 hour at 24 hours of competition and the samples were subjected to whole-genome sequencing to track D246N Hoc and Δ21bp *goF* mutations after 24 hours of competition. Estimated selection coefficients could be positive ($s > 0$), neutral ($s = 0$) or negative ($s < 0$). D) D246N Hoc and Δ21bp *goF* mutational frequencies measured from ten independent gut-on-a-chip replicates (N = 10) between the initial inoculum i.e. T = 0 and 24 hours. B) D246N Hoc and Δ21bp *goF* mutational frequencies measured from three independent gut-on-a-chip replicates (N = 3) between the initial inoculum i.e. T = 0 and 24 hours. D246N Hoc and Δ21bp *goF* mutational frequencies measured from ten independent

gut-on-a-chip replicates (N = 10) between the initial inoculum i.e. T = 0 and 24 hours. E) Plot of estimated mean selection coefficient for D246N Hoc and ∆21bp *goF* mutation across ten experimental replicates (N = 10). Black solid line in panel D represents the initial (T = 0) average frequency of D246N Hoc mutation at 45.8% and ∆21bp *goF* mutation at 46.7%, across ten experimental replicates (N = 10). Line with error bars represent mean ± SEM across ten (N = 10) experimental replicates. P-values in were derived from unpaired two-tailed t-test between coefficients of D246N Hoc and ∆21bp *goF* mutations against *s* = 0 (no selection), respectively.

Table 1: Calculation of selection coefficient for Fig.7C

	Percentage (%) reads			**Absolute reads** = % reads × sequence coverage		
Genotype	Replicate	T = 0	T = 24 hrs	Replicate	T = 0	T = 24 hrs
D246N Hoc (mutant)	1	43.8	41.2	1	3324	2849
	2	44.8	99.0	2	3607	8520
	3	45.0	75.2	3	3786	6117
	4	46.3	46.4	4	5402.701	5303.706
	5	46.3	69.4	5	5402.701	7624.006
	6	46.3	40.2	6	5402.701	4919.797
	7	46.3	44.4	7	5402.701	5865.906
	8	46.3	48.6	8	5402.701	6209.914
	9	46.3	34.7	9	5402.701	5544.054
	10	46.3	41.5	10	5402.701	6225.042
∆21bp *goF* (mutant)	1	42.9	41.5	1	3255	2870
	2	44.2	99.0	2	3558	8520
	3	44.4	73.0	3	3735	5938
	4	47.9	47.3	4	5589.403	5406.579
	5	47.9	67.4	5	5589.403	7404.294
	6	47.9	40	6	5589.403	4895.32
	7	47.9	48.6	7	5589.403	6420.789
	8	47.9	48.8	8	5589.403	6235.469
	9	47.9	35.3	9	5589.403	5639.916
	10	47.9	41.9	10	5589.403	6285.042
Wildtype *hoc*	1	56.2	58.8	1	4265	4066
	2	55.2	1.0	2	4444	86

	3	55.0	24.8	3	4267	2017
	4	53.7	53.6	4	6266.199	6126.694
	5	53.7	30.6	5	6266.199	3361.594
	6	53.7	59.8	6	6266.199	7318.503
	7	53.7	55.6	7	6266.199	7345.594
	8	53.7	51.4	8	6266.199	6567.686
	9	53.7	65.3	9	6266.199	10433.05
	10	53.7	58.5	10	6266.199	8775.059
Wildtype *goF*	1	57.1	58.5	1	4333	4046
	2	55.8	1.0	2	4492	86
	3	55.6	27.0	3	4678	2196
	4	52.1	52.7	4	6079.497	6023.821
	5	52.1	32.6	5	6079.497	3581.306
	6	52.1	60	6	6079.497	7342.98
	7	52.1	51.4	7	6079.497	6790.711
	8	52.1	51.2	8	6079.497	6542.131
	9	52.1	64.7	9	6079.497	10337.18
	10	52.1	58.1	10	6079.497	8715.058

Sequencing coverage

Selection coefficient, *s*
$$= ln\left(\frac{Mutant\ genotype_{T=24}/WT\ genotype_{T=24}}{Mutant\ genotype_{T=0}/WT\ genotype_{T=0}}\right)$$

Genes	Replicate	T = 0	T = 24 hrs	Genotype	Replicate	*s*	**Mean *s***
hoc	1	7588.3	6915.6	D246N Hoc (mutant)	1	-0.106	**0.607**
	2	8050.9	8606.3		2	4.804	
	3	8413.2	8133.8		3	1.310	
	4	11669	11430.4		4	0.004	
	5	11669	10985.6		5	0.967	
	6	11669	12238.3		6	-0.249	
	7	11669	13211.5		7	-0.077	
	8	11669	12777.6		8	0.092	
	9	11669	15977.1		9	-0.484	
	10	11669	15000.1		10	-0.195	
goF	1	7588.3	6915.6	Δ21bp *goF* (mutant)	1	-0.057	**0.575**
	2	8050.9	8606.3		2	4.828	
	3	8413.2	8133.8		3	1.220	
	4	11669	11430.4		4	-0.024	
	5	11669	10985.6		5	0.810	

6	11669	12238.3		6	-0.321
7	11669	13211.5		7	0.028
8	11669	12777.6		8	0.036
9	11669	15977.1		9	-0.522
10	11669	15000.1		10	-0.243

2.5. Hoc mutation alters phage mucus-adherence phenotype.

Phage adherence to mucus has been described as a mechanism that facilitates phage enrichment and persistence within the mammalian mucosal layers (11). For T4 phage, this adherence phenotype is facilitated by the outer capsid protein Hoc, which has three externally-displayed immunoglobulin (Ig)-like domains and a highly-conserved fourth C-terminal capsid-binding domain (30, 31). The D246N Hoc mutation removes an acidic residue (aspartic acid) and replaces it with a neutral residue (asparagine). This mutation is located within the third Ig-like domain, potentially altering Hoc binding affinity to mucin glycans (Fig.8A). To test for altered glycan adherence, we fluorescently labelled whole phage particles of wildtype Hoc, D246N::Δ*goF* , and Δ*hoc* genotypes, and assayed for glycan binding on a microarray printed with 153 unique glycan structures (Annex 3). Binding was measured as fold-changes relative to the array background signal and verified for P-value significance. Overall, we were able to observe binding of whole phages across seven glycan families. D246N::Δ*goF* phages generally exhibited altered glycan-binding compared to wildtype phage while, Δ*hoc* phages had lower overall fold-change intensities relative to wildtype and D246N::Δ*goF* phages (Fig.8B, whole phages). This highlights that the majority of binding events were Hoc-mediated. Between the D246N::Δ*goF* and wildtype phage, the D246N mutation chiefly impacted Hoc-binding to glycans terminating with fucose, galactose and N-acetylglucosamine (GlcNac) motifs; all of which are common motifs added to core glycosylation structures found in mucin along the gastrointestinal tract (32).

To further investigate the specificity of Hoc-glycan interactions, we recombinantly-expressed wildtype and D246N Hoc proteins (Figs.8C and 8D) and tested the proteins

on the glycan array. We showed that the Hoc protein-glycan binding largely matched whole phage binding results (Fig.8B, recombinant Hoc protein). Next, surface plasmon resonance (SPR) was adopted to quantify the binding strength between glycans and surface-immobilised Hoc proteins. We focused on a subset of 26 glycans that were amenable for SPR measurements taken in solution under flow (see Annex 3 for full glycan array analysis). The SPR data demonstrated that both wildtype and D246N Hoc-glycan binding was specific for interactions with the same subset of fucosylated glycans (Fig.8B, Hoc-glycan SPR). Furthermore, the D246N Hoc protein had higher dissociation values (K_D), indicating weaker binding to a number of fucosylated glycans than the wildtype Hoc (Figs.8B, Hoc-glycan SPR and Annex 4). Fucosylated mucin glycans are ubiquitous along the human gastrointestinal tract in individuals possessing a functional copy of the α-1,2-fucosyltransferase (*FUT2*) gene (known as “secretors”) (33). Our gut-on-a-chip HT29-MTX-E12 cell line possesses *FUT2* and is capable of producing a fucosylated mucus layer in-line with the “secretor” phenotype (34).

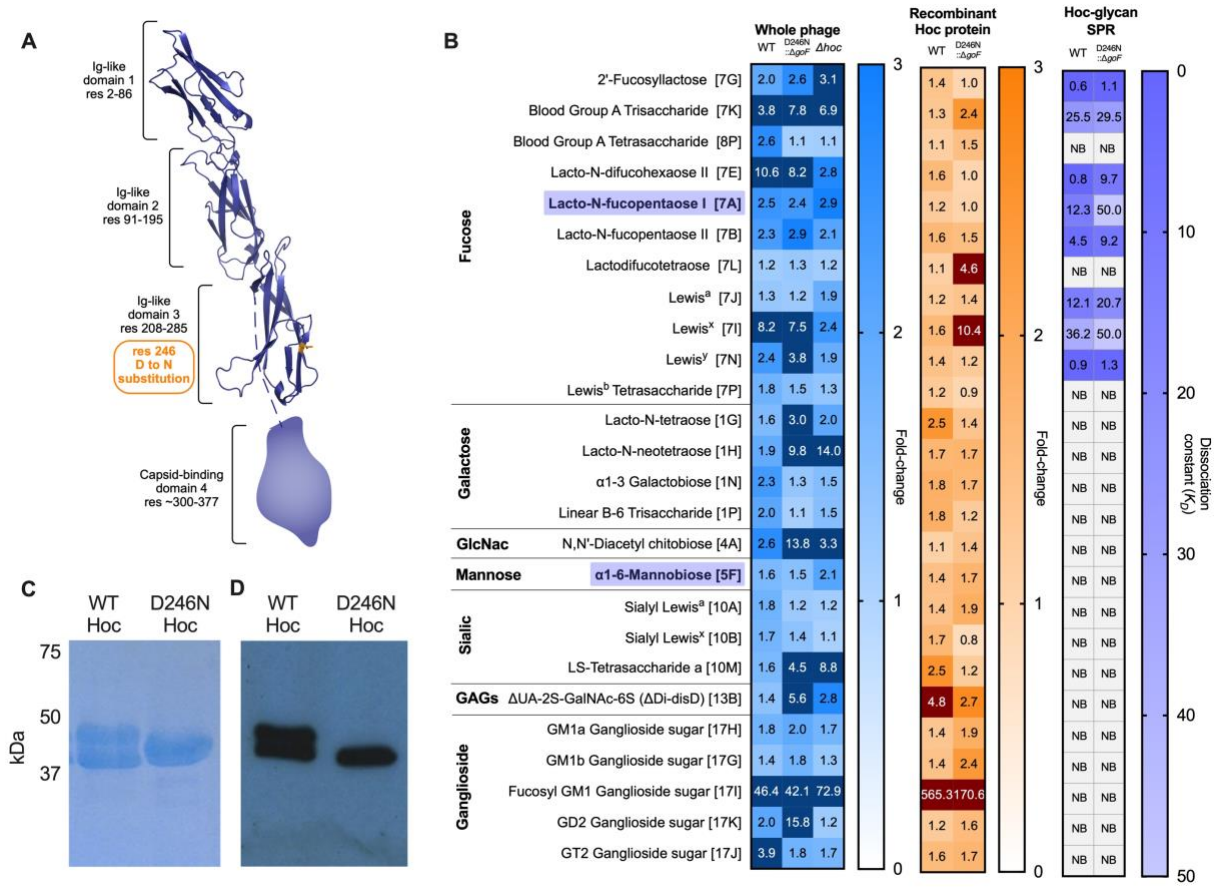

Fig.8 D246N Hoc mutation reduces binding affinity to fucosylated glycans. A) T4 Hoc protein structure model demonstrating the position of D246N mutation within the third Ig-like domain, highlighted in orange. The capsid-binding fourth domain was not modelled due to the lack of structural homologues in Protein Data Bank (PDB). B) Normalised fold-change fluorescence intensities of 26 top glycan array hits (glycan ID corresponding to Annex 3 as indicated in square brackets) of labelled, ultrapurified whole phages: wildtype [WT], D246N::Δ*goF* phage and Δ*hoc* – blue heatmap; and recombinantly expressed Hoc proteins: WT and D246N – orange heatmap; followed by SPR assessing glycan-to-Hoc protein binding strength – purple heatmap. Numerical values in glycan array heatmaps represent fold-change magnitude normalised against background fluorescence where dark-colour panels indicate high fold-change values that were out-of-bounds from heatmap gradient. Numerical values in SPR heatmap represent dissociation constant (K_D) values where higher K_D values indicate lower binding affinity. “NB” in SPR heatmap indicates no binding event. Bolded and purple-

highlighted glycans 7A (Lacto-N-fucopentaose I) and 5F (α-1,6-mannobiose) represent the glycans selected for phage retention and washout experiments in Fig.9A. C) Coomassie stained SDS-PAGE of purified His-WT Hoc and His-D246N Hoc. WT Hoc purified as a doublet. D) Subsequent probing of Western transfer with anti-His antibodies (R&D Systems) shows that both the full-length and partially degraded WT Hoc are His-tagged, implying C-terminal degradation of the protein. The D246N Hoc mutant has also undergone truncation from the C-terminus to produce a stable N-terminally His-tagged Hoc protein of the same size as the WT degradation product. These events did not impact upon the three N-terminal Ig-like domains, with the loss of approximately 5kDa from the C-terminus of the fourth domain (the capsid binding domain).

With this knowledge, we proceeded to validate the glycan-binding phenotype of D246N::Δ*goF* phage within the gut-on-a-chip mucosal environment. We tested this by competing the D246N::Δ*goF* phage against the wildtype Hoc phage in a phage retention and washout assay within the gut-on-a-chip, under the presence of either a fucosylated (Lacto-N-fucopentaose I [7A]) or non-fucosylated (α-1,6-mannobiose [5F]) glycan (Fig.9A). Importantly, the fucosylated glycan chosen (Lacto-N-fucopentaose I [7A]) showed a ~4-fold reduction in dissociation values (K_D) between the wildtype and D246N::Δ*goF* phages, while the non-fucosylated glycan showed no interaction with either phages (Fig.8B). We initiated the experiment by infusing three replicate devices, each with a 1:1 ratio of wildtype Hoc and D246N::Δ*goF* phages suspended in either fucosylated or non-fucosylated glycan solutions (Fig.9B), followed by washout of the phages from the devices using the same glycan solutions. We posit that the wildtype Hoc phage, possessing higher affinity to dissolved fucosylated glycans, will be competitively sequestered from the mucus layer during the initial infusion, while

D246N::Δ*goF* phage, with its lower affinity to fucosylated glycans, will be selectively retained in the mucus. Consequently, during the washout we expect higher recovery of D246N::Δ*goF* phage for extended periods over the wildtype Hoc phage. To determine the fraction of D246N::Δ*goF* phage recovered from the total phage infused, we utilised a wildtype Hoc phage possessing amber mutations on genes *43* and *44* (herein known as T4 am*43*$^{-}$/*44*$^{-}$) that was permissive only on *E. coli* strain SupE, while the D246N::Δ*goF* phage was permissive on both *E. coli* strains B and SupE. Our results showed that in the presence of the fucosylated glycan Lacto-N-fucopentaose I [7A], the D246N::Δ*goF* phage was consistently recovered at higher levels in the first two hours of washout and remained detectable up to four hours, whereas the wildtype Hoc phage was eliminated by four hours (Figs.9C and 9E). Conversely, in the control setting with non-fucosylated glycan α-1,6-mannobiose [5F], fewer D246N::Δ*goF* phage were recovered compared to wildtype Hoc phages in the first one and a half hours, followed by recovery at approximately equal proportions up to four hours of washout (Figs.9D and 9E). Collectively, this indicates that more D246N::Δ*goF* phage were retained and recovered from devices perfused with fucosylated glycan over non-fucosylated glycan, as predicted from our SPR results (Fig.8B). In summary, we demonstrate that the T4 phage outer capsid protein Hoc binds specifically to fucosylated glycans and exhibited changes in glycan-binding affinity through mutation in the protein's Ig-like binding domain. On a broader perspective, our results revealed the capacity of phages to mutate phage display proteins in order to adapt to the tripartite conditions imparted by the gut-on-a-chip mucosal environment.

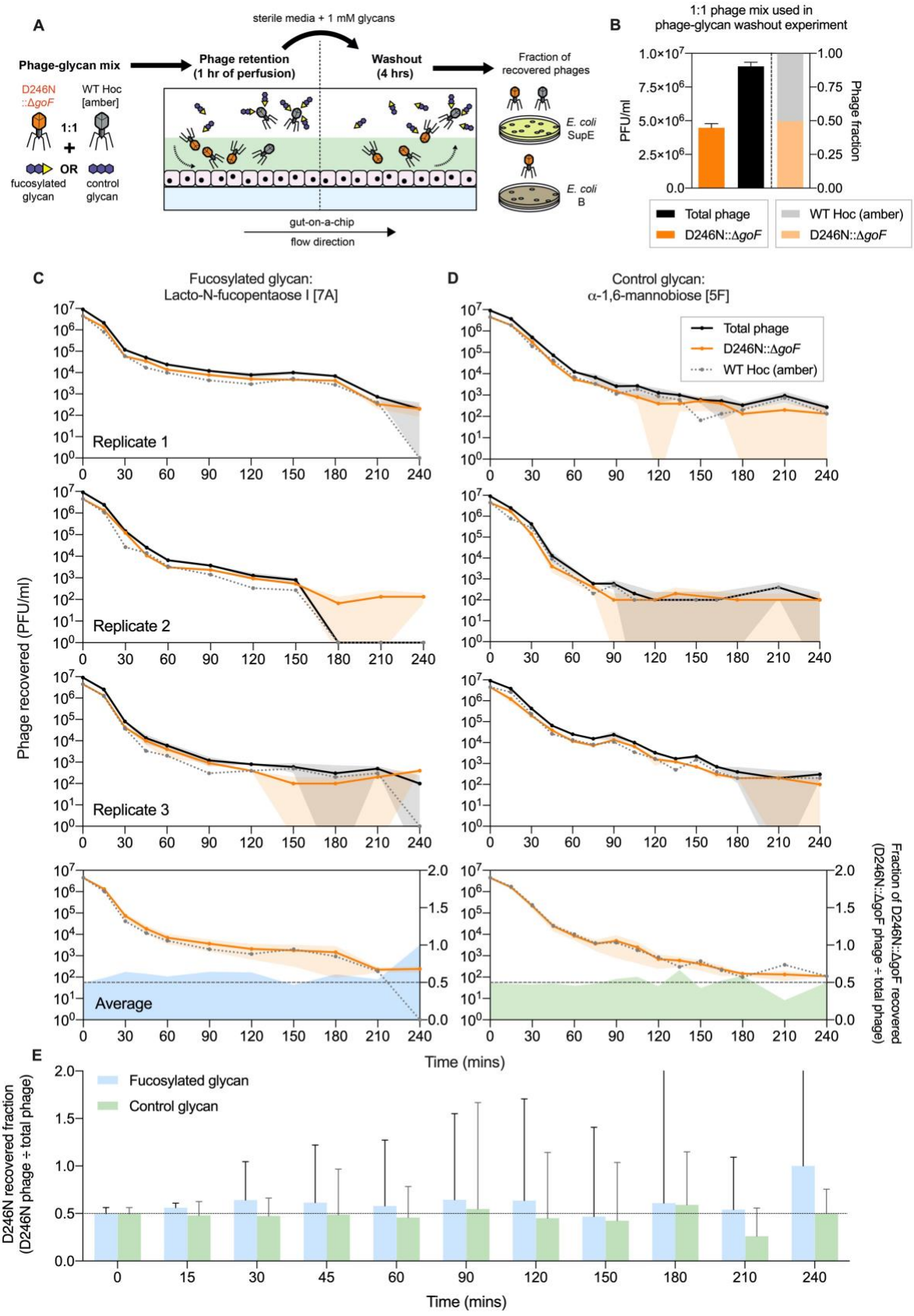
A
sterile media + 1 mM glycans
Phage-glycan mix
Phage retention (1 hr of perfusion)
Washout (4 hrs)
Fraction of recovered phages
D246N ::ΔgoF
WT Hoc [amber]
1:1
OR
fucosylated glycan
control glycan
E. coli SupE
E. coli B
gut-on-a-chip
flow direction
B
1:1 phage mix used in phage-glycan washout experiment
PFU/ml
Phage fraction
Total phage
D246N::ΔgoF
WT Hoc (amber)
C
Fucosylated glycan: Lacto-N-fucopentaose I [7A]
D
Control glycan: α-1,6-mannobiose [5F]
Replicate 1
Replicate 2
Replicate 3
Average
Phage recovered (PFU/ml)
Fraction of D246N::ΔgoF recovered (D246N::ΔgoF phage ÷ total phage)
Time (mins)
E
Fucosylated glycan
Control glycan
D246N recovered fraction (D246N phage ÷ total phage)
Time (mins)

Fig.9 Phage evolved in mammalian mucus layer exhibit altered mucus adherence phenotype. A) Experimental set-up for phage retention and washout from the gut-on-a-chip, where equal proportions of WT Hoc (with *am43⁻/44⁻* mutation) and D246N::Δ*goF* phages in 1 mM glycan solutions were perfused in the gut-on-a-chip for an hour during the retention phase. Subsequently, sterile media supplemented with 1 mM glycan, was perfused for 4 hours to initiate phage washout from the mucus layer. Washouts were collected at set time intervals and phages were quantified via selective plating on *E. coli* SupE (permissive for both WT Hoc [*am43⁻/44⁻*] and D246N::Δ*goF* phage) and *E. coli* B (only permissive for D246N::Δ*goF* phage). B) Phage stock titre and 1:1 fraction of D246N::Δ*goF* phage and wildtype (WT) Hoc with amber *43⁻/44⁻* mutation phage used to inoculate the gut-on-a-chip replicates for competitive phage-glycan washout. Bar chart in is plotted as mean ± SEM of three biological replicates (N = 3). C) Washout of wildtype Hoc and D246N::Δ*goF* phages from the gut-on-a-chip under flow with 1 mM of fucosylated glycan 7A (Lacto-N-fucopentaose I) or D) control glycan 5F (α-1,6-mannobiose) over 4 hours. Line graphs of total phage (black) and D246N::Δ*goF* phage (orange) with shaded regions are plotted along the left y-axis as mean ± SEM of three technical replicates (n = 3) for each biological replicate i.e. “Replicates 1, 2 and 3”; while the graph labelled “Average” is plotted as mean ± SEM of the aforementioned biological replicates (N = 3). The grey dotted line represents the expected number of WT Hoc phage recovered by subtracting D246N::Δ*goF* phage from the total phage number recovered. Total phage plot was not included in the “Average” graph to highlight quantitative difference between D246N::Δ*goF* and WT Hoc phage. Shaded regions extending along the x-axis and right y-axis of the “Average” plot, represent the D246N::Δ*goF* phage fraction over the total phage number recovered (D246N::Δ*goF* phage ÷ total phage recovered) from the gut-on-a-chip across time. The dotted line at 0.5 represents the expected fraction if D246N::Δ*goF* phage and the WT Hoc (amber *43⁻/44⁻* mutant) phages were recovered in equal proportions. E) Comparison on the D246N::Δ*goF* phage fraction recovered from the gut-on-a-chip at each sampled timepoint between the fucosylated and control glycan conditions. The bar chart is plotted as mean ±

SEM of three biological replicates per timepoint (N = 3). The dotted line at 0.5 represents the expected fraction if D246N::Δ*goF* phage and the WT Hoc (amber *43⁻/44⁻* mutant) phages were recovered in equal proportions.

3. Discussion

Phages are largely considered inert with respect to the mammalian “host” and chiefly respond to antagonistic selection from their immediate replicative bacterial hosts. However, the mammalian milieu – in this case, the gut mucosa – is also a complex environment that can impose additional selection pressures such as mucus turnover dynamics and glycosylation that act on both bacterial and viral entities (33, 35, 36). Under these mucosal selection pressures, phage variants arising from propagation on resident bacterial populations that display competitive advantage will be retained and further propagated. Our gut-on-a-chip system recapitulates these selection pressures and hence favours phage phenotypes that persist within the mucosal layer. Here, we adopt the model phage T4 which has previously been demonstrated to adhere to mucus (11). By experimentally evolving the phage within the gut-on-a-chip mucosa inoculated with bacterial hosts, we revealed the capacity of the phage to evolve its mucus-binding domains within a tripartite setting, resulting in enhanced persistence within the mucosal environment.

Phage-bacteria population dynamics were unique between independent gut-on-a-chip populations (Figs.2C and 3B). Similarly, disparity was also observed in mutations emerging from independently evolving phage populations in the gut-on-chip (Fig.3A). This led us to speculate that stochastic ecological effects arising from demographic noise and mucosal spatial complexity (37), could be key factors in determining mucosal selection within independent gut environments. On a broader perspective, these observations may partly reflect on the interpersonal variations seen in gut viral community dynamics (5, 38), although more nuanced empirical approaches are warranted to test these speculations. Despite the ecological variation and mutational

disparity between gut-on-a-chip phage populations, we acquired a genetically-recombined phage mutant exhibiting altered affinity towards fucosylated glycans (Fig.8B) via a mutation in the phage Hoc mucus-adhering domain (Fig.8A).

We demonstrated that the acquired phage Hoc mutant conferred a fitness advantage within the mucus layer by altering phage Hoc affinity to mucin glycans, specifically by decreasing affinity to fucosylated glycan structures (Figs.7C and 8B). While diminished phage glycan-binding may appear counterintuitive as a fitness advantage for persistence in the mucosal environment, we note that: i) the exact glycosylation profile and glycan abundance of the gut-on-a-chip mucus layer were unknown and that, ii) our SPR screen was limited to a small subset of fucosylated glycans. Nonetheless, we were able to show that the Hoc mutation lent a detectable phenotypic response within the mucosal environment when titrated against fucosylated and non-fucosylated glycans (Figs.9C – 9E). Collectively, these provided empirical support for the capacity of phages to adapt to mucin glycosylation, which subsequently enhanced phage persistence and propagation within the gut-on-a-chip mucosal environment.

Mucin fucosylation is widespread along the gastrointestinal tract of functional *FUT2* human genotypes (known as “secretors”), especially within the proximal and distal colon (36). This suggests that the human host genotype and glycosylation demography directly influences gut phage biogeography at the inter- and intra-individual level, respectively. Moreover, the majority of the gut phageome possesses open reading frames for variable glycan-binding superfamily domains (39, 40). The model T4 phage adopted in this study is one of such phages with glycan-binding domains and is also a natural component of the human gut phageome in both healthy

and diseased states (41–43). While not all phages possess capsid display Ig-like domains, these domains are found within approximately a quarter of sequenced *Caudovirales* phages to-date (18). However, since most gut phages remain unannotated despite recent sequencing and genome assembly efforts (44, 45), there exists an immense abundance, diversity and prevalence of phage structural domains that could play similar roles in associating with the mammalian entity such as, proteoglycan-binding domains (15), C-type lectin folds (39, 46), and the Ig-folds of *Bacteroides*-associated carbohydrate-binding often N-terminal (BACON) domains (47). This suggests that gut phages have immense adaptive freedom to respond and co-evolve with an individual's unique mucosal glycosylation patterns to foster persistence (11).

Given the potential diversity of gut phages with capsid display proteins – which can accommodate large sequence variations – coupled with the individuality of the mammalian gut, the evolutionary potential between phages and their mammalian environment remains largely untapped. Our study represents an initial foray into this evolutionary potential between phages and their mammalian "host". We posit that the mammalian gut has a significant role in selecting successful phage variants that emerge and persist in the gut, which will then propagate and potentially recombine to promote the fixation of beneficial mutations within the population. This subsequently dictates the phage populations that will reside and further engage in evolution with both the individual's gut microbiome and gut environment. In a broader view, this tripartite evolutionary interplay might lend stable, long-term and highly personalised viromes and microbiomes, often recapitulated in human metagenomic cohort studies (5, 44). To this, we also envisage future directions towards human host-centric

intelligent phage design in synergy with host-directed phage evolution for highly personalised medicine and refined *in vivo* phage applications.

4. Methods and materials

4.1. Culture protocol for bacteria, phage and tissue culture cell lines.

Escherichia coli strain B was used for all experiments and was grown in LB medium (10 g Tryptone, 10 g NaCl, 5 g yeast extract in 1 L of sterile dH_2O) at 37°C with agitation. T4 phage, which uses *E. coli* strain B as a replicative host, was used for all experiments except T4 replication-negative *43*$^-$ (DNA polymerase) and *44*$^-$ (polymerase clamp holder subunit) i.e. T4 *am43*$^-$*/44*$^-$ phage, that only uses amber-permissive host *E. coli* SupE to replicate. The cell line used was a human colon-derived tumorigenic goblet cell, HT29-MTX-E12, obtained from the European Collection of Authenticated Cell Cultures and cultured at 37°C with 5% CO_2 in complete media: DMEM with 10% FBS, 1× MEM non-essential amino acids and 1× penicillin-streptomycin antibiotics (ThermoFisher Scientific). Terminal cellular differentiation was induced with 10 µM N-[N-(3,5-Difluorophenacetyl)-L-alanyl]-S-phenylglycine t-butyl ester (DAPT; Sigma-Aldrich) while mucus-secretion was enhanced with 10 nM phorbol 12-myristate 13-acetate (PMA; Sigma-Aldrich).

4.2. Fabricating the gut-on-a-chip mould and device.

A chip mould with 500 µm wide and 350 µm high channel was designed using SolidWorks® 2017 (Dassault Systèmes). The moulds were then 3D-printed and surface-salinized at Melbourne Centre for Nanofabrication (MCN), Victoria. The chips were manufactured by casting a 10:1 mixture of Sylgard™ PDMS and its curing agent respectively (Dowsil, USA), onto the moulds and were cured at 90°C until completely solidified. The chips were then removed, trimmed and their inlet and outlet ports were punched. Subsequently, the chips were washed in pentane and acetone to remove residual uncured PDMS followed by plasma bonding the chip onto a glass slide to

enclose the chip channel. The chip channel was ethanol (80%v/v)-sterilised, UV-sterilised and pre-treated with 1:50 MaxGel^{TM} ECM (Sigma-Aldrich). The channel was then seeded with 10 µl of HT29-MTX-E12 cells at 3.0×10^5 cells. The seeded chip was incubated statically for 16 hours to allow cell attachment. This was followed by perfusing the attached cells with complete media for 24 hours at 40 µl/hr flow rate to establish a confluent cell layer. The cell layer was then perfused with antibiotic-free media supplemented with cell-inducers DAPT and PMA, for another 24 hours at 120 µl/hr to purge residual antibiotic-containing media from the channel environment and to promote terminal cellular differentiation and mucus secretion by the cell layer. Perfusion was mediated by a 10-channel syringe pump (KD Scientific, USA) with the gut-on-a-chip maintained within an incubator at 37°C with 5% CO_2 to ensure optimal conditions for cell culture growth and maintenance in the channel.

4.3. Scanning electron microscopy (SEM) of the gut-on-a-chip mucosal epithelium.

The HT29-MTX-E12 mucosal epithelium (cultivated as described previously) in the gut-on-a-chip was fixed with fresh methanol Carnoy solution [60% (v/v) absolute methanol, 30% chloroform and 10% glacial acetic acid] at 4°C for 3 hours. The PDMS encasing of the gut-on-a-chip was carefully trimmed and removed using a sharp scalpel to expose the fixed mucosal epithelium. The exposed epithelium was then immersed in 70% (v/v) ethanol for 30 minutes followed by further dehydration with graded ethanol at 85%, 95%, 100% and 100% for 20 minutes each. Residual ethanol was then evaporated with a critical point dryer and the sample was mounted on a standard SEM metal stub, followed by sample coating with a ~10 nm gold layer. The mucosal epithelium was imaged using a FEG-SEM ThermoFisher Elstar G4

(ThermoFisher) operating at an accelerating voltage of 2 kV using secondary electrons at a working distance of 4 mm in immersion mode via the through lens detector (TLD).

4.4. High temporal resolution gut-on-a-chip phage-bacteria sampling.

An in-house automated dispensing platform was constructed to aid sample collection from the gut-on-a-chip over 24 hours at 30-minute intervals. The platform consisted of conveyer belts connected to 5V motors powered by an Arduino circuit board (Arduino, Italy). Two conveyer belt systems were aligned perpendicular to each other allowing motion along the X-Y plane. A custom-made tube holder was connected to the conveyer belt system that holds the gut-on-a-chip tube over the 96-well plate to facilitate sample dispensing into wells. Time-steps for dispensing at 30-minute intervals were coded into Arduino in C++ using Arduino Integrated Development Environment (IDE). For a user-friendly interface, the code was translated onto a virtual switch board executable program using LabVIEW v.2020 (National Instruments, USA). The temporal experiment is initiated by perfusing the gut-on-a-chip with 10^4 colony forming units (CFU) of *E. coli* B followed by 10^4 PFU of T4 phages and the device was allowed to run for 24 hours under a 120 µl/hr flow rate whilst connected to the automated dispensing platform to collect egressing fluid samples. In between the gut-on-a-chip and the dispensing platform, the egressing fluid was channelled through an 80°C-heated blank chip to arrest phage and bacterial replication during their egress from the gut-on-a-chip before dispensing. Phages and bacteria from the heat-inactivated samples were quantified using qPCR using SYBR Green I Master with the Lightcycler® 480 (Roche). qPCR primers and cycling protocols for *E. coli* B were as described (48) using 1 µl of template. T4 protocols was adapted from (49) using forward primer: 5'- AGGAGTTATATCAACTGTAA - 3', and reverse primer: 5'-

ATCTAGGATTCTGTACTGTT - 3', with the following cycling protocol: initial denaturation at 95°C for 5 minutes; 40 cycles at 95°C for 30 seconds, 56°C for 30 seconds, 72°C for 30 seconds; using 1 µl of template. Standard curves (Table 2) for phages were generated via 10-fold dilution in PCR-grade H_2O of a T4 phage stock at concentration 7×10^9 PFU/ml; hence, standardising the curve based on PFU/ml.

Table 2: T4 phage qPCR standard curve

Primary phage stock concentration: 7×10^9 PFU/ml
Dilution: 10-dilution series

Gut-on-a-chip replicate 1

Phage concentration (PFU/ml)	Log (Phage concentration)	Average quantification cycle (C_T)
7×10^8	8.85	16.3
7×10^7	7.85	20.0
7×10^6	6.85	23.8
7×10^5	5.85	27.3
7×10^4	4.85	31.2

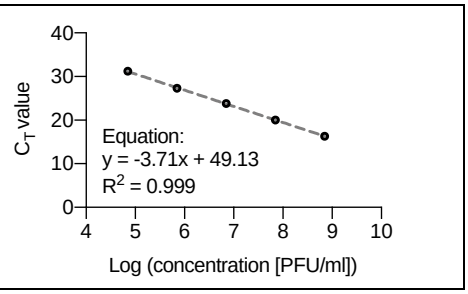

Gut-on-a-chip replicate 2

Phage concentration (PFU/ml)	Log (Phage concentration)	Average quantification cycle (C_T)
7×10^8	8.85	16.6
7×10^7	7.85	20.1
7×10^6	6.85	24.0
7×10^5	5.85	27.7
7×10^4	4.85	31.3

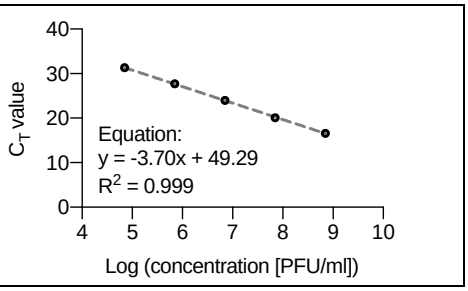

Gut-on-a-chip replicate 3

Phage concentration (PFU/ml)	Log (Phage concentration)	Average quantification cycle (C_T)
7×10^8	8.85	16.6
7×10^7	7.85	20.0
7×10^6	6.85	23.8
7×10^5	5.85	27.7
7×10^4	4.85	31.3

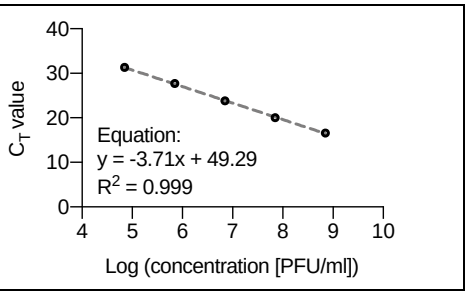

Standard curve for bacteria was similarly diluted in 10-fold using genomic DNA extracted via GenElute Bacterial Genomic DNA kit following manufacturer's protocol (Sigma-Aldrich), from a known concentration of bacterial culture at 7×10^7 CFU/ml

(Table 3). Each chip replicate generates 48 unique timepoint heat-inactivated samples from sampling at 30-minute intervals over 24 hours. qPCR for each timepoint was carried in three technical replicate (n = 3) lending 144 qPCR sample reactions (48 × 3) per experimental replicate. There are three experimental replicates in total (N = 3). Due to the small sample volume, 1 µl of sample was directly used without prior DNA extraction to avoid sample loss and inaccuracy.

Table 3: *E. coli* B qPCR standard curve

Bacterial concentration (prior to DNA extraction): 7×10^7 CFU/ml
Dilution: 10-dilution series

Gut-on-a-chip replicate 1

Bacterial concentration (CFU/ml)	Log (Phage concentration)	Average quantification cycle (C_T)
7×10^7	7.85	16.9
7×10^6	6.85	21.9
7×10^5	5.85	28.1
7×10^4	4.85	32.1
7×10^3	3.85	35.0

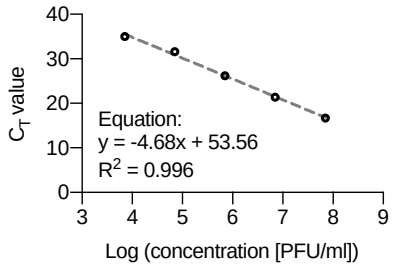

Gut-on-a-chip replicate 2

Bacterial concentration (CFU/ml)	Log (Phage concentration)	Average quantification cycle (C_T)
7×10^7	7.85	16.7
7×10^6	6.85	21.4
7×10^5	5.85	26.2
7×10^4	4.85	31.6
7×10^3	3.85	35.0

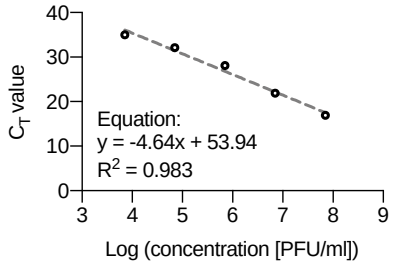

Gut-on-a-chip replicate 3

Bacterial concentration (CFU/ml)	Log (Phage concentration)	Average quantification cycle (C_T)
7×10^7	7.85	15.9
7×10^6	6.85	21.3
7×10^5	5.85	25.5
7×10^4	4.85	30.4
7×10^3	3.85	35.0

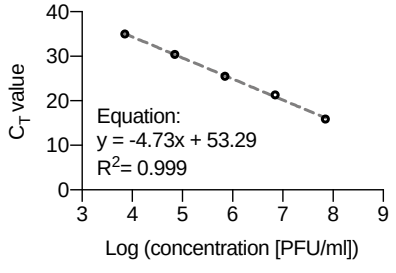

4.5. Phage experimental evolution in gut-on-a-chip.

10^4 PFU of T4 phages were perfused through the gut-on-a-chip followed by 10^4 CFU of *E. coli* B to supply the phages with hosts to replicate within the chip. The co-culture in each chip was maintained under a 120 µl/hr flow rate with antibiotic-free media for 24 hours under 37°C with 5% CO_2 conditions. Subsequently, the mucus and the cell layer were collected via washes with 1 × DPBS and 0.25% Trypsin (ThermoFisher Scientific). The chip sample was centrifuged to obtain the bacterial cell pellet, which was resuspended in 100 µl 1 × DPBS. The supernatant containing the phages was treated with 10% chloroform to obtain a purified phage lysate. Phages and bacteria were enumerated using soft-agar overlay assay and colony spot assay, respectively. For our phage passage protocol, 10^4 phage PFU were taken from the purified phage (supernatant) lysate to inoculate a new gut-on-a-chip with 10^4 ancestral *E. coli* B CFU. We adopted this passage protocol for a total of 5 passages. In our control experimental evolution, a shaking test-tube was used in place of the gut-on-a-chip within the flow set-up. The passage protocol in the control experiment was the same as the passages of the gut-on-a-chip phage experimental evolution.

4.6. Phage DNA isolation, purification, sequencing and analyses.

To obtain sufficient DNA yield for sequencing, phages from all transfers including the ancestral phage population were amplified to high titres ($\geq 10^9$/ml). The phages were amplified by inoculating 30 µl of phage lysate sample into 3 ml of *E. coli* B bacteria in exponential phase (OD_{600} = 0.3). The inoculum was incubated for a maximum of 4 hours at 37°C with agitation to maximise the probability of all phage genotypes in expanding without interference from host-induced bottlenecks at late stage

incubations. This was followed by 10% chloroform treatment to purify the amplified phage lysate. Phages were concentrated and ultrapurified following the phage-on-tap protocol (50). 1 ml of each ultrapurified phage passage lysate was treated with 10 µl Ambion^{TM} DNase I (ThermoFisher Scientific) and 20 µl RNase (Sigma-Aldrich) to eliminate bacterial genome contamination. Subsequently, the lysates underwent phage DNA extraction using Phage DNA Isolation Kit (Norgen Biotek®, Canada) as per manufacturer protocol with the following modification to maximise DNA yield: 10 µl of 20 mg/ml Proteinase K (Sigma-Aldrich) per 1 ml of amplified phage lysate and incubated at 55°C for 1.5 hours. Phage DNA quality and concentrations were assessed via Nanodrop $A_{260/280}$ (ThermoFisher Scientific) readout and QuBit® Fluorometric Quantification High Sensitivity assay (ThermoFisher Scientific), respectively. Phage DNA samples were sequenced using Illumina HiSeq® 150bp paired-end chemistry (GeneWiz®, Hong Kong) and read alignments to T4 reference genome (23) (NCBI GenBank ID: MT984581.1) were performed via the Breseq (51) Polymorphism Mixed Population pipeline with filter settings turned off to maximise variant calling. *De novo* mutation hits were derived by comparing evolved phage population hits with ancestral background mutations using Breseq's -gdtools SUBTRACT and COMPARE commands. *De novo* mutations were assessed and manually counted to compare *de novo* mutation frequencies between gut-on-a-chip and test-tube experimentally evolved phage populations as described in Annex 2.

Data and code availability. Paired-end raw sequence reads from phage experimental evolution populations (1 ancestor and 30 evolved populations: 15 gut-on-a-chip populations and 15 test-tube populations) were deposited in the National Center for Biotechnology Information-Sequence Read Archive (NCBI-

SRA) under the accession SRA: PRJNA737295. Sample command line instruction for sequence alignment and mutational calling using Breseq is provided as follows:

```
#Breseq script for HPC cluster job submission

#!/bin/bash
#SBATCH --job-name=Mutational_calling_analysis
#SBATCH --mail-type=all
#SBATCH --mail-user=wai.chin@monash.edu
#SBATCH --cpus-per-task=10

echo "This script is running on:"
hostname

#add date and time for record
date_time=$(date +%F_%T | tr -d ':,-')

#load Breseq external dependencies (bowtie2 and R)
module load bowtie2/2.3.5 R/3.5.1 breseq/0.33.2

#run script
#replicate = j #passage = i
for j in 1 2 3
do
for i in 0 1 2 3 4 5
        do echo ANALYSING "$i"_L3_1.fq.gz "$i"_L3_2.fq.gz
        breseq -j 8 -p --polymorphism-reject-indel-homopolymer-length 0 -
-polymorphism-reject-surrounding-homopolymer-length   0   --polymorphism-
bias-cutoff 0 \
      -o R1_T"$i" -r T4_sequence.gbk "$i"_L3_1.fq "$i"_L3_2.fq
done
done

#Normalising data
for j in 1 2 3
do
for i in 1 2 3 4 5 6 7 8 9 10
do
gdtools NORMALIZE -o T"$i"GC"$j".gd -r T4_sequence.gb T"$i"GC"$j"_rerun.gd
done
done

#Subtract from ancestor T0
for j in 1 2 3
do
for i in 1 2 3 4 5 6 7 8 9 10
do
gdtools SUBTRACT -o T"$i"GC"$j"_subtracted.gd T"$i"GC"$j".gd T0.gd
done
done

#Comparing de novo mutations across trasnfers
for i in 1 2 3
```

```
do
gdtools     COMPARE     -o     GC"$i"_vsT0.html     -r     T4_sequence.gb
T*GC"$i"_subtracted.gd
done
```

4.7. Lytic phage recombination assay.

T4 Δ21bp *goF* mutant was isolated from transfer 4 chip-evolved replicate 1 population by isolating phage plaques from soft-agar overlay. The phage isolates were PCR-screened and Sanger-sequenced with the flanking *goF* primers i.e. forward: 5' – GCATTAATCAGCATCAGTAC -3' and reverse: 5' – AAGACGGCACAACTTACTGG – 3', with the following PCR protocol: initial denaturation at 95°C for 10 minutes; 34 cycles at 95°C for 10 seconds, 57°C for 15 seconds, 72°C for 60 seconds; and final elongation at 72°C for 5 minutes. T4 *hoc* knockout (Δ*hoc*) phage was also PCR-amplified and sequence-confirmed using the flanking *hoc* primers i.e. forward: 5' – GCTGAAACTCCTGATTGGAAATCTCACCC – 3' and reverse: 5' – GCCCATAATACAGCCACTTCTTTTGCC – 3', with the following PCR protocol: initial denaturation at 95°C for 10 minutes; 34 cycles at 95°C for 30 seconds, 60°C for 60 seconds, 72°C for 90 seconds; and final elongation at 72°C for 10 minutes. The verified phages were amplified and chloroform-purified to high titre ($\geq 10^9$ PFU/ml), respectively. The phages were diluted in SM buffer (5.8 g NaCl, 2.0 g $MgSO_4.7H_2O$, 50 ml 1 M Tris-HCl pH 7.4 in 1 L ddH_2O) to obtain a 1:1 phage mix containing Δ21bp *goF* and Δ*hoc* at 1×10^9 PFU/ml. 1 ml of the mixture was reserved as an initial condition control to test for 1:1 mix accuracy. The remaining mixture was used to prepare four experimental set-ups: two replicates of MOI = 10 and two replicates at MOI = 0.1. In MOI 10, 1 ml of the 1×10^9 PFU/ml mixture was added to 1 ml of 1×10^8 CFU/ml *E. coli* B; while in MOI 0.1, the phage mixture was diluted to 1×10^7 PFU/ml

before adding to 1×10^8 CFU/ml *E. coli* B. The co-cultures were then incubated at 37°C with 150 rpm agitation for 30 minutes to allow a one-step T4 phage growth curve. The co-cultures were subsequently quenched with 10% chloroform. The phages in co-culture and the reserved initial condition phage mix were plated via soft-agar overlay. Single plaque cores were obtained from well-separated plaques, resuspended in 100 µl SM buffer, and PCR screened for recombinants (double mutant: ∆21bp *goF* + ∆*hoc* or WT recombinant T4 genotypes) using flanking *goF* primers and internal *hoc* primers. Internal *hoc* PCR primers were, forward: 5' - ACATTATCTACGCTCCAAGC – 3' and reverse: 5' - ATCTAGGATTCTGTACTGTT - 3', with the following protocol: 95°C for 10 minutes; 34 cycles at 95°C for 10 seconds, 56°C for 15 seconds, 72°C for 60 seconds; and final elongation at 72°C for 5 minutes. All PCR products were loaded on 2% agarose gel, stained with SYBR™ Gold Nucleic Acid Gel Stain (ThermoFisher Scientific), for 30 minutes at 60V and subsequently, 30 minutes at 50V to allow better separation between the WT and ∆21bp *goF* product. Both *goF* and *hoc* PCR products were matched to their sample of origin in the agarose gel run. The frequency of recombinants was quantified based on the *goF* PCR product size and the presence and absence of *hoc* PCR product.

4.8. Sequencing-based phage competition assay.

Wildtype T4 phage and experimentally evolved D246N T4 mutant phage were isolated via plaque coring as previously described. The cores were resuspended in 100 µl of SM buffer and samples were PCR-amplified with flanking *hoc* primers i.e. forward: 5' – GCCCATAATACAGCCACTTCTTTTGCC – 3' and reverse: 5' – GCTGAAACTCCTGATTGGAAATCTCACCC – 3', with the following protocol: initial denaturation at 95°C for 10 minutes; 30 cycles at 95°C for 30 seconds, 60°C for 60

seconds, 72°C for 90 seconds; and final elongation at 72°C for 10 minutes. The verified phages were amplified and chloroform-purified to high titre ($\geq 10^9$ PFU/ml), respectively. The amplified phages were diluted in antibiotic-free tissue culture media to obtain a 1:1 phage mix containing WT and D246N phages at 2×10^6 PFU (1×10^6 PFU each). 1×10^6 PFU of the phage mix was reserved as an initial condition i.e. T = 0 control. Three gut-on-a-chip replicates were each infused with 10^6 CFU *E. coli* B bacteria followed by 1×10^6 PFU phage mix at 120 µl/hr flow rate. The inoculated devices were maintained at 120 µl/hr for 24 hours and egressing fluid samples were collected for 1 hour at the 24-hour timepoint. Fluid samples were collected in 1 ml SM buffer to rapidly dilute the collected phages and bacteria to limit further phage adsorption during sample collection. Collected samples were then amplified, DNA-extracted, sequenced and analysed as previously outlined to track the frequency of D246N mutant phage as it competes with WT T4 phage over 24 hours. Selection coefficients were calculated as described in Table 1 based on absolute reads, obtained by multiplying read depth and coverage, of the mutation.

4.9. Molecular cloning of recombinant Hoc protein expression strains.

Wildtype Hoc T4 phage and D246N Hoc T4 phage genomic DNA were extracted as described above. The respective *hoc* genes were PCR-amplified using primers designed with NcoI/SpeI restriction sites i.e. forward: 5' – CCTCCATGGCGATGACTTTTACAGTTGATATAAC – 3' and reverse: 5' – TTGACTAGTTATGGATAGGTATAGATGATAC – 3', with the following protocol: initial denaturation at 98°C for 5 minutes; 36 cycles at 98°C for 30 seconds, 58°C for 30 seconds, 72°C for 120 seconds; and final elongation at 72°C for 5 minutes. The amplified *hoc* products were gel-extracted following manufacturer's protocol

(GenElute™ Gel Extraction Kit, Sigma Aldrich). Wildtype and D246N *hoc* genes were individually cloned in-frame to expression vector pPROEX-HTb, containing an N-terminal hexa-His sequence. Briefly, the amplified *hoc* product and pPROEX-HTb were digested with NcoI and SpeI (New England Biolabs) at 37°C overnight, followed by ligation at room temperature for 2 hours. The ligated expression vector was transformed into NEB 5α Competent *E. coli* as per manufacturer's protocol (New England Biolabs) and plated on LB medium supplemented with 100 µg/ml ampicillin, where colonies were PCR-screened as above mentioned. PCR-positive colonies were grown and the vector was extracted using GenElute Plasmid Miniprep Kit following manufacturer's protocol (Sigma-Aldrich). The vector was then transformed into expression strain *E. coli* BL21(DE) Star as follows. *E. coli* BL21(DE) Star was grown in LB medium to OD_{600} 0.4 at 37°C. 5 ml of culture was centrifuged at 4°C and the pellet was washed thrice with 1 ml ice-cold 10% glycerol between centrifugations. The pellet was resuspended in 50 µl of ice-cold 10% glycerol and added with 3 µl of the expression vector. The mixture was transferred into a 0.1 cm electroporation cuvette (BioRad) and pulsed at 1.8 kV. Electroporated cells were recovered in 1 ml pre-warmed LB medium for 1 hour at 37°C and subsequently plated on LB medium supplemented with 100 µg/ml ampicillin to recover Hoc expression strains.

4.10. Recombinant Hoc protein expression, purification and modelling.

Hoc expression strains were grown in Terrific Broth (with shaking) to OD_{600} 0.8 at 37°C. Expression was induced with 0.2 mM IPTG, incubation temperature dropped to 18°C and cells collected by centrifugation the following morning. Cell pellets were resuspended in 20 mM Tris pH8, 300 mM NaCl, 20 mM imidazole, 0.5 mM $MgCl_2$, 1× complete EDTA-free protease inhibitor (Roche) and lysed through an Avestin

Emulsiflex C3 cell press. Following centrifugation at 18000 ×g the soluble fraction was applied to a 5 ml HisTrap HP column (GE Healthcare). The column was washed and protein eluted along a gradient using 20 mM Tris pH8, 400 mM NaCl, 1 M imidazole. The peak fraction (eluting at ~150 mM imidazole) was pooled and further purified over size exclusion chromatography on a HiLoad 16/600 Superdex 200 pg column (GE Healthcare) equilibrated in SEC buffer (20 mM Tris pH 8.0 and 150 mM NaCl). The Hoc proteins each eluted as a single monomeric peak and were run on reducing SDS-PAGE and verified by anti-His western (R&D Systems) (Figs.8C and 8D). Proteins were concentrated to 1 mg/ml, EDTA added to 0.5 mM final and aliquots snap-frozen in liquid nitrogen. The structural model of the T4 Hoc protein was generated using Phyre2 server (52) and modelled upon the crystal structure of the three N-terminal IgG domains of phage RB49 Hoc protein (PDB ID: 3SHS). The capsid binding domain could not be accurately modelled due to a lack of solved structural homologues.

4.11. Glycan array printing.

Glycan arrays consisting of 150 diverse glycans (DextraLabs) in the absence of spacers were taken from existing glycan libraries (53–55). Glycans were amine functionalized as previously described (56) and subsequently printed as described (57). Briefly, glycosylamines were suspended in 1:1 dimethylformamide (DMF) : dimethyl sulfoxide (DMSO) at a concentration of 500 µM and printed onto SuperEpoxy3 glass slides (ArrayIt) using a SpotBot Extreme array spotter (ArrayIT) in a six-pin subarray print per glass slide format. All glycans were printed in replicates of four, including four AlexaFlour 555/647 and FITC control spots, per subarray using 946MP4 pins and a contact time of 1 second at 50% relative humidity, with pins being reloaded after every 8 spots. DMF : DMSO was also printed as blanks controls. The

printed arrays were subsequently acetylated in 25% (v/v) acetic anhydride in methanol at 4˚C for 15 min, and then neutralized in 1:1 ethanolamine : DMF. Finally, glycan arrays were washed with 100% ethanol and dried in an empty 50 mL tube by centrifugation for 5 min at 200 ×g. Glycan arrays were vacuum sealed and stored at 4°C.

4.12. T4 phage labelling and glycan array hybridization.

To label T4 phages (wildtype [WT], D246N Hoc or Δ*hoc),* stocks were diluted to 10^8 phages/mL in SM buffer and allowed to incubate with SYBR green dye (1:1000) (Molecular Probes) in the dark at 4°C for 1 hour. Excess dye was removed by three consecutive washes with 1 mL of SM buffer using an Amicon ultrafiltration tube (100 kDa). A buffer-exchange through three consecutive washes with 1 mL of array phosphate buffered saline (PBS) (50 mM PBS, 1.8 mM $MgCl_2$ and 1.8 mM $CaCl_2$, pH 7.4) was similarly performed using Amicon ultrafiltration tubes (100 kDa) (Merck). SYBR-labelled phages were prepared fresh daily and immediately applied to glycan arrays after buffer-exchange. Before hybridizations, glycan array slides were blocked in 0.5% BSA in array PBS for 5 min at room-temperature (RT). After washing with array PBS, slides were dried through centrifugation and a Gene Frame (1.7 × 2.8 cm, 125 µL, Abgene) was used to isolate the arrays prior to the addition of the labelled phage. 10^8 of either SYBR labelled WT, D246N Hoc or Δ*hoc* T4 phages were applied to individual glycan arrays as a 1 mL bubble and allowed to hybridize at RT for 1 hour in the dark. In the final 5 minutes of incubation, phages were fixed through the addition of formaldehyde into the same bubble (final concentration 4%). Following hybridization, glycans arrays were gently washed three times for 5 min in array PBS and finally dried through centrifugation.

4.13. WT and D246N Hoc protein labelling and glycan array hybridization.

Labelling of recombinant WT and D246N Hoc proteins was performed using their respective hexa-His-tags. Here, 1 µg of each protein was incubated at a molar ratio of 1:2:4 with anti-His-tag mouse monoclonal antibody (Cell Signalling Technology), anti-mouse-IgG-Alexa647 conjugated rabbit polyclonal antibody (Life Technologies) and goat conjugated anti-rabbit-IgG-Alexa647 polyclonal antibody (Life Technologies) in 1 mL Array PBS. This complex was allowed to hybridize in the dark at 4˚C for 15 min. As described previously, gene frames were used to isolate glycan arrays, and Alexa647 labelled recombinant Hoc proteins were applied as a bubble for 1 hour at RT and allowed to hybridize. Glycan arrays were subsequently washed for three times for 5 min in array PBS, and dried through centrifugation.

4.14. Fluorescent image acquisition and data processing.

Fluorescence intensities of the array spots were measured with the Innoscan 1100AL (Innopsys) scanner using either the 488 nm (SYBR) or 635 nm (A647) laser excitation wavelength depending on the sample. The Image analysis was carried out using the inbuilt imaging software, MAPIX (Innopsys). Raw glycan signals were exported into Microsoft Excel 2016. The mean background was calculated from the average of DMF/DMSO blanks on the array plus three standard deviations. This was subtracted from each glycan to generate an adjusted signal. A one tailed t-test was performed with significance set at $p = 0.05$. Binding events confirmed across 3 arrays were compiled as heatmaps representing t-test and fold increases above background.

4.15. Surface plasmon resonance detection.

Surface plasmon resonance (SPR) experiments to confirm glycan hits and elucidate differences in binding affinity between the WT and D246N Hoc proteins were performed using a Pioneer FE SPR system (Pioneer). WT and D246N Hoc proteins were loaded onto channels 1 and 2 of a HisCap biosensor (Satorious) and channel 3 was blank immobilized to enable reference subtraction in PBS. A minimum of 5000 relative units (RU) of either Hoc protein was immobilized using the nitrilotriacetic acid (NTA)-Nickel capture system modified from reference (58). Here, the hexa-His-tag allows capture of the Hoc proteins in the correct orientation and subsequent covalent crosslinking prevents protein from dissociating over the course of the SPR run. In brief, nickel was bound to the HisCap biosensor using $NiSO_4$ in running buffer. The carboxymethylated dextran (CMD) surface was then activated using N-hydroxysuccinimide (NHS)/1-ethyl-3(3-dimethylaminopropyl)-carbodiimide hydrochloride (EDC). Each protein was subsequently immobilized at flow rate of 10 µL/min for 10 min. Uncoupled amine reactive sites of the CMD were blocked through an injection of ethanolamine and finally 0.35 M EDTA was injected to remove any poorly associated protein. A maximum concentration of 100 µM of selected glycans was tested using a OneStep analysis programmed using the Pioneer instrument. OneStep was performed with 75% loop volume and a 3% sucrose control. Glycans were flowed at 40 µL/min with a dissociation time of 180s (Annex 4). Subsequent regeneration of the surface was performed with TE buffer for 60s at 50 µL/min and 60s dissociation. Blanks were run periodically every 2 cycles. Analysis of SPR sensorgrams to determine glycan dissociation constants (K_D) was performed separately with the Qdat analysis software package (Biologic Software, Campbell, Australia). All analyses were performed on two independently prepared HisCap chips with each protein loaded twice and glycans tested in duplicate per run. SPR responses

less than 5 RU were deemed insignificant and attributed to non-specific interaction of the glycan with the positively charged HisCap chip surface.

4.16. Phage retention and washout assay.

A 1:1 phage mix consisting of D246N Hoc T4 phage and a WT T4 Hoc phage (am*43*$^{-}$*/44*$^{-}$) was prepared in antibiotic-free tissue culture media at 1 mM final glycan concentration of glycans α-1,6-mannobiose (DextraLabs) or Lacto-N-fucopentaose I (DextraLabs). The 1:1 phage ratio was verified by plating on *E. coli* SupE and *E. coli* B lawns in triplicates where, the amber phage only plaques on an amber mutant permissive host, *E. coli* SupE while D246N::Δ*goF* phage plaques on both *E. coli* SupE and *E. coli* B. Hence, we were able to quantify the D246N::Δ*goF* phage (on *E. coli* B) and the amber mutant phage via subtraction (total plaques from *E. coli* SupE – total plaques from *E. coli* B). Three replicate gut-on-a-chips were infused with 1×10^7 PFU/ml of 1:1 phage-glycan mix for 1 hour at 120 µl/hr (Figs.9A and 9B). After which, the devices were perfused with sterile antibiotic-free tissue culture media supplemented with 1 mM of the appropriate glycan for 4 hours. Device effluents were collected in equal volumes of SM buffer every 15 minutes for the first hour and every 30 minutes for the subsequent hours. The phage timepoints were quantified by spot-plating the device effluents on both *E. coli* B and *E. coli* SupE lawns to assess for phage washout.

4.17. Statistical analysis

All analyses for statistical significance were performed with Prism software (GraphPad Prism 9). Unless stated otherwise, all experiments were performed with three experimental replicates (N = 3) with three repeated measures i.e. technical replicates

(n = 3). Data are plotted as mean ± SEM of experimental replicates (N) or technical replicates (n) as defined within the figure legends. Statistical details for t-tests were reported in text with the appropriate figure; this includes t values, degrees of freedom (d.f.) and P values. Significant values are designated as $P < 0.05$ and non-significant values as $P \geq 0.05$, unless stated otherwise.

References

1. A. Buckling, P. B. Rainey, Antagonistic coevolution between a bacterium and a bacteriophage. *Proc. R. Soc. B Biol. Sci.* **269**, 931–936 (2002).
2. A. R. Hall, P. D. Scanlan, A. Buckling, Bacteria-phage coevolution and the emergence of generalist pathogens. *Am. Nat.* **177**, 44–53 (2011).
3. A. Betts, O. Kaltz, M. E. Hochberg, Contrasted coevolutionary dynamics between a bacterial pathogen and its bacteriophages. *Proc. Natl. Acad. Sci. U. S. A.* **111**, 11109–11114 (2014).
4. S. Paterson, *et al.*, Antagonistic coevolution accelerates molecular evolution. *Nature* **464**, 275–278 (2010).
5. A. Reyes, *et al.*, Viruses in the faecal microbiota of monozygotic twins and their mothers. *Nature* **466**, 334–338 (2010).
6. A. Reyes, M. Wu, N. P. McNulty, F. L. Rohwer, J. I. Gordon, Gnotobiotic mouse model of phage-bacterial host dynamics in the human gut. *Proc. Natl. Acad. Sci. U. S. A.* **110**, 20236–20241 (2013).
7. L. De Sordi, V. Khanna, L. Debarbieux, The Gut Microbiota Facilitates Drifts in the Genetic Diversity and Infectivity of Bacterial Viruses. *Cell Host Microbe* **22**, 801-808.e3 (2017).
8. L. De Sordi, M. Lourenço, L. Debarbieux, “I will survive”: A tale of bacteriophage-bacteria coevolution in the gut. *Gut Microbes* **10**, 92–99 (2019).
9. M. K. Mirzaei, C. F. Maurice, Ménage à trois in the human gut: Interactions between host, bacteria and phages. *Nat. Rev. Microbiol.* **15**, 397–408 (2017).
10. F. Bäckhed, R. E. Ley, J. L. Sonnenburg, D. A. Peterson, J. I. Gordon, Host-bacterial mutualism in the human intestine. *Science (80-.).* **307**, 1915–1920 (2005).

11. J. J. Barr, *et al.*, Bacteriophage adhering to mucus provide a non-host-derived immunity. *Proc. Natl. Acad. Sci. U. S. A.* **110**, 10771–10776 (2013).
12. J. J. Barr, *et al.*, Subdiffusive motion of bacteriophage in mucosal surfaces increases the frequency of bacterial encounters. *Proc. Natl. Acad. Sci. U. S. A.* **112**, 13675–13680 (2015).
13. G. M. F. Almeida, E. Laanto, R. Ashrafi, L. R. Sundberg, Bacteriophage adherence to mucus mediates preventive protection against pathogenic bacteria. *MBio* **10**, 1–12 (2019).
14. J. Shan, *et al.*, Bacteriophages are more virulent to bacteria with human cells than they are in bacterial culture; Insights from HT-29 cells. *Sci. Rep.* **8**, 5091 (2018).
15. S. I. Green, *et al.*, Targeting of Mammalian Glycans Enhances Phage Predation in the Gastrointestinal Tract. *MBio* **12** (2021).
16. M. Lourenço, *et al.*, The Spatial Heterogeneity of the Gut Limits Predation and Fosters Coexistence of Bacteria and Bacteriophages. *Cell Host Microbe* **28**, 390-401.e5 (2020).
17. G. C. Hansson, Mucins and the Microbiome. *Annu. Rev. Biochem.* **89**, 769–793 (2020).
18. J. S. Fraser, Z. Yu, K. L. Maxwell, A. R. Davidson, Ig-Like Domains on Bacteriophages: A Tale of Promiscuity and Deceit. *J. Mol. Biol.* **359**, 496–507 (2006).
19. H. J. Kim, H. Li, J. J. Collins, D. E. Ingber, Contributions of microbiome and mechanical deformation to intestinal bacterial overgrowth and inflammation in a human gut-on-a-chip. *Proc. Natl. Acad. Sci. U. S. A.* **113**, E7–E15 (2016).
20. S. Jalili-Firoozinezhad, *et al.*, A complex human gut microbiome cultured in an

anaerobic intestine-on-a-chip. *Nat. Biomed. Eng.* **3**, 520–531 (2019).

21. T. Pelaseyed, *et al.*, The mucus and mucins of the goblet cells and enterocytes provide the first defense line of the gastrointestinal tract and interact with the immune system. *Immunol. Rev.* **260**, 8–20 (2014).
22. C. Tropini, K. A. Earle, K. C. Huang, J. L. Sonnenburg, The Gut Microbiome: Connecting Spatial Organization to Function. *Cell Host Microbe* **21**, 433–442 (2017).
23. D. Subedi, J. J. Barr, Temporal Stability and Genetic Diversity of 48-Year-Old T-Series Phages. *mSystems* **6** (2021).
24. B. Sanson, M. Uzan, “Sequence and characterization of the bacteriophage T4 comCα gene product, a possible transcription antitermination factor” (1992).
25. E. S. Miller, *et al.*, Bacteriophage T4 Genome. *Microbiol. Mol. Biol. Rev.* **67**, 86–156 (2003).
26. B. M, N. NG, Bacteriophage T4 RNase H removes both RNA primers and adjacent DNA from the 5’ end of lagging strand fragments. *J. Biol. Chem.* **276**, 28516–28524 (2001).
27. G. I. Lang, *et al.*, Pervasive genetic hitchhiking and clonal interference in forty evolving yeast populations. *Nature* **500**, 571–574 (2013).
28. M. J. McDonald, D. P. Rice, M. M. Desai, Sex speeds adaptation by altering the dynamics of molecular evolution. *Nature* **531**, 233–236 (2016).
29. G. Mosig, The effect of multiplicity of infection on recombination values in bacteriophage T 4 D. *Z. Vererbungsl.* **93**, 280–286 (1962).
30. T. Sathaliyawala, *et al.*, Functional analysis of the highly antigenic outer capsid protein, Hoc, a virus decoration protein from T4-like bacteriophages. *Mol. Microbiol.* **77**, 444–455 (2010).

31. A. Fokine, *et al.*, Structure of the Three N-Terminal Immunoglobulin Domains of the Highly Immunogenic Outer Capsid Protein from a T4-Like Bacteriophage. *J. Virol.* **85**, 8141–8148 (2011).

32. L. E. Tailford, E. H. Crost, D. Kavanaugh, N. Juge, Mucin glycan foraging in the human gut microbiome. *Front. Genet.* **5**, 81 (2015).

33. J. M. Pickard, A. V. Chervonsky, Intestinal Fucose as a Mediator of Host–Microbe Symbiosis. *J. Immunol.* **194**, 5588–5593 (2015).

34. M. T. Cairns, *et al.*, Glycosylation-related gene expression in HT29-MTX-E12 cells upon infection by Helicobacter pylori. *World J. Gastroenterol.* **23**, 6817–6832 (2017).

35. J. K. Gustafsson, *et al.*, Dynamic changes in mucus thickness and ion secretion during citrobacter rodentium infection and clearance. *PLoS One* **8** (2013).

36. P. C. Kashyap, *et al.*, Genetically dictated change in host mucus carbohydrate landscape exerts a diet-dependent effect on the gut microbiota. *Proc. Natl. Acad. Sci. U. S. A.* **110**, 17059–17064 (2013).

37. M. Vellend, Conceptual synthesis in community ecology. *Q. Rev. Biol.* **85**, 1689–1699 (2010).

38. E. S. Lim, *et al.*, Early life dynamics of the human gut virome and bacterial microbiome in infants. *Nat. Med.* **21**, 1228–1234 (2015).

39. S. Minot, S. Grunberg, G. D. Wu, J. D. Lewis, F. D. Bushman, Hypervariable loci in the human gut virome. **109** (2012).

40. B. E. Dutilh, *et al.*, A highly abundant bacteriophage discovered in the unknown sequences of human faecal metagenomes. *Nat. Commun.* **5**, 1–11 (2014).

41. T. S. Dhillon, E. K. S. Dhillon, H. C. Chau, W. K. Li, A. H. Tsang, Studies on bacteriophage distribution: virulent and temperate bacteriophage content of mammalian feces. *Appl. Environ. Microbiol.* **32**, 68–74 (1976).

42. H. W. Ackermann, T. M. Nguyen, Sewage coliphages studied by electron microscopy. *Appl. Environ. Microbiol.* **45**, 1049–1059 (1983).

43. K. Furuse, *et al.*, Bacteriophage distribution in human faeces: Continuous survey of healthy subjects and patients with internal and leukaemic diseases. *J. Gen. Virol.* **64**, 2039–2043 (1983).

44. A. N. Shkoporov, *et al.*, The Human Gut Virome Is Highly Diverse, Stable, and Individual Specific. *Cell Host Microbe* **26**, 527-541.e5 (2019).

45. L. F. Camarillo-Guerrero, A. Almeida, G. Rangel-Pineros, R. D. Finn, T. D. Lawley, Massive expansion of human gut bacteriophage diversity. *Cell* **184**, 1098-1109.e9 (2021).

46. S. A. McMahon, *et al.*, The C-type lectin fold as an evolutionary solution for massive sequence variation. *Nat. Struct. Mol. Biol.* **12**, 886–892 (2005).

47. P. A. de Jonge, F. A. B. von Meijenfeldt, L. E. van Rooijen, S. J. J. Brouns, B. E. Dutilh, Evolution of BACON Domain Tandem Repeats in crAssphage and Novel Gut Bacteriophage Lineages. *Viruses* **11**, 1085 (2019).

48. C. Lee, S. Lee, S. G. Shin, S. Hwang, Real-time PCR determination of rRNA gene copy number: Absolute and relative quantification assays with Escherichia coli. *Appl. Microbiol. Biotechnol.* **78**, 371–376 (2008).

49. M. Fittipaldi, *et al.*, Discrimination of infectious bacteriophage T4 virus by propidium monoazide real-time PCR. *J. Virol. Methods* **168**, 228–232 (2010).

50. N. Bonilla, *et al.*, Phage on tap-a quick and efficient protocol for the preparation of bacteriophage laboratory stocks. *PeerJ* **2016**, e2261 (2016).

51. D. E. Deatherage, C. C. Traverse, L. N. Wolf, J. E. Barrick, Detecting rare structural variation in evolving microbial populations from new sequence junctions using breseq. *Front. Genet.* **5**, 1–16 (2015).

52. L. A. Kelley, S. Mezulis, C. M. Yates, M. N. Wass, M. J. Sternberg, The Phyre2 web portal for protein modeling, prediction and analysis. *Nat. Protoc.* **10**, 845–858 (2016).

53. O. Blixt, *et al.*, Printed covalent glycan array for ligand profiling of diverse glycan binding proteins. *Proc. Natl. Acad. Sci. U. S. A.* **101**, 17033–17038 (2004).

54. N. X. Arndt, J. Tiralongo, P. D. Madge, M. Von Itzstein, C. J. Day, Differential carbohydrate binding and cell surface glycosylation of human cancer cell lines. *J. Cell. Biochem.* **112**, 2230–2240 (2011).

55. M. E. Huflejt, *et al.*, Anti-carbohydrate antibodies of normal sera: Findings, surprises and challenges. *Mol. Immunol.* **46**, 3037–3049 (2009).

56. C. J. Day, *et al.*, Differential Carbohydrate Recognition by Campylobacter jejuni Strain 11168: Influences of Temperature and Growth Conditions. *PLoS One* **4**, e4927 (2009).

57. O. Cooper, *et al.*, Functional Microarray Platform with Self-Assembled Monolayers on 3C-Silicon Carbide. *Langmuir* **36**, 13181–13192 (2020).

58. F. S. Willard, D. P. Siderovski, Covalent immobilization of histidine-tagged proteins for surface plasmon resonance. *Anal. Biochem.* **353**, 147–149 (2006).

Chapter IV
Virulent and temperate phage dynamics within the mucosal environment

This chapter is written as a research article with journal submission planned within the first quarter of 2022. Submission is targeted to *The ISME Journal* as an Article. The version embedded represents an extended manuscript version to match the format of this thesis.

Virulent and temperate phage dynamics within the mucosal environment

Wai Hoe Chin[1], Ciaren Kett[1], Nan Hao[2], Keith Shearwin[2], Adrian Neild[3] and Jeremy J. Barr[1]*

[1] School of Biological Sciences, Monash University, VIC, 3800, Australia

[2] Molecular and Biomedical Sciences, The University of Adelaide, SA, 5005, Australia

[3] Department of Mechanical and Aerospace Engineering, Monash University, VIC, 3800, Australia

* Corresponding author: jeremy.barr@monash.edu

* Co-corresponding author: wai.chin@monash.edu

Abstract

Bacteriophages (phages in short) are chiefly classified as virulent or temperate. Virulent phages propagate in a strictly lytic manner while temperate phages alternate between the lytic and lysogenic lifecycles. Two key phage ecological hypotheses are Kill-the-Winner (KtW), which describes a lytic-dominant phage regime, and Piggyback-the-Winner (PtW), which depicts a lysogeny-dominant regime. Estimating the extent of lysis and lysogeny underlying phage-bacterial communities is key in predicting population trends and ecology. To this, we empirically tested lytic and lysogenic phage lifecycles within an *in vitro* lab-on-a-chip (to wit, gut-on-a-chip) device that recapitulates a gut mucosal environment. Here, we maintained isogenic populations of virulent and temperate phages where, lysogens arising from temperate phage lysogeny are susceptible to virulent phage superinfection but not temperate phages. By tracking the community overtime, we revealed that phage-bacteria dynamics were highly stochastic when establishing within the mucosal surface. Superinfection immunity specific to temperate phages was a key contributor in enabling KtW and PtW regimes to co-exist and drive unique phage-bacteria dynamics. Crucially, we demonstrated that phage-to-bacteria ratios were poor predictors of phage regimes compared to temporal population density data obtained through our multispecies quantitative PCR design. Thus, we present our study as a proof-of-concept towards integrated quantitative approaches in assessing lytic and lysogenic propensities within experimental ecosystems.

1. Introduction

Bacteriophages (phages in short) are obligate bacterial viruses that form the abundant majority of viruses in the human gut (1, 2). There, phages exert evolutionary and ecological pressure by infecting and propagating on bacterial members of the gut microbiome (3, 4). Phages are commonly classified as virulent or temperate based on their adopted lifecycles (3). Virulent phages exclusively propagate via the lytic life cycle while temperate phages alternate between the lytic and lysogenic lifecycles. Lysogeny is described by phage genome integration into bacterial host DNA resulting in a state of co-existence where the phage is now known as a prophage and the bacterium with the prophage is termed a lysogen. Evidently, the lytic lifecycle almost always lends host mortality while lysogeny maintains host survival by establishing phage dormancy. Estimating the extent of lysis and lysogeny underlying phage-bacterial communities is key in predicting population trends and identifying ecological parameters such as phage-host encounter probabilities and host lysis rates (5–7). These predictions and parameters subsequently provide the foundations to further describe the composition and functional ecology of viral and microbial communities within an ecosystem.

To-date, there are two ecological hypotheses that were conceptualised to describe underlying phage regimes based on their lytic and lysogenic extents. The Kill-the-Winner (KtW) hypothesis describes a lytic-driven phage community where bacterial populations experience density-dependent lytic predation by virulent phages (8). This density-dependent lysis renders the most abundant phage and bacterial ranks i.e. the “winners”, amenable to succession by rarer phage-host pairs depending on selection by the niche. This – on average – enables KtW to promote and maintain phage-bacteria diversity within an ecosystem (9, 10). On the other hand, the Piggyback-the-

Winner (PtW) hypothesis describes a temperate phage community exhibiting lysogeny in a density-dependent manner (6, 11). Here, phages infecting the most abundant bacterial host population favour lysogeny over the lytic lifecycle (hence, phages "piggybacking" the "winning" bacterial population). Unlike virulent phages where free virion abundances can be explicitly quantified to estimate lytic propensities, lysogeny is much harder to estimate within the environment. Studies to-date, typically estimate lysogeny by correlating read abundance data trends between viral genes associated with lysogeny and viral abundance (6, 7). While exploring trends derived from metagenomic sequence data can be insightful, findings should be considered provisional until empirically tested.

The human gut is a vibrant ecosystem that comprises a diverse and abundant phage and bacteria community, which we collectively refer to as our gut virome and microbiome, respectively (3). Given the implications of the gut microbiome on human health and well-being (12), there is a mounting imperative to understand the influence of phages on the state of our gut microbiome. Recent studies on gut virome metagenomics have uncovered a virulent gut phage majority which was largely unnoticed in previous studies (13, 14), such as the discovery of the crAssphage (15, 16). In addition, temporal analysis of the virulent phage majority revealed rapid evolution and succession of phage variants within a one-year period, which is reflective of phage diversification driven by KtW dynamics (13). Collectively, this suggests that the phage regime of the human gut virome is predominantly lytic. However, much less is known regarding the dynamics of the temperate phage minority in the gut amongst these recent studies.

Our study represents the first empirical attempt at directly assessing lytic and lysogenic propensities of phages with their bacterial host within a mucosal environment. We first established a model phage-bacteria community consisting of isogenic virulent and temperate λ phages with a single naïve bacterial host population. Importantly, superinfection exclusion conferred by temperate phage lysogeny protects against repeated temperate phage infection, but not against the virulent phage. We tested our model phage-bacteria community in batch culture experiments and showed that traditional culture-based conditions fostered a predominantly lytic propagation and co-existence of virulent and temperate phages. Following this, we established a quantitative PCR (qPCR) methodology to feasibly assess the model phage-bacteria community at high temporal resolution within the gut-on-a-chip mucosal niche. Phage-bacteria dynamics were highly unique across replicate mucosal populations. We demonstrated that these disparities were driven by subtle interactions between co-existing KtW lytic and PtW lysogenic regimes within our mucosal populations. To that, we also reported the capacity for temperate phages to establish lytic monopoly within the mucosal niche despite competing with strictly lytic virulent phages. Crucially, superinfection immunity specific to temperate phages was a key ecological mechanism in promoting virulent phage and lytic-lysogenic co-existence within the mucosal niche. Finally, we presented a case against PBR as a quantitative metric to infer underlying phage regimes, and that integrated quantitative approaches – such as temporal tracking of population densities – should be implemented in future studies in order to reliably describe viral strategies within an ecosystem.

2. Results

2.1. Virulent and temperate phages co-exist in test-tube batch culture.

To investigate the population ecology between a virulent and a temperate phage, we established a simple phage-bacteria community consisting of a two isogenic λ phages and a single naïve bacterial host species susceptible to both λ phages (*Escherichia coli* E4643; herein referred to as the "non-lysogen"). The isogenic λ phages comprise of a temperate λ phage i.e. λ^{TEMP} harbouring a kanamycin resistance gene, and a virulent λ phage mutant i.e. λ^{VIR}. The virulent phage cannot enter into lysogeny due to mutations in the lytic-repressor binding sites (17) and a previously undescribed partial deletion in the *attP* site, responsible for facilitating prophage integration (Annex 5). The temperate phage can only infect non-lysogen bacteria, which results in either lytic propagation or the formation of a lysogen. Superinfection immunity conferred by the λ^{TEMP} prophage protects the lysogen against repeated infections by λ^{TEMP} phages. Meanwhile, the virulent phage is capable of infecting and superinfecting non-lysogen and lysogen hosts respectively, lending lytic cell death as the virulent phage propagates (Fig.1A). This allows us to assess competition between virulent and temperate phage populations without introducing a pre-emptive selection bias for lysogens via complete superinfection immunity. Finally, we validated that there were no intrinsic growth differences between non-lysogens and lysogens that would otherwise influence phage dynamics in this simple community (Fig.1B).

To test this phage-bacteria community, we ran two replicate experiments in test-tube batch cultures for 24 hours. The batch culture was initiated with 10^4 plaque forming units (PFU)/ml of 1:1 virulent and temperate phages and 10^4 colony forming units (CFU)/ml of naïve, pure culture non-lysogens (Figs.1C and 1D). The batch cultures

were sampled hourly for 8 hours, followed by a single sample at 24 hours. Subsequently, phages and bacteria were quantified by traditional plating and qPCR for each sampled timepoint to assess phage-bacteria temporal dynamics (Fig.1D).

Plating results from both replicate batch cultures demonstrated that virulent and temperate phage populations expanded drastically between 5 to 8 hours post-inoculation (p.i.), indicating lytic propagation of both phages. Phage propagation was supported by an exponentially growing non-lysogen population, particularly at densities between 10^8 to 10^9 CFU/ml. The non-lysogen experienced a population crash between 7 to 8 hours p.i., coinciding with a crossing point where the phage populations overtook and dominated the batch culture (Fig.1E). Beyond 8 hours, both virulent and temperate phage populations co-existed and were maintained at densities of ~10^{10} PFU/ml, respectively (Fig.1E). Meanwhile, the non-lysogen population recovered and persisted at ~10^9 CFU/ml, which suggests the emergence of phage resistance as a contributor to the batch culture's steady-state; albeit this was not verified in our experiments.

Despite the strong lytic regime by both virulent and temperate phages, we saw the emergence of lysogens between 4 to 6 hours of incubation in both replicate batch cultures (Fig.1E). This indicated that a small subset of infections by temperate phages resulted in lysogeny. However, the lysogen population subsequently declined beyond 7 hours p.i. in one replicate and was outside of detectable plating ranges at 24 hours in the remaining replicate (Fig.1E). Since the lysogen is protected from temperate phage via superinfection exclusion, the lysogen population decline was likely attributed to lytic predation by the virulent phage. In summary, phage dynamics in

batch cultures were chiefly lytic, although a minor proportion of temperate phage infections resulted in lysogeny, which was subsequently predated by virulent phages. Crucially, the dynamics observed were repeatable across both experimental replicates (Fig.1E).

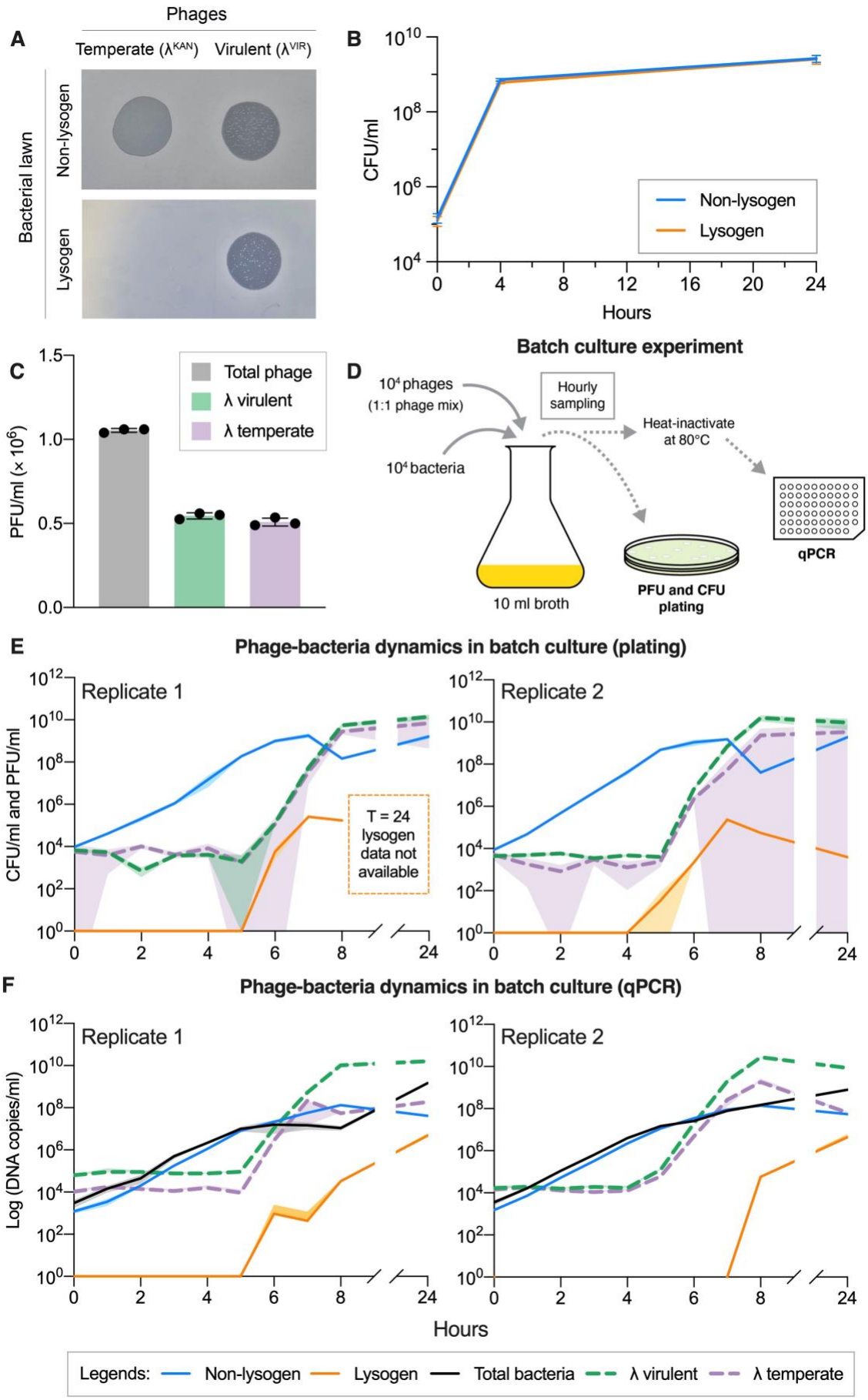
A
Phages
Temperate (λ^KAN)
Virulent (λ^VIR)
Bacterial lawn
Non-lysogen
Lysogen
B
CFU/ml
Hours
Non-lysogen
Lysogen
C
PFU/ml (× 10^6)
Total phage
λ virulent
λ temperate
D
Batch culture experiment
10^4 phages
(1:1 phage mix)
10^4 bacteria
Hourly sampling
Heat-inactivate at 80°C
qPCR
10 ml broth
PFU and CFU plating
E
Phage-bacteria dynamics in batch culture (plating)
Replicate 1
Replicate 2
CFU/ml and PFU/ml
T = 24 lysogen data not available
F
Phage-bacteria dynamics in batch culture (qPCR)
Replicate 1
Replicate 2
Log (DNA copies/ml)
Hours
Legends:
Non-lysogen
Lysogen
Total bacteria
λ virulent
λ temperate

Fig.1 Virulent and temperate phage dynamics in *in vitro* batch cultures. A) Spot of isogenic virulent λ^{VIR} and temperate λ^{TEMP} phage lysates on bacterial lawns of *E. coli* E4643 (non-lysogens) and *E. coli* E4643::λ^{TEMP} (lysogens) demonstrating superinfection immunity by λ^{TEMP} prophage against temperate phage superinfection but not against virulent phage. B) Growth curve of non-lysogen and lysogen from three independent replicate growth experiments (N = 3). C) Standardised phage titre of 1:1 mix of isogenic virulent and temperate λ phages used in batch culture and mucosal experiments. D) Schematic of batch culture experiment initiated with 10^4 PFU/ml of the 1:1 mix of isogenic λ phages and 10^4 CFU/ml naïve non-lysogen bacteria. The batch culture was sampled at every hour up to 8 hours followed by a final sample collected at 24 hours. Samples aliquots for qPCR were heat-inactivated at 80°C to arrest phage and bacterial replication. Phages and bacteria were quantified via plating and qPCR techniques. E) Phage-bacteria population densities in batch culture experiments from plating and F) qPCR quantification. Shaded regions represent mean ± SEM of three technical replicates (n = 3) for each independent experimental replicate for panels D and E. Lysogen density at 24 hours for test-tube replicate 1 was below detection from the dilution range plated. qPCR limit-of-detections (LODs) were removed for better visualisation of phage and bacterial density trajectories. Complete plot with LODs is available in Annex 6.

2.2. Assessing quantitative agreement between plating and quantitative PCR.

We next sought to establish a high-throughput quantitative method to measure phage-bacteria densities overtime. To that, we developed a multiple primer set to distinguish and quantify the individual phage and bacterial members via qPCR (Figs.1F and 2A). We first designed primers to detect extracellular phage virions. Virulent phages virions were detected via flanking primers which leveraged a ~6kb deletion affecting the *attP* site that is not present in the temperate phage (Annex 5). This enabled us to differentiate virulent phage virions from its temperate counterpart, where primers

detecting temperate phage virions immediately flank the intact *attP* integration site. Meanwhile, total bacterial density was quantified using a previously validated qPCR primer set targeting the 16S *rRNA* sequence (18). Non-lysogens were quantified via primers flanking the *attB* prophage integration site on the bacterial chromosome. Finally, temperate phage integration into the bacterial chromosome generates two novel junctions *attL* and *attR*, which are composites of *attB* and *attP* sites post-integration. We leveraged the forward *attP* and reverse *attB* primers to uniquely detect lysogens by flanking the *attR* junction. Given that *attB* flanking sequence are part of the bacterial chromosome, this composite primer set neither detects virulent nor temperate phage virions, while the *attP* prophage-targeting primer discriminates against bacterial non-lysogens.

To assess quantitative agreement between plating and qPCR techniques, we performed linear regressions and correlations of phage and bacterial densities (Fig.2B) between plating and qPCR data from the batch culture replicates (Figs.1E and 1F). The increase in virulent and temperate phage densities captured by qPCR were largely similar to plating results. The exception being temperate phages at 8 and 24 hours, where qPCR temperate phage densities were underestimated within a range of 1 to 1.5 orders of magnitude relative to plating results (Figs.1E and 1F). Nonetheless, we demonstrated good correlation between plating and qPCR phage densities with a mean R^2 value of 0.97 and 0.82 for virulent and temperate phage fractions, respectively (Fig.2B, λ virulent and λ temperate). The best-fit linear regressions were also generally statistically non-significant from the ideal line-of-fit (i.e. perfect correlation between plating and qPCR), with the exception of virulent

phages from replicate 1 due to datapoints overestimating phage densities by an order of magnitude during the initial 5 hours (Figs.1F and 2B, λ virulent replicate 1).

qPCR density outputs for non-lysogens in both replicates also reflected increasing bacterial densities from plating results. However, these densities were gradually underestimated with increasing microbial densities relative to plating densities (Figs.1F and 2B, non-lysogens). This was also reiterated from the qPCR of total bacterial densities overtime using a previously validated 16S primer set (18)(Figs.1F and 2B, total bacteria), which indicate that the tendency to underestimate at higher bacterial densities was a consistent artefact in our qPCR approach. Despite this, both plating-to-qPCR linear regressions for non-lysogens and total bacteria densities correlated well with mean R^2 values of 0.92 and 0.89, respectively. Furthermore, best-fit regressions for both non-lysogens and total bacteria densities across all experimental replicates were not statistically significant from their respective ideal lines-of-fit (Fig.2B, non-lysogens and total bacteria).

Meanwhile, assessing correlation through linear regression of the lysogen density was precluded by insufficient non-zero datapoints from both batch culture plating and qPCR outputs (Figs.1E and 1F, lysogens). To this, we established a proxy assessment of lysogen qPCR-to-plating agreement by regularly sampling and quantifying a growing pure lysogen culture for up to 6 hours. Unlike the other datasets, lysogen qPCR outputs were consistently underestimated by two orders of magnitude across the plating density range (Fig.2B, lysogens). This was reflected by a high correlation coefficient i.e. $R^2 = 0.986$, and a non-statistically significant slope with the ideal line-of-fit, apart from the ~2-log displacement along the plating axis (Fig.2B, lysogens). We

speculate that this underestimation may be attributed to prophage induction within our heat-inactivated sample, which would have abrogated the *attR* junction to render our primers unable to detect and quantify lysogens. Despite this, we did not implement *ad hoc* adjustments on our lysogen datasets, given the already complex data outputs from our “multi-species” qPCR approach. In summary, our qPCR methodology was able to capture overall population density trends for individual members of the isogenic phage and bacteria community, albeit with a cautionary note on the underestimation of bacterial lysogens.

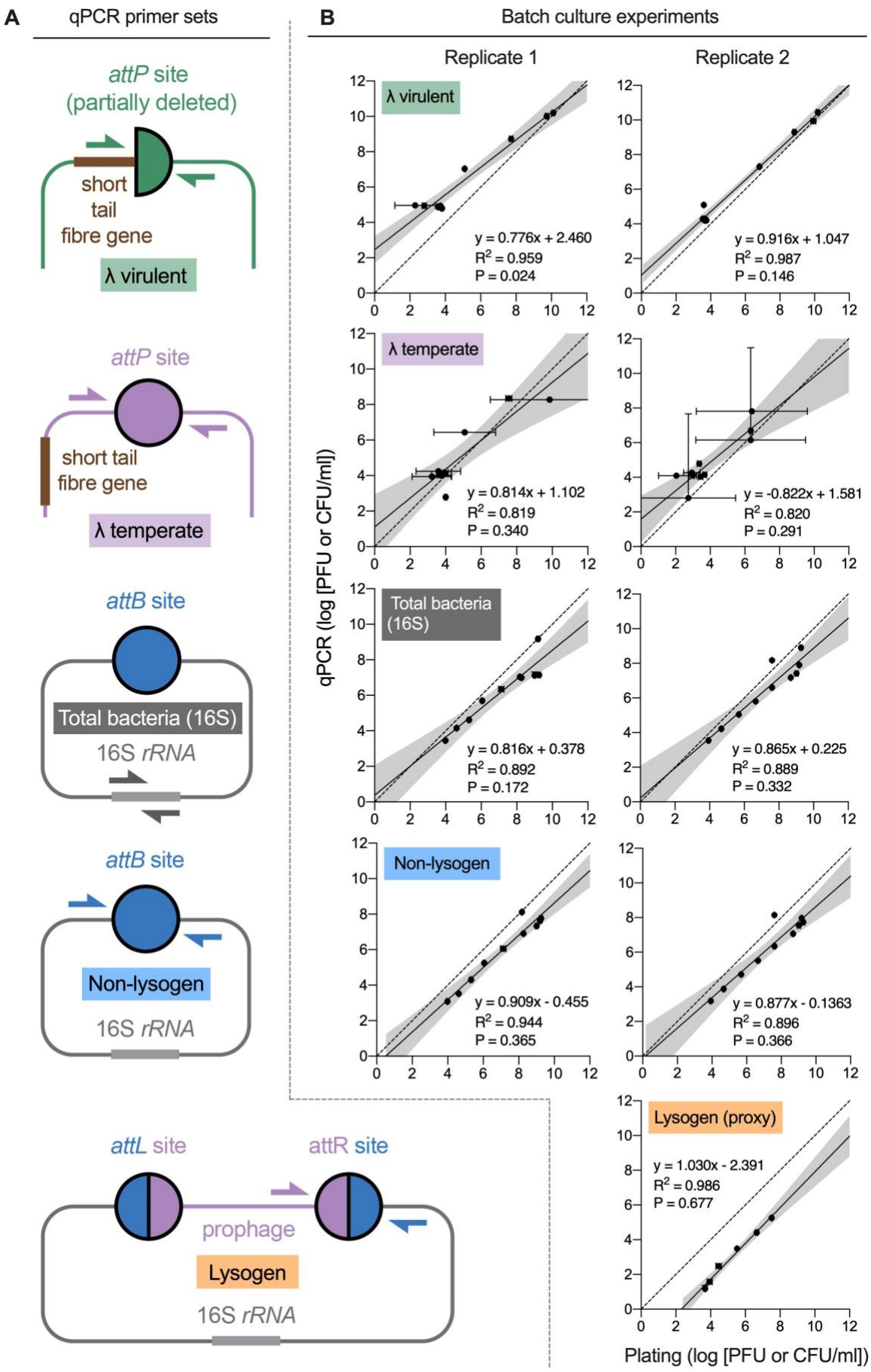
A
qPCR primer sets
attP site
(partially deleted)
short
tail
fibre gene
λ virulent
attP site
short tail
fibre gene
λ temperate
attB site
Total bacteria (16S)
16S rRNA
attB site
Non-lysogen
16S rRNA
attL site
attR site
prophage
Lysogen
16S rRNA
B
Batch culture experiments
Replicate 1
Replicate 2
λ virulent
y = 0.776x + 2.460
R2 = 0.959
P = 0.024
y = 0.916x + 1.047
R2 = 0.987
P = 0.146
λ temperate
y = 0.814x + 1.102
R2 = 0.819
P = 0.340
y = -0.822x + 1.581
R2 = 0.820
P = 0.291
Total bacteria (16S)
y = 0.816x + 0.378
R2 = 0.892
P = 0.172
y = 0.865x + 0.225
R2 = 0.889
P = 0.332
Non-lysogen
y = 0.909x - 0.455
R2 = 0.944
P = 0.365
y = 0.877x - 0.1363
R2 = 0.896
P = 0.366
Lysogen (proxy)
y = 1.030x - 2.391
R2 = 0.986
P = 0.677
qPCR (log [PFU or CFU/ml])
Plating (log [PFU or CFU/ml])

Fig.2 Phage and bacteria quantitative agreement between plating and qPCR methodologies. A) Schematic of primer sets (solid coloured arrows) used to distinguish and quantify the individual members of the isogenic phage and bacterial hosts community. Virulent phage was differentiated from temperate phage by primers that leverage a partial (~6kb deletion) affecting the *attP* integration site of the virulent phage mutant. Total bacterial density was quantified using a 16S *rRNA* qPCR primer set (18), while non-lysogens were enumerated using primers flanking the *attB* integration site on the bacterial chromosome. Lysogens were uniquely quantified by a combination of forward *attP* and reverse *attB* primers flanking the integrated *attR* site between the prophage and the bacterial chromosome, respectively. B) Data points plotted for phage or bacterial densities derived from matching timepoints between plating and qPCR experiments from Figs.1E and 1F, except for lysogens where a growing pure lysogen culture was used as a proxy to assess quantitative agreement between plating and qPCR enumeration. Error bars on individual plots represent mean ± SEM from three technical replicates (n = 3). Dotted line along the diagonal (equation: y = x) represents the ideal line-of-fit between plating and qPCR outputs as a benchmark against the best-fit line (solid line). The best-fit line (solid line) was generated from a linear regression analysis with reported line equation, R^2-values and P-values of slopes tested against the ideal line-of-fit. Shaded regions represent the 95% confidence interval along the best-fit line. P-values were derived from a two-tailed t-test between the slopes of the best-fit line (solid line) and the ideal line-of-fit (dotted line).

2.3. Co-existing lytic and lysogenic lifecycles lends stochastic phage-bacteria dynamics within the mucosal layer.

With the established qPCR protocol for high-throughput tracking of phage and bacteria densities, we sought to assess the early establishing dynamics of virulent and temperate phages within a mucosal environment with high temporal resolution. To that, we manufactured gut-on-a-chip devices to recapitulate key features of the *in vivo* gut mucosa, as previously described (19). The single-channel device was seeded with human colon tumorigenic cell line HT29-MTX-E12, and was grown for two days to achieve confluency, followed by an overnight chemical induction to enhance mucus production. The device was then perfused with 10^5 absolute CFU of non-lysogens followed by 10^5 absolute PFU of the 1:1 virulent and temperate phage mix (Fig.1B). Thereafter, the devices were maintained under a flow rate of 200 µl/hr, corresponding to 20 complete channel turnovers per hour and a shear stress of 0.042 dyne/cm^2, which is within the physiological range observed in the human gut (20). The device was connected to an automated dispensing platform where egressing sample from the device was rapidly heat-inactivated to arrest phage-bacteria growth and dispensed in a 96-well plate at 30-minute intervals. Samples were collected until the endpoint of the gut-on-a-chip indicated by the loss of mucosal viability from dense bacterial growth, which ranged from 30 to 36 hours p.i..

Unlike batch culture observations (Figs.1E and 1F), phage-bacteria dynamics were highly unique between replicate gut-on-a-chip devices despite inoculating with similar founding phage and bacterial densities. Virulent and temperate phages densities were near or under the limit-of-detection (LOD; refer to Annex 6 for plots including LOD thresholds) in the first 10 hours across all gut-on-a-chip replicates, except for replicate

1 (Fig.3B). Here, both virulent and temperate phages expanded overtime, with temperate phages lagging in comparison to its virulent counterpart. Meanwhile, the phages in the second replicate remained largely under LOD until 18 hours, where both phages species were reliably detected thereafter. However, the overall phage densities at replicate 2 endpoint was lower across all three replicates. We posit that this may be attributed to either poor initial phage retention or a significant early crash in the bacterial population; where the latter would have severely depleted host availability during early phage establishment in the mucosal environment. Finally, both phages in replicate 3 expanded exponentially at 16 hours p.i. but in contrast to replicate 1, temperate phage growth was more rapid in relative to the virulent phage; thus, lending to temperate phage predominance at the endpoint of replicate 3. In all replicates, the non-lysogen bacterial population experienced an initial population crash between 1 – 3 hours p.i. However, this was followed by gradual population recovery and maintenance throughout the experimental duration. Meanwhile, lysogens – a product of lysogeny by temperate phages – emerged in only two of three replicates but chiefly persisted in replicate 1.

Collectively, all replicate populations demonstrated virulent and temperate phage co-existence within the mucosal environment. However, the different extent of lysogeny was a significant delineating ecological outcome across all replicate populations in the mucosal niche. We posit that this is likely driven by the disparate phage dynamics in each replicate which led to varying extents of lytic and lysogenic pressures overtime. In replicate 1, early population dynamics was likely dictated by temperate phage lysogeny, leading to robust establishment of the lysogen population within the mucosa. Following this, the lysogen population became an additional – and significant – host

source for virulent phage lytic propagation through superinfection, thereby enabling virulent phages to dominate the mucosal niche. Subsequently, the co-existence of all phage and bacterial “species” in replicate 1 was likely mediated by a balance between lytic and lysogenic regimes; chiefly, by virulent phages on lysogens and temperate phages of non-lysogens, respectively. Meanwhile, both virulent and temperate phages in replicate 2 demonstrated a minor concurrent lytic propagation on the non-lysogen population. However, no lysogens were reported largely due to the low overall temperate phage density throughout the experimental duration. Finally, phage dynamics in replicate 3 was highlighted by a preceding rapid lytic expansion of the temperate phage, which was followed gradually by the virulent phage. Following the robust establishment of temperate phages in the mucosa, a subset of temperate phages infections resulted in lysogens, indicating a lytic-to-lysogenic switch of temperate phage regimes. However, in contrast to replicate 1, the establishment of lysogens in replicate 3 was likely inhibited by superinfection from a pre-established virulent phage population.

In addition to population dynamics, we asked if the phage-to-bacteria ratio (PBR) is a reliable indicator of underlying phage regimes; given its popularity as a common metric reported in various studies to imply underlying phage propagation strategies (6–8, 21, 22). A PBR at 10:1 or higher is commonly attributed to a lytic phage regime that is reflective of KtW, while a PBR less than 10:1 indicates a predominantly lysogenic regime, reflective of PtW. PBR at peak viral and microbial densities were 100:1, 0.001:1 and 10:1 across replicates 1 to 3, respectively. By common definitions, these PBR would suggest KtW lytic regimes in replicates 1 and 3, and a PtW lysogenic regime in replicate 2. However, following previous descriptions of phage dynamics in

the respective replicate mucosal populations, we demonstrated that PBR alone is not an accurate metric to imply underlying phage regimes. Furthermore, PBR undermines the contextual details of population dynamics, namely, the ecological interactions between lytic and lysogenic regimes. It was only by leveraging temporal population density data that we were able to describe the complex interplay between lytic and lysogenic lifecycles to lend the disparate ecological outcomes across the replicate mucosal populations. In summary, our results underscored the need to supplement PBR with additional population metrics to more precisely describe phage regimes within a given niche.

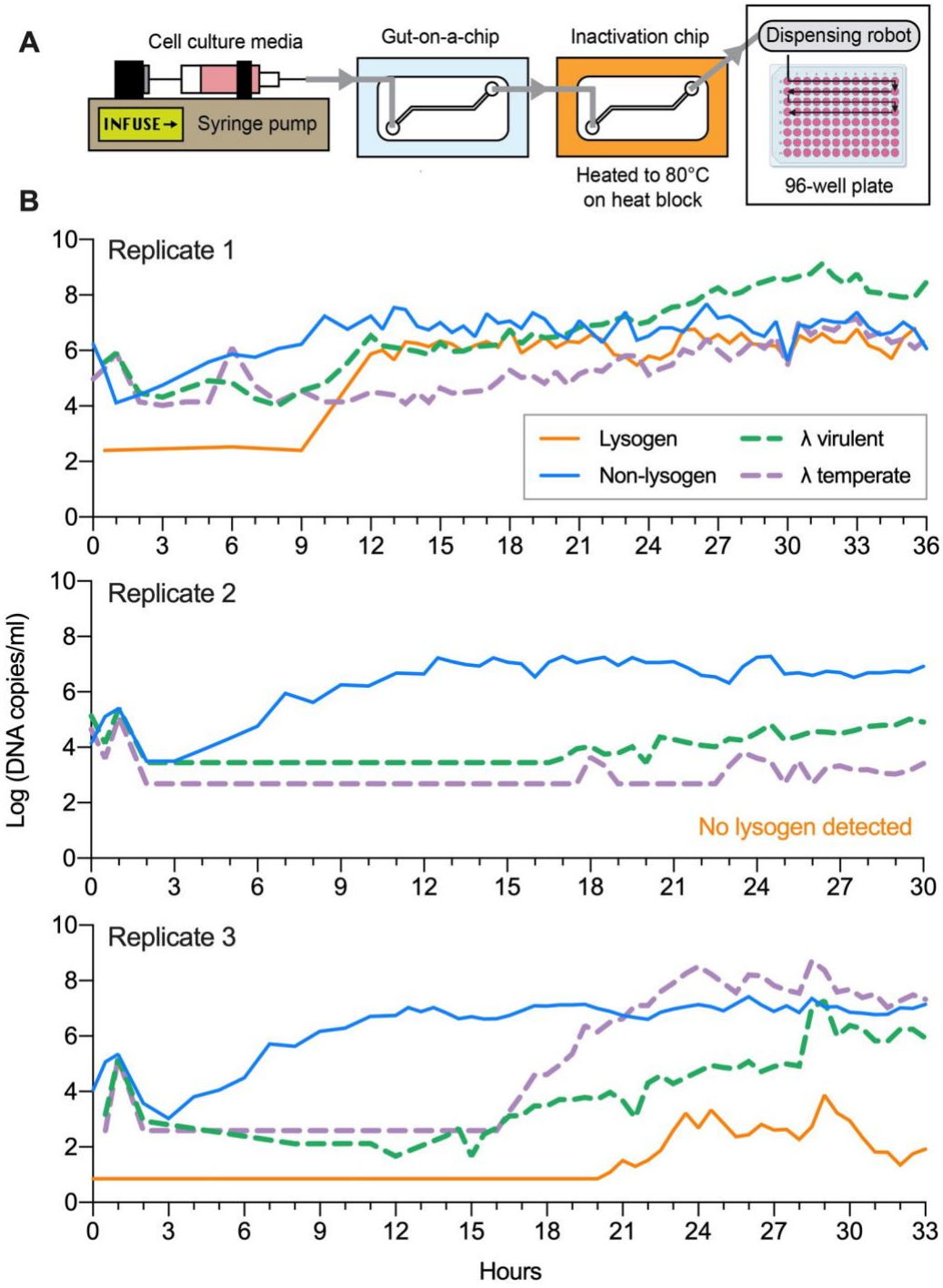

Fig.3 Virulent and temperate phage dynamics in gut-on-a-chip mucosal environment. A) Schematic of the gut-on-a-chip set-up with device perfusion driven by syringe pump. Fluid egress from the device containing representative phage and bacteria populations is heat-inactivated followed by sample collection in a 96-well plate by an automated dispensing platform. B) Phage-bacteria population densities derived from qPCR quantification of heat-inactivated samples across three independent gut-on-a-chip replicates. Data is plotted at a resolution of 30-minute intervals

with each datapoint represented by one qPCR technical replicate (n = 1). qPCR limit-of-detections (LODs) were removed for better visualisation of phage and bacterial density trajectories. Complete plot with LODs is available in Annex 6.

3. Discussion

The human gut environment is abundant with virulent and temperate phages (23). However, the extent of phage-mediated lysis and lysogeny within the gut mucosal environment remains elusive and an empirical challenge to test. Our study represents a pioneering attempt at assessing lytic and lysogenic dynamics within a mucosal surface by adopting a reductionistic experimental design in three key areas. Firstly, we leveraged the gut-on-a-chip to recapitulate a simplified mucosal environment with active turnover dynamics (19). While our mucosal system does not represent the full complexity of an *in vivo* gut, the gut-on-a-chip provided an innovative middle-ground between static cell cultures and animal models to test viral and microbial ecology within an amenable and tractable mucosal setting. Secondly, we set-up an isogenic phage community of virulent and temperate λ phages that were capable of infecting a shared bacterial host, as a model phage-bacteria community in our study (Figs.1A and 1E). In doing so, our study does not encompass the effects of phage-host diversity in order to minimise the complexity of our model system. Under a low diversity setting, phage-bacteria encounters will largely result in productive infections (24). However, in more natural settings where viral and microbial diversity is typically high (25, 26), productive encounters are likely lower due to increased probability of incompatible phage-host encounters. Hence, in maintaining simplicity, our study is limited to a case of low population diversity with high evenness (i.e. the inoculated phage and bacteria population sizes are similar). Thirdly, the experiments were performed within a half-hourly time resolution, compared to conventional phage ecological studies that are typically undertaken within timescales of days to months (27, 28). This limits our study to early establishing dynamics of phages and bacteria within the mucosal environment, instead of assessing long-term population dynamics and equilibria. We

also acknowledge that lytic and lysogenic regimes in our experiments were extrapolated based on phage-bacterial population densities derived from qPCR. While we did establish good correlations between qPCR and plating techniques from our batch culture population datasets (Figs.1E and 1F), highly precise quantitation was affected by underestimation in lysogen densities and more generally, at higher densities across all other phage and bacterial species (Fig.2B).

Despite the limitations, we reported that establishing dynamics of the phage-bacteria populations were highly unique across independent mucosal environments (Fig.3B); in contrast with repeatable population dynamics observed in batch culture experiments (Figs.1E and 1F). This may be attributed to ecological factors intrinsic to the mucosal environment, which could contribute to the stochastic variations observed across gut-on-a-chip replicate populations. Particularly, mucosal heterogeneity and turnover dynamics could influence the phage-bacterial population sizes that successfully establishes within the mucosal surface (29–31). This may lend variations in initial population demography between the replicate mucosal settings, subsequently leading to widely different population trajectories and distinct ecological outcomes (Fig.3B)(32). At a broader context, demographic stochasticity acts as a primary source of variation during microbial and viral colonisation of the mucosa. This may in part, contribute to the uniqueness of gut viromes observed in human cohorts, even in cases of monozygotic twins whose gut settings are conceptually identical in biology (13, 33).

Virus-to-microbe ratios – in our case, PBRs – are commonly reported as a metric to infer the underlying viral propagation strategies within an ecosystem. Ratios of 10:1 and higher typically implies a KtW lytic regime, where the higher phage density relative

to bacteria is conferred by robust density-dependent lytic activity (8). Meanwhile, ratios that contract from 10:1 were explained by the PtW lysogeny model due to increasing lysogenic activity at higher bacterial densities (6). However, using PBR as a sole metric to infer underlying viral regimes presents a two-pronged conundrum. Firstly, it sets an unintended precedence to interpret KtW and PtW as mutually exclusive phenomena based on the 10:1 threshold. Secondly, a ratio is essentially a single data snapshot of community sampled at a specific timepoint of a specific niche. Evidently, this does not entail sufficient information on the particular sampled population to draw upon ecological conclusions. By leveraging high-resolution temporal tracking of phage-bacterial densities in the mucosal environment (Figs.2B and 3), we were able to: i) demonstrate that PBR alone is not an accurate metric on inferring phage propagation regimes, and ii) reveal the complex interplay between lytic and lysogenic viral dynamics underlying phage-bacteria communities within the mucosa.

Based on PBR alone, two of our three mucosal replicates would have been inferred to demonstrate predominantly lytic regimes associated with KtW (Fig.3B, replicates 1 and 3) while the remaining would be deemed to exhibit a lysogenic regime associated with PtW (Fig.3B, replicate 2). Instead, we reported the co-occurrence of lytic and lysogenic phage regimes and their interactions within the mucosal niche in replicates 1 and 3. In the case of replicate 1, we demonstrated that both virulent and temperate phages along with lysogens and non-lysogens, were able to co-exist within the mucosal niche (Fig.3B, replicate 1). We reported that the community was initiated by a robust lysogenic regime, resulting in the establishment of lysogens in the mucosa. The lysogens subsequently fuelled lytic propagation of virulent phages through superinfection which, not only led to an overall lysogeny-to-lytic switch in the

community, but also inhibited lysogens from completely dominating the mucosal niche. Ultimately, the balance between viral lysogeny and lysis in the mucosal community contributed to the maintenance of viral and microbial “diversity” within the mucosa (Fig.3B, replicate 1). In contrast to replicate 1, a preceding lytic phage regime in replicate 3 led to a robust establishment of temperate and virulent phage populations within the mucosa. While subsequent temperate phage infections facilitated the emergence of lysogens, the lysogen population was likely suppressed by lytic pressure from virulent phages. Collectively, the disparity in population outcomes between replicates 1 and 3 hints at the ecological impact imparted by the preceding order of lytic or lysogenic regimes within a phage-bacterial community. Finally, closer inspection of phage dynamics in replicate 2 revealed that the low PBR observed was not accompanied by the emergence of lysogens. Rather, both lytic and temperate phages were exhibiting lytic propagation to emerge above detection levels overtime (Fig.3B, replicate 2). Based on our population density data, it is likely that the low PBR was a stochastic case of poor early phage establishment in the mucosal environment, and not a reflection of an underlying lysogenic phage regime.

Superinfection exclusion was a significant driver underlying the phage regimes in our mucosal populations. In our model phage-bacteria community, superinfection exclusion conferred by prophages only confers immunity against repeated infections by temperate phages but not against virulent phages (Fig.1A). This recapitulates a scenario where superinfection exclusion is specific to the infecting temperate phage species. Superinfection exclusion is generally regarded as a fitness advantage within the community by protecting lysogens against repeated infection by the same or closely-related temperate phages (34). Our study revealed that the benefits of this

immunity were tempered under the presence of a virulent phage species capable of productive superinfection on lysogens. In the mucosal surface, superinfection immunity may have allowed lysogens to emerge by conferring partial relief of lytic pressure from temperate phages (Fig.3B, replicates 1 and 3). However, the lysogen population subsequently becomes a secondary host for lytic propagation by virulent phages. This suggests that superinfection immunity is counterproductive in facilitating temperate phage propagation via lysogeny, and is in fact, a mechanistic driver behind the complex and concurrent lytic and lysogeny viral dynamics – at least within the context of our isogenic phage community. Furthermore, this counterproductivity may be further exacerbated by lysogens becoming 'sinks' for adsorbed temperate phage virions. In this case, selection would favour temperate phages to propagate via the lytic lifecycle in order to compete with its virulent counterpart, as observed in batch cultures and the mucosal niche (Figs.1E and 3B).

In summary, our study demonstrated the complex interactions between lytic and lysogenic regimes in an isogenic phage community within the mucosal niche. Within the broader context of KtW and PtW theories, our empirical study offers a potential parsimonious description for both ecological phenomena to occur simultaneously in a phage-bacterial community. Depending on the extent and order of predominant viral regimes, viral communities may shift along the KtW-PtW spectrum, leading to variations in community composition and diversity. Moreover, superinfection by virulent phages was a significant ecological mechanism in facilitating concurrent lytic and lysogenic strategies; particularly by enabling virulent phages to exert sustained control on the overall bacterial population (i.e. lysogens and non-lysogens). At a much broader level, this may in part, explain the predominant abundance of virulent phages

over temperate ones within the human gut virome (13, 14). Crucially, we were able to underscore the limitation of PBR as a predictive ecological metric on underlying phage propagation strategies. We argued that PBR (and more generally, virus-to-microbe ratios) should be decoupled from their ecological connotations, where high PBRs does not necessarily translate to lytic-dominant regimes and vice versa with low PBRs and lysogeny-dominant regimes. Instead, integrated quantitative approaches should be adopted to provide essential contextual evidence in drawing reliable conclusions on viral regimes. Ultimately, our study hints at the much grander challenges ahead in predicting phage-bacteria population dynamics *in vivo*, especially where phage-bacteria communities and the gut environment are more heterogeneous and complex. We envisaged that our proof-of-concept study would inspire future work to embrace integrated experimental approaches to investigate phage strategies under more representative communities and niches.

4. Methods and materials

5.1. Culture protocol for phage, bacteria and tissue culture cell lines.

Isogenic virulent λ phage mutant (λ^{VIR}) and temperate λ phage with kanamycin resistance (λ^{TEMP}) along with bacterial hosts *Escherichia coli* strain E4643 (non-lysogen) and *E. coli* strain E4643 lysogen with λ^{TEMP} prophage (*E. coli* E4643::λ^{TEMP} i.e. lysogen) were kindly gifted by Keith Shearwin, University of Adelaide, SA. Both phages were propagated on *E. coli* strain E4643 grown in LB medium (10 g Tryptone, 10 g NaCl, 5 g yeast extract in 1 L of sterile dH_2O) at 37°C with agitation. *E. coli* E4643::λ^{TEMP} was grown similarly in LB supplemented with 50 µg/ml Kanamycin and was used to selectively plate λ^{VIR} (since λ^{TEMP} cannot superinfect the lysogen). The cell line used in the gut-on-a-chip was a human colon-derived tumorigenic goblet cell, HT29-MTX-E12, obtained from the European Collection of Authenticated Cell Cultures and cultured at 37°C with 5% CO_2 in complete media: DMEM with 10% FBS, 1× MEM non-essential amino acids and 1× penicillin-streptomycin antibiotics (ThermoFisher Scientific). Terminal cellular differentiation was induced with 10 µM N-[N-(3,5-Difluorophenacetyl)-L-alanyl]-S-phenylglycine t-butyl ester (DAPT; Sigma-Aldrich) while mucus-secretion was enhanced with 10 nM phorbol 12-myristate 13-acetate (PMA; Sigma-Aldrich).

5.2. Batch culture experiments.

10 ml of prewarmed LB at 37°C was inoculated with 1×10^4 CFU/ml of *E. coli* E4643 and 1×10^4 absolute PFU/ml of 1:1 mix of λ^{VIR}:λ^{TEMP} phages (i.e. MOI 1). The co-culture was briefly vortex and 560 µl of sample was collected immediately (T = 0 sample) of which; 100 µl was heat-inactivated for 5 minutes at 85°C to arrest phage

and bacteria growth followed by storage at 4°C for qPCR quantification, 400 µl was treated with 10% chloroform to obtain the phage fraction, and 60 µl was 10-fold serially diluted in technical triplicates (20 µl per technical replicate) followed by spotting the dilutions on LB agar (total bacterial count) and LB agar supplemented with 50 µg/ml Kanamycin (λ^{TEMP} bacterial lysogen count). Non-lysogenic fraction was obtained by subtraction of lysogens from total bacterial count. Chloroform-treated phage fractions were serially diluted and quantified in three technical replicates via soft-agar overlays with pure cultures of naïve non-lysogens (total phage count) and lysogens (λ^{VIR} phage count). The fraction of λ^{TEMP} phage was obtained by subtraction of λ^{VIR} phage from total phage count. The batch culture was incubated at 37°C under agitation and sampled every hour for 8 hours, followed by a sample at 24 hours. Heat-inactivated samples were qPCR quantified using SYBR Green I Master with the Lightcycler® 480 (Roche) with the following primer sets and their corresponding cycling protocols listed in Table 1. Standard curves for each experimental replicate are included as Annex 7.

Table 1: qPCR primer sets and cycling protocols

				Cycling protocol (40 cycles)			
Primer sets	Forward primer (5' → 3')	Reverse primer (5' → 3')	Initial denaturation	Denaturation	Annealing	Extension	Product size (bp)
16S (total bacteria)	GCTACAATGGCG CATACAAA	TTCATGGAGTCG AGTTGCAG	95°C 10 mins	95°C 10 s	60°C 10 s	72°C 10 s	101
λ^{VIR}	ATCCACAGTTAAA GGAACCAACAC	CTGATAGTGACC TGTTCGTTGC		95°C 10 s	66°C 10 s	72°C 10 s	142
λ^{TEMP}	TCTCTGGAGTGC GACAGGTT	CTGATAGTGACC TGTTCGTTGC		95°C 30 s	66°C 30 s	72°C 30 s	287
Non-lysogen	CGCCAAAAGCCA ATGCCAGC	CAAGCGCCTCGA TTACTGCGATG		95°C 10 s	66°C 10 s	72°C 10 s	130
Lysogen	TCTCTGGAGTGC GACAGGTT	CAAGCGCCTCGA TTACTGCGATG		95°C 30 s	68°C 30 s	72°C 30 s	248

5.3. Assessing plating and qPCR quantitative agreement.

Population density data of individual phage and bacterial species from batch culture experiments were log-transformed and plotted on linear x- and y-axes representing log-plating densities and -qPCR densities, respectively. Each data plot representing the plating and qPCR population density values was also timepoint-matched. Correlation between plating and qPCR results was assessed using a simple linear regression which also reported the coefficient of determination R^2. The linear regression i.e. the best line-of-fit, was statistically compared to an ideal line-of-fit i.e. $y = x$, using a two-tailed test on a null hypothesis that the slopes between the best and ideal lines-of-fit are identical (PRISM 9.0.0). Plating and qPCR dataset for lysogens was obtained by growing a pure culture of 10^4 CFU/ml *E. coli* E4643::λ^{TEMP} lysogen in 10 ml LB broth, supplemented with 50 µg/ml Kanamycin. The culture was incubated at 37°C with agitation and 200 µl was collected hourly up to 6 hours. Each sample aliquot was divided equally where 100 µl was quantified via spot-plating while the remaining 100 µl was heat-inactivated at 85°C for 5 minutes for qPCR quantification; both techniques were performed with technical triplicates (n = 3). Data obtained was plotted on log-transformed axes where correlation and linear regression analyses were performed as described.

5.4. Gut-on-a-chip fabrication.

A chip mould with 500 µm wide and 350 µm high channel was designed using SolidWorks® 2017 (Dassault Systèmes). The moulds were then 3D-printed and surface-salinized at Melbourne Centre for Nanofabrication (MCN), Victoria. The chips were manufactured by casting a 10:1 mixture of Sylgard™ PDMS and its curing agent respectively (Dowsil, USA), onto the moulds and were cured at 90°C until completely solidified. The chips were then removed, trimmed and their inlet and outlet ports were

punched. Subsequently, the chips were washed in pentane and acetone to remove residual uncured PDMS followed by plasma bonding the chip onto a glass slide to enclose the chip channel. The chip channel was ethanol (80%v/v)-sterilised, UV-sterilised and pre-treated with 1:50 MaxGel^{TM} ECM (Sigma-Aldrich). The channel was then seeded with 10 µl of HT29-MTX-E12 cells at 3.0×10^7 cells/ml. The seeded chip was incubated statically for 16 hours to allow cell attachment. This was followed by perfusing the attached cells with complete media for 48 hours at 40 µl/hr flow rate to establish a confluent cell layer. The cell layer was then perfused with antibiotic-free media supplemented with cell-inducers DAPT and PMA, for another 24 hours at 200 µl/hr to purge residual antibiotic-containing media from the channel environment and to promote terminal cellular differentiation and mucus secretion by the cell layer. Perfusion was mediated by a double-channel syringe pump (KD Scientific, USA).

5.5. Phage-bacteria ecology in the gut-on-a-chip

An in-house automated dispensing platform was constructed to aid sample collection from the gut-on-a-chip over 24 hours at 30-minute intervals. The platform consisted of conveyer belts connected to 5V motors powered by an Arduino circuit board (Arduino, Italy). Two conveyer belt systems were aligned perpendicular to each other allowing motion along the X-Y plane. A custom-made tube holder was connected to the conveyer belt system that holds the gut-on-a-chip tube over the 96-well plate to facilitate sample dispensing into wells. Time-steps for dispensing at 30-minute intervals were coded into Arduino in C++ using Arduino Integrated Development Environment (IDE). For a user-friendly interface, the code was translated onto a virtual switch board executable program using LabVIEW v.2020 (National Instruments, USA). The temporal experiment is initiated by perfusing the gut-on-a-chip with 10^5 colony

forming units (CFU) of *E. coli* B followed by 10^5 PFU of T4 phages and the device was allowed to run for 24 hours under a 200 µl/hr flow rate whilst connected to the automated dispensing platform to collect egressing fluid samples. In between the gut-on-a-chip and the dispensing platform, the egressing fluid was channelled through an 80°C-heated blank chip to arrest phage and bacterial replication during their egress from the gut-on-a-chip before dispensing. Phages and bacteria from the heat-inactivated samples were quantified via qPCR using SYBR Green I Master with the Lightcycler® 480 (Roche) following cycling protocols from Table 1. Given the large sample number and primer sets and the reliability of our standard curves, each mucosal-derived sample were quantified via one qPCR technical replicate (n = 1); excluding standard curve templates which were carried out in technical triplicates (n = 3). Standard curves for each experimental replicate are included as Annex 7.

References

1. M. Breitbart, *et al.*, Metagenomic analyses of an uncultured viral community from human feces. *J. Bacteriol.* **185**, 6220–6223 (2003).
2. M. S. Kim, E. J. Park, S. W. Roh, J. W. Bae, Diversity and abundance of single-stranded DNA viruses in human feces. *Appl. Environ. Microbiol.* **77**, 8062–8070 (2011).
3. M. K. Mirzaei, C. F. Maurice, Ménage à trois in the human gut: Interactions between host, bacteria and phages. *Nat. Rev. Microbiol.* **15**, 397–408 (2017).
4. P. D. Scanlan, Bacteria–Bacteriophage Coevolution in the Human Gut: Implications for Microbial Diversity and Functionality. *Trends Microbiol.* **25**, 614–623 (2017).
5. C. H. Wigington, *et al.*, Re-examination of the relationship between marine virus and microbial cell abundances. *Nat. Microbiol. 2016 13* **1**, 1–9 (2016).
6. B. Knowles, *et al.*, Lytic to temperate switching of viral communities. *Nature* **531**, 466–470 (2016).
7. F. H. Coutinho, *et al.*, Marine viruses discovered via metagenomics shed light on viral strategies throughout the oceans. *Nat. Commun. 2017 81* **8**, 1–12 (2017).
8. T. F. Thingstad, Elements of a theory for the mechanisms controlling abundance, diversity, and biogeochemical role of lytic bacterial viruses in aquatic systems. *Limnol. Oceanogr.* **45**, 1320–1328 (2000).
9. T. F. Thingstad, S. Vage, J. E. Storesund, R. A. Sandaa, J. Giske, A theoretical analysis of how strain-specific viruses can control microbial species diversity. *Proc. Natl. Acad. Sci. U. S. A.* **111**, 7813–7818 (2014).
10. S. Maslov, K. Sneppen, Population cycles and species diversity in dynamic

Kill-the-Winner model of microbial ecosystems. *Sci. Rep.* **7**, 1–8 (2017).

11. C. B. Silveira, A. Luque, F. Rohwer, The landscape of lysogeny across microbial community density, diversity and energetics. *Environ. Microbiol.* **23**, 4098–4111 (2021).
12. A. B. Shreiner, J. Y. Kao, V. B. Young, The gut microbiome in health and in disease. *Curr. Opin. Gastroenterol.* **31**, 69 (2015).
13. A. N. Shkoporov, *et al.*, The Human Gut Virome Is Highly Diverse, Stable, and Individual Specific. *Cell Host Microbe* **26**, 527-541.e5 (2019).
14. A. C. Gregory, *et al.*, The Gut Virome Database Reveals Age-Dependent Patterns of Virome Diversity in the Human Gut. *Cell Host Microbe* **28**, 724-740.e8 (2020).
15. B. E. Dutilh, *et al.*, A highly abundant bacteriophage discovered in the unknown sequences of human faecal metagenomes. *Nat. Commun.* **5**, 1–11 (2014).
16. A. N. Shkoporov, *et al.*, ΦCrAss001 represents the most abundant bacteriophage family in the human gut and infects Bacteroides intestinalis. *Nat. Commun. 2018 91* **9**, 1–8 (2018).
17. T. Maniatis, *et al.*, Recognition sequences of repressor and polymerase in the operators of bacteriophage lambda. *Cell* **5**, 109–113 (1975).
18. C. Lee, S. Lee, S. G. Shin, S. Hwang, Real-time PCR determination of rRNA gene copy number: Absolute and relative quantification assays with Escherichia coli. *Appl. Microbiol. Biotechnol.* **78**, 371–376 (2008).
19. W. H. Chin, *et al.*, Bacteriophage adaptation to a mammalian mucosa reveals a trans-domain evolutionary axis. *bioRxiv*, 2021.05.11.443681 (2021).
20. H. J. Kim, D. Huh, G. Hamilton, D. E. Ingber, Human Gut-on-a-Chip inhabited

by microbial flora that experiences intestinal peristalsis-like motions and flow. *Lab Chip* **12**, 2165–74 (2012).

21. C. H. Wigington, *et al.*, Re-examination of the relationship between marine virus and microbial cell abundances. *Nat. Microbiol. 2016 13* **1**, 1–9 (2016).
22. J. S. Paterson, *et al.*, A hydrocarbon-contaminated aquifer reveals a Piggyback-the-Persistent viral strategy. *FEMS Microbiol. Ecol.* **95** (2019).
23. A. N. Shkoporov, C. Hill, Bacteriophages of the Human Gut: The “Known Unknown” of the Microbiome. *Cell Host Microbe* **25**, 195–209 (2019).
24. A. Luque, C. B. Silveira, Quantification of Lysogeny Caused by Phage Coinfections in Microbial Communities from Biophysical Principles. *mSystems* **5** (2020).
25. L. F. Camarillo-Guerrero, A. Almeida, G. Rangel-Pineros, R. D. Finn, T. D. Lawley, Massive expansion of human gut bacteriophage diversity. *Cell* **184**, 1098-1109.e9 (2021).
26. C. Huttenhower, *et al.*, Structure, function and diversity of the healthy human microbiome. *Nat. 2012 4867402* **486**, 207–214 (2012).
27. E. S. Lim, *et al.*, Early life dynamics of the human gut virome and bacterial microbiome in infants. *Nat. Med.* **21**, 1228–1234 (2015).
28. G. Liang, *et al.*, The stepwise assembly of the neonatal virome is modulated by breastfeeding. *Nat. 2020 5817809* **581**, 470–474 (2020).
29. V. Gouyer, F. Gottrand, J.-L. Desseyn, The Extraordinarily Complex but Highly Structured Organization of Intestinal Mucus-Gel Unveiled in Multicolor Images. *PLoS One* **6**, e18761 (2011).
30. H. Schneider, T. Pelaseyed, F. Svensson, M. E. V. Johansson, Study of mucin turnover in the small intestine by in vivo labeling. *Sci. Reports 2018 81* **8**, 1–11

(2018).

31. H. Li, *et al.*, The outer mucus layer hosts a distinct intestinal microbial niche. *Nat. Commun. 2015 61* **6**, 1–13 (2015).

32. H. Brüssow, Microbiota and the human nature: Know thyself. *Environ. Microbiol.* **17**, 10–15 (2015).

33. P. J. Turnbaugh, *et al.*, A core gut microbiome in obese and lean twins. *Nature* **457**, 480 (2009).

34. J. Bondy-Denomy, *et al.*, Prophages mediate defense against phage infection through diverse mechanisms. *ISME J. 2016 1012* **10**, 2854–2866 (2016).

Chapter V

Concluding remarks and phages *in vivo* moving forward

Conclusion

1. Studying phages *in vivo* is just … really hard!

The reputation of phages as harmless viruses to humans is well-accepted within the scientific and medical communities on the basis that phages do not exploit eukaryotic cells to propagate (1). However, whether phages are truly “inert” within the human body remains an enigmatic inquiry. This is especially resounding within the human gut where a large density of phages exists as a natural viral component (2). As my literature review has brought to light, key questions on phage interactions with the gut microbiome and the human gut itself have only began to unfold in the recent decade. With that, we still lack adequate fundamental understanding of phages in the gut, particularly within the areas of their evolution and ecology. Both of which are pertinent in describing the nature of our native gut phages and their potential ramifications on the overall gut ecosystem and ultimately, our health.

Challenges to-date are largely centred on disentangling the nuances of phage evolutionary and ecological interactions within the gut niche. Often, these interactions – particularly at higher ecological levels (e.g. community and ecosystem levels) – become exponentially intricate and intangible (3). Studies were also chiefly reporting from an observational stance, particularly via gut content metagenomics (4–7). However, these observations remain largely untested in the empirical sense. This is further exacerbated by the lack of a physiologically relevant yet experimentally tractable model gut system. Currently, most studies adopt either overly simplistic *in vitro* cell cultures or vastly elaborate gut animal models. Collectively, these challenges reiterate our necessity for interdisciplinary and integrated approaches (3), in order to uncover some of the fundamental workings of the viral dark matter that resides within

our gut. In this spirit, my thesis represents some initial forays into these challenges and fundamental questions on phage evolution and ecology in the gut; with the hope that foundations here would seed further fundamental explorations and even, offer novel approaches for advancing applied phage research.

2. Organ-on-a-chips: Giving more experimental control to the scientist

The first step in this foray is through the fabrication of a gut-on-a-chip microfluidic device. This device serves as a middle-ground between traditional *in vitro* cultures and *in vivo* models. By that, the gut-on-a-chip offers two major advantages: i) recapitulating relevant physiological gut conditions; and ii) providing *in vitro* experimental amenability while minimising the intractability commonly encountered with elaborate animal gut models. Given these incredible advantages pertaining to the organ-on-a-chip platform, I encouraged the wider community of phage biologists – in an opinion article encompassing my first thesis chapter – to embrace this technological innovation for future explorations of phages and microbes *in vivo* (8).

A significant challenge to embracing the organ-on-a-chip platform is the highly interdisciplinary nature of the technology; beginning with engineering principles such as microfabrication and lithography, all the way to mammalian cell culture, organ physiology and microbiology. Not only would an individual require a nominal grasp on the backgrounds across the relevant disciplines, but to also master key techniques specific to each discipline in order to adequately oversee the organ-on-a-chip from the beginning to the end. From experience, these factors could deter prospective researchers from investing valuable time and resources in establishing a functional organ-on-a-chip platform. To this, my second thesis chapter presented a step-by-step

guide on how to fabricate a simple gut-on-a-chip, and to operate and maintain the device for downstream experimentation. I also covered key troubleshooting points that will hopefully aid prospective researchers through the technical trials and tribulations that may await. Ultimately, by establishing this protocol, I also envisage that prospective researchers will leverage upon the technical foundations to innovate and enhance the platform. Indeed, this foundation could also lead to the conceptualisation of other organ models depending on the research question of interest. Overall, this adds to the strengths of the organ-on-a-chip platform in its capacity for further complexity and flexibility where necessary.

3. Playing with phages in the gut-on-a-chip: What I have learnt?

Several studies have leveraged gut-on-a-chips of various designs and intricacies in microbiological investigations that range from microbial colonisation, infection dynamics and mucosal immunology (9–13). Nonetheless, and to the best of my knowledge, my thesis represents the first applications of the gut-on-a-chip in studying phage evolution and ecology within the mammalian gut context. In my third chapter, I leveraged the gut-on-a-chip as a platform to experimentally evolve phages within a life-like mucosal environment. In doing so, I have demonstrated that selection pressures from the gut mucosa, particularly mucus turnover and glycosylation patterns, can directly drive phage evolution to favour mucus-adherence phenotypes (14). This subsequently lent phages with enhanced phage persistence within the mucosal environment. These mucosal selection pressures would not have otherwise been recapitulated in traditional static cell culture, nor easily controlled and manipulated in animal models. By demonstrating that phages can directly respond to mucosal selection pressures, I have expanded phage evolution beyond the

conventional confines of phage-bacteria co-evolution. This may have significant ramifications on future gut virome studies, particularly in expanding the spotlight to also encompass for human host factors such as mucin glycosylation genotypes. Indeed, the ability of phages to evolve to the human gut mucosa in light of previous studies demonstrating mucosal selectivity on phages, may set the foundations for phage-mammalian co-evolution in the gut. Eventually, this co-evolution could contribute to the uniqueness and individuality of our gut virome (6). Perhaps, the missing puzzle to the story of our gut virome is not solely narrated by our gut microbiome but also the gut habitat itself. With that, findings within my third thesis chapter provide empirical support for a three-way (i.e. tripartite) co-evolution between phages, bacteria and their mammalian gut niche (15).

In my fourth thesis chapter, I shifted my focus to address an ecological query on phage-bacteria population dynamics in the gut mucosal environment. This query stems from the collective evidence that the human gut virome is a composite of virulent and temperate phages (2, 6, 16). Estimating the prevalence and interplay between phage-mediated lysis and lysogeny is essential to describe the emergent phage-bacteria population dynamics in the gut. In doing so, we may also begin to identify often intangible, fundamental ecological mechanisms that govern phage-bacteria populations in the gut. However, there is hitherto no direct empirical investigations on the extents of lytic and lysogenic lifecycles within the phage-predominant gut virome. To this, I leveraged the experimental amenability of the gut-on-a-chip and the quantitative throughput from quantitative PCR to track phage-bacteria densities in the mucosal layer at high temporal resolution. I was able to demonstrate that the establishing dynamics between isogenic virulent and temperate phages within the

mucosa were highly stochastic. This stochasticity emerged from subtle interplays between lytic and lysogenic phage regimes. To which, I identified superinfection exclusion as a key ecological mechanism that drove the concurrent lytic and lysogenic strategies in the mucosal environment. Crucially, I argued that phage-to-bacteria ratios (PBR) are poor predictors and descriptors of underlying phage regimes. Therefore, I proposed that other quantitative metrics, such as temporal density data, should be leveraged *in lieu* of PBR to construct reliable ecological depictions of phages within an ecosystem. While an isogenic community is a far cry from representing a highly diverse natural gut virome and microbiome, the findings in this chapter serves as a pioneering illustration that we can overcome some of the empirical challenges in testing phage ecological hypotheses by adopting an integrated experimental approach.

4. Phages *in vivo* and beyond

We are only at the tip of the iceberg in our understanding of the roles that phages play within our bodies and how they affect us from a daily to long-term basis. Undoubtedly, exploring phages *in vivo* becomes exponentially nuanced and challenging as we investigate from the sub-cellular level up to the collective human super-organism. Tackling this will require a concerted effort from prospective researchers to leverage the scientific synergy that comes with interdisciplinary collaborations. As we move towards a future where multidisciplinary sciences becomes increasingly commonplace, our shared expertise will further stretch the boundaries of technological innovations and empirical ideologies. Ultimately, this may lend innovative and novel approaches that could someday revolutionise our empirical ways not only within phage biology, but also within the broader context of microbial sciences. In this space, I hope

that the adjective “intractable” in microbial sciences would someday imply a scientific “challenge” to be taken head-on, as opposed to an “impossibility”.

The COVID-19 pandemic has undoubtedly shifted the public spotlight on microbial sciences and translational medicine. While any form of scientific awareness is always welcomed, an inevitable side-effect of “headline” microbial pathogens such as the current SARS-CoV-2 virus, is a highly biased and negative perception towards the viral and microbial world. Human viral pathogens as such are in fact, the minority of a much larger, global and historic landscape of viruses; namely, phages. Indeed, phages are some of the earliest viruses that have contributed to the evolution of life itself. Since then, phages have co-existed and evolved alongside increasingly complex multicellular lifeforms including humans (17). Given the eons of evolutionary history between phages and eukaryotes, there is a wealth of evolutionary traits that remains undiscovered and untapped within the space of fundamental and applied phage sciences, which could someday benefit humanity. Essentially, it is too easy – and somewhat ignorant – to imply that the human-phage relationship is irrelevant purely on the basis that phages do not bear harm by exploiting eukaryotes as replicative hosts. In addition to shedding light on the very nature of our harmonic co-existence with phages, we might consider leveraging our expanding knowledge to also balance out the negative connotations that are often associated with “viruses”. The normalisation of phages within the public view is even more resounding considering that we are still dealing with an underlying antibiotic resistance pandemic; to which phages are increasingly viable as therapeutic alternatives against recalcitrant and life-threatening bacterial infections *in vivo* (18). Just like there are “friendly” bacteria, we

also have “friendly” viruses (i.e. phages) living amongst and within us. Let us give them the welcome and scientific curiosity they deserve.

References

1. C. Brives, J. Pourraz, Phage therapy as a potential solution in the fight against AMR: obstacles and possible futures. *Palgrave Commun. 2020 61* **6**, 1–11 (2020).
2. A. N. Shkoporov, C. Hill, Bacteriophages of the Human Gut: The “Known Unknown” of the Microbiome. *Cell Host Microbe* **25**, 195–209 (2019).
3. S. Widder, *et al.*, Challenges in microbial ecology: building predictive understanding of community function and dynamics. *ISME J. 2016 1011* **10**, 2557–2568 (2016).
4. M. Breitbart, *et al.*, Metagenomic analyses of an uncultured viral community from human feces. *J. Bacteriol.* **185**, 6220–6223 (2003).
5. S. Minot, *et al.*, Rapid evolution of the human gut virome. *Proc. Natl. Acad. Sci. U. S. A.* **110**, 12450–12455 (2013).
6. A. N. Shkoporov, *et al.*, The Human Gut Virome Is Highly Diverse, Stable, and Individual Specific. *Cell Host Microbe* **26**, 527-541.e5 (2019).
7. L. F. Camarillo-Guerrero, A. Almeida, G. Rangel-Pineros, R. D. Finn, T. D. Lawley, Massive expansion of human gut bacteriophage diversity. *Cell* **184**, 1098-1109.e9 (2021).
8. W. H. Chin, J. J. Barr, Phage research in “organ-on-chip” devices. *Microbiol. Aust.* **40**, 28–32 (2019).
9. P. Shah, *et al.*, A microfluidics-based in vitro model of the gastrointestinal human–microbe interface. *Nat. Commun. 2016 71* **7**, 1–15 (2016).
10. H. J. Kim, H. Li, J. J. Collins, D. E. Ingber, Contributions of microbiome and mechanical deformation to intestinal bacterial overgrowth and inflammation in a human gut-on-a-chip. *Proc. Natl. Acad. Sci. U. S. A.* **113**, E7–E15 (2016).

11. W. Shin, H. J. Kim, Intestinal barrier dysfunction orchestrates the onset of inflammatory host-microbiome cross-talk in a human gut inflammation-on-a-chip. *Proc. Natl. Acad. Sci. U. S. A.* **115**, E10539–E10547 (2018).
12. R. Villenave, *et al.*, Human Gut-On-A-Chip Supports Polarized Infection of Coxsackie B1 Virus In Vitro. *PLoS One* **12**, e0169412 (2017).
13. A. Sontheimer-Phelps, *et al.*, Human Colon-on-a-Chip Enables Continuous In Vitro Analysis of Colon Mucus Layer Accumulation and Physiology. *Cmgh* **9**, 507–526 (2020).
14. W. H. Chin, *et al.*, Bacteriophage adaptation to a mammalian mucosa reveals a trans-domain evolutionary axis. *bioRxiv*, 2021.05.11.443681 (2021).
15. J. J. Barr, Missing a Phage: Unraveling Tripartite Symbioses within the Human Gut. *mSystems* **4** (2019).
16. M.-S. Kim, J.-W. Bae, Lysogeny is prevalent and widely distributed in the murine gut microbiota. *ISME J. 2018 124* **12**, 1127–1141 (2018).
17. E. V. Koonin, V. V. Dolja, A virocentric perspective on the evolution of life. *Curr. Opin. Virol.* **3**, 546–557 (2013).
18. F. L. Gordillo Altamirano, J. J. Barr, Phage therapy in the postantibiotic era. *Clin. Microbiol. Rev.* **32** (2019).

Annex

Annex 1: Background mutations in ancestral phage population. Background mutations from the founding (ancestral) phage population that were subtracted from the experimental evolution phage transfers.

Position	Gene	Description	Mutation	Annotation	Frequency
1,968	*rIIA* ←	protector from prophage-induced early lysis	T→G	E74D (GA<u>A</u>→GA<u>C</u>)	100%
4,843	*DNA-dependent ATPase_ topoisomerase II in T4 and related phages an insertion splits the large Topo II subunit in two parts (gp60 and gp39); gp39 topoisomerase II_ large subunit_ N-terminalregion* ←	topoisomerase II, large subunit	T→C	I159V (<u>A</u>TA→<u>G</u>TA)	100%
10,948	*Dda.1 hypothetical protein* ←	hypothetical protein	G→A	P26S (<u>C</u>CT→<u>T</u>CT)	100%
40,649	*gp55.2 hypothetical protein* ←	hypothetical protein	T→C	Q41Q (CA<u>A</u>→CA<u>G</u>)	100%
60,931	*Tk.4 conserved hypothetical protein* ←	hypothetical protein	+ACAATC	coding (447/468 nt)	7.80%
61,272	*Tk.4 conserved hypothetical protein* ←	hypothetical protein	T→C	S36G (<u>A</u>GT→<u>G</u>GT)	100%
83,815	*C-terminus is predicted integral membrane domain; gp7 baseplate wedge initiator* →	baseplate wedge initiator	T→C	F259S (T<u>T</u>T→T<u>C</u>T)	100%
92,379:2	*can be added after phage completion; responsible for irreversible adsorption to host cells; gp12 Short tail fibers → / → neck or collar protein; gp13 neck protein*	short tail fibers protein/neck protein	+AG	intergenic (+267/-1213)	100%
92,379:4	*can be added after phage completion; responsible for irreversible adsorption to host cells; gp12 Short tail fibers → / → neck or collar protein; gp13 neck protein*	short tail fibers protein/neck protein	+C	intergenic (+267/-1213)	63.60%
92,379:5	*can be added after phage completion; responsible for irreversible adsorption to host*	short tail fibers protein/neck protein	+T	intergenic (+267/-1213)	63.60%

	cells; gp12 Short tail fibers → / → neck or collar protein; gp13 neck protein				
92,379:6	*can be added after phage completion; responsible for irreversible adsorption to host cells; gp12 Short tail fibers → / → neck or collar protein; gp13 neck protein*	short tail fibers protein/neck protein	+T	intergenic (+267/-1213)	63.60%
92,379:7	*can be added after phage completion; responsible for irreversible adsorption to host cells; gp12 Short tail fibers → / → neck or collar protein; gp13 neck protein*	short tail fibers protein/neck protein	+T	intergenic (+267/-1213)	63.60%
92,379:8	*can be added after phage completion; responsible for irreversible adsorption to host cells; gp12 Short tail fibers → / → neck or collar protein; gp13 neck protein*	short tail fibers protein/neck protein	+G	intergenic (+267/-1213)	63.60%
92,379:9	*can be added after phage completion; responsible for irreversible adsorption to host cells; gp12 Short tail fibers → / → neck or collar protein; gp13 neck protein*	short tail fibers protein/neck protein	+G	intergenic (+267/-1213)	63.60%
92,379:10	*can be added after phage completion; responsible for irreversible adsorption to host cells; gp12 Short tail fibers → / → neck or collar protein; gp13 neck protein*	short tail fibers protein/neck protein	+C	intergenic (+267/-1213)	63.60%
92,379:12	*can be added after phage completion; responsible for irreversible adsorption to host cells; gp12 Short tail*	short tail fibers protein/neck protein	+C	intergenic (+267/-1213)	63.60%

	fibers → / → neck or collar protein; gp13 neck protein				
151,878	*gp34 long tail fiber_ proximal subunit →*	long tail fiber, proximal subunit	A→C	Q356H (CAA→CAC)	100%
154,663	*gp34 long tail fiber_ proximal subunit →*	long tail fiber, proximal subunit	+TTGAATGGG	coding (3853/3870 nt)	10.70%
161,334:1	*arn ←*	inhibitor of MrcBC restriction endonuclease	+T	coding (259/285 nt)	100%

Annex 2: *De novo* mutations in experimental evolution phage transfers (gut-on-a-chip and test-tube replicates)

2.1. Gut-on-a-chip replicate 1

Total *de novo* mutation count: Transfers 1 – 5 (8); Transfer 6 – 10 (6)

					Transfer										
Position	**Gene**	**Description**	**Mutation**	**Annotation**	**1**	**2**	**3**	**4**	**5**	**6**	**7**	**8**	**9**	**10**	**Notes**
5,945	*goF* ←	mRNA metabolism modulator	Δ21 bp	coding (290-310/426 nt)	21.30%	49.90%	66.70%	72.00%	16.90%	30.00%	0.00%	0.00%	0.00%	0.00%	Counted
47,443	*also found in phage RB49; gp49.1 conserved protein of unknown function* ←	hypothetical protein	+TCTTCCGGC	coding (66/156 nt)	0.00%	0.00%	0.00%	6.00%	0.00%	0.00%	0.00%	0.00%	0.00%	0.00%	Counted
61,386	*vs* ←	valyl-tRNA synthetase modifier	C→T	L112L (TTG→TTA)	22.70%	26.20%	0.00%	0.00%	0.00%	0.00%	0.00%	0.00%	0.00%	0.00%	Counted
87,089	*gp8 baseplate wedge subunit* →	baseplate wedge subunit	$(TAT)_{3\rightarrow4}$	coding (959/1005 nt)	0.00%	0.00%	0.00%	0.00%	0.00%	0.00%	0.00%	0.00%	0.00%	8.30%	Counted
92,379:1	*can be added after phage completion; responsible for irreversible adsorption to host cells; gp12*	short tail fibers protein/neck protein	+AAG	intergenic (+267/-1213)	100.00%	0.00%	0.00%	0.00%	0.00%	0.00%	0.00%	0.00%	0.00%	0.00%	Alignment artefact; not counted

	Short tail fibers → / → neck or collar protein; gp13 neck protein														
92,379:9	*can be added after phage completion; responsible for irreversible adsorption to host cells; gp12 Short tail fibers → / → neck or collar protein; gp13 neck protein*	short tail fibers protein/neck protein	+GCCC	intergenic (+267/-1213)	100.00%	0.00%	0.00%	0.00%	0.00%	0.00%	0.00%	0.00%	0.00%	0.00%	Alignment artefact; not counted
92,379:11	*can be added after phage completion; responsible for irreversible adsorption to host cells; gp12 Short tail fibers → / → neck or collar protein;*	short tail fibers protein/neck protein	+C	intergenic (+267/-1213)	0.00%	0.00%	50.00%	0.00%	0.00%	0.00%	0.00%	0.00%	0.00%	0.00%	Alignment artefact; not counted

	gp13 neck protein														
110,582	*hoc* ←	head outer capsid protein	C→T	D246N (GAT→AAT)	44.60%	31.60%	31.40%	83.30%	18.30%	31.20%	5.40%	5.40%	0.00%	5.40%	Counted
146,596	*Frd.3 hypothetical protein* ←	hypothetical protein	A→G	M70T (ATG→ACG)	15.90%	8.30%	0.00%	0.00%	0.00%	0.00%	0.00%	0.00%	0.00%	0.00%	Counted
148,062	*segG* ←	homing endonuclease	+ATA	coding (482/633 nt)	0.00%	0.00%	0.00%	6.40%	0.00%	0.00%	0.00%	0.00%	0.00%	0.00%	Counted
156,811	*gp37 long tail fiber_ distal subunit* →	long tail fiber, distal subunit	24 bp→24 bp	coding (268-291/3081 nt)	0.00%	0.00%	8.10%	0.00%	0.00%	0.00%	10.10%	11.20%	0.00%	0.00%	Counted
156,819	*gp37 long tail fiber_ distal subunit* →	long tail fiber, distal subunit	C→G	V92V (GTC→GTG)	0.00%	0.00%	0.00%	0.00%	6.00%	6.40%	0.00%	0.00%	5.80%	0.00%	Counted
156,830	*gp37 long tail fiber_ distal subunit* →	long tail fiber, distal subunit	T→C	I96T (ATT→ACT)	0.00%	0.00%	0.00%	0.00%	0.00%	0.00%	0.00%	0.00%	5.70%	0.00%	Counted
161,336:1	*arn* ←	inhibitor of McrBC restriction endonuclease	+T	coding (257/285 nt)	0.00%	0.00%	0.00%	0.00%	0.00%	100.00%	100.00%	100.00%	100.00%	100.00%	Alignment artefact; not counted

2.2. Gut-on-a-chip replicate 2

Total *de novo* mutation count: Transfers 1 – 5 (5); Transfer 6 – 10 (9)

					Transfer										
Position	**Gene**	**Description**	**Mutation**	**Annotation**	**1**	**2**	**3**	**4**	**5**	**6**	**7**	**8**	**9**	**10**	**Notes**
2,436	*rIIA.1 hypothetical protein ← I ← a 50-bp segment is inserted in T4 gene 60 that forms an mRNA secondary structure that is translationally bypassed; topoisomerase II in T4 and related phages an insertion splits the large Topo II subunit in two parts (gp60 and gp39); gp60 topoisomerase II_ large subunit_ C-terminalregion*	hypothetical protein/topoisomerase II, large subunit	Δ1 bp	intergenic (-33/+22)	0.00 %	0.00 %	0.00 %	0.00 %	0.00 %	0.00 %	0.00 %	0.00 %	5.30 %	27.00 %	Counted

13,279:1	*ModA.2 hypothetical protein ←*	hypothetical protein	+A	coding (88/183 nt)	0.00 %	0.00 %	0.00 %	0.00 %	0.00 %	0.00 %	0.00 %	0.00 %	0.00 %	9.30 %	Counted
13,279:2	*ModA.2 hypothetical protein ←*	hypothetical protein	+A	coding (88/183 nt)	0.00 %	0.00 %	0.00 %	0.00 %	0.00 %	0.00 %	0.00 %	0.00 %	0.00 %	9.30 %	Counted
19,648	*gp61.2 hypothetical protein ←*	hypothetical protein	G→A	H33Y (CAT →TAT)	8.20 %	0.00 %	0.00 %	0.00 %	0.00 %	0.00 %	0.00 %	0.00 %	0.00 %	0.00 %	Counted
31,984	*gp45 also is required for synthesis of late RNA_ acting as a 'mobile enhancer' and in effect taking the place of a -35 region for the T4 sigma factor responsible for late transcription ; gp45 sliding clamp_ DNA polymerase accessory protein ←*	sliding clamp, DNA polymerase accessory protein	T→C	K203E (AAA →GAA)	0.00 %	0.00 %	0.00 %	0.00 %	0.00 %	0.00 %	0.00 %	0.00 %	0.00 %	9.80 %	Counted
50,245	*NrdC.4 conserved hypothetical protein ←*	hypothetical protein	A→G	F220L (TTT →CTT)	7.80 %	0.00 %	0.00 %	0.00 %	0.00 %	0.00 %	0.00 %	0.00 %	0.00 %	0.00 %	Counted
55,310	*NrdC.10 conserved hypothetical*	hypothetical protein/hypo	T→C	intergenic (-3/+112)	0.00 %	0.00 %	0.00 %	0.00 %	0.00 %	0.00 %	8.90 %	30.10%	30.30%	36.20 %	Counted

	protein ← / ← NrdC.11 conserved hypothetical protein	thetical protein													
64,151	*Vs.7 conserved hypothetical protein ←*	hypothetical protein	Δ1 bp	coding (95/330 nt)	10.10%	0.00 %	0.00 %	0.00 %	0.00 %	0.00 %	0.00 %	0.00 %	0.00 %	0.00 %	Counted
92,379:2	*can be added after phage completion; responsible for irreversible adsorption to host cells; gp12 Short tail fibers → / → neck or collar protein; gp13 neck protein*	short tail fibers protein/neck protein	+A	intergenic (+267/-1213)	0.00 %	0.00 %	0.00 %	100.00%	0.00 %	0.00 %	0.00 %	0.00 %	0.00 %	0.00 %	Alignment artefact; not counted
92,379:8	*can be added after phage completion; responsible for irreversible adsorption to host cells; gp12 Short tail fibers → / →*	short tail fibers protein/neck protein	+GGC	intergenic (+267/-1213)	100.00%	0.00 %	0.00 %	0.00 %	0.00 %	0.00 %	0.00 %	0.00 %	0.00 %	0.00 %	Alignment artefact; not counted

	neck or collar protein; gp13 neck protein														
142,788	*NrdA.1 conserved hypothetical protein* ←	hypothetical protein	A→G	R71R (CGT→CGC)	0.00%	5.20%	0.00%	0.00%	0.00%	0.00%	0.00%	0.00%	0.00%	0.00%	Counted
149,857	*rnh* ←	ribonuclease	C→T	G284S (GGC→AGC)	0.00%	0.00%	0.00%	0.00%	0.00%	0.00%	0.00%	16.80%	23.00%	15.80%	Counted
156,814	*gp37 long tail fiber_ distal subunit* →	long tail fiber, distal subunit	G→T	G91C (GGC→TGC)	0.00%	0.00%	0.00%	0.00%	0.00%	0.00%	0.00%	0.00%	0.00%	5.10%	Counted
156,819	*gp37 long tail fiber_ distal subunit* →	long tail fiber, distal subunit	C→G	V92V (GTC→GTG)	0.00%	0.00%	0.00%	0.00%	0.00%	7.10%	6.00%	6.20%	6.40%	7.30%	Counted
156,830	*gp37 long tail fiber_ distal subunit* →	long tail fiber, distal subunit	T→C	I96T (ATT→ACT)	0.00%	0.00%	0.00%	0.00%	0.00%	0.00%	0.00%	6.30%	0.00%	7.20%	Counted
157,090	*gp37 long tail fiber_ distal subunit* →	long tail fiber, distal subunit	C→T	R183C (CGC→TGC)	7.90%	0.00%	0.00%	0.00%	0.00%	0.00%	0.00%	0.00%	0.00%	0.00%	Counted
161,336:1	*arn* ←	inhibitor of MrcBC restriction endonuclease	+T	coding (257/285 nt)	0.00%	0.00%	0.00%	0.00%	0.00%	100.00%	100.00%	100.00%	100.00%	100.00%	Alignment artefact; not counted

2.3. Gut-on-a-chip replicate 3

Total *de novo* mutation count: Transfers 1 – 5 (5); Transfer 6 – 10 (9)

					Transfers										
Position	**Gene**	**Description**	**Mutation**	**Annotation**	**1**	**2**	**3**	**4**	**5**	**6**	**7**	**8**	**9**	**10**	**Notes**
27,080	*Imm.1 hypothetical predicted membrane protein ← / ← core DNA polymerase of T4 replisome_ 3'-5' exonuclease ; gp43 DNA polymerase*	putative membrane protein/DNA polymerase	$(A)_{6\rightarrow5}$	intergenic (-82/+103)	0.00 %	0.00 %	0.00 %	0.00 %	0.00 %	0.00 %	10.50%	0.00 %	0.00 %	0.00 %	Counted
83,139	*C-terminus is predicted integral membrane domain; gp7 baseplate wedge initiator →*	baseplate wedge initiator	T→A	Y34N (TAT →AAT)	0.00 %	0.00 %	0.00 %	0.00 %	0.00 %	0.00 %	0.00 %	0.00 %	0.00 %	62.10%	Counted
83,141	*C-terminus is predicted integral membrane domain; gp7 baseplate wedge initiator →*	baseplate wedge initiator	T→A	Y34* (TAT →TAA)	0.00 %	0.00 %	0.00 %	0.00 %	0.00 %	0.00 %	0.00 %	0.00 %	0.00 %	61.80%	Counted
83,142	*C-terminus is predicted integral membrane domain; gp7 baseplate*	baseplate wedge initiator	T→A	F35I (TTT→ ATT)	0.00 %	0.00 %	0.00 %	0.00 %	0.00 %	0.00 %	0.00 %	0.00 %	0.00 %	61.80%	Counted

	wedge initiator →														
83,144	*C-terminus is predicted integral membrane domain; gp7 baseplate wedge initiator →*	baseplate wedge initiator	T→A	F35L (TTT →TTA)	0.00 %	0.00 %	0.00 %	0.00 %	0.00 %	0.00 %	0.00 %	0.00 %	0.00 %	61.90%	Counted
83,719	*C-terminus is predicted integral membrane domain; gp7 baseplate wedge initiator →*	baseplate wedge initiator	A→G	D227G (GAC→GGC)	0.00 %	0.00 %	0.00 %	0.00 %	0.00 %	0.00 %	0.00 %	0.00 %	0.00 %	11.10%	Counted
92,379:1	*can be added after phage completion; responsible for irreversible adsorption to host cells; gp12 Short tail fibers → / → neck or collar protein; gp13 neck protein*	short tail fibers protein/neck protein	+A	intergenic (+267/-1213)	0.00 %	0.00 %	0.00 %	0.00 %	0.00 %	0.00 %	0.00 %	100.00%	0.00 %	0.00 %	Alignment artefact; not counted
92,379:1	*can be added after phage*	short tail fibers	+GAA	intergenic (+267/-1213)	0.00 %	0.00 %	0.00 %	0.00 %	0.00 %	0.00 %	0.00 %	0.00 %	100.00%	0.00 %	Alignment artefa

	completion; responsible for irreversible adsorption to host cells; gp12 Short tail fibers → / → neck or collar protein; gp13 neck protein	protein/neck protein													ct; not counted
92,379:2	*can be added after phage completion; responsible for irreversible adsorption to host cells; gp12 Short tail fibers → / → neck or collar protein; gp13 neck protein*	short tail fibers protein/neck protein	+CTT	intergenic (+267/-1213)	0.00%	0.00%	0.00%	0.00%	0.00%	0.00%	0.00%	100.00%	0.00%	0.00%	Alignment artefact; not counted
92,379:2	*can be added after phage completion; responsible for irreversible adsorption*	short tail fibers protein/neck protein	+T	intergenic (+267/-1213)	0.00%	0.00%	0.00%	0.00%	0.00%	0.00%	0.00%	0.00%	100.00%	0.00%	Alignment artefact; not counted

	to host cells; gp12 Short tail fibers → / → neck or collar protein; gp13 neck protein														
92,379:3	*can be added after phage completion; responsible for irreversible adsorption to host cells; gp12 Short tail fibers → / → neck or collar protein; gp13 neck protein*	short tail fibers protein/neck protein	+CC	intergenic (+267/-1213)	0.00 %	0.00 %	0.00 %	0.00 %	0.00 %	0.00 %	0.00 %	100.00%	0.00 %	0.00 %	Alignment artefact; not counted
92,379:3	*can be added after phage completion; responsible for irreversible adsorption to host cells; gp12 Short tail fibers → / → neck or*	short tail fibers protein/neck protein	+T	intergenic (+267/-1213)	0.00 %	0.00 %	0.00 %	0.00 %	0.00 %	0.00 %	0.00 %	0.00 %	100.00%	0.00 %	Alignment artefact; not counted

	collar protein; gp13 neck protein														
92,379:4	*can be added after phage completion; responsible for irreversible adsorption to host cells; gp12 Short tail fibers → / → neck or collar protein; gp13 neck protein*	short tail fibers protein/neck protein	+GCCC	intergenic (+267/-1213)	0.00 %	0.00 %	0.00 %	0.00 %	0.00 %	0.00 %	0.00 %	0.00 %	100.00%	0.00 %	Alignment artefact; not counted
94,566	*neck or collar protein; gp14 neck protein →*	neck protein	G→A	R15H (CGC →CAC)	0.00 %	0.00 %	0.00 %	0.00 %	0.00 %	0.00 %	0.00 %	0.00 %	9.50 %	0.00 %	Counted
104,272	*head scaffolding protein_ degraded by gp21 protease; gp22 prohead core scaffold protein →*	prohead core scaffold protein	+AGA	coding (188/810 nt)	0.00 %	0.00 %	0.00 %	6.00 %	0.00 %	0.00 %	0.00 %	0.00 %	0.00 %	0.00 %	Counted

127,179	*ATP-dependent DNA ligase; gp30 DNA ligase ←*	DNA ligase	A→G	I12I (ATT→ATC)	24.10%	18.90%	0.00%	0.00%	0.00%	0.00%	0.00%	0.00%	0.00%	0.00%	Counted
132,573	*cd ←*	dCMP deaminase	C→T	G45R (GGG→AGG)	18.20%	10.80%	0.00%	0.00%	0.00%	0.00%	0.00%	0.00%	0.00%	0.00%	Counted
146,887	*Frd.3 hypothetical protein ← / ← DNA replication_ recombination and repair protein_ helix-destabilizing; gp32 single-stranded DNA binding protein*	hypothetical protein/single-stranded DNA binding protein	Δ1 bp	intergenic (-83/+63)	8.90%	0.00%	0.00%	0.00%	0.00%	0.00%	0.00%	0.00%	0.00%	0.00%	Counted
156,811	*gp37 long tail fiber_ distal subunit →*	long tail fiber, distal subunit	24 bp→24 bp	coding (268-291/3081 nt)	0.00%	0.00%	0.00%	0.00%	0.00%	9.70%	10.40%	10.60%	0.00%	0.00%	Counted
156,819	*gp37 long tail fiber_ distal subunit →*	long tail fiber, distal subunit	C→G	V92V (GTC→GTG)	0.00%	0.00%	0.00%	0.00%	0.00%	0.00%	0.00%	0.00%	6.60%	6.00%	Counted
160,776	*t →*	holin lysis mediator	G→A	A185T (GCT→ACT)	10.50%	0.00%	0.00%	0.00%	0.00%	0.00%	0.00%	0.00%	0.00%	0.00%	Counted
161,336:1	*arn ←*	inhibitor of McrBC restriction endonuclease	+T	coding (257/285 nt)	0.00%	0.00%	0.00%	0.00%	0.00%	100.00%	100.00%	100.00%	100.00%	100.00%	Alignment artefact; not counted

2.4. Test tube replicate 1

Total *de novo* mutation count: 2

					Transfers					
Position	**Gene**	**Description**	**Mutation**	**Annotation**	**1**	**2**	**3**	**4**	**5**	**Notes**
92,379:1	*can be added after phage completion; responsible for irreversible adsorption to host cells; gp12 Short tail fibers → / → neck or collar protein; gp13 neck protein*	short tail fibers protein/neck protein	+A	intergenic (+267/-1213)			100%			Alignment artefact; not counted
92,379:1	*can be added after phage completion; responsible for irreversible adsorption to host cells; gp12 Short tail fibers → / → neck or collar protein; gp13 neck protein*	short tail fibers protein/neck protein	+GAA	intergenic (+267/-1213)		100%				Alignment artefact; not counted
92,379:2	*can be added after phage completion; responsible for irreversible adsorption to host cells; gp12 Short tail fibers → / → neck or collar protein; gp13 neck protein*	short tail fibers protein/neck protein	+GC	intergenic (+267/-1213)			100%			Alignment artefact; not counted
92,379:2	*can be added after phage completion; responsible for*	short tail fibers protein/neck protein	+T	intergenic (+267/-1213)		100%				Alignment artefact;

	irreversible adsorption to host cells; gp12 Short tail fibers → / → neck or collar protein; gp13 neck protein									not counted
92,379:3	*can be added after phage completion; responsible for irreversible adsorption to host cells; gp12 Short tail fibers → / → neck or collar protein; gp13 neck protein*	short tail fibers protein/neck protein	+CC	intergenic (+267/-1 213)			100%			Alignment artefact; not counted
156,811	*gp37 long tail fiber_ distal subunit →*	long tail fiber, distal subunit	24 bp→24 bp	coding (268-291/3 081 nt)	11.20 %	0.00%	0.00%	0.00%	0.00%	Counted
156,819	*gp37 long tail fiber_ distal subunit →*	long tail fiber, distal subunit	C→G	V92V (GT<u>C</u>→GT<u>G</u>)	0.00%	0.00%	0.00%	0.00%	6.90%	Counted

2.5. Test-tube replicate 2

Total *de novo* mutation count: 4

Position	Gene	Description	Mutation	Annotation	1	2	3	4	5	Notes
131,182	*rIII ← / ← replaces GroES as cochaperone with GroEL for head (gp23) assembly and also affects topoisomerase; gp31 head assembly cochaperone with GroEL*	lysis inhibition accessory protein/head assembly cochaperone with GroEL	$(ATT)_{3\rightarrow4}$	intergenic (-143/+5)	0.00%	0.00%	0.00%	8.90%	0.00%	Counted
156,811	*gp37 long tail fiber_ distal subunit →*	long tail fiber, distal subunit	24 bp→24 bp	coding (268-291/3081 nt)	0.00%	0.00%	0.00%	0.00%	10.50 %	Counted
156,819	*gp37 long tail fiber_ distal subunit →*	long tail fiber, distal subunit	C→G	V92V (GT<u>C</u>→GT<u>G</u>)	6.60%	6.90%	0.00%	0.00%	0.00%	Counted
156,830	*gp37 long tail fiber_ distal subunit →*	long tail fiber, distal subunit	T→C	I96T (A<u>T</u>T→A<u>C</u>T)	6.40%	0.00%	0.00%	0.00%	0.00%	Counted

2.6. Test-tube replicate 3

Total *de novo* mutation count: 10

Position	Gene	Description	Mutation	Annotation	1	2	3	4	5	Notes
8,770	*dexA* ←	exonuclease A	G→A	S42L (TCA→TTA)	11.70%	0.00%	0.00%	0.00%	0.00%	Counted
26,855	*Imm.1 hypothetical predicted membrane protein* ←	putative membrane protein	A→G	A48A (GCT→GCC)	11.40%	5.10%	0.00%	0.00%	0.00%	Counted
82,636	*baseplate wedge; gp6 baseplate wedge subunit* →	baseplate wedge subunit	C→T	P526S (CCT→TCT)	0.00%	5.50%	5.50%	5.70%	5.80%	Counted
87,621	*tail fiber connector and trigger for tail sheath contraction; gp9 baseplate wedge tail fiber connector* →	baseplate wedge tail fiber connector	C→T	S141S (AGC→AGT)	50.60%	52.30%	49.70%	52.30%	54.00%	Counted
107,067	*segD* ←	homing endonuclease	$(T)_{6\rightarrow5}$	coding (133/672 nt)	0.00%	5.10%	0.00%	0.00%	0.00%	Counted
132,573	*cd* ←	dCMP deaminase	C→T	G45R (GGG→AGG)	49.40%	51.10%	50.10%	53.00%	53.20%	Counted
141,329	*nrdA* ←	aerobic NDP reductase, large subunit	G→A	A452V (GCT→GTT)	12.00%	0.00%	0.00%	0.00%	0.00%	Counted
156,811	*gp37 long tail fiber_ distal subunit* →	long tail fiber, distal subunit	24 bp→24 bp	coding (268-291/3081 nt)	0.00%	0.00%	0.00%	9.60%	0.00%	Counted
156,819	*gp37 long tail fiber_ distal subunit* →	long tail fiber, distal subunit	C→G	V92V (GTC→GTG)	6.60%	6.60%	6.50%	0.00%	5.60%	Counted
156,830	*gp37 long tail fiber_ distal subunit* →	long tail fiber, distal subunit	T→C	I96T (ATT→ACT)	6.70%	0.00%	6.60%	0.00%	5.80%	Counted

Annex 3: Glycan array heatmap (whole phages and recombinant purified Hoc proteins)

3.1. Whole phage glycan array

GROUP	GLYCAN	WT - 10^8 TTEST	WT - 10^8 FOLD	D246N - 10^8 TTEST	D246N - 10^8 FOLD	Δ*hoc* - 10^8 TTEST	Δ*hoc* - 10^8 FOLD	STRUCTURE
GALACTOSE	1A							Lacto-N-Biose I
	1B							N-Acetyllactosamine
	1C							β-1-4-Galactosyl-Galactose
	1D							β-1-6 Galactosyl-N-acetyl Glucosamine
	1E							β-1-3 Galactosyl-N-acetyl Galactosamine
	1F							β-1-3 Gal-N-Acetyl Galactosaminyl-β1-4 Gal-β1-4-Glc
	1G							Lacto-N-tetraose
	1H							Lacto-N-neotetraose
	1I							Lacto-N-neohexaose
	1J							Lacto-N-hexaose
	1K							Globotriose
	1L							Tn Antigen GalNAcα1-O-Ser
	1M							Galactosyl-Tn Antigen
	1N							α1-3 Galactobiose
	1O							Linear B-2 Trisaccharide
	1P							Linear B-6 Trisaccharide
	2A							α1-3, β1-4, α1-3 Galactotetraose
	2B							Galβ1-6Gal
	2C							GalNAcβ1-3Gal
	2D							GalNAcβ1-4Gal
	2E							Galα1-4Galβ1-4GlcNAc
	2F							GalNAcα1-3Galβ1-4Glc
	2G							iso-Lacto-N-octaose
GlcNAc	4A							N,N'-Diacetyl chitobiose
	4B							N,N',N''-Triacetyl chitotriose
	4C							N,N',N'',N'''-Tetraacetyl chitotetraose
	4D							N,N',N'',N''',N'''',N'''''-Hexaacetyl chitohexaose

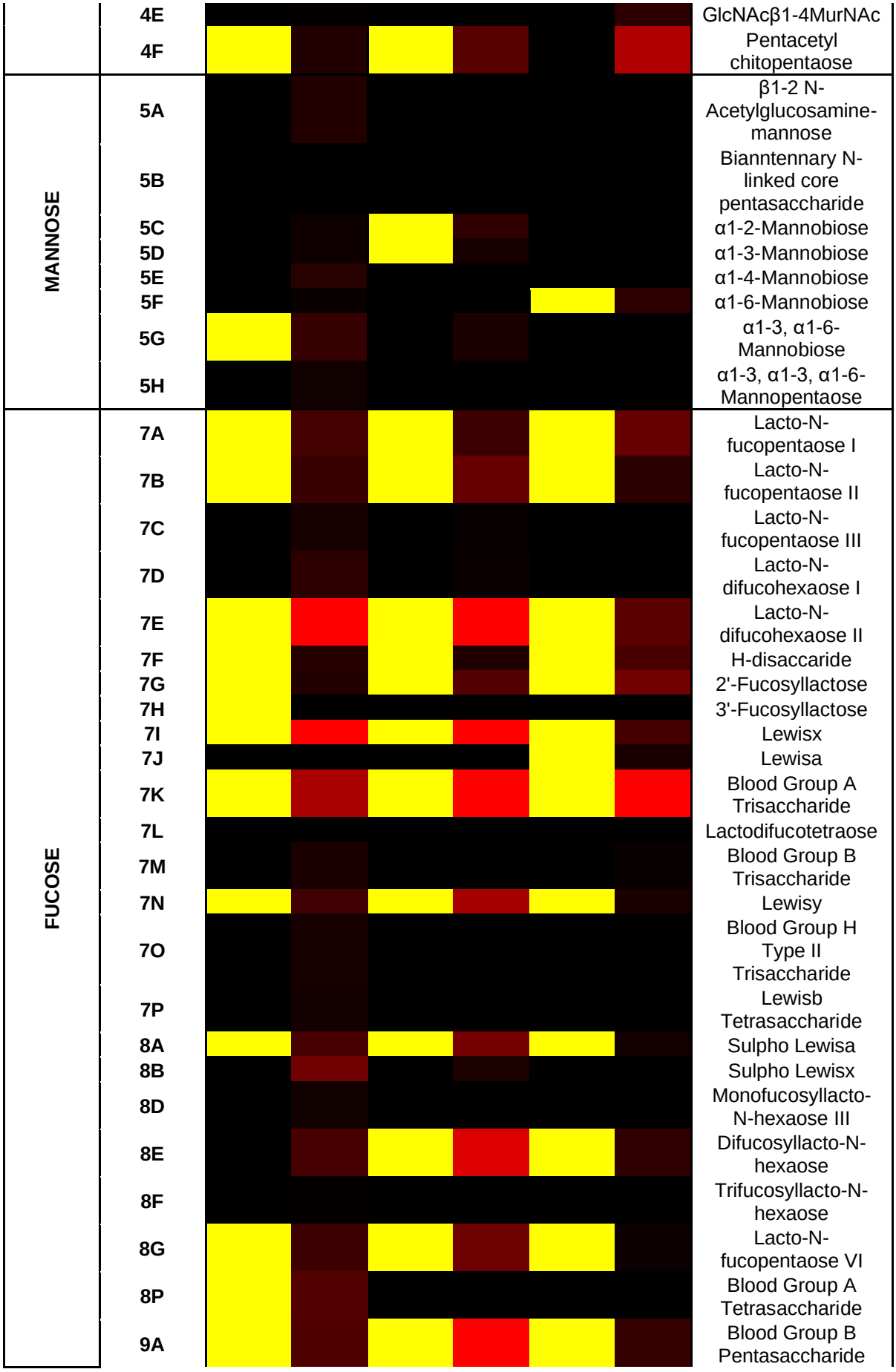
4E
GlcNAcβ1-4MurNAc
4F
Pentacetyl chitopentaose
MANNOSE
5A
β1-2 N-Acetylglucosamine-mannose
5B
Biantennary N-linked core pentasaccharide
5C
α1-2-Mannobiose
5D
α1-3-Mannobiose
5E
α1-4-Mannobiose
5F
α1-6-Mannobiose
5G
α1-3, α1-6-Mannobiose
5H
α1-3, α1-3, α1-6-Mannopentaose
FUCOSE
7A
Lacto-N-fucopentaose I
7B
Lacto-N-fucopentaose II
7C
Lacto-N-fucopentaose III
7D
Lacto-N-difucohexaose I
7E
Lacto-N-difucohexaose II
7F
H-disaccaride
7G
2'-Fucosyllactose
7H
3'-Fucosyllactose
7I
Lewisx
7J
Lewisa
7K
Blood Group A Trisaccharide
7L
Lactodifucotetraose
7M
Blood Group B Trisaccharide
7N
Lewisy
7O
Blood Group H Type II Trisaccharide
7P
Lewisb Tetrasaccharide
8A
Sulpho Lewisa
8B
Sulpho Lewisx
8D
Monofucosyllacto-N-hexaose III
8E
Difucosyllacto-N-hexaose
8F
Trifucosyllacto-N-hexaose
8G
Lacto-N-fucopentaose VI
8P
Blood Group A Tetrasaccharide
9A
Blood Group B Pentasaccharide

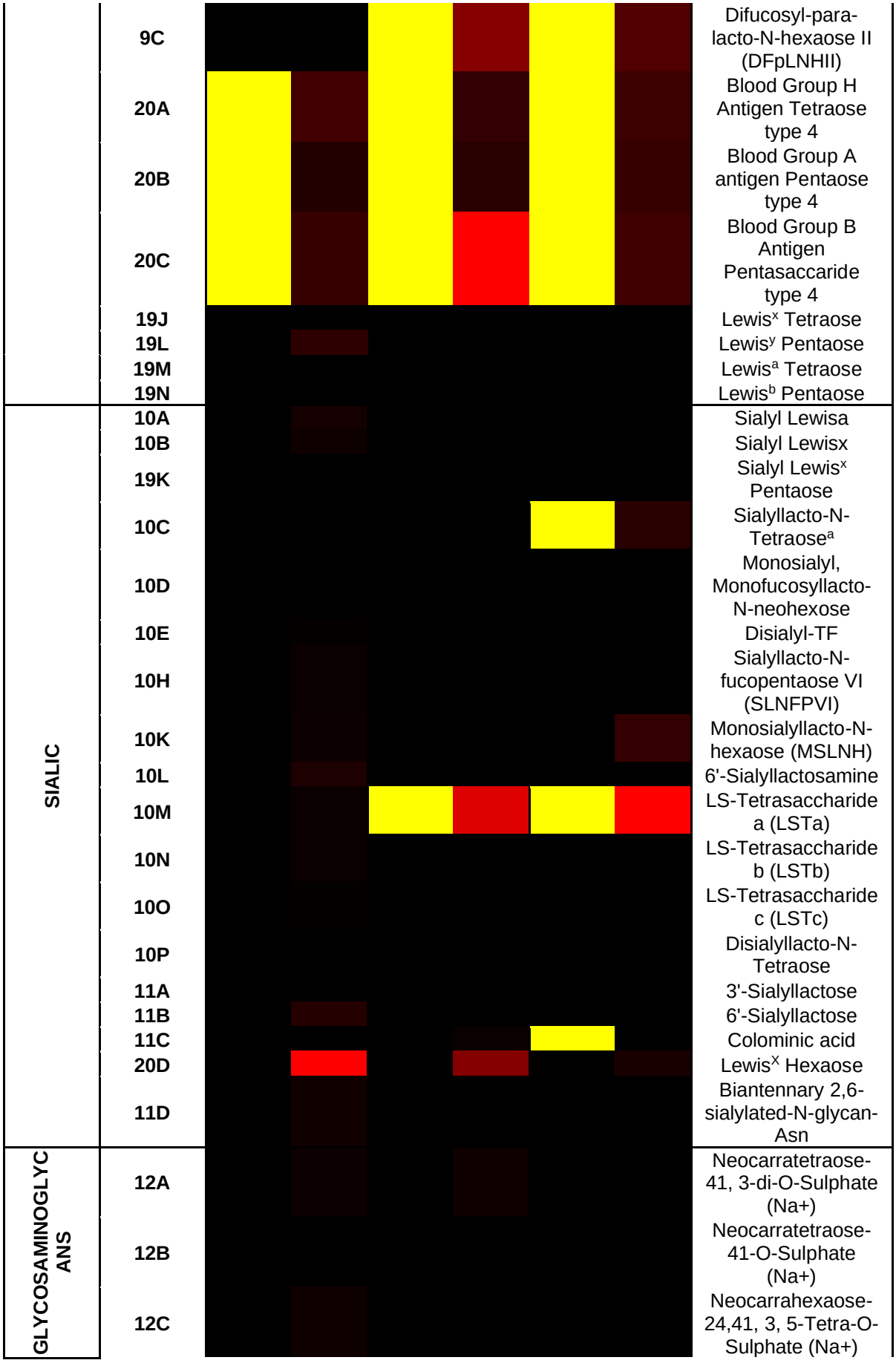
9C
Difucosyl-para-lacto-N-hexaose II (DFpLNHII)
20A
Blood Group H Antigen Tetraose type 4
20B
Blood Group A antigen Pentaose type 4
20C
Blood Group B Antigen Pentasaccaride type 4
19J
Lewis^x Tetraose
19L
Lewis^y Pentaose
19M
Lewis^a Tetraose
19N
Lewis^b Pentaose
SIALIC
10A
Sialyl Lewisa
10B
Sialyl Lewisx
19K
Sialyl Lewis^x Pentaose
10C
Sialyllacto-N-Tetraose^a
10D
Monosialyl, Monofucosyllacto-N-neohexose
10E
Disialyl-TF
10H
Sialyllacto-N-fucopentaose VI (SLNFPVI)
10K
Monosialyllacto-N-hexaose (MSLNH)
10L
6'-Sialyllactosamine
10M
LS-Tetrasaccharide a (LSTa)
10N
LS-Tetrasaccharide b (LSTb)
10O
LS-Tetrasaccharide c (LSTc)
10P
Disialyllacto-N-Tetraose
11A
3'-Sialyllactose
11B
6'-Sialyllactose
11C
Colominic acid
20D
Lewis^X Hexaose
11D
Biantennary 2,6-sialylated-N-glycan-Asn
GLYCOSAMINOGLYCANS
12A
Neocarratetraose-41, 3-di-O-Sulphate (Na+)
12B
Neocarratetraose-41-O-Sulphate (Na+)
12C
Neocarrahexaose-24,41, 3, 5-Tetra-O-Sulphate (Na+)

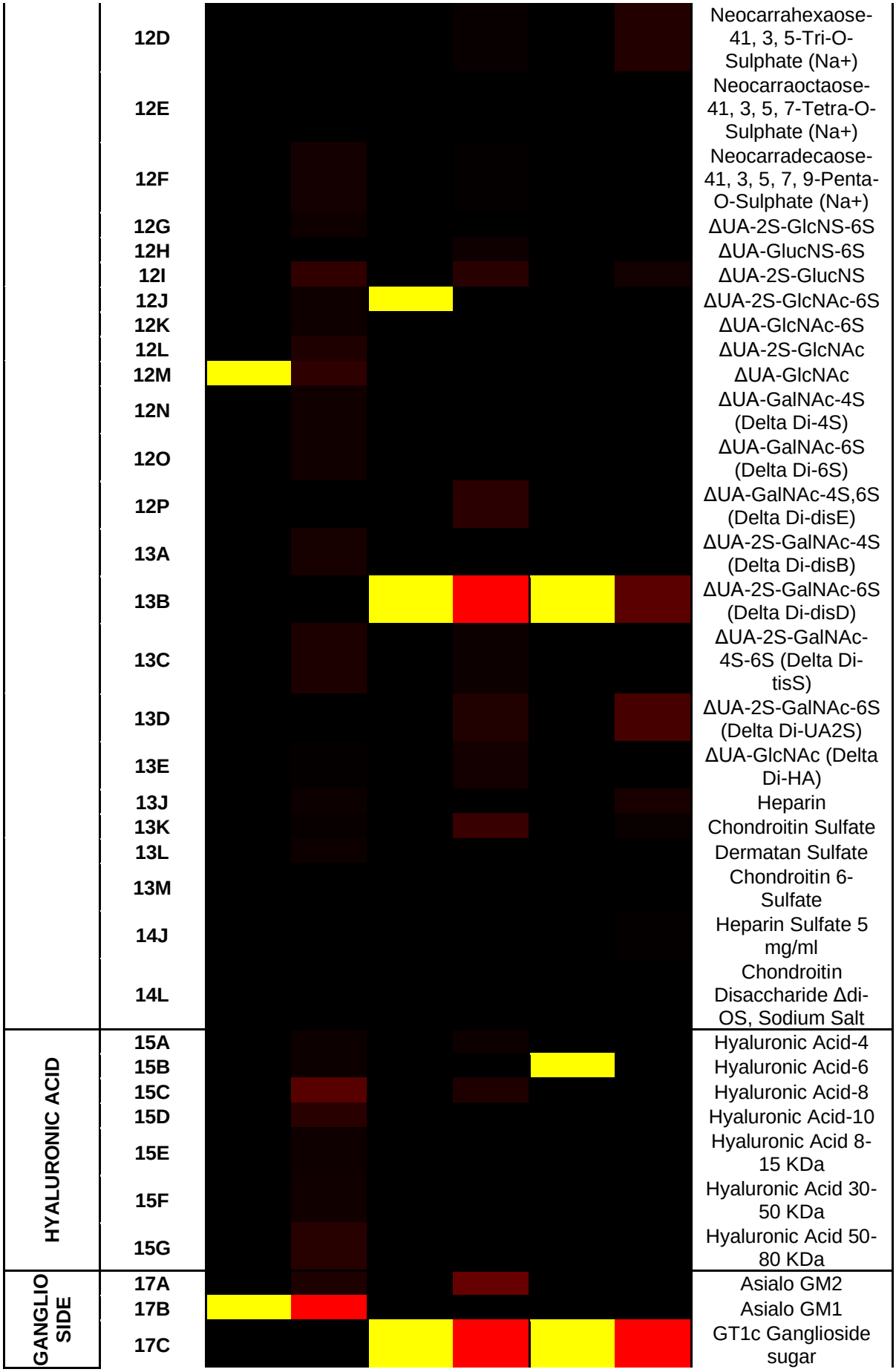
12D
Neocarrahexaose-41, 3, 5-Tri-O-Sulphate (Na+)
12E
Neocarraoctaose-41, 3, 5, 7-Tetra-O-Sulphate (Na+)
12F
Neocarradecaose-41, 3, 5, 7, 9-Penta-O-Sulphate (Na+)
12G
ΔUA-2S-GlcNS-6S
12H
ΔUA-GlucNS-6S
12I
ΔUA-2S-GlucNS
12J
ΔUA-2S-GlcNAc-6S
12K
ΔUA-GlcNAc-6S
12L
ΔUA-2S-GlcNAc
12M
ΔUA-GlcNAc
12N
ΔUA-GalNAc-4S (Delta Di-4S)
12O
ΔUA-GalNAc-6S (Delta Di-6S)
12P
ΔUA-GalNAc-4S,6S (Delta Di-disE)
13A
ΔUA-2S-GalNAc-4S (Delta Di-disB)
13B
ΔUA-2S-GalNAc-6S (Delta Di-disD)
13C
ΔUA-2S-GalNAc-4S-6S (Delta Di-tisS)
13D
ΔUA-2S-GalNAc-6S (Delta Di-UA2S)
13E
ΔUA-GlcNAc (Delta Di-HA)
13J
Heparin
13K
Chondroitin Sulfate
13L
Dermatan Sulfate
13M
Chondroitin 6-Sulfate
14J
Heparin Sulfate 5 mg/ml
14L
Chondroitin Disaccharide Δdi-OS, Sodium Salt
HYALURONIC ACID
15A
Hyaluronic Acid-4
15B
Hyaluronic Acid-6
15C
Hyaluronic Acid-8
15D
Hyaluronic Acid-10
15E
Hyaluronic Acid 8-15 KDa
15F
Hyaluronic Acid 30-50 KDa
15G
Hyaluronic Acid 50-80 KDa
GANGLIO SIDE
17A
Asialo GM2
17B
Asialo GM1
17C
GT1c Ganglioside sugar

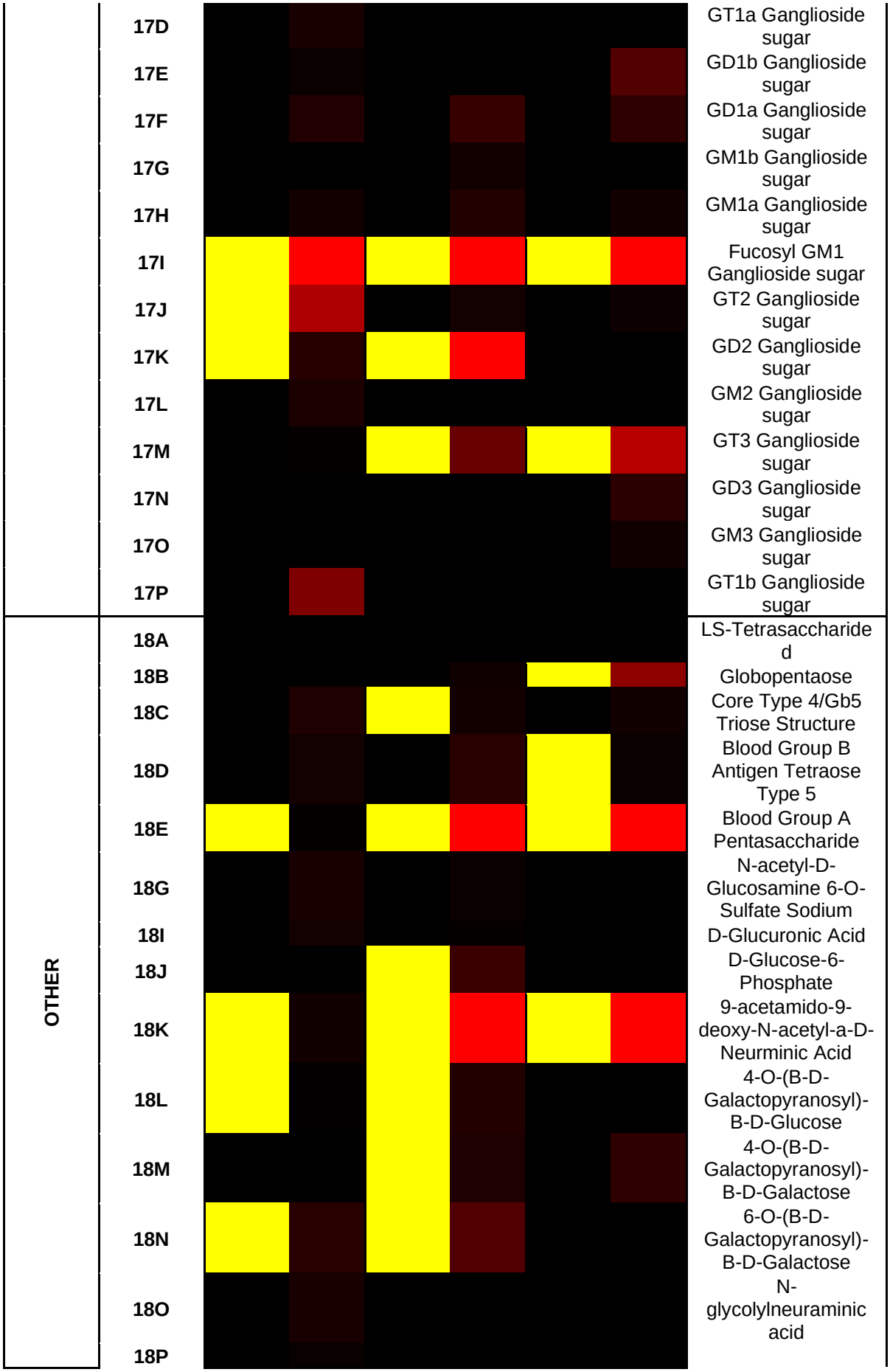
17D
GT1a Ganglioside sugar
17E
GD1b Ganglioside sugar
17F
GD1a Ganglioside sugar
17G
GM1b Ganglioside sugar
17H
GM1a Ganglioside sugar
17I
Fucosyl GM1 Ganglioside sugar
17J
GT2 Ganglioside sugar
17K
GD2 Ganglioside sugar
17L
GM2 Ganglioside sugar
17M
GT3 Ganglioside sugar
17N
GD3 Ganglioside sugar
17O
GM3 Ganglioside sugar
17P
GT1b Ganglioside sugar
OTHER
18A
LS-Tetrasaccharide d
18B
Globopentaose
18C
Core Type 4/Gb5 Triose Structure
18D
Blood Group B Antigen Tetraose Type 5
18E
Blood Group A Pentasaccharide
18G
N-acetyl-D-Glucosamine 6-O-Sulfate Sodium
18I
D-Glucuronic Acid
18J
D-Glucose-6-Phosphate
18K
9-acetamido-9-deoxy-N-acetyl-a-D-Neurminic Acid
18L
4-O-(B-D-Galactopyranosyl)-B-D-Glucose
18M
4-O-(B-D-Galactopyranosyl)-B-D-Galactose
18N
6-O-(B-D-Galactopyranosyl)-B-D-Galactose
18O
N-glycolylneuraminic acid
18P

	19O	[redacted]	Maltotriose
	19P		Maltotetraose

3.2. Recombinant Hoc protein glycan array

GROUP	GLYCAN	WT - 1 ug TTEST	WT - 1 ug FOLD	D246N - 1 ug TTEST	D246N - 1 ug FOLD	NAME
GALACTOSE	1A					Lacto-N-Biose I
	1B					N-Acetyllactosamine
	1C					β-1-4-Galactosyl-Galactose
	1D					β-1-6 Galactosyl-N-acetyl Glucosamine
	1E					β-1-3 Galactosyl-N-acetyl Galactosamine
	1F					β-1-3 Gal-N-Acetyl Galactosaminyl-β1-4 Gal-β1-4-Glc
	1G					Lacto-N-tetraose
	1H					Lacto-N-neotetraose
	1I					Lacto-N-neohexaose
	1J					Lacto-N-hexaose
	1K					Globotriose
	1L					Tn Antigen GalNAcα1-O-Ser
	1M					Galactosyl-Tn Antigen
	1N					α1-3 Galactobiose
	1O					Linear B-2 Trisaccharide
	1P					Linear B-6 Trisaccharide
	2A					α1-3, β1-4, α1-3 Galactotetraose
	2B					Galβ1-6Gal
	2C					GalNAcβ1-3Gal
	2D					GalNAcβ1-4Gal
	2E					Galα1-4Galβ1-4GlcNAc
	2F					GalNAcα1-3Galβ1-4Glc
	2G					iso-Lacto-N-octaose
GlcNAc	4A					N,N'-Diacetyl chitobiose
	4B					N,N',N''-Triacetyl chitotriose
	4C					N,N',N'',N'''-Tetraacetyl chitotetraose
	4D					N,N',N'',N''',N'''',N''''-Hexaacetyl chitohexaose
	4E					GlcNAcβ1-4MurNAc
	4F					Pentacetyl chitopentaose
MANNOSE	5A					β1-2 N-Acetylglucosamine-mannose
	5B					Bianntennary N-linked core pentasaccharide
	5C					α1-2-Mannobiose
	5D					α1-3-Mannobiose
	5E					α1-4-Mannobiose
	5F					α1-6-Mannobiose
	5G					α1-3, α1-6-Mannobiose
	5H					α1-3, α1-3, α1-6-Mannopentaose
FUCOSE	7A					Lacto-N-fucopentaose I
	7B					Lacto-N-fucopentaose II
	7C					Lacto-N-fucopentaose III
	7D					Lacto-N-difucohexaose I
	7E					Lacto-N-difucohexaose II
	7F					H-disaccaride
	7G					2'-Fucosyllactose
	7H					3'-Fucosyllactose

	7I	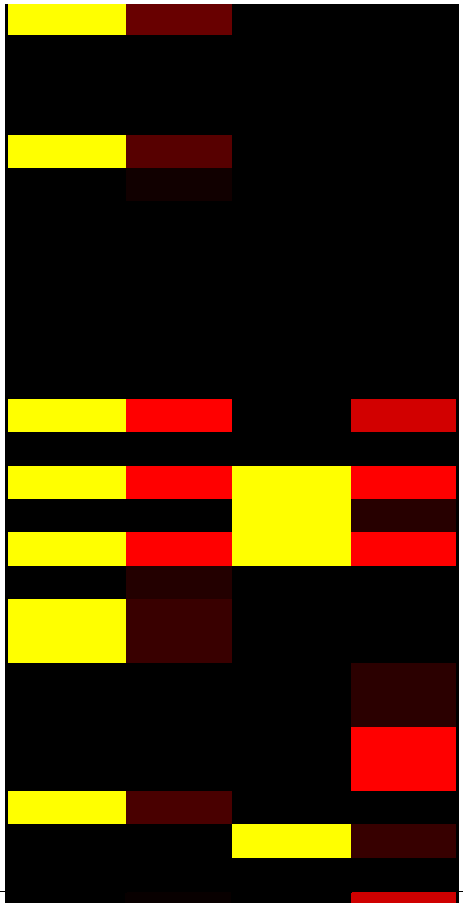	Lewis^{x}
	7J		Lewis^{a}
	7K		Blood Group A Trisaccharide
	7L		Lactodifucotetraose
	7M		Blood Group B Trisaccharide
	7N		Lewisy
	7O		Blood Group H Type II Trisaccharide
	7P		Lewisb Tetrasaccharide
	8A		Sulpho Lewis^{a}
	8B		Sulpho Lewis^{x}
	8D		Monofucosyllacto-N-hexaose III
	8E		Difucosyllacto-N-hexaose
	8F		Trifucosyllacto-N-hexaose
	8G		Lacto-N-fucopentaose VI
	8P		Blood Group A Tetrasaccharide
	9A		Blood Group B Pentasaccharide
	9C		Difucosyl-para-lacto-N-hexaose II
	20A		Blood Group H Antigen Tetraose type 4
	20B		Blood Group A antigen Pentaose type 4
	20C		Blood Group B Antigen Pentasaccaride type 4
	19J		Lewis^{x} Tetraose
	19L		Lewis^{y} Pentaose
	19M		Lewis^{a} Tetraose
SIALIC	**10A**		Sialyl Lewis^{a}
	10B		Sialyl Lewis^{x}
	10C		Sialyllacto-N-Tetraose^{a}
	10D		Monosialyl, Monofucosyllacto-N-neohexose
	10E		Disialyl-TF
	10H		Sialyllacto-N-fucopentaose VI
	10K		Monosialyllacto-N-hexaose
	10L		6'-Sialyllactosamine
	10M		LS-Tetrasaccharide a
	10N		LS-Tetrasaccharide b
	10O		LS-Tetrasaccharide c
	10P		Disialyllacto-N-Tetraose
	11A		3'-Sialyllactose
	11B		6'-Sialyllactose
	11C		Colominic acid
	20D		Lewis^{X} Hexaose
GLYCOSAMINOGLYCANS	**12A**		Neocarratetraose-41, 3-di-O-Sulphate (Na^{+})
	12B		Neocarratetraose-41-O-Sulphate (Na+)
	12C		Neocarrahexaose-24,41, 3, 5-tetra-*O*-sulphate (Na^{+})
	12D		Neocarrahexaose-41, 3, 5-tri-*O*-sulphate (Na^{+})
	12E		Neocarraoctaose-41, 3, 5, 7-tetra-*O*-sulphate (Na^{+})
	12F		Neocarradecaose-41, 3, 5, 7, 9-penta-*O*-sulphate (Na^{+})

	12G	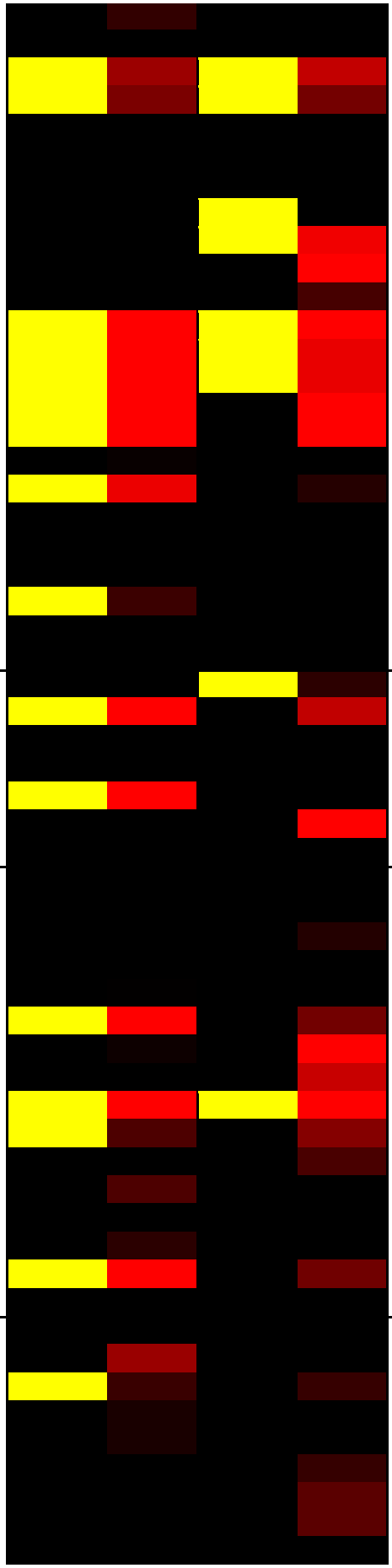	ΔUA-2S-GlcNS-6S
	12H		ΔUA-GlucNS-6S
	12I		ΔUA-2S-GlucNS
	12J		ΔUA-2S-GlcNAc-6S
	12K		ΔUA-GlcNAc-6S
	12L		ΔUA-2S-GlcNAc
	12M		ΔUA-GlcNAc
	12N		ΔUA-GalNAc-4S (Delta Di-4S)
	12O		ΔUA-GalNAc-6S (Delta Di-6S)
	12P		ΔUA-GalNAc-4S,6S (Delta Di-disE)
	13A		ΔUA-2S-GalNAc-4S (Delta Di-disB)
	13B		ΔUA-2S-GalNAc-6S (Delta Di-disD)
	13C		ΔUA-2S-GalNAc-4S-6S (Delta Di-tisS)
	13D		ΔUA-2S-GalNAc-6S (Delta Di-UA2S)
	13E		ΔUA-GlcNAc (Delta Di-HA)
	13J		Heparin
	13K		Chondroitin Sulfate
	13L		Dermatan Sulfate
	13M		Chondroitin 6-Sulfate
	14J		Heparin Sulfate 5 mg/ml
	14L		Chondroitin Disaccharide Δdi-OS, Sodium Salt
HYALURONIC ACID	15A		Hyaluronic Acid-4
	15B		Hyaluronic Acid-6
	15C		Hyaluronic Acid-8
	15D		Hyaluronic Acid-10
	15E		Hyaluronic Acid 8-15 KDa
	15F		Hyaluronic Acid 30-50 KDa
	15G		Hyaluronic Acid 50-80 KDa
GANGLIOSIDE	17A		Asialo GM2
	17B		Asialo GM1
	17C		GT1c Ganglioside sugar
	17D		GT1a Ganglioside sugar
	17E		GD1b Ganglioside sugar
	17F		GD1a Ganglioside sugar
	17G		GM1b Ganglioside sugar
	17H		GM1a Ganglioside sugar
	17I		Fucosyl GM1 Ganglioside sugar
	17J		GT2 Ganglioside sugar
	17K		GD2 Ganglioside sugar
	17L		GM2 Ganglioside sugar
	17M		GT3 Ganglioside sugar
	17N		GD3 Ganglioside sugar
	17O		GM3 Ganglioside sugar
	17P		GT1b Ganglioside sugar
OTHER	18A		LS-Tetrasaccharide d
	18B		Globopentaose
	18C		Core Type 4/Gb5 Triose Structure
	18D		Blood Group B Antigen Tetraose Type 5
	18E		Blood Group A Pentasaccharide
	18G		N-acetyl-D-Glucosamine 6-O-Sulfate Sodium
	18I		D-Glucuronic Acid

	18J	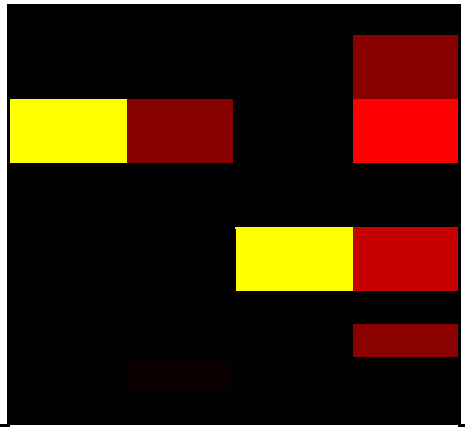	D-Glucose-6-Phosphate
	18K		9-acetamido-9-deoxy-N-acetyl-α-D-Neurminic Acid
	18L		4-O-(β-D-Galactopyranosyl)-β-D-Glucose
	18M		4-O-(β-D-Galactopyranosyl)-β-D-Galactose
	18N		6-O-(β-D-Galactopyranosyl)-β-D-Galactose
	18O		N-glycolylneuraminic acid
	18P		
	19O		Maltotriose
	19P		Maltotetraose

Annex 4: Hoc-glycan surface plasmon resonance (SPR) sensorgrams

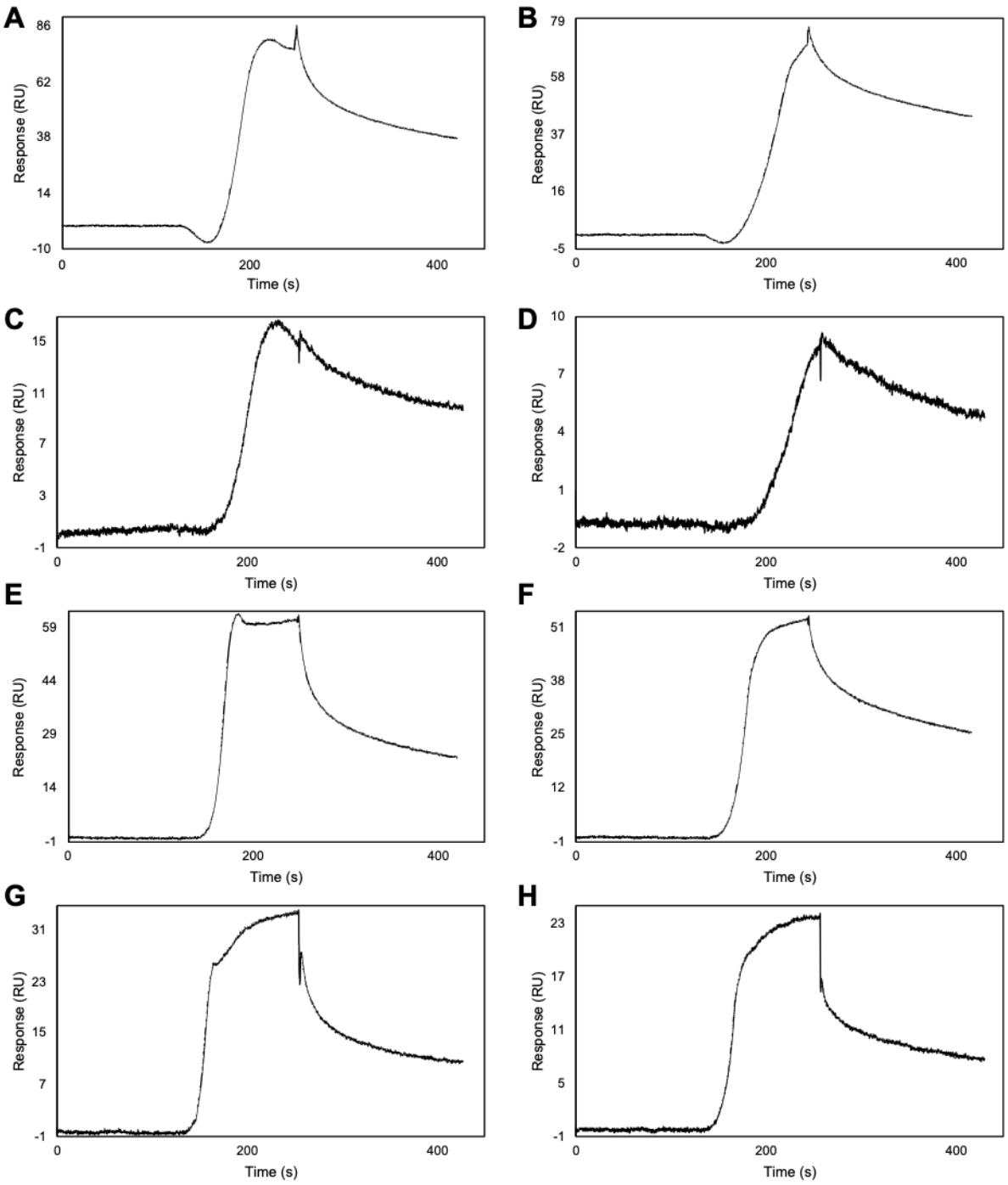

Annex 4: SPR sensorgrams of the WT Hoc (left column) and D246N Hoc mutant (right column) with various glycans using OneStep analysis. (A-B) 2'-Fucosyllactose; (C-D) Lacto-N-difucohexaose II; (E-F) Lewis^{y}, and (G-H) Lacto-N-fucopentaose II.

Annex 4 (continued)

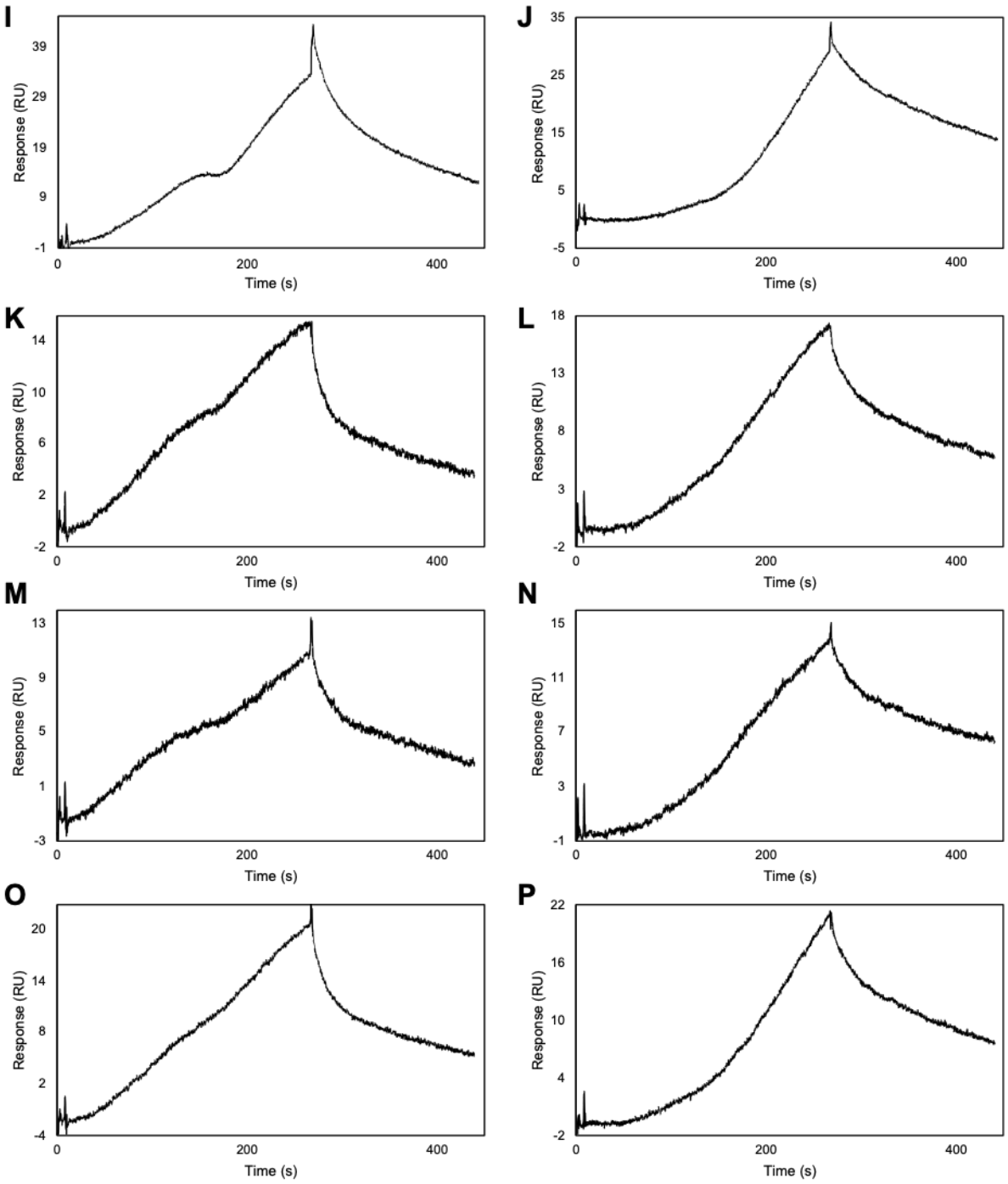

Annex 4 (continued): SPR sensorgrams of the WT Hoc (left column) and D246N Hoc mutant (right column) with various glycans using OneStep analysis. (I-J) Lacto-N-fucopentaose I; (K-L) Lewis^{a}; (M-N) Blood Group A Trisaccharide, and (O-P) Lewis^{x}.

Annex 5: 6kb-deletion affecting short tail fibre and *attP* site in virulent phage (λ^{VIR})

```
Temperate       1201 cactgaccggaacgccaacagcaccaaccgcgctcaggggaacaaacaat   1250
                     ||||||||||||||||||||||||||||||||||||||||||||||||||||
Virulent        1201 cactgaccggaacgccaacagcaccaaccgcgctcaggggaacaaacaat   1250

Temperate       1251 acccagattgcgaacaccgcttttgtactggccgcgattgcagatgttat   1300
                     ||||||||||||||||||||||||||||||||||||||||||||||||||||
Virulent        1251 acccagattgcgaacaccgcttttgtactggccgcgattgcagatgttat   1300

Temperate       1301 cgacgcgtcacctgacgcactgaatacgctgaatgaactggccgcagcgc   1350
                     ||||||||||||||||||||||||||||||||||||||||||||||||||||
Virulent        1301 cgacgcgtcacctgacgcactgaatacgctgaatgaactggccgcagcgc   1350

                           Short tail fibre START >
Temperate       1351 tcgggaatgatccagattttgctaccaccATGactaacgcgcttgcgggt   1400
                     ||||||||||||||||||||||||||||||||||||||||||||||||||||
Virulent        1351 tcgggaatgatccagattttgctaccaccatgactaacgcgcttgcgggt   1400

Temperate       1401 aaacaaccgaagaatgcgacactgacggcgctggcagggctttccacggc   1450
                     ||||||||||||||||||||||||||||||||||||||||||||||||||||
Virulent        1401 aaacaaccgaagaatgcgacactgacggcgctggcagggctttccacggc   1450
x
Temperate       1451 gaaaaataaattaccgtattttgcggaaaatgatgccgccagcctgactg   1500
                     ||||||||||||||||||||||||||||||||||||||||||||||||||||
Virulent        1451 gaaaaataaattaccgtattttgcggaaaatgatgccgccagcctgactg   1500

Temperate       1501 aactgactcaggttggcagggatattctggcaaaaaattccgttgcagat   1550
                     ||||||||||||||||||||||||||||||||||||||||||||||||||||
Virulent        1501 aactgactcaggttggcagggatattctggcaaaaaattccgttgcagat   1550

Temperate       1551 gttcttgaataccttggggccggtgagaattcggcctttccggcaggtgc   1600
                     ||||||||||||||||||||||||||||||||||||||||||||||||||||
Virulent        1551 gttcttgaataccttggggccggtgagaattcggcctttccggcaggtgc   1600

Temperate       1601 gccgatcccgtggccatcagatatcgttccgtctggctacgtcctgatgc   1650
                     ||||||||||||||||||||||||||||||||||||||||||||||||||||
Virulent        1601 gccgatcccgtggccatcagatatcgttccgtctggctacgtcctgatgc   1650

Temperate       1651 aggggcaggcgtttgacaaatcagcctacccaaaacttgctgtcgcgtat   1700
                     ||||||||||||||||||||||||||||||||||||||||||||||||||||
Virulent        1651 aggggcaggcgtttgacaaatcagcctacccaaaacttgctgtcgcgtat   1700

Temperate       1701 ccatcgggtgtgcttcctgatatgcgaggctggacaatcaaggggaaacc   1750
                     ||||||||||||||||||||||||||||||||||||||||||||||||||||
Virulent        1701 ccatcgggtgtgcttcctgatatgcgaggctggacaatcaaggggaaacc   1750

Temperate       1751 cgccagcggtcgtgctgtattgtctcaggaacaggatggaattaagtcgc   1800
                     ||||||||||||||||||||||||||||||||||||||||||||||||||||
Virulent        1751 cgccagcggtcgtgctgtattgtctcaggaacaggatggaattaagtcgc   1800

Temperate       1801 acacccacagtgccagtgcatccggtacggatttggggacgaaaaccaca   1850
                     ||||||||||||||||||||||||||||||||||||||||||||||||||||
Virulent        1801 acacccacagtgccagtgcatccggtacggatttggggacgaaaaccaca   1850

Temperate       1851 tcgtcgtttgattacgggacgaaaacaacaggcagtttcgattacggcac   1900
                     ||||||||||||||||||||||||||||||||||||||||||||||||||||
Virulent        1851 tcgtcgtttgattacgggacgaaaacaacaggcagtttcgattacggcac   1900

Temperate       1901 caaatcgacgaataacacgggggctcatgctcacagtctgagcggttcaa   1950
                     ||||||||||||||||||||||||||||||||||||||||||||||||||||
Virulent        1901 caaatcgacgaataacacgggggctcatgctcacagtctgagcggttcaa   1950

Temperate       1951 caggggccgcgggtgctcatgcccacacaagtggtttaaggatgaacagt   2000
                     ||||||||||||||||||||||||||||||||||||||||||||||||||||
```

```
Virulent        1951 caggggccgcgggtgctcatgcccacacaagtggtttaaggatgaacagt   2000

Temperate       2001 tctggctggagtcagtatggaacagcaaccattacaggaagtttatccac   2050
                     ||||||||||||||||||||||||||||||||||||||||||||||||||
Virulent        2001 tctggctggagtcagtatggaacagcaaccattacaggaagtttatccac   2050

Temperate       2051 agttaaaggaaccagcacacagggtattgcttatttatcgaaaacggaca   2100
                     ||||||||||||||.||||||||||||||||||
Virulent        2051 agttaaaggaaccaAcacacagggtattgctta----------------   2083
                                     6kb DELETION >

Temperate       2101 gtcagggcagccacagtcactcattgtccggtacagccgtgagtgccggt   2150

Virulent        2084 --------------------------------------------------   2083

Temperate       2151 gcacatgcgcatacagttggtattggtgcgcaccagcatccggttgttat   2200

Virulent        2084 --------------------------------------------------   2083

Temperate       2201 cggtgctcatgcccattctttcagtattggttcacacggacacaccatca   2250

Virulent        2084 --------------------------------------------------   2083

Temperate       2251 ccgttaacgctgcgggtaacgcggaaaacaccgtcaaaaacattgcattt   2300

Virulent        2084 --------------------------------------------------   2083

                         Short tail fibre STOP >
Temperate       2301 aactatattgtgaggcttgcaTAAtggcattcagaatgagtgaacaacca   2350

Virulent        2084 --------------------------------------------------   2083

Temperate       2351 cggaccataaaaatttataatctgctggccggaactaatgaatttattgg   2400

Virulent        2084 --------------------------------------------------   2083

Temperate       2401 tgaaggtgacgcatatattccgcctcataccggtctgcctgcaaacagta   2450

Virulent        2084 --------------------------------------------------   2083

Temperate       2451 ccgatattgcaccgccagatattccggctggctttgtggctgttttcaac   2500

Virulent        2084 --------------------------------------------------   2083

Temperate       2501 agtgatgaggcatcgtggcatctcgttgaagaccatcggggtaaaaccgt   2550

Virulent        2084 --------------------------------------------------   2083

Temperate       2551 ctatgacgtggcttccggcgacgcgttatttatttctgaactcggtccgt   2600

Virulent        2084 --------------------------------------------------   2083

Temperate       2601 taccggaaaattttacctggttatcgccgggaggggaatatcagaagtgg   2650

Virulent        2084 --------------------------------------------------   2083

Temperate       2651 aacggcacagcctgggtgaaggatacggaagcagaaaaactgttccggat   2700

Virulent        2084 --------------------------------------------------   2083

Temperate       2701 ccgggaggcggaagaaacaaaaaaaagcctgatgcaggtagccagtgagc   2750

Virulent        2084 --------------------------------------------------   2083

Temperate       2751 atattgcgccgcttcaggatgctgcagatctggaaattgcaacgaaggaa   2800

Virulent        2084 --------------------------------------------------   2083
```

```
Temperate       2801 gaaacctcgttgctggaagcctggaagaagtatcgggtgttgctgaaccg   2850
Virulent        2084 ---------------------------------------------------   2083
Temperate       2851 tgttgatacatcaactgcacctgatattgagtggcctgctgtccctgtta   2900
Virulent        2084 ---------------------------------------------------   2083
Temperate       2901 tggagtaatcgttttgtgatatgccgcagaaacgttgtatgaaataacgt   2950
Virulent        2084 ---------------------------------------------------   2083
Temperate       2951 tctgcggttagttagtatattgtaaagctgagtattggtttatttggcga   3000
Virulent        2084 ---------------------------------------------------   2083
Temperate       3001 ttattatcttcaggagaataatggaagttctatgactcaattgttcatag   3050
Virulent        2084 ---------------------------------------------------   2083
Temperate       3051 tgtttacatcaccgccaattgcttttaagactgaacgcatgaaatatggt   3100
Virulent        2084 ---------------------------------------------------   2083
Temperate       3101 ttttcgtcatgttttgagtctgctgttgatatttctaaagtcggtttttt   3150
Virulent        2084 ---------------------------------------------------   2083
Temperate       3151 ttcttcgttttctctaactattttccatgaaatacatttttgattattat   3200
Virulent        2084 ---------------------------------------------------   2083
Temperate       3201 ttgaatcaattccaattacctgaagtctttcatctataattggcattgta   3250
Virulent        2084 ---------------------------------------------------   2083
Temperate       3251 tgtattggtttattggagtagatgcttgcttttctgagccatagctctga   3300
Virulent        2084 ---------------------------------------------------   2083
Temperate       3301 tatccaaatgaagccataggcatttgttattttggctctgtcagctgcat   3350
Virulent        2084 ---------------------------------------------------   2083
Temperate       3351 aacgccaaaaaatatatttatctgcttgatcttcaaatgttgtattgatt   3400
Virulent        2084 ---------------------------------------------------   2083
Temperate       3401 aaatcaattggatggaattgtttatcataaaaaattaatgtttgaatgtg   3450
Virulent        2084 ---------------------------------------------------   2083
Temperate       3451 ataaccgtcctttaaaaaagtcgtttctgcaagcttggctgtatagtcaa   3500
Virulent        2084 ---------------------------------------------------   2083
Temperate       3501 ctaactcttctgtcgaagtgatatttttaggcttatctaccagttttaga   3550
Virulent        2084 ---------------------------------------------------   2083
Temperate       3551 cgctctttaatatcttcaggaattattttattgtcatattgtatcatgct   3600
Virulent        2084 ---------------------------------------------------   2083
Temperate       3601 aaatgacaatttgcttatggagtaatcttttaattttaaataagttattc   3650
Virulent        2084 ---------------------------------------------------   2083
```

```
Temperate       3651 tcctggcttcatcaaataaagagtcgaatgatgttggcgaaatcacatcg   3700
Virulent        2084 ---------------------------------------------------   2083

Temperate       3701 tcacccattggattgtttatttgtatgccaagagagttacagcagttata   3750
Virulent        2084 ---------------------------------------------------   2083
Temperate       3751 cattctgccatagattatagctaaggcatgtaataattcgtaatctttta   3800
Virulent        2084 ---------------------------------------------------   2083
Temperate       3801 gcgtattagcgacccatcgtctttctgatttaataatagatgattcagtt   3850
Virulent        2084 ---------------------------------------------------   2083
Temperate       3851 aaatatgaaggtaatttcttttgtgcaagtctgactaacttttttatacc   3900
Virulent        2084 ---------------------------------------------------   2083
Temperate       3901 aatgtttaacatactttcatttgtaataaactcaatgtcattttcttcaa   3950
Virulent        2084 ---------------------------------------------------   2083
Temperate       3951 tgtaagatgaaataagagtagcctttgcctcgctatacatttctaaatcg   4000
Virulent        2084 ---------------------------------------------------   2083
Temperate       4001 ccttgtttttctatcgtattgcgagaatttttagcccaagccattaatgg   4050
Virulent        2084 ---------------------------------------------------   2083
Temperate       4051 atcatttttccatttttcaataacattattgttataccaaatgtcatatc   4100
Virulent        2084 ---------------------------------------------------   2083
Temperate       4101 ctataatctggtttttgtttttttgaataataaatgttactgttcttgcg   4150
Virulent        2084 ---------------------------------------------------   2083
Temperate       4151 gtttggaggaattgattcaaattcaagcgaaataattcagggtcaaaata   4200
Virulent        2084 ---------------------------------------------------   2083
Temperate       4201 tgtatcaatgcagcatttgagcaagtgcgataaatctttaagtcttcttt   4250
Virulent        2084 ---------------------------------------------------   2083
Temperate       4251 cccatggtttttagtcataaaactctccattttgataggttgcatgcta   4300
Virulent        2084 ---------------------------------------------------   2083
Temperate       4301 gatgctgatatattttagaggtgataaaattaactgcttaactgtcaatg   4350
Virulent        2084 ---------------------------------------------------   2083
Temperate       4351 taatacaagttgtttgatctttgcaatgattcttatcagaaaccatatag   4400
Virulent        2084 ---------------------------------------------------   2083
Temperate       4401 taaattagttacacaggaaatttttaatattattattatcattcattatg   4450
Virulent        2084 ---------------------------------------------------   2083
Temperate       4451 tattaaaattagagttgtggcttggctctgctaacacgttgctcatagga   4500
```

```
Virulent       2084 --------------------------------------------------   2083
Temperate      4501 gatatggtagagccgcagacacgtcgtatgcaggaacgtgctgcggctgg   4550
Virulent       2084 --------------------------------------------------   2083

Temperate      4551 ctggtgaacttccgatagtgcgggtgttgaatgatttccagttgctaccg   4600
Virulent       2084 --------------------------------------------------   2083
Temperate      4601 attttacatatttttgcatgagagaatttgtaccacctcccaccgacca   4650
Virulent       2084 --------------------------------------------------   2083
Temperate      4651 tctatgactgtacgccactgtccctaggactgctatgtgccggagcggac   4700
Virulent       2084 --------------------------------------------------   2083
Temperate      4701 attacaaacgtccttctcggtgcatgccactgttgccaatgacctgccta   4750
Virulent       2084 --------------------------------------------------   2083
Temperate      4751 ggaattggttagcaagttactaccggattttgtaaaaacagccctcctca   4800
Virulent       2084 --------------------------------------------------   2083
Temperate      4801 tataaaaagtattcgttcacttccgataagcgtcgtaattttctatcttt   4850
Virulent       2084 --------------------------------------------------   2083
Temperate      4851 catcatattctagatccctctgaaaaaatcttccgagtttgctaggcact   4900
Virulent       2084 --------------------------------------------------   2083
Temperate      4901 gatacataactcttttccaataattggggaagtcattcaaatctataata   4950
Virulent       2084 --------------------------------------------------   2083
Temperate      4951 ggtttcagatttgcttcaataaattctgactgtagctgctgaaacgttgc   5000
Virulent       2084 --------------------------------------------------   2083
Temperate      5001 ggttgaactatatttccttataacttttacgaaagagtttctttgagtaa   5050
Virulent       2084 --------------------------------------------------   2083
Temperate      5051 tcacttcactcaagtgcttccctgcctccaaacgatacctgttagcaata   5100
Virulent       2084 --------------------------------------------------   2083
Temperate      5101 tttaatagcttgaaatgatgaagagctctgtgtttgtcttcctgcctcca   5150
Virulent       2084 --------------------------------------------------   2083
Temperate      5151 gttcgccgggcattcaacataaaaactgatagcacccggagttccggaaa   5200
Virulent       2084 --------------------------------------------------   2083
Temperate      5201 cgaaatttgcatatacccattgctcacgaaaaaaaatgtccttgtcgata   5250
Virulent       2084 --------------------------------------------------   2083
Temperate      5251 tagggatgaatcgcttggtgtacctcatctactgcgaaaacttgaccttt   5300
Virulent       2084 --------------------------------------------------   2083
```

```
Temperate       5301 ctctcccatattgcagtcgcggcacgatggaactaaattaataggcatca   5350
Virulent        2084 ----------------------------------------------------   2083
Temperate       5351 ccgaaaattcaggataatgtgcaataggaagaaaatgatctatatttttt   5400
Virulent        2084 ----------------------------------------------------   2083

Temperate       5401 gtctgtcctatatcaccacaaaatggacatttttcacctgatgaaacaag   5450
Virulent        2084 ----------------------------------------------------   2083
Temperate       5451 catgtcatcgtaatatgttctagcgggtttgtttttatctcggagattat   5500
Virulent        2084 ----------------------------------------------------   2083
Temperate       5501 tttcataaagcttttctaatttaacctttgtcaggttaccaactactaag   5550
Virulent        2084 ----------------------------------------------------   2083
Temperate       5551 gttgtaggctcaagagggtgtgtcctgtcgtaggtaaataactgacctgt   5600
Virulent        2084 ----------------------------------------------------   2083
Temperate       5601 cgagcttaatattctatattgttgttctttctgcaaaaaagtggggaagt   5650
Virulent        2084 ----------------------------------------------------   2083
Temperate       5651 gagtaatgaaattatttctaacatttatctgcatcataccttccgagcat   5700
Virulent        2084 ----------------------------------------------------   2083
Temperate       5701 ttattaagcatttcgctataagttctcgctggaagaggtagttttttcat   5750
Virulent        2084 ----------------------------------------------------   2083
Temperate       5751 tgtactttaccttcatctctgttcattatcatcgcttttaaaacggttcg   5800
Virulent        2084 ----------------------------------------------------   2083
Temperate       5801 accttctaatcctatctgaccattataatttttagaatggtttcataag   5850
Virulent        2084 ----------------------------------------------------   2083
Temperate       5851 aaagctctgaatcaacggactgcgataataagtggtggtatccagaattt   5900
Virulent        2084 ----------------------------------------------------   2083
Temperate       5901 gtcacttcaagtaaaaacacctcacgagttaaaacacctaagttctcacc   5950
Virulent        2084 ----------------------------------------------------   2083
Temperate       5951 gaatgtctcaatatccggacggataatatttattgcttctcttgaccgta   6000
Virulent        2084 ----------------------------------------------------   2083
Temperate       6001 ggactttccacatgcaggattttggaacctcttgcagtactactggggaa   6050
Virulent        2084 ----------------------------------------------------   2083
Temperate       6051 tgagttgcaattattgctacaccattgcgtgcatcgagtaagtcgcttaa   6100
Virulent        2084 ----------------------------------------------------   2083
Temperate       6101 tgttcgtaaaaaagcagagagcaaaggtggatgcagatgaacctctggtt   6150
```

```
Virulent       2084 --------------------------------------------------   2083
Temperate      6151 catcgaataaaactaatgacttttcgccaacgacatctactaatcttgtg   6200
Virulent       2084 --------------------------------------------------   2083
Temperate      6201 atagtaaataaaacaattgcatgtccagagctcattcgaagcagatattt   6250
Virulent       2084 --------------------------------------------------   2083

Temperate      6251 ctggatattgtcataaaacaatttagtgaatttatcatcgtccacttgaa   6300
Virulent       2084 --------------------------------------------------   2083
Temperate      6301 tctgtggttcattacgtcttaactcttcatatttagaaatgaggctgatg   6350
Virulent       2084 --------------------------------------------------   2083
Temperate      6351 agttccatatttgaaaagttttcatcactacttagtttttgatagcttc   6400
Virulent       2084 --------------------------------------------------   2083
Temperate      6401 aagccagagttgtctttttctatctactctcatacaaccaataaatgctg   6450
Virulent       2084 --------------------------------------------------   2083
Temperate      6451 aaatgaattctaagcggagatcgcctagtgattttaaactattgctggca   6500
Virulent       2084 --------------------------------------------------   2083
Temperate      6501 gcattcttgagtccaatataaaagtattgtgtacctttgctgggtcagg   6550
Virulent       2084 --------------------------------------------------   2083
Temperate      6551 ttgttctttaggaggagtaaaaggatcaaatgcactaaacgaaactgaaa   6600
Virulent       2084 --------------------------------------------------   2083
Temperate      6601 caagcgatcgaaaatatccctttgggattcttgactcgataagtctatta   6650
Virulent       2084 --------------------------------------------------   2083
Temperate      6651 ttttcagagaaaaaatattcattgttttctgggttggtgattgcaccaat   6700
Virulent       2084 --------------------------------------------------   2083
Temperate      6701 cattccattcaaaattgttgttttaccacacccattccgcccgataaaag   6750
Virulent       2084 --------------------------------------------------   2083
Temperate      6751 catgaatgttcgtgctgggcatagaattaaccgtcacctcaaaaggtata   6800
Virulent       2084 --------------------------------------------------   2083
Temperate      6801 gttaaatcactgaatccgggagcacttttctattaaatgaaaagtggaa   6850
Virulent       2084 --------------------------------------------------   2083
Temperate      6851 atctgacaattctggcaaaccatttaacacacgtgcgaactgtccatgaa   6900
Virulent       2084 --------------------------------------------------   2083
Temperate      6901 tttctgaaagagttacccctctaagtaatgaggtgttaaggacgctttca   6950
Virulent       2084 --------------------------------------------------   2083
```

```
Temperate       6951 ttttcaatgtcggctaatcgatttggccatactactaaatcctgaatagc   7000
Virulent        2084 ------------------------------------------------   2083
Temperate       7001 tttaagaaggttatgtttaaaaccatcgcttaatttgctgagattaacat   7050
Virulent        2084 ------------------------------------------------   2083
Temperate       7051 agtagtcaatgctttcacctaaggaaaaaaacatttcagggagttgactg   7100
Virulent        2084 ------------------------------------------------   2083

Temperate       7101 aatttttttatctattaatgaataagtgcttacttcttcttttgacctac   7150
Virulent        2084 ------------------------------------------------   2083
Temperate       7151 aaaaccaattttaacatttccgatatcgcatttttcaccatgctcatcaa   7200
Virulent        2084 ------------------------------------------------   2083
Temperate       7201 agacagtaagataaaacattgtaacaaaggaatagtcattccaaccatct   7250
Virulent        2084 ------------------------------------------------   2083
Temperate       7251 gctcgtaggaatgccttatttttttctactgcaggaatatacccgcctct   7300
Virulent        2084 ------------------------------------------------   2083
Temperate       7301 ttcaataacactaaactccaacatatagtaacccttaattttattaaaat   7350
Virulent        2084 ------------------------------------------------   2083
Temperate       7351 aaccgcaatttatttggcggcaacacaggatctctctttaagttactct   7400
Virulent        2084 ------------------------------------------------   2083
Temperate       7401 ctattacatacgttttccatctaaaaattagtagtattgaacttaacggg   7450
Virulent        2084 ------------------------------------------------   2083
Temperate       7451 gcatcgtattgtagttttccatatttagctttctgcttccttttggataa   7500
Virulent        2084 ------------------------------------------------   2083
Temperate       7501 cccactgttattcatgttgcatggtgcactgtttataccaacgatatagt   7550
Virulent        2084 ------------------------------------------------   2083
Temperate       7551 ctattaatgcatatatagtatcgccgaacgattagctcttcaggcttctg   7600
Virulent        2084 ------------------------------------------------   2083
Temperate       7601 aagaagcgtttcaagtactaataagccgatagatagccacggacttcgta   7650
Virulent        2084 ------------------------------------------------   2083
Temperate       7651 gccatttttcataagtgttaacttccgctcctcgctcataacagacattc   7700
Virulent        2084 ------------------------------------------------   2083
Temperate       7701 actacagttatggcggaaaggtatgcatgctgggtgtggggaagtcgtga   7750
Virulent        2084 ------------------------------------------------   2083
Temperate       7751 aagaaaagaagtcagctgcgtcgtttgacatcactgctatcttcttactg   7800
```

```
Virulent       2084 ------------------------------------------------   2083

                                        attP site >
Temperate      7801 gttatgcaggtcgtagtgggtggcacacaaagcTTTGCACTGGATTGCGA   7850

Virulent       2084 ------------------------------------------------   2083

Temperate      7851 GGCTTTGTGCTTCTCTGGAGTGCGACAGGTTTGATGACAAAAAATTAGCG   7900

Virulent       2084 ------------------------------------------------   2083

Temperate      7901 CAAGAAGACAAAAATCACCTTGCGCTAATGCTCTGTTACAGGTCACTAAT   7950

Virulent       2084 ------------------------------------------------   2083

Temperate      7951 ACCATCTAAGTAGTTGATTCATAGTGACTGCATATGTTGTGTTTTACAGT   8000

Virulent       2084 ------------------------------------------------   2083

Temperate      8001 ATTATGTAGTCTGTTTTTTATGCAAAATCTAATTTAATATATTGATATTT   8050

Virulent       2084 ------------------------------------------------   2083

Temperate      8051 ATATCATTTTACGTTTCTCGTTCAGCTTTTTTATACTAAGTTGGCATTAT   8100
                                                  ||||||||||||||||||||
Virulent       2084 ----------------------------TTTATACTAAGTTGGCATTAT   2104
                                                 < 6kb DELETION

Temperate      8101 AAAAAAGCATTGCTTATCAATTTGTTGCAACGAACAGGTCACTATCAGTC   8150
                    ||||||||||||||||||||||||||||||||||||||||||||||||||
Virulent       2105 AAAAAAGCATTGCTTATCAATTTGTTGCAACGAACAGGTCACTATCAGTC   2154

Temperate      8151 AAAATAAAATCATTATTTGATTTCAATTTTGTCCCACTCCCTGCCTCTGT   8200
                    ||||||||||||||||||||||||||||||||||||||||||||||||||||
Virulent       2155 AAAATAAAATCATTATTTGATTTCAATTTTGTCCCACTCCCTGCCTCTGT   2204

Temperate      8201 CATCACGATACTGTGATGccatggtgtccgacttatgcccgagaagatgt   8250
                    ||||||||||||||||||||||||||||||||||||||||||||||||||||
Virulent       2205 CATCACGATACTGTGATGccatggtgtccgacttatgcccgagaagatgt   2254
```

Annex 6: qPCR limit of detections (LODs) for isogenic λ phages and bacteria population replicates.

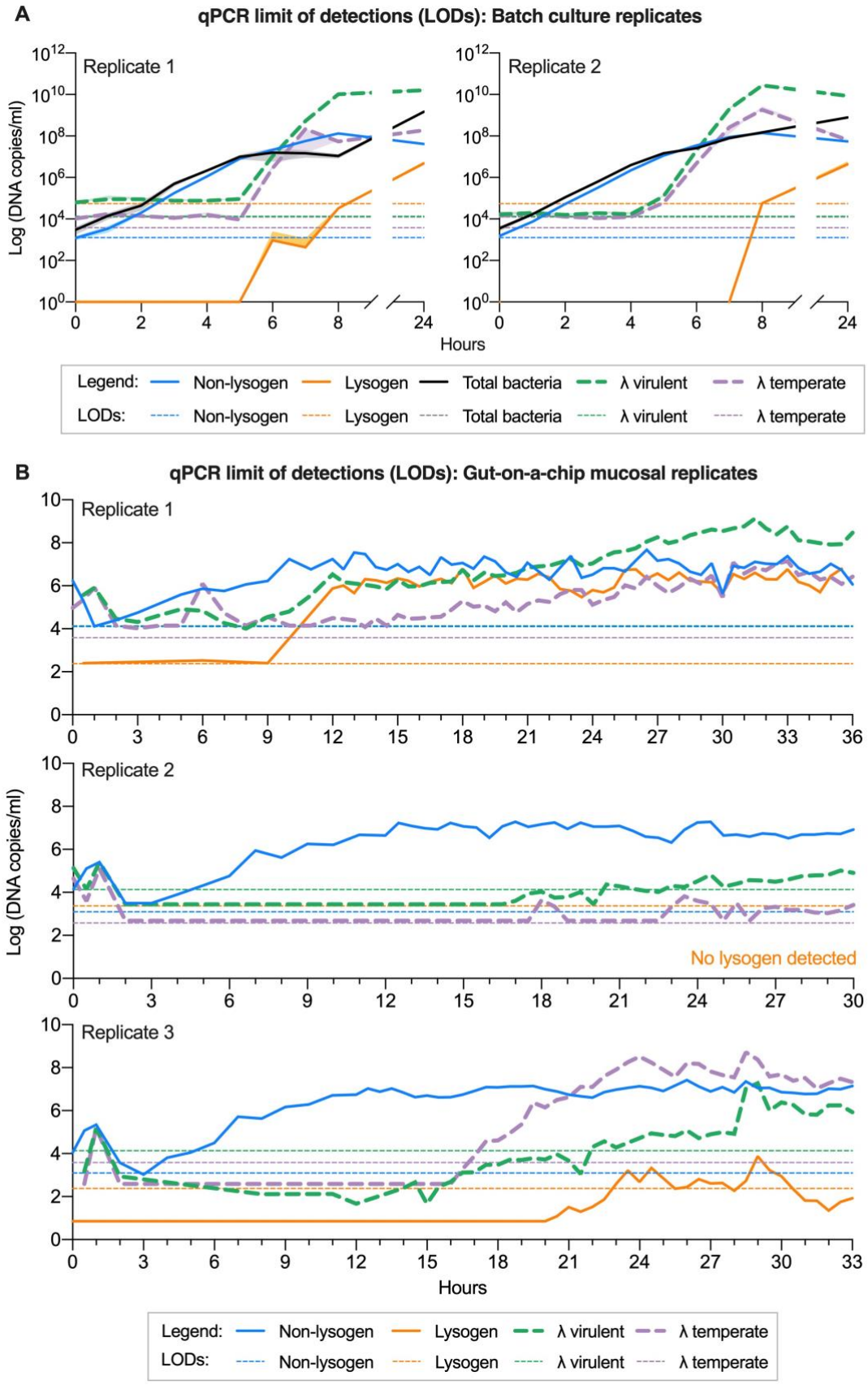

Annex 6: **qPCR limit of detections (LODs) for isogenic λ phages and bacteria population replicates.** Phage-bacteria population densities derived from qPCR quantification of heat-inactivated samples across A) two independent batch culture replicates (N = 2) and B) three independent gut-on-a-chip mucosal replicates (N = 3). Hourly datapoints in panel A, including the 24-hour timepoint in replicate 2, were represented by three qPCR technical replicates (n = 3). Data in panel B is plotted at a resolution of 30-minute intervals with each sampled datapoint represented by one qPCR technical replicate (n = 1). Horizontal dotted lines represent the respective LODs for the respective phage and bacterial species derived from the lowest limit of standard curves (see Annex 7). Standard curves for all phage and bacterial species in both batch culture and gut-on-a-chip mucosal replicates, were derived from three qPCR technical replicates (n = 3).

Annex 7: qPCR standard curves for batch culture and gut-on-a-chip experimental replicates

7.1. Batch culture replicate 1 standard curves

λ^{VIR}

Phage concentration (PFU/ml)	Log (Phage concentration)	Average quantification cycle (C_T)
1.36×10^9	9.13	12.7
1.36×10^8	8.13	16.3
1.36×10^7	7.13	19.8
1.36×10^6	6.13	24.6
1.36×10^5	5.13	31.0
1.36×10^4	4.13	35.0

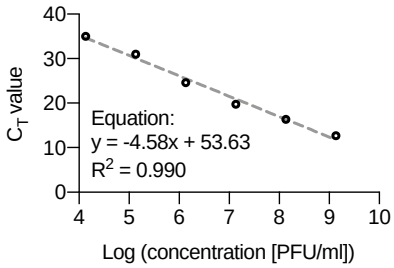

λ^{TEMP}

Phage concentration (PFU/ml)	Log (Phage concentration)	Average quantification cycle (C_T)
3.82×10^7	7.58	17.3
3.82×10^6	6.58	21.2
3.82×10^5	5.58	24.8
3.82×10^4	4.58	28.8
3.82×10^3	3.58	31.8

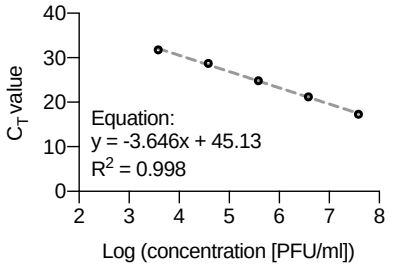

Non-lysogens

Bacteria concentration (CFU/ml)	Log (Phage concentration)	Average quantification cycle (C_T)
1.27×10^8	8.10	14.1
1.27×10^7	7.10	17.5
1.27×10^6	6.10	20.8
1.27×10^5	5.10	24.6
1.27×10^4	4.10	28.6

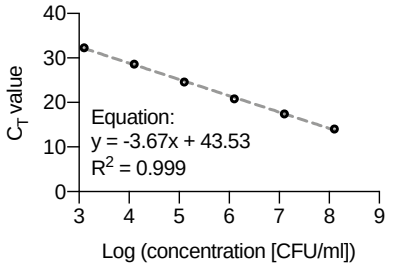

Lysogens

Bacteria concentration (CFU/ml)	Log (Phage concentration)	Average quantification cycle (C_T)
5.52×10^8	8.74	10.2
5.52×10^7	7.74	13.7
5.52×10^6	6.74	17.3
5.52×10^5	5.74	21.6
5.52×10^4	4.74	26.3

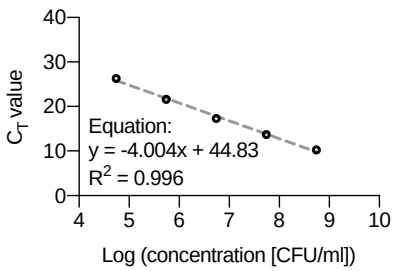

Total bacteria (16S)

Bacteria concentration (CFU/ml)	Log (Phage concentration)	Average quantification cycle (C_T)
1.27×10^8	8.10	12.3
1.27×10^7	7.10	15.6
1.27×10^6	6.10	19.8
1.27×10^5	5.10	25.5
1.27×10^4	4.10	30.6

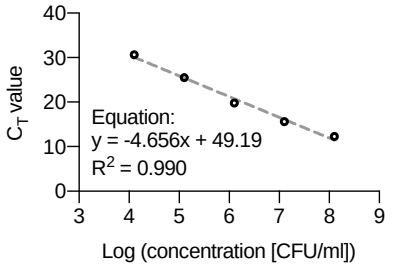

7.2. Batch culture replicate 2 standard curves

λ^{VIR}

Phage concentration (PFU/ml)	Log (Phage concentration)	Average quantification cycle (C_T)
1.36×10^9	9.13	12.7
1.36×10^8	8.13	15.7
1.36×10^7	7.13	19.2
1.36×10^6	6.13	23.1
1.36×10^5	5.13	27.2
1.36×10^4	4.13	32.3

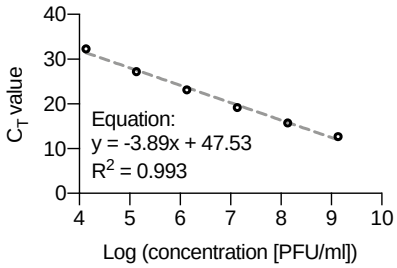

λ^{TEMP}

Phage concentration (PFU/ml)	Log (Phage concentration)	Average quantification cycle (C_T)
3.82×10^7	7.58	17.5
3.82×10^6	6.58	20.3
3.82×10^5	5.58	23.6
3.82×10^4	4.58	28.2
3.82×10^3	3.58	33.1

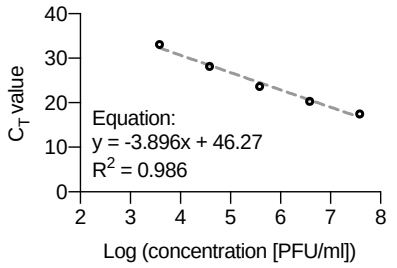

Non-lysogens

Bacteria concentration (CFU/ml)	Log (Phage concentration)	Average quantification cycle (C_T)
1.27×10^8	8.10	14.1
1.27×10^7	7.10	17.5
1.27×10^6	6.10	20.8
1.27×10^5	5.10	24.6
1.27×10^4	4.10	28.6

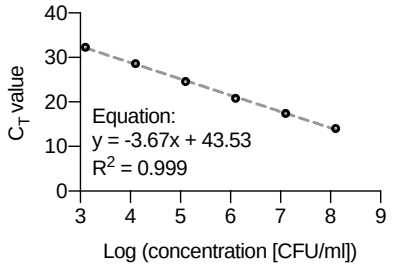

Lysogens

Bacteria concentration (CFU/ml)	Log (Phage concentration)	Average quantification cycle (C_T)
5.52×10^8	8.74	10.2
5.52×10^7	7.74	13.7
5.52×10^6	6.74	17.3
5.52×10^5	5.74	21.6
5.52×10^4	4.74	26.3

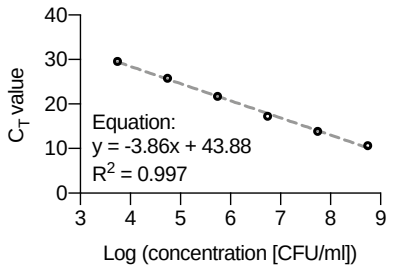

Total bacteria (16S)

Bacteria concentration (CFU/ml)	Log (Phage concentration)	Average quantification cycle (C_T)
1.27×10^8	8.10	12.9
1.27×10^7	7.10	16.6
1.27×10^6	6.10	20.8
1.27×10^5	5.10	25.9
1.27×10^4	4.10	30.3
1.27×10^3	3.10	34.7

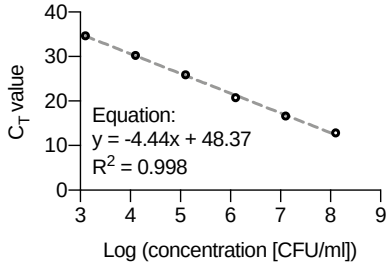

7.3. Gut-on-a-chip replicate 1 standard curves

λ^{VIR}

Phage concentration (PFU/ml)	Log (Phage concentration)	Average quantification cycle (C_T)
1.36×10^9	9.13	12.6
1.36×10^8	8.13	17.6
1.36×10^7	7.13	19.5
1.36×10^6	6.13	23.5
1.36×10^5	5.13	28.2
1.36×10^4	4.13	31.9

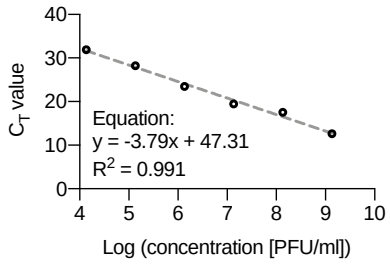

λ^{TEMP}

Phage concentration (PFU/ml)	Log (Phage concentration)	Average quantification cycle (C_T)
3.82×10^7	7.58	17.1
3.82×10^6	6.58	20.6
3.82×10^5	5.58	23.8
3.82×10^4	4.58	28.4
3.82×10^3	3.58	33.5

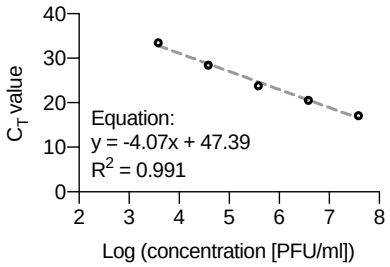

Non-lysogens

Bacteria concentration (CFU/ml)	Log (Phage concentration)	Average quantification cycle (C_T)
1.27×10^8	8.10	14.2
1.27×10^7	7.10	17.6
1.27×10^6	6.10	21.4
1.27×10^5	5.10	24.9
1.27×10^4	4.10	30.5

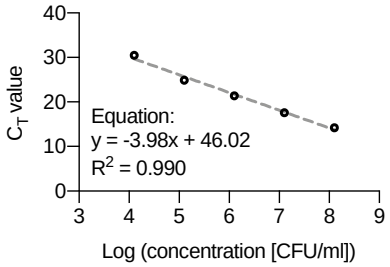

Lysogens

Bacteria concentration (CFU/ml)	Log (Phage concentration)	Average quantification cycle (C_T)
2.37×10^7	7.37	12.5
2.37×10^6	6.37	16.6
2.37×10^5	5.37	21.0
2.37×10^4	4.37	25.6
2.37×10^3	3.37	32.6
2.37×10^2	2.37	35.0

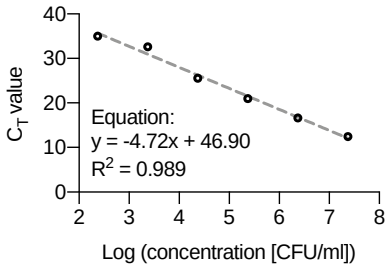

7.4. Gut-on-a-chip replicate 2 standard curves

λ^{VIR}

Phage concentration (PFU/ml)	Log (Phage concentration)	Average quantification cycle (C_T)
1.36×10^9	9.13	13.9
1.36×10^8	8.13	17.5
1.36×10^7	7.13	21.1
1.36×10^6	6.13	25.0
1.36×10^5	5.13	29.3
1.36×10^4	4.13	32.1

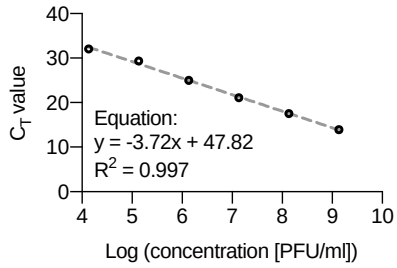

λ^{TEMP}

Phage concentration (PFU/ml)	Log (Phage concentration)	Average quantification cycle (C_T)
3.82×10^7	7.58	18.0
3.82×10^6	6.58	21.5
3.82×10^5	5.58	24.9
3.82×10^4	4.58	28.3
3.82×10^3	3.58	32.5
3.82×10^2	2.58	35.0

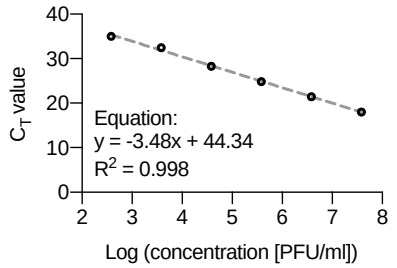

Non-lysogens

Bacteria concentration (CFU/ml)	Log (Phage concentration)	Average quantification cycle (C_T)
1.27×10^8	8.10	14.0
1.27×10^7	7.10	17.5
1.27×10^6	6.10	20.7
1.27×10^5	5.10	25.0
1.27×10^4	4.10	28.4
1.27×10^3	3.10	31.2

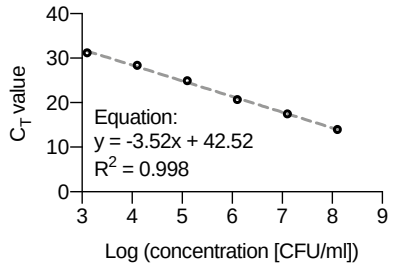

Lysogens

Bacteria concentration (CFU/ml)	Log (Phage concentration)	Average quantification cycle (C_T)
2.37×10^7	7.37	14.8
2.37×10^6	6.37	17.5
2.37×10^5	5.37	21.2
2.37×10^4	4.37	25.2
2.37×10^3	3.37	29.7

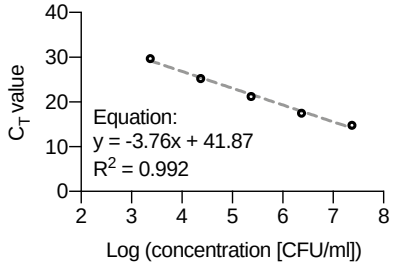

7.5. Gut-on-a-chip replicate 3 standard curves

λ^{VIR}

Phage concentration (PFU/ml)	Log (Phage concentration)	Average quantification cycle (C_T)
1.36×10^9	9.13	13.9
1.36×10^8	8.13	16.9
1.36×10^7	7.13	20.1
1.36×10^6	6.13	24.0
1.36×10^5	5.13	27.7
1.36×10^4	4.13	31.6

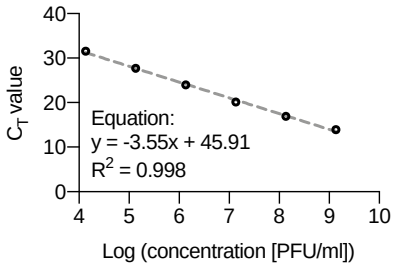

λ^{TEMP}

Phage concentration (PFU/ml)	Log (Phage concentration)	Average quantification cycle (C_T)
3.82×10^7	7.58	17.9
3.82×10^6	6.58	21.4
3.82×10^5	5.58	24.6
3.82×10^4	4.58	28.2
3.82×10^3	3.58	31.7
3.82×10^2	2.58	35.0

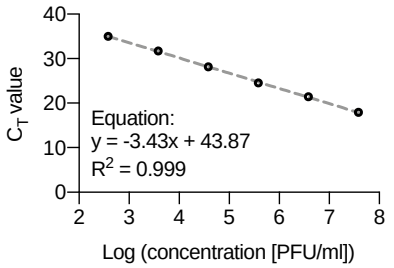

Non-lysogens

Bacteria concentration (CFU/ml)	Log (Phage concentration)	Average quantification cycle (C_T)
1.27×10^8	8.10	13.2
1.27×10^7	7.10	16.6
1.27×10^6	6.10	20.1
1.27×10^5	5.10	24.1
1.27×10^4	4.10	28.4
1.27×10^3	3.10	31.5

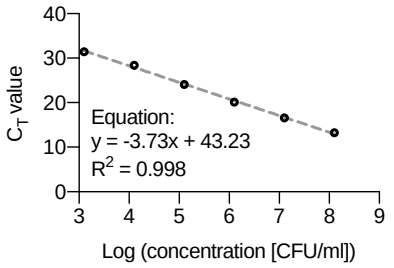

Lysogens

Bacteria concentration (CFU/ml)	Log (Phage concentration)	Average quantification cycle (C_T)
2.37×10^7	7.37	13.4
2.37×10^6	6.37	16.3
2.37×10^5	5.37	19.7
2.37×10^4	4.37	23.5
2.37×10^3	3.37	27.2
2.37×10^2	2.37	29.5